Spectroscopic Studies On Light Harvesting Materials Toward Enhanced Solar Energy Conversion

THESIS

SUBMITTED FOR THE DEGREE OF

DOCTOR OF PHILOSOPHY (SCIENCE)

BY

SAMIM SARDAR

DEPARTMENT OF CHEMISTRY

UNIVERSITY OF CALCUTTA

2016

To My Mother

Acknowledgements

At this moment of accomplishment, first and foremost, I owe my deepest gratitude to my research supervisor, Professor Samir Kumar Pal, for providing me the opportunity to work under his supervision. This work would not have been possible without his thoughtful guidance, warm encouragement, unconditional support, constant motivation, constructive criticism and inexhaustible help. I am extremely fortunate to have such an enthusiastic supervisor who sacrifices all his leisure for our academic success and always available to answer our queries despite his busy schedule. Sir has patiently provided guidance during the crucial moments in my work while simultaneously allowing me to express my ideas and work independently. I am grateful to him for allowing me to explore new areas of research, interact and collaborate with talented researchers from a number of different national and international institutes. I also thank him for providing me with the opportunity to work with a talented team of researchers and an excellent research environment.

I would like to thank Prof. Peter Lemmens of TU Braunschweig, Germany, Prof. Joydeep Dutta of KTH Royal Institute of Technology, Sweden, Prof. Omar F. Mohammed of KAUST, KSA, Prof. Saleh A. Ahmed of Umm Al-Qura University, KSA, Dr. Hynd Remita of Université Paris-Sud, France, Dr. Srabanti Ghosh, CGCRI, India and Dr. Chinmoy Bhattacharya of IIEST, India for fruitful collaborations.

I express my gratitude to all the faculty members and the staffs of S. N. Bose National Centre for Basic Sciences for their assistances in my research career. I acknowledge S. N. Bose National Centre for Basic Sciences for providing the research fellowship and Department of Science and Technology (DST), India for projects.

I'd like to express my sincere thanks to all my seniors and colleagues for providing a stimulating and enriching environment. Special thanks to Dr. Soumik Sarkar for helping me at the initial stage of my research work. I am also thankful to Siddhi di for helping me in the experiments related to biology. I am grateful to Nabarun for helping me out from many technical difficulties during my works related to solar cells. Special thanks to Jayita and Siddhi di for their assistance in formatting and proof-reading my thesis. My sincere appreciation goes to all my seniors: Dr. Abhinandan Makhal, Dr. Subrata Batabyal, Dr. Nirmal Goswami, Dr. Ranajay Saha, Dr. Tanumay Mondal, Dr. Surajit Rakshit, Dr. Anupam Giri, Dr. Soma Banerjee, Dr. Prasanna Kumar Mondal and all the present group members: Siddhi di, Nabarun, Susobhan, Prasenjit, Damayanti, Priya, Dr. Shreyasi Dutta, Tuhin, Jayita, Aniruddha, Probir, Ramesh and Soumendra da for providing a homely and a cheerful environment, and also for assisting me in research. A very special thanks to Nabarun and Susobhan with whom I shared many glorious moments over a long period of time. I will always miss their company in future. I also want to thank all my friends for the good times I shared with them. I pay tribute to all my teachers throughout my life.

Finally, I would like to pay high regards to my mother and all family members who support me through thick and thin, with love and affection. Without their sacrifices, moral support and blessings, this thesis would not have taken its shape.

Dated:
Department of Chemical, Biological and Macromolecular Sciences,
S. N. Bose National Centre for Basic Sciences,
Salt Lake, Kolkata 700106, India *(Samim Sardar)*

CONTENTS

Chapter 1

Introduction

1.1. Background

The sun is a star which is directly or indirectly the main source of energy in the solar system and essential for the existence of life. Solar radiation has been used by humanity in all ages as a renewable energy resource. The mammoth power that the Sun continuously delivers to Earth, 1.2×10^5 terawatts, dwarfs every other renewable or nonrenewable energy sources. The amount of energy humans use annually, about 4.6×10^{20} joules, is delivered to Earth by the Sun in one hour. Sunlight can be converted into electrical energy, chemical energy and thermal energy. The discovery of photovoltaic effect by Becquerel in 1839 and the invention of the first photovoltaic cell in the early 1950s opened entirely new perspectives on the use of solar energy for the production of electricity. Since then, the development of solar technologies continues at an unprecedented rate. Today, renewable energy accounts for over 20% of total global electricity generation. The current cost of solar technologies commercially available in the market is very high compared to the cheap fossil fuels. Due to the limited storage and adverse effect of the fossil fuels to the environment, the development of low-cost and high-efficiency photovoltaic device concepts using renewable and environment friendly resources is necessary to meet the increasing energy demand. Solar radiation can also yield chemical fuel via natural photosynthesis in green plants or artificial photosynthesis in human-engineered systems. In the 1970s, artificial photosynthesis gained huge interest because of the oil crisis. In addition, increasing environmental pollution issues prompt for finding potential solutions via solar energy routes to clean up water and environmental pollutions.

1.2. "Nanotechnology" for Solar Energy Conversion:

The term "nanotechnology" was first defined by Norio Taniguchi as follows: "nanotechnology mainly consists of the process of separation, consolidation, and deformation of materials by one atom or one molecule". It is the area of science and technology where extremely small size plays a critical role. By convention, dimensions between 1 and 100 nanometer (nm) are known as the nanoscale i.e., on the scale of 1 billionth to several tens of billionths of a meter. However, nanotechnology enables not only the miniaturization but also the precise manipulation of atoms and molecules to design and control the properties of the nanomaterials/nanosystems. Nanotechnology is extremely important because of their potential application in optoelectronics, catalysis, sensing, biology and medicine [1-5].

Due to the growing threat of pollution, global warming, and energy crises caused by our strong dependence on the shrinking supply of nonrenewable fossil fuels, the search for clean and renewable alternative energy resources is one of the most urgent challenges to the sustainable development of human civilization. In this direction, nanotechnology provides a powerful tool to develop cost-effective and efficient solar energy conversion systems. The interaction of light with the material can be tailored by modulating the size of the material in the nanoscale regime using quantum confinement effect. Nanotechnology enables the processing of low-cost semiconductors into photovoltaic and photocatalytic devices. The development of photocatalysis using nanomaterials has attracted wide spread attention of researchers for the last few years due to its less environmental pollution and higher amount of energy saving. Higher photocatalytic properties of nanomaterials are currently being used to convert solar energy into chemical energy to further oxidize the organic pollutants present in the waste water or minimize materials to get useful components together with hydrogen and hydrocarbons.

1.3. Scope of the Spectroscopic Investigation on Light Harvesting Materials toward Enhanced Solar Energy Conversion:

The efficient conversion of solar photons into electricity and chemical energy via cost effective solar devices is one of the most important scientific challenges in the recent time. For the last few decades, semiconductor nanostructure materials such as TiO_2, ZnO have been widely used in waste water purification and solar energy conversion [6-11]. However, the large bandgap of TiO_2 (~3.2 eV) and ZnO (~3.37 eV) requires excitation only at wavelengths less than 390 nm [12-13]. In this respect, the popular TiO_2, ZnO can only utilize ~5% of the incoming solar energy, thus restricting its practical applications as efficient solar light harvester. The key to the efficient solar energy conversion is the development of high performance functional materials which has well matched photo absorption with the solar spectrum, an efficient photoexcited charge separation to prevent electron–hole recombination and an adequate energy of charges to carry out the desired process. Many efforts have been made to trigger the optical response of the wide band gap semiconductors into the visible region by metal-ion doping [14], non-metal doping [15-16], noble metal deposition [17-18], narrow-bandgap semiconductors coupling [19-22], conducting polymer sensitization [23-24], and dye sensitization [25-30]. The formation of organic-inorganic and inorganic-inorganic light harvesting materials allows both a broader range of solar light absorption and an efficient charge separation. However, the activity of such heterogeneous systems critically depends on the charge dynamics across the involved nanostructured interface [31].

The key focus of this thesis is to investigate the photoinduced dynamical processes across the heterogeneous interface which is important from both fundamental and application perspectives, such as, efficient photocatalysts, photovoltaic devices and photo-medicines. Light harvesting materials used in

photocatalysis (PC) and dye sensitized solar cells (DSSC) are related to ultrafast excited state charge transfer across the interface [32-33]. Thus a precise knowledge of excited state charge transfer across oxide surfaces is important to fully understand the microscopic mechanism related to technologically important processes of PC and DSSC, both of which indeed have strong social impact. In one of our studies, we have investigated the role of central metal ion in biologically important organic pigment hematoporphyrin (HP) functionalized TiO_2 nanoparticles (NPs). The study reveals the role of iron ion and its oxidation states in electron transfer processes and its implications in the photocatalytic activity and photoresponse of the nanohybrid. In another study, we have functionalized zinc phthalocyanine (ZnPc) with two carboxyl groups containing a biologically important ligand, tartrate, using a facile wet chemistry route and duly sensitized ZnO to form nanohybrids for application in photocatalytic devices. Ultrafast photoinduced charge separation and charge recombination processes at the semiconductor-semiconductor (PbS-ZnO) interface are explored for efficient solar light harvesting. The incorporation of semiconductor nanocrystals into conjugated polymers can sensitize the semiconductor nanocrystals for renewable energy applications. In a recent study, we have explored the charge transfer mechanism in a heterostructure based on poly(diphenylbutadiyne) (PDPB) nanofibers and ZnO NPs by using the steady state and picosecond-resolved fluorescence studies. In order to fabricate efficient and low cost devices, we have tailored both the active electrode with silver modified TiO_2 (Ag-TiO_2) as well as the counter electrode (CE) with Pt-reduced graphene oxide (Pt@RGO) nanocomposites in a DSSC. The synergistic combination of both modified electrodes leads to an improved light to electrical energy conversion with an overall efficiency of 8%. In another study, we have employed carbonate doped TiO_2 mesoporous microspheres (doped MS) in photoanode of a N719 dye containing solar cell. Most importantly, for the first time we have demonstrated that the solar cells with doped MS offers better efficiency (7.6%) in light harvesting compared to MS

without doping (5.2%). In recent times, significant achievements in the use of ZnO NPs have been made as delivery vehicles of drugs and also to modulate the drug activity in the nanohybrid. The present research includes the exploration of the photoinduced ultrafast dynamics in a well-known cancer drug, protoporphyrin IX (PP) sensitized with ZnO NPs (PP−ZnO). We have successfully showed that the PP−ZnO nanohybrid exhibits enhanced activity in PDT compared to that of only PP. Here, ZnO NPs act as drug delivery vehicle and also facilitate the charge separation which eventually enhances the drug activity. In another study, we have explored the potential use of ZnO NPs as a phototherapeutic agent, by controlling the surface defect states of the NPs through a post-annealing treatment in oxygen rich atmosphere, in order to efficiently degrade bilirubin (BR) molecules through photocatalysis.

The experimental tools used for studying the dynamical processes involve picosecond-resolved carrier relaxation dynamics, such as, photoinduced electron transfer (PET) and Förster resonance energy transfer (FRET). Langmuir−Hinshelwood (L−H) model is used for surface catalysis. The different experimental techniques employed for the structural and functional characterization of the light harvesting materials include steady-state UV-VIS absorption and fluorescence, thermogravimetric analysis (TGA), Fourier transform infrared spectroscopy (FTIR), Raman scattering, dynamic light scattering (DLS), powder X-ray diffraction (XRD), cyclic voltammetry (CV), Field Emission scanning electron microscopy (FESEM), high-resolution transmission electron microscopy (HRTEM) and X-ray photoelectron spectroscopy (XPS). The DSSCs were fabricated and characterized by using photocurrent−voltage (J−V) measurements, incident photon-to-current conversion efficiency (IPCE) measurements, photovoltage decay measurements and electrochemical impedance spectroscopy. Furthermore, bacterial culture technique is also used to study the photodynamic activity.

1.4. Objective:

The use of nanoscale materials for efficient solar light harvesting has attracted immense attention in the recent time in order to address the energy and environmental issues. Among them, semiconductor materials such as TiO_2, ZnO have been widely used in the field of photocatalysis and dye-sensitized solar cells. However, due to limited visible-light activity and low photo-conversion efficiency, ZnO/TiO_2 needs to be modified to design heterostructures with efficient charge separation. The objective of this thesis is to unravel the ultrafast dynamical processes across the interface of heterostructures to enhance the solar light harvesting efficiency. The special emphasis has been given to the correlation between the ultrafast processes at the interface and their implications in the light harvesting applications.

In order to sensitize the oxides in the visible light, sensitization with visible light absorbing dyes is a prevalent solution. A considerable research effort in this direction stems from the desire to make cost effective and environment-compatible dye sensitized nanostructure-based solar light harvesting devices [34-35]. The synthesis and purification of best performing ruthenium-based dyes for the solar light harvesting devices is expensive [36]. In the context of cost and biocompatibility, porphyrin and phthalocyanine based solar devices are gaining great interest in the contemporary literature [37-42]. The incorporation of metal ions in the central cavity of porphyrin in the proximity of host semiconductor for efficient decontamination of drinking water is a subject of several recent reports [43-45]. Tuning the photo response [46], stability of the dyes upon metalation [47] and efficiency of photo injected electron [48] are studied in a series of reports [49]. However, correlation between the spectroscopic studies and their implication in light harvesting applications is sparse in the literature. One of our studies in this direction is aimed to investigated the critical role of central metal ions (Fe^{3+}/Fe^{2+}) incorporated in hematoporphyrin-TiO_2 nanohybrid in interfacial carrier dynamics

and its implications in solar light harvesting [26]. In order to attach porphyrin or phthalocyanine dyes to the wide band gap semiconductors, the dye must have an anchoring group or need to be modified to have an anchoring group. To avoid the modification of the dye which eventually increases the cost, we have functionalized zinc phthalocyanine (ZnPc) with two carboxyl groups containing a biologically important ligand, tartrate, using a facile wet chemistry route and duly sensitized ZnO nanostructures to form nanohybrids for potential application in photocatalytic devices [30].

As the stability of an organic dye on a wide band gap oxide material is an issue, another approach beside the organic dye sensitization is to combine the material with a semiconductor that has a narrow band gap and an energetically high-lying conduction band [50]. In this direction, Kamat [51] and co-workers show photoinduced electron transfer from CdSe quantum dots (QDs) of different sizes to three unique metal oxide (TiO_2, ZnO and SnO_2) and suggest that in addition to electron transfer at the QD-metal oxide interface, other loss mechanisms play key roles in the determination of overall device efficiency. In this direction, we have explored the ultrafast photoinduced charge separation and charge recombination processes at the semiconductor-semiconductor (PbS-ZnO) interface for efficient solar light harvesting [22]. The PbS-ZnO nanocomposite lead to efficient photovoltaics but their photocatalytic properties remain poor. This anomaly has been explained from the spectroscopic studies.

One of the most interesting ways to make heterostructures in the recent literature is amalgamation of semiconductor nanocrystals and polymers for the development of multifunctional materials that demonstrate superior electrical, optical and mechanical properties [52-56]. Thus, incorporation of semiconductor nanocrystals into conjugated polymers can sensitize the semiconductor nanocrystals for renewable energy applications such as bulk heterojunction–type photovoltaics and photocatalysis [57-62]. A series of heterojunctions based on

heterojunctions such as TiO_2-PANI, TiO_2-P3HT have been studied for the harvesting of visible light [63-67]. There is a common consensus that heterojunctions facilitate the migration of photoexcited electrons and holes across the interfaces to enhance charge separation. However, very few direct experimental evidences or spectroscopic observations have been explored to establish the charge transfer mechanism at the heterostructure interface. In one of the studies, we have explored the charge transfer mechanism in a heterostructure based on poly(diphenylbutadiyne) (PDPB) nanofibers [68] and ZnO NPs by using the steady state and picosecond-resolved photoluminescence studies [24].

Among various technologies, dye-sensitized solar cells (DSSCs) have attracted widespread attention as a solar energy conversion technology because of abundantly available low cost materials, ease of fabrication and relatively high photon to current conversion efficiency [7, 39, 69-73]. Extensive efforts have been made to improve the efficiency of DSSC by engineering all the components. In order to modulate the photoanode, thickness of the nanocrystalline titanium dioxide layer has been extensively studied to improve both the photocurrent and photovoltage [74-75]. Generally, lowering the thickness of the active layer reduces the recombination at the interface between electrode and electrolyte which in turn increases the efficiency. However, the dye loading also decreases with decreasing thickness resulting in lower photocurrents. To combat this problem, surface modification of semiconductor NPs with plasmonic metal nanostructures such as gold, silver and copper have been investigated recently [18, 76-81]. However, significant improvement of the photovoltage by surface modification with silver is reported sparsely in the literature. In this direction, we have tailored both the active electrode with silver modified TiO_2 (Ag-TiO_2) as well as the counter electrode (CE) with Pt-reduced graphene oxide (Pt@RGO) nanocomposites to realize efficient and low cost devices [82]. In another study, we have used

carbonate doped TiO_2 mesoporous microspheres (doped MS) in photoanode of a N719 dye containing solar cell [83].

In recent years, use of nanotechnology in medical science is gaining a lot of attention across the world. Research focusing on the use of various nanostructured materials in different areas, such as for drug delivery [84], cancer treatments [85-86] etc. is underway. Out of the numerous nanostructured materials, ZnO is one of the most promising materials for the applications in the medical fields due to its biocompatibility, biodegradability and non-toxicity [87]. Furthermore, defect mediated energy emitted from the ZnO nanostructures can also effectively degrade various organic compounds in water through Förster Resonance Energy Transfer (FRET) [88]. In this direction, we have explored the potential use of ZnO NPs as a phototherapeutic agent, by controlling the surface defect states of the NPs through a post-annealing treatment in oxygen rich atmosphere, in order to efficiently degrade BR molecules through FRET [89]. In another study, we have explored the key photoinduced dynamics in ZnO NPs upon complexation with a model cancer drug protoporphyrin IX (PP) [27]. We have also used the nanohybrid in a model photodynamic therapy application in a light sensitized bacteriological culture experiment. The exploration of key photoinduced dynamics in the porphyrin based nanohybrids will be helpful in designing future photodynamic agents.

1.5. Summary of the Work Done:

1.5.1. Excited State Dynamics of a Light Harvesting Molecule in the Proximity of Wide Band Gap Semiconductor Nanostructures:

1.5.1.1. Role of Central Metal Ion in Hematoporphyrin-Functionalized Titania in Solar Energy Conversion Dynamics [26]: In this study, we have investigated the efficacy of electron transfer processes in hematoporphyrin (HP) and iron

hematoporphyrin ((Fe)HP) sensitized titania as potential materials for capturing and storing solar energy. Steady-state and picosecond-resolved fluorescence studies show the efficient photoinduced electron transfer processes in hematoporphyrin-TiO_2 (HP-TiO_2) and Fe(III)-hematoporphyrin-TiO_2 (Fe(III)HP-TiO_2) nanohybrids, which reveal the role of central metal ions in electron transfer processes. The bidentate covalent attachment of HP onto TiO_2 particulates is confirmed by FTIR, Raman scattering and X-ray photoelectron spectroscopy (XPS) studies. The iron oxidation states and the attachment of iron to porphyrin through pyrrole nitrogen atoms were investigated by cyclic voltametry and FTIR studies, respectively. We also investigated the potential application of HP-TiO_2 and Fe(III)HP-TiO_2 nanohybrids for the photodegradation of a model organic pollutant methylene blue (MB) in aqueous solution under wavelength dependent light irradiation. To further investigate the role of iron oxidation states in electron transfer processes, photocurrent measurements were done by using Fe(III) and Fe(II) ions in porphyrin. This work demonstrates the role of central metal ions in fundamental electron transfer processes in porphyrin sensitized titania and its implication in dye-sensitized device performance.

1.5.1.2. Ultrafast Dynamics at the Zinc Phthalocyanine/Zinc Oxide Nanohybrid Interface for Efficient Solar Light Harvesting in the near Red Region [30]: Phthalocyanine-based light harvesting nanomaterials are attractive due to their low cost, eco-friendly properties and sensitivity in the red region of the solar spectrum. However, for any practical application, phthalocyanines need to be chemically modified for anchoring groups with wide-band semiconducting nanomaterials. In this study, zinc phthalocyanine (ZnPc) was functionalized with two carboxyl groups containing a biologically important ligand, tartrate, using a facile wet chemistry route and duly sensitized zinc oxide (ZnO) to form nanohybrids for application in photocatalytic devices. The nanohybrids have been characterized using a high-resolution transmission/scanning electron microscope

(HRTEM, FEG-SEM), X-ray diffraction (XRD), steady-state infrared/UV-VIS absorption and emission spectroscopy for their structural details and optical properties, whereas the ultrafast dynamical events, which are key for understanding the photocatalytic activities, were monitored using picosecond resolution fluorescence techniques. More specifically, vibrational spectroscopy (FTIR) revealed the covalent connection of ZnPc with the host ZnO nanoparticles via the tartrate ligand. The efficiency of the material for photocatalysis under red light irradiation was found to be significantly enhanced compared to bare ZnO. To make a prototype for a potential application in a flow device for water decontamination, we have sensitized ZnO nanorods (ZnO NR) with tartrate-functionalized ZnPc. The molecular proximity of ZnPc to the ZnO surface has been confirmed by picosecond resolution Förster resonance energy transfer (FRET). The excited-state electron transfer dynamics, as revealed by a picosecond resolution fluorescence study (TCSPC), is in good agreement with the enhanced charge separation at the interface of the nanohybrid. The enhanced photoresponse, wavelength-dependent photocurrent of the sensitized nanorods and photodegradation of a model water pollutant in a prototype device format confirmed the potential use of the nanohybrids in water purification.

1.5.2. Key Interfacial Carrier Dynamics in Inorganic-Inorganic Nanohybrids for Enhanced Light Harvesting Application:

1.5.2.1. Interfacial Carrier Dynamics in PbS-ZnO Light Harvesting Assemblies and their Potential Implication in Photovoltaic/ Photocatalysis Application [22]: In many cases light harvesting nanomaterials are commonly applied as photovoltaics as well as photocatalyst materials. However, such a dual use depends critically on the charge dynamics across the involved nanostructured interface. Here, we have investigated PbS-ZnO light harvesting assemblies (LHAs) that can lead to efficient photovoltaics. In contrast, their photocatalytic properties remain poor. We demonstrate that fundamental, ultrafast photoinduced charge

separation and charge recombination processes at the semiconductor-semiconductor interface are key factors for the dual application of LHAs. In the course of our investigation, we have synthesized and characterized the PbS-ZnO LHAs using high resolution transmission electron microscopy (HRTEM) and UV-VIS absorption spectroscopy. Picosecond-resolved photoluminescence study has been employed to investigate the ultrafast interfacial charge transfer dynamics within the LHA upon photoexcitation. Picosecond-resolved PL-quenching of ZnO NPs show FRET from donor ZnO NPs to the acceptor PbS QDs and the latter has been employed to confirm the proximity of PbS to the host ZnO with molecular resolution. The photocatalytic activity of PbS−ZnO LHAs is probed by monitoring the photoreduction of the test contaminant MB and correlated with ultrafast spectroscopic studies on LHAs. This allows a conclusion on the role of ultrafast electron shuttling across the interface in making the electron unavailable for a reduction of MB. The prospective use of the LHAs in photovoltaics is investigated by photoelectrochemical studies where working electrodes of PbS-ZnO LHAs show higher photocurrents than that of bare ZnO NPs. This clearly indicates that the presence of an Indium tin oxide (ITO) substrate provides directionality to the shuttling electrons at the PbS-ZnO interface. The exploration of interfacial carrier dynamics in PbS-ZnO LHAs will be helpful in improving the design and efficiency of future solar energy harvesting devices.

1.5.3. Ultrafast Carrier Dynamics in Inorganic-Organic Nanohybrid for Enhanced Solar Light Harvesting:

1.5.3.1. Enhanced Charge Separation and FRET at Heterojunctions between Semiconductor Nanoparticles and Conducting Polymer Nanofibers for Efficient Solar Light Harvesting [24]: Energy harvesting from solar light employing nanostructured materials offer an economic way to resolve energy and environmental issues. We have developed an efficient light harvesting heterostructure based on poly(diphenylbutadiyne) (PDPB) nanofibers and ZnO

NPs via a solution phase synthetic route. ZnO NPs (~20 nm) were homogeneously loaded onto the PDPB nanofibers as evident from several analytical and spectroscopic techniques. The photoinduced electron transfer from PDPB nanofibers to ZnO NPs has been confirmed by steady state and picosecond-resolved photoluminescence studies. The co-sensitization for multiple photon harvesting (with different energies) at the heterojunction has been achieved via a systematic extension of conjugation from monomeric to polymeric diphenyl butadiyne moiety in the proximity of the ZnO NPs. On the other hand, energy transfer from the surface defects of ZnO NPs (~5 nm) to PDPB nanofibers through FRET confirms the close proximity with molecular resolution. The manifestation of efficient charge separation has been realized with ~5 fold increase in photocatalytic degradation of organic pollutants in comparison to polymer nanofibers counterpart under visible light irradiation. Our results provide a novel approach for the development of nanoheterojunctions for efficient light harvesting which will be helpful in designing future solar devices.

1.5.4. Essential Dynamics in Plasmonic Nanostructure for Enhanced Solar Photovoltaic Application:

1.5.4.1. Enhanced Photovoltage in DSSC: Synergistic Combination of Silver Modified TiO_2 Photoanode and Low Cost Counter Electrode [82]: In this study, we have tailored both the active electrode with silver modified TiO_2 (Ag-TiO_2) as well as the counter electrode (CE) with Pt-reduced graphene oxide (Pt@RGO) nanocomposites to realize efficient and low cost devices. The synergistic combination of both modified electrodes leads to an improved light to electrical energy conversion with an overall efficiency of 8%. An increase in the photovoltage (Voc) of ~16% (0.74 to 0.86 V) is achieved using Ag-TiO_2 in comparison to the bare TiO_2. This can be attributed to the shifting of the quasi-Fermi level of the TiO_2 photoanode close to the conduction band in presence of Ag

NPs due to the formation of schottky barrier. On the other hand, the facile synthesis of Pt NPs on RGO nanosheets by photo-reduction method without using chemical reducing or stabilizing agents demonstrates a higher efficiency than Pt as a CE due to cooperation of the catalytic activity of Pt and the high electron conductivity of the RGO as stable supporting material having more interfacial active sites. The quantity of Pt in the Pt@RGO nanocomposites is 10 times lower than in the Pt CE which reduces the cost and makes it viable for large scale commercial utilization.

1.5.5. Facile Carbonate Doping in Mesoporous TiO_2 Microspheres for Dye Sensitized Solar Cell with Enhanced Efficiency:

1.5.5.1. Carbonate Doping in TiO_2 Microsphere: The Key Parameter Influencing Others for Efficient Dye Sensitized Solar Cell [83]: Four key parameters namely light trapping, density of light harvesting centre, photoinduced electron injection and electron transport without self-recombination are universally important across all kinds of solar cells. In this study, we have considered the parameters in the context of a model Dye Sensitized Solar Cell (DSSC). Our experimental studies reveal that carbonate doping of TiO_2 mesoporous microspheres (doped MS) makes positive influence to all the above mentioned key parameters responsible for the enhanced solar cell efficiency. A simple method has been employed to synthesize the doped MS for the photoanode of a N719 (ruthenium dye)-based DSSC. A detailed electron microscopy has been used to characterize the change in morphology of the MS upon doping. The optical absorption spectrum of the doped MS reveals significant shift of TiO_2 (compared to that of the MS without doping) towards maximum solar radiance (~500 nm) and the excellent scattering in the entire absorption band of the sensitizing dye (N719). Finally, and most importantly, for the first time we have demonstrated that the solar cells with doped MS offers better efficiency (7.6%) in light harvesting compared to MS

without doping (5.2%) and also reveal minimum self recombination of photoelectrons in the redox chain.

1.5.6. Key Light Harvesting Dynamics in Various Nanostructures for Biomedical Application:

1.5.6.1. Modulation of Defect Mediated Energy Transfer from ZnO Nanoparticles for the Photocatalytic Degradation of Bilirubin [89]: In recent years, nanotechnology has gained significant interest for applications in the medical field. In this regard, utilization of the ZnO NPs for the efficient degradation of bilirubin (BR) via photocatalysis technique was explored. BR is a water insoluble byproduct of heme catabolism that can cause jaundice when its excretion is impaired. The ZnO NP activated photocatalytic degradation of BR through a non-radiative energy transfer pathway can be influenced by the surface defect states (mainly the oxygen vacancies) of the catalyst nanoparticles, which was modulated via a simple post-annealing treatment in oxygen rich atmosphere. The mechanism of the energy transfer process between the ZnO NPs and the surface adsorbed BR molecules was studied using steady state and picosecond-resolved fluorescence spectroscopy technique. Correlation of photocatalytic degradation and time-correlated single photon counting (TCSPC) studies revealed that the defect engineered ZnO NPs obtained through post-annealing treatments led to an efficient decomposition of BR molecules enabled by FRET process.

1.5.6.2. Direct Observation of Key Photoinduced Dynamics in a Potential Nano-delivery Vehicle of Cancer Drugs [27]: In recent times, significant achievements in the use of ZnO NPs as delivery vehicles of cancer drugs have been made. The present study is an attempt to explore the key photoinduced dynamics in ZnO NPs upon complexation with a model cancer drug protoporphyrin IX (PP). The nanohybrid has been characterized by FTIR, Raman scattering and UV-VIS absorption spectroscopy. Picosecond-resolved FRET from the defect mediated

emission of ZnO NPs to PP has been used to study the formation of the nanohybrid at the molecular level. Picosecond-resolved fluorescence studies of PP−ZnO nanohybrids reveal efficient electron migration from photoexcited PP to ZnO, eventually enhancing the ROS activity. The dichlorofluorescin (DCFH) oxidation and no oxidation of luminol in PP/PP-ZnO nanohybrids upon green light illumination indicate that the nature of ROS is essentially singlet oxygen rather superoxide anions. Direct evidence of the role of electron transfer as a key player for enhanced ROS generation from the nanohybrid is also clear from the photocurrent measurement studies. We have also used the nanohybrid in a model photodynamic therapy application in a light sensitized bacteriological culture experiment.

1.6. Plan of Thesis:

The plan of the thesis is as follows:

Chapter 1: This chapter gives a brief introduction to the scope and motivation behind the thesis work. A brief summary of the work done is also included in this chapter.

Chapter 2: This chapter provides a brief overview of the steady-state and dynamical tools, the structural aspects of dyes and fluorescent probes used in the experiments.

Chapter 3: Details of instrumentation, data analysis and experimental procedures have been discussed in this chapter.

Chapter 4: In this chapter, the fundamental electron and energy transfer processes in dye sensitized wide band gap semiconductors are investigated. The role of central metal ion in the porphyrin sensitized titania is explored as a means of harvesting solar energy. ZnO nanostructures are sensitized with ZnPc through a tartrate ligand and fabricated a prototype device for the degradation of organic polllutants.

Chapter 5: Dynamical processes in PbS-ZnO light harvesting assemblies upon photoexcitation and their implications in photocatalytic and photovoltaic applications is elaborated in this chapter.

Chapter 6: The co-sensitization of ZnO NPs by multiple states of polymer nanofibers originated from oligomeric and polymer chain unit which leads to enhanced photocatalytic activity and photoresponse is discussed in the chapter.

Chapter 7: In order to enhance the solar cell efficiency, the modifications of both the photoanode and counter electrode by using Ag-TiO_2 and Pt@RGO have been described in this chapter.

Chapter 8: In this chapter, the use of carbonate doped TiO_2 microspheres in the photoanode of a DSSC to optimize several key parameters has been presented.

Chapter 9: The modulation of defect state emission of ZnO NPs to degrade bilirubin via FRET process is discussed. The use of ZnO NPs as drug delivery vehicle of a well-known cancer drug protoporphyrin IX has also been described in this chapter.

References

[1] P.K. Jain, X. Huang, I.H. El-Sayed, M.A. El-Sayed, Noble Metals on the Nanoscale: Optical and Photothermal Properties and Some Applications in Imaging, Sensing, Biology, and Medicine, *Acc. Chem. Res.* 41 (2008) 1578-1586.

[2] P.C. Ray, Size and Shape Dependent Second Order Nonlinear Optical Properties of Nanomaterials and Their Application in Biological and Chemical Sensing, *Chem. Rev.* 110 (2010) 5332-5365.

[3] P.V. Kamat, Meeting the Clean Energy Demand: Nanostructure Architectures for Solar Energy Conversion, *J. Phys. Chem. C* 111 (2007) 2834-2860.

[4] E. Serrano, G. Rus, J. García-Martínez, Nanotechnology for Sustainable Energy, *Renew. Sustainable Energy Rev.* 13 (2009) 2373-2384.

[5] A.S. Arico, P. Bruce, B. Scrosati, J.-M. Tarascon, W. van Schalkwijk, Nanostructured Materials for Advanced Energy Conversion and Storage Devices, *Nat. Mater.* 4 (2005) 366-377.

[6] A. Fujishima, K. Honda, Electrochemical Photolysis of Water at a Semiconductor Electrode, *Nature* 238 (1972) 37-38.

[7] B. O'Regan, M. Gratzel, A Low-Cost, High-Efficiency Solar Cell Based on Dye-Sensitized Colloidal TiO_2 Films, *Nature* 353 (1991) 737-740.

[8] N. Serpone, A.V. Emeline, Semiconductor Photocatalysis — Past, Present, and Future Outlook, *J. Phys. Chem. Lett.* 3 (2012) 673-677.

[9] O. Legrini, E. Oliveros, A.M. Braun, Photochemical Processes for Water Treatment, *Chem. Rev.* 93 (1993) 671-698.

[10] M.A. Fox, M.T. Dulay, Heterogeneous Photocatalysis, *Chem. Rev.* 93 (1993) 341-357.

[11] M.R. Hoffmann, S.T. Martin, W. Choi, D.W. Bahnemann, Environmental Applications of Semiconductor Photocatalysis, *Chem. Rev.* 95 (1995) 69-96.

[12] J. Schneider, M. Matsuoka, M. Takeuchi, J. Zhang, Y. Horiuchi, M. Anpo, D.W. Bahnemann, Understanding TiO_2 Photocatalysis: Mechanisms and Materials, *Chem. Rev.* 114 (2014) 9919-9986.

[13] M.D. Hernandez-Alonso, F. Fresno, S. Suarez, J.M. Coronado, Development of Alternative Photocatalysts to TiO_2: Challenges and Opportunities, *Energy Environ. Sci.* 2 (2009) 1231-1257.

[14] C. Chen, X. Li, W. Ma, J. Zhao, H. Hidaka, N. Serpone, Effect of Transition Metal Ions on the TiO_2-Assisted Photodegradation of Dyes under Visible Irradiation: A Probe for the Interfacial Electron Transfer Process and Reaction Mechanism, *J. Phys. Chem. B* 106 (2002) 318-324.

[15] R. Asahi, T. Morikawa, T. Ohwaki, K. Aoki, Y. Taga, Visible-Light Photocatalysis in Nitrogen-Doped Titanium Oxides, *Science* 293 (2001) 269-271.

[16] N. Lu, X. Quan, J. Li, S. Chen, H. Yu, G. Chen, Fabrication of Boron-Doped TiO_2 Nanotube Array Electrode and Investigation of Its Photoelectrochemical Capability, *J. Phys. Chem. C* 111 (2007) 11836-11842.

[17] X.Z. Li, F.B. Li, Study of Au/Au^{3+}-TiO_2 Photocatalysts toward Visible Photooxidation for Water and Wastewater Treatment, *Environ. Sci. Technol.* 35 (2001) 2381-2387.

[18] S. Sarkar, A. Makhal, T. Bora, S. Baruah, J. Dutta, S.K. Pal, Photoselective Excited State Dynamics in ZnO-Au Nanocomposites and Their Implications in Photocatalysis and Dye-Sensitized Solar Cells, *Phys. Chem. Chem. Phys.* 13 (2011) 12488-12496.

[19] Z. Zhang, W. Wang, L. Wang, S. Sun, Enhancement of Visible-Light Photocatalysis by Coupling with Narrow-Band-Gap Semiconductor: A Case Study on Bi_2S_3/Bi_2WO_6, *ACS Appl. Mater. Interfaces* 4 (2012) 593-597.

[20] J. Jiang, X. Zhang, P. Sun, L. Zhang, ZnO/BiOI Heterostructures: Photoinduced Charge-Transfer Property and Enhanced Visible-Light Photocatalytic Activity, *J. Phys. Chem. C* 115 (2011) 20555-20564.

[21] G.-S. Li, D.-Q. Zhang, J.C. Yu, A New Visible-Light Photocatalyst: CdS Quantum Dots Embedded Mesoporous TiO_2, *Environ. Sci. Technol.* 43 (2009) 7079-7085.

[22] S. Sardar, P. Kar, S. Sarkar, P. Lemmens, S.K. Pal, Interfacial Carrier Dynamics in PbS-ZnO Light Harvesting Assemblies and Their Potential Implication in Photovoltaic/ Photocatalysis Application, *Sol. Energ. Mat. Sol. Cells* 134 (2015) 400-406.

[23] H. Zhang, R. Zong, J. Zhao, Y. Zhu, Dramatic Visible Photocatalytic Degradation Performances Due to Synergetic Effect of TiO_2 with PANI, *Environ. Sci. Technol.* 42 (2008) 3803-3807.

[24] S. Sardar, P. Kar, H. Remita, B. Liu, P. Lemmens, S.K. Pal, S. Ghosh, Enhanced Charge Separation and FRET at Heterojunctions between Semiconductor Nanoparticles and Conducting Polymer Nanofibers for Efficient Solar Light Harvesting, *Sci. Rep.* 5 (2015) 17313.

[25] S. Sarkar, A. Makhal, T. Bora, K. Lakhsman, A. Singha, J. Dutta, S.K. Pal, Hematoporphyrin–ZnO Nanohybrids: Twin Applications in Efficient Visible-Light Photocatalysis and Dye-Sensitized Solar Cells, *ACS Appl. Mater. Interfaces* 4 (2012) 7027-7035.

[26] S. Sardar, S. Sarkar, M.T.Z. Myint, S. Al-Harthi, J. Dutta, S.K. Pal, Role of Central Metal Ions in Hematoporphyrin-Functionalized Titania in Solar Energy Conversion Dynamics, *Phys. Chem. Chem. Phys.* 15 (2013) 18562-18570.

[27] S. Sardar, S. Chaudhuri, P. Kar, S. Sarkar, P. Lemmens, S.K. Pal, Direct Observation of Key Photoinduced Dynamics in a Potential Nano-Delivery Vehicle of Cancer Drugs, *Phys. Chem. Chem. Phys.* 17 (2015) 166-177.

[28] S. Sardar, P. Kar, S.K. Pal, The Impact of Central Metal Ions in Porphyrin Functionalized ZnO/TiO_2 for Enhanced Solar Energy Conversion, *J. Mat. NanoSci.* 1 (2014) 12-30.

[29] P. Kar, S. Sardar, E. Alarousu, J. Sun, Z.S. Seddigi, S.A. Ahmed, E.Y. Danish, O.F. Mohammed, S.K. Pal, Impact of Metal Ions in Porphyrin-Based Applied

Materials for Visible-Light Photocatalysis: Key Information from Ultrafast Electronic Spectroscopy, *Chem. Eur. J.* 20 (2014) 10475-10483.

[30] Z.S. Seddigi, S.A. Ahmed, S. Sardar, S. K. Pal, Ultrafast Dynamics at the Zinc Phthalocyanine/Zinc Oxide Nanohybrid Interface for Efficient Solar Light Harvesting in the near Red Region, *Sol. Energ. Mat. Sol. Cells* 143 (2015) 63-71.

[31] P.V. Kamat, Manipulation of Charge Transfer across Semiconductor Interface. A Criterion That Cannot Be Ignored in Photocatalyst Design, *J. Phys. Chem. Lett.* 3 (2012) 663-672.

[32] S.G. Kumar, L.G. Devi, Review on Modified TiO_2 Photocatalysis under UV/Visible Light: Selected Results and Related Mechanisms on Interfacial Charge Carrier Transfer Dynamics, *J. Phys. Chem. A* 115 (2011) 13211-13241.

[33] J. Nieto-Pescador, B. Abraham, L. Gundlach, Photoinduced Ultrafast Heterogeneous Electron Transfer at Molecule-Semiconductor Interfaces, *J. Phys. Chem. Lett.* 5 (2014) 3498-3507.

[34] H. Zhou, T. Fan, D. Zhang, Biotemplated Materials for Sustainable Energy and Environment: Current Status and Challenges, *ChemSusChem* 4 (2011) 1344-1387.

[35] Y. Sun, Q. Wu, G. Shi, Graphene Based New Energy Materials, *Energy Environ. Sci.* 4 (2011) 1113-1132.

[36] L.M. Peter, The Grätzel Cell: Where Next?, *J. Phys. Chem. Lett.* 2 (2011) 1861-1867.

[37] N. Robertson, Optimizing Dyes for Dye-Sensitized Solar Cells, *Angew. Chem. Int. Ed.* 45 (2006) 2338-2345.

[38] H. Hayashi, I.V. Lightcap, M. Tsujimoto, M. Takano, T. Umeyama, P.V. Kamat, H. Imahori, Electron Transfer Cascade by Organic/Inorganic Ternary Composites of Porphyrin, Zinc Oxide Nanoparticles, and Reduced Graphene Oxide on a Tin Oxide Electrode That Exhibits Efficient Photocurrent Generation, *J. Am. Chem. Soc.* 133 (2011) 7684-7687.

[39] A. Yella, H.-W. Lee, H.N. Tsao, C. Yi, A.K. Chandiran, M.K. Nazeeruddin, E.W.-G. Diau, C.-Y. Yeh, S.M. Zakeeruddin, M. Grätzel, Porphyrin-Sensitized Solar Cells with Cobalt (II/III)–Based Redox Electrolyte Exceed 12 Percent Efficiency, *Science* 334 (2011) 629-634.

[40] L.-L. Li, E.W.-G. Diau, Porphyrin-Sensitized Solar Cells, *Chem. Soc. Rev.* 42 (2013) 291-304.

[41] M.-y. Duan, J. Li, G. Mele, C. Wang, X.-f. Lu¨, G. Vasapollo, F.-x. Zhang, Photocatalytic Activity of Novel Tin Porphyrin/TiO_2 Based Composites, *J. Phys. Chem. C* 114 (2010) 7857-7862.

[42] S.D. Oosterhout, M.M. Wienk, S.S. van Bavel, R. Thiedmann, L. Jan Anton Koster, J. Gilot, J. Loos, V. Schmidt, R.A.J. Janssen, The Effect of Three-Dimensional Morphology on the Efficiency of Hybrid Polymer Solar Cells, *Nat. Mater.* 8 (2009) 818-824.

[43] W.-j. Sun, J. Li, G.-p. Yao, M. Jiang, F.-x. Zhang, Efficient Photo-Degradation of 4-Nitrophenol by Using New Cupp-TiO_2 Photocatalyst under Visible Light Irradiation, *Catal. Commun.* 16 (2011) 90-93.

[44] T. Shiragami, J. Matsumoto, H. Inoue, M. Yasuda, Antimony Porphyrin Complexes as Visible-Light Driven Photocatalyst, *J. Photochem. Photobiol. C* 6 (2005) 227-248.

[45] W.-j. Sun, J. Li, G.-p. Yao, F.-x. Zhang, J.-L. Wang, Surface-Modification of TiO_2 with New Metalloporphyrins and Their Photocatalytic Activity in the Degradation of 4-Notrophenol, *Appl. Surf. Sci.* 258 (2011) 940-945.

[46] H.-P. Lu, C.-Y. Tsai, W.-N. Yen, C.-P. Hsieh, C.-W. Lee, C.-Y. Yeh, E.W.-G. Diau, Control of Dye Aggregation and Electron Injection for Highly Efficient Porphyrin Sensitizers Adsorbed on Semiconductor Films with Varying Ratios of Coadsorbate, *J. Phys. Chem. C* 113 (2009) 20990-20997.

[47] S. Afzal, W.A. Daoud, S.J. Langford, Photostable Self-Cleaning Cotton by a Copper(II) Porphyrin/TiO_2 Visible-Light Photocatalytic System, *ACS Appl. Mater. Interfaces* 5 (2013) 4753-4759.

[48] E.M. Barea, V. Gónzalez-Pedro, T. Ripollés-Sanchis, H.-P. Wu, L.-L. Li, C.-Y. Yeh, E.W.-G. Diau, J. Bisquert, Porphyrin Dyes with High Injection and Low Recombination for Highly Efficient Mesoscopic Dye-Sensitized Solar Cells, *J. Phys. Chem. C* 115 (2011) 10898-10902.

[49] M.K. Panda, K. Ladomenou, A.G. Coutsolelos, Porphyrins in Bio-Inspired Transformations: Light-Harvesting to Solar Cell, *Coord. Chem. Rev.* 256 (2012) 2601-2627.

[50] P.V. Kamat, Quantum Dot Solar Cells. Semiconductor Nanocrystals as Light Harvesters, *J. Phys. Chem. C* 112 (2008) 18737-18753.

[51] K. Tvrdy, P.A. Frantsuzov, P.V. Kamat, Photoinduced Electron Transfer from Semiconductor Quantum Dots to Metal Oxide Nanoparticles, *Proc. Natl. Acad. Sci.* 108 (2011) 29-34.

[52] A.C. Balazs, T. Emrick, T.P. Russell, Nanoparticle Polymer Composites: Where Two Small Worlds Meet, *Science* 314 (2006) 1107-1110.

[53] S. Ghosh, A.H. Khan, S. Acharya, Fabrication of Highly Stable, Hybrid PbS Nanocomposites in Pamam Dendrimer Matrix for Photodetection, *J. Phys. Chem. C* 116 (2012) 6022-6030.

[54] S. Ghosh, D. Ghosh, P.K. Bag, S.C. Bhattacharya, A. Saha, Aqueous Synthesis of ZnTe/Dendrimer Nanocomposites and Their Antimicrobial Activity: Implications in Therapeutics, *Nanoscale* 3 (2011) 1139-1148.

[55] S. Sinha Ray, Polylactide-Based Bionanocomposites: A Promising Class of Hybrid Materials, *Acc. Chem. Res.* 45 (2012) 1710-1720.

[56] L. Di Michele, A. Zaccone, E. Eiser, Analytical Theory of Polymer-Network-Mediated Interaction between Colloidal Particles, *Proc. Natl. Acad. Sci.* 109 (2012) 10187-10192.

[57] Y. Wang, Q. Wang, X. Zhan, F. Wang, M. Safdar, J. He, Visible Light Driven Type II Heterostructures and Their Enhanced Photocatalysis Properties: A Review, *Nanoscale* 5 (2013) 8326-8339.

[58] N. Zhang, S. Liu, Y.-J. Xu, Recent Progress on Metal Core@Semiconductor Shell Nanocomposites as a Promising Type of Photocatalyst, *Nanoscale* 4 (2012) 2227-2238.

[59] Y. Qu, X. Duan, Progress, Challenge and Perspective of Heterogeneous Photocatalysts, *Chem. Soc. Rev.* 42 (2013) 2568-2580.

[60] Q. Li, X. Jin, X. Yang, C. Chen, Z. Chen, Y. Qin, T.-h. Wei, W. Sun, Reducing the Excess Energy Offset in Organic/Inorganic Hybrid Solar Cells: Toward Faster Electron Transfer, *Appl. Catal., B* 162 (2015) 524-531.

[61] X. Jin, W. Sun, Z. Chen, T. Wei, C. Chen, X. He, Y. Yuan, Y. Li, Q. Li, Exciton Generation/Dissociation/Charge-Transfer Enhancement in Inorganic/Organic Hybrid Solar Cells by Robust Single Nanocrystalline Lnpxoy (Ln = Eu, Y) Doping, *ACS Appl. Mater. Interfaces* 6 (2014) 8771-8781.

[62] G. Xing, N. Mathews, S. Sun, S.S. Lim, Y.M. Lam, M. Grätzel, S. Mhaisalkar, T.C. Sum, Long-Range Balanced Electron- and Hole-Transport Lengths in Organic-Inorganic $CH_3NH_3PbI_3$, *Science* 342 (2013) 344-347.

[63] D. Wang, J. Zhang, Q. Luo, X. Li, Y. Duan, J. An, Characterization and Photocatalytic Activity of Poly(3-Hexylthiophene)-Modified TiO_2 for Degradation of Methyl Orange under Visible Light, *J. Hazard. Mater.* 169 (2009) 546-550.

[64] G. Liao, S. Chen, X. Quan, H. Chen, Y. Zhang, Photonic Crystal Coupled TiO_2/Polymer Hybrid for Efficient Photocatalysis under Visible Light Irradiation, *Environ. Sci. Technol.* 44 (2010) 3481-3485.

[65] Q. Luo, L. Bao, D. Wang, X. Li, J. An, Preparation and Strongly Enhanced Visible Light Photocatalytic Activity of TiO_2 Nanoparticles Modified by Conjugated Derivatives of Polyisoprene, *J. Phys. Chem. C* 116 (2012) 25806-25815.

[66] Z.L. Wang, Nanostructures of Zinc Oxide, *Mater. Today* 7 (2004) 26-33.

[67] Z. Pei, L. Ding, M. Lu, Z. Fan, S. Weng, J. Hu, P. Liu, Synergistic Effect in Polyaniline-Hybrid Defective ZnO with Enhanced Photocatalytic Activity and Stability, *J. Phys. Chem. C* 118 (2014) 9570-9577.

[68] S. Ghosh, N.A. Kouamé, L. Ramos, S. Remita, A. Dazzi, A. Deniset-Besseau, P. Beaunier, F. Goubard, P.-H. Aubert, H. Remita, Conducting Polymer Nanostructures for Photocatalysis under Visible Light, *Nat. Mater.* 14 (2015) 505-511.

[69] S. Mathew, A. Yella, P. Gao, R. Humphry-Baker, F.E. CurchodBasile, N. Ashari-Astani, I. Tavernelli, U. Rothlisberger, K. NazeeruddinMd, M. Grätzel, Dye-Sensitized Solar Cells with 13% Efficiency Achieved through the Molecular Engineering of Porphyrin Sensitizers, *Nat. Chem.* 6 (2014) 242-247.

[70] M. Grätzel, Dye-Sensitized Solar Cells, *J. Photochem. Photobiol. C* 4 (2003) 145-153.

[71] M. Grätzel, Recent Advances in Sensitized Mesoscopic Solar Cells, *Acc. Chem. Res.* 42 (2009) 1788-1798.

[72] M. Graetzel, R.A.J. Janssen, D.B. Mitzi, E.H. Sargent, Materials Interface Engineering for Solution-Processed Photovoltaics, *Nature* 488 (2012) 304-312.

[73] K. Lee, S.W. Park, M.J. Ko, K. Kim, N.-G. Park, Selective Positioning of Organic Dyes in a Mesoporous Inorganic Oxide Film, *Nat. Mater.* 8 (2009) 665-671.

[74] K. Hara, T. Horiguchi, T. Kinoshita, K. Sayama, H. Sugihara, H. Arakawa, Highly Efficient Photon-to-Electron Conversion with Mercurochrome-Sensitized Nanoporous Oxide Semiconductor Solar Cells, *Sol. Energ. Mat. Sol. Cells* 64 (2000) 115-134.

[75] S. Ito, T. Kitamura, Y. Wada, S. Yanagida, Facile Fabrication of Mesoporous TiO_2 Electrodes for Dye Solar Cells: Chemical Modification and Repetitive Coating, *Sol. Energ. Mat. Sol. Cells* 76 (2003) 3-13.

[76] S.D. Standridge, G.C. Schatz, J.T. Hupp, Distance Dependence of Plasmon-Enhanced Photocurrent in Dye-Sensitized Solar Cells, *J. Am. Chem. Soc.* 131 (2009) 8407-8409.

[77] Y. Li, H. Wang, Q. Feng, G. Zhou, Z.-S. Wang, Gold Nanoparticles Inlaid TiO_2 Photoanodes: A Superior Candidate for High-Efficiency Dye-Sensitized Solar Cells, *Energ. Environ. Sci.* 6 (2013) 2156-2165.

[78] C. Andrei, E. Lestini, S. Crosbie, C. de Frein, T. O'Reilly, D. Zerulla, Plasmonic Enhancement of Dye Sensitized Solar Cells Via a Tailored Size-Distribution of Chemically Functionalized Gold Nanoparticles, *PLoS One* 9 (2014) e109836.

[79] S. Linic, P. Christopher, D.B. Ingram, Plasmonic-Metal Nanostructures for Efficient Conversion of Solar to Chemical Energy, *Nat. Mater.* 10 (2011) 911-921.

[80] T. Bora, H.H. Kyaw, S. Sarkar, S.K. Pal, J. Dutta, Highly Efficient ZnO/Au Schottky Barrier Dye-Sensitized Solar Cells: Role of Gold Nanoparticles on the Charge-Transfer Process, *Beilstein J. Nanotechnol.* 2 (2011) 681-690.

[81] Z. Hai, N. El Kolli, D.B. Uribe, P. Beaunier, M. Jose-Yacaman, J. Vigneron, A. Etcheberry, S. Sorgues, C. Colbeau-Justin, J. Chen, H. Remita, Modification of TiO_2 by Bimetallic Au-Cu Nanoparticles for Wastewater Treatment, *J. Mater. Chem. A* 1 (2013) 10829-10835.

[82] S. Sardar, S. Ghosh, H. Remita, P. Kar, B. Liu, C. Bhattacharya, P. Lemmens, S.K. Pal, Enhanced Photovoltage in DSSC: Synergistic Combination of Silver Modified TiO_2 Photoanode and Low Cost Counter Electrode, *RSC Adv.* 6 (2016) 33433-33442.

[83] Z.S. Seddigi, S.A. Ahmed, S. Sardar, S.K. Pal, Carbonate Doping in TiO_2 Microsphere: The Key Parameter Influencing Others for Efficient Dye Sensitized Solar Cell, *Sci. Rep.* 6 (2016) 23209.

[84] G.F. Paciotti, L. Myer, D. Weinreich, D. Goia, N. Pavel, R.E. McLaughlin, L. Tamarkin, Colloidal Gold: A Novel Nanoparticle Vector for Tumor Directed Drug Delivery, *Drug Deliv.* 11 (2004) 169-183.

[85] X. Wu, H. Liu, J. Liu, K.N. Haley, J.A. Treadway, J.P. Larson, N. Ge, F. Peale, M.P. Bruchez, Immunofluorescent Labeling of Cancer Marker Her2 and Other Cellular Targets with Semiconductor Quantum Dots, *Nat. Biotechnol.* 21 (2002) 41-46.

[86] L.R. Hirsch, R.J. Stafford, J.A. Bankson, S.R. Sershen, B. Rivera, R.E. Rrice, J.D. Hazle, N.J. Halas, J.L. West, Nanoshell-Mediated Near-Infrared Thermal Therapy

of Tumors under Magnetic Resonance Guidance, *Proc. Natl. Acad. Sci. USA* 100 (2011) 13549-13554.

[87] J. Zhou, N.S. Xu, Z.L. Wang, Dissolving Behavior and Stability of ZnO Wires in Biofluids: A Study on Biodegradability and Biocompatibility of ZnO Nanostructures, *Adv. Mater.* 18 (2006) 2432–2435.

[88] S. Sarkar, A. Makhal, S. Baruah, M.A. Mahmood, J. Dutta, S.K. Pal, Nanoparticle-Sensitized Photodegradation of Bilirubin and Potential Therapeutic Application, *J. Phys. Chem. C* 116 (2012) 9608-9615.

[89] T. Bora, K.K. Lakshman, S. Sarkar, A. Makhal, S. Sardar, S.K. Pal, J. Dutta, Modulation of Defect-Mediated Energy Transfer from ZnO Nanoparticles for the Photocatalytic Degradation of Bilirubin, *Beilstein J. Nanotechnol.* 4 (2013) 714-725.

Chapter 2

An Overview of Experimental Techniques and Systems

In order to investigate the dynamical processes involved in the light harvesting materials, different steady-state and dynamical tools have been employed. These include photoinduced electron transfer (PET), Förster resonance energy transfer (FRET), Langmuir−Hinshelwood (L−H) model for surface catalysis, photocurrent−voltage (I−V) characterization, incident photon to current conversion efficiency measurement and photovoltage decay measurement of photovoltaic solar cells. In this chapter, we have included a brief discussion about the above mentioned tools. Overviews of the various systems, probes and solar cell dyes used in the studies have also been provided.

2.1. Steady-state and Dynamical Tools:

2.1.1. Photoinduced Electron Transfer (PET): PET can be described as the movement of an electron caused by the absorption of light from an electron-rich species (D) to an electron deficient species (A), as shown in equation 2.1.

$$D + A \rightarrow D^+ + A^- \qquad (2.1)$$

The first law of photochemistry tells us that a photoinduced process must be initiated by the absorption of light. In PET, the absorbing species can either be a donor, the acceptor, or a ground-state complex between the donor and acceptor, often referred to as a charge transfer complex. These possibilities are shown in equations 2.2−2.4.

$$D \xrightarrow{h\upsilon} D^* + A \longrightarrow D^+ + A^- \qquad (2.2)$$

$$A \xrightarrow{h\upsilon} A^* + D \longrightarrow D^+ + A^- \qquad (2.3)$$

$$(D \cdots A) \xrightarrow{h\upsilon} (D \cdots A)^* \longrightarrow D^+ + A^- \qquad (2.4)$$

Transport of charges or excitons are commonly seen as fundamental processes in many optoelectronic devices as well as biological systems. The creation, diffusion, and annihilation of excitons and the mobility of charges are some of the key processes in many devices that interconvert electric and light energies [1-2]. PET is an important process in many biochemical systems, such as those in respiration and photosynthesis [3-4]. To gain a deep understanding for these systems, it is important to describe the rates of these processes with a few empirically derived parameters [5-6]. Therefore, it has become increasingly important to develop computational techniques that allow us to calculate the rate of charge or energy transport. In our systems the apparent rate constants, k_{nr}, were determined for the nonradiative processes by comparing the lifetimes of donor in the absence (τ_0) and in the presence (τ) of an acceptor, using equation 2.5 [7].

$$k_{nr} = 1/\langle \tau \rangle - 1/\langle \tau_0 \rangle \qquad (2.5)$$

This thesis demonstrates several PET processes, particularly in light-harvesting materials and discusses the consequences of various interfacial electron transfer processes. In heterogeneous photocatalysis, the photoinduced charge separation in the photocatalyst is necessary and several strategies have been employed to facilitate the charge separation. In dye/quantum dot-sensitized solar cells (DSSC/QDSC), a series of charge transfer processes had to occur cooperatively so that the electrical output can be harnessed efficiently. These include (i) electron injection from excited dye/QD into metal oxides, (ii) electron transport to the collecting electrode surface, (iii) hole transfer to the redox couple, and (iv) regeneration of the redox couple at the counter electrode. A major force that counteracts these favourable processes (i−iv) is the charge recombination of electrons at the electrolyte interface. The matching of the band energies of the two semiconductors facilitates desired functionality either to induce electron−hole recombination (e.g., light-emitting diodes) or to improve charge separation by driving electrons and holes in two different nanoparticles (e.g., QDSC). In each

instance where semiconductor nanocrystals are implemented into a practical device, PET reactions are intimately involved, and they dictate overall functionality. This thesis focuses on the recent progresses made in understanding the kinetics and mechanistic aspects of various PET processes at the semiconductor interface and their role in optimization of solar cell performance.

2.1.2. Förster Resonance Energy Transfer (FRET): FRET is an electrodynamic phenomenon involving the nonradiative transfer of the excited state energy from the donor dipole (D) to an acceptor dipole (A) in the ground state (Figure 2.1a). Basically, FRET is of two types: (i) homo-molecular FRET and (ii) hetero-molecular FRET. In the former case the same fluorophore acts both as energy donor and acceptor, while in the latter case two different molecules act as donor and acceptor.

Each donor-acceptor (D-A) pair participating in FRET is characterized by a distance known as Förster distance (R_0) i.e., the D-A separation at which energy transfer is 50% efficient. The rate of resonance energy transfer (k_T) from donor to an acceptor is given by [8],

$$k_T = \frac{1}{\tau_D}\left(\frac{R_0}{r}\right)^6 \tag{2.6}$$

where τ_D is the lifetime of the donor in the absence of acceptor and r is the donor to acceptor (D-A) distance. The rate of transfer of donor energy depends upon the extent of overlap of the emission spectrum of the donor with the absorption spectrum of the acceptor ($J(\lambda)$), the quantum yield of the donor (Q_D), the relative orientation of the donor and acceptor transition dipoles (κ^2) and the distance between the donor and acceptor molecules (r) (Figure 2.1b). In order to estimate FRET efficiency of the donor and hence to determine distances between donor-acceptor pairs, the methodology described below is followed [8]. R_0 is given by,

$$R_0 = 0.211\left[\kappa^2 n^{-4} Q_D J(\lambda)\right]^{1/6} \text{ (in Å)} \tag{2.7}$$

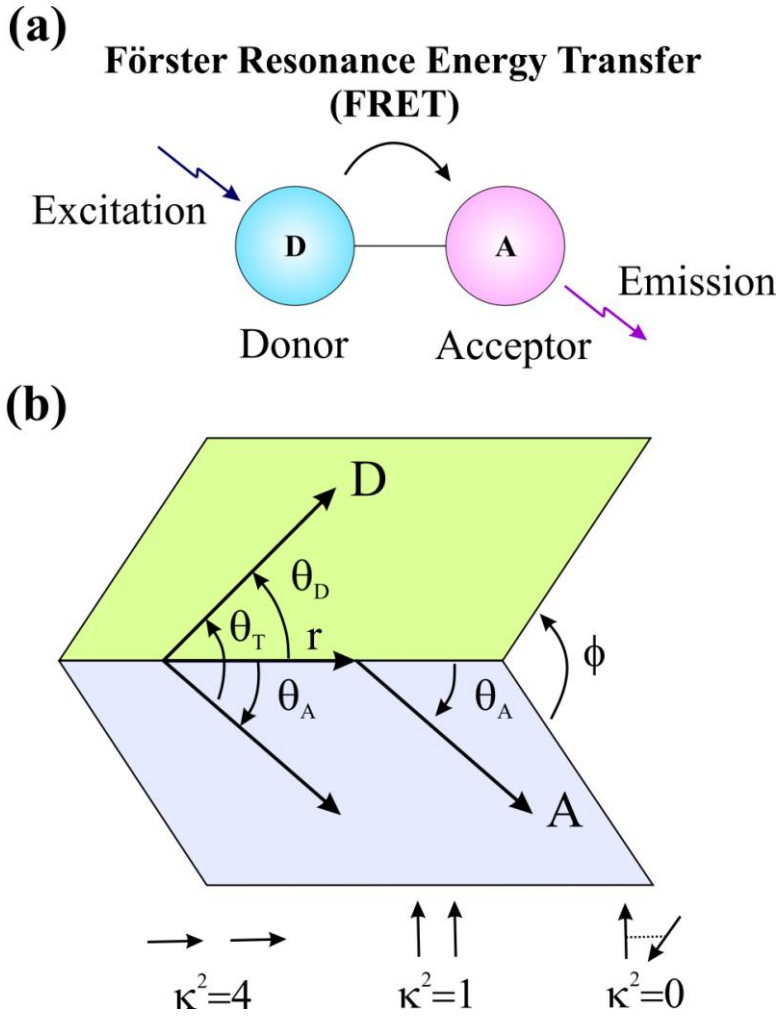

Figure 2.1. *(a) Schematic illustration of the FRET process. (b) Dependence of the orientation factor* κ^2 *on the directions of the emission and absorption dipoles of the donor and acceptor, respectively.*

where n is the refractive index of the medium, Q_D is the quantum yield of the donor and $J(\lambda)$ is the overlap integral. κ^2 is defined as,

$$\kappa^2 = \left(\cos\theta_T - 3\cos\theta_D \cos\theta_A\right)^2 = \left(\sin\theta_D \sin\theta_A \cos\varphi - 2\cos\theta_D \cos\theta_A\right)^2 \qquad (2.8)$$

where θ_T is the angle between the emission transition dipole of the donor and the absorption transition dipole of the acceptor, θ_D and θ_A are the angles between these dipoles and the vector joining the donor and acceptor and φ is angle between the planes of the donor and acceptor (Figure 2.1b). κ^2 value can vary from 0 to 4. For collinear and parallel transition dipoles, $\kappa^2 = 4$; for parallel dipoles, $\kappa^2 = 1$; and for perpendicularly oriented dipoles, $\kappa^2 = 0$. For donor and acceptors that

randomize by rotational diffusion prior to energy transfer, the magnitude of κ^2 is assumed to be 2/3. However, in systems where there is a definite site of attachment of the donor and acceptor molecules, to get physically relevant results, the value of κ^2 has to be estimated from the angle between the donor emission and acceptor absorption dipoles [9]. $J(\lambda)$, the overlap integral, which expresses the degree of spectral overlap between the donor emission and the acceptor absorption, is given by,

$$J(\lambda) = \frac{\int_0^\infty F_D(\lambda)\varepsilon_A(\lambda)\lambda^4 d\lambda}{\int_0^\infty F_D(\lambda) d\lambda} \tag{2.9}$$

where $F_D(\lambda)$ is the fluorescence intensity of the donor in the wavelength range of λ to $\lambda+d\lambda$ and is dimensionless. $\varepsilon_A(\lambda)$ is the extinction coefficient (in $M^{-1}cm^{-1}$) of the acceptor at λ. If λ is in nm, then $J(\lambda)$ is in units of $M^{-1}\,cm^{-1}\,nm^4$.

Once the value of R_0 is known, the efficiency of energy transfer can be calculated. The efficiency of energy transfer (E) is the fraction of photons absorbed by the donor which are transferred to the acceptor and is defined as,

$$E = \frac{k_T(r)}{\tau_D^{-1} + k_T(r)} \tag{2.10}$$

$$\text{Or, } E = \frac{R_0^6}{r^6 + R_0^6} \tag{2.11}$$

For D-A systems decaying with multiexponential lifetimes, E is calculated from the amplitude weighted lifetimes $\langle\tau\rangle = \sum_i \alpha_i \tau_i$ of the donor in absence (τ_D) and presence (τ_{DA}) of the acceptor as,

$$E = 1 - \frac{\tau_{DA}}{\tau_D} \tag{2.12}$$

The D-A distances can be measured using equations (2.11) and (2.12).

2.1.3. Data Analysis of Time-Resolved Fluorescence Transients: Curve fitting of the time-resolved fluorescence transients was carried out using a nonlinear least square fitting procedure to a function (2.13) comprised of convolution of the IRF

$$(X(t) = \int_0^t E(t')R(t-t')dt') \tag{2.13}$$

(E(t)) with a sum of exponentials (2.14) with pre-exponential factors (B_i),

$$(R(t) = A + \sum_{i=1}^{N} B_i e^{-t/\tau_i}) \tag{2.14}$$

characteristic lifetimes (τ_i) and a background (A). Relative concentration in a multiexponential decay is expressed as (2.15).

$$c_n = \frac{B_n}{\sum_{i=1}^{N} B_i} \times 100 \tag{2.15}$$

The average lifetime (amplitude-weighted) of a multiexponential decay is expressed as,

$$\tau_{av} = \sum_{i=1}^{N} c_i \tau_i \tag{2.16}$$

2.1.4. Langmuir−Hinshelwood (L−H) Model: In the Langmuir−Hinshelwood (L−H) model of heterogeneous surface reactions, the rate of the photochemical degradation can be expressed in general terms for both the oxidant (e.g., O_2) and the reductant (e.g., $CHCl_3$) as follows:

$$-\frac{d[\mathrm{Re}\,d]}{dt} = -\frac{d[Ox]}{dt} = k_d \theta_{\mathrm{Red}} \theta_{Ox} \tag{2.17}$$

where, k_d is the photodegradation rate constant, θ_{Red} represents the fraction of the electron-donating reductant (e.g., chloroform) adsorbed to the surface, and θ_{Ox} represents the corresponding fraction of the electron-accepting oxidant (e.g., oxygen) adsorbed to the surface. This treatment is subjected to the assumptions that sorption of both the oxidant and the reductant is a rapid equilibrium process

in both the forward and reverse directions and that the rate-determining step of the reaction involves both species present in a monolayer at the solid-liquid interface. The Langmuir adsorption coefficient, *K*, for adsorption of each reactant is assumed to be readily determined from a classical Langmuir adsorption isotherm. In this case, the surface concentration of the reactants is related to their corresponding activities or concentrations in the bulk aqueous phase as follows:

$$R_0 = \frac{dC_0}{dt} = \frac{k_{L-H} K C_0}{1 + K C_0} \tag{2.18}$$

where, C_0 is the initial concentration of reactants, k_{L-H} is the Langmuir–Hinshelwood (L–H) rate constant, and R_0 is the rate of reaction. If the initial concentration of the reactant solution is sufficiently low ($KC_0 << 1$), the equation 2.18 can be simplified to an apparent first-order equation:

$$R_0 = k_{L-H} K C_0 = k_{app} C_0 \tag{2.19}$$

where, k_{app} is the apparent first-order rate constant. If the initial concentration of the BR solution is sufficiently high ($KC_0 >> 1$), the equation 2.18 can be simplified to a zero-order rate equation:

$$R_0 = k_{L-H} \tag{2.20}$$

The L−H model appears to be a promising tool that has a number of applications in semiconductor photocatalysis such as dye degradation, air purification, water disinfection, hazardous waste remediation, and water purification. In addition, the basic research that underlies the application of this potential tool is forging a better understanding of the complex heterogeneous photochemistry of metal oxide systems in multiphasic environments.

2.1.5. Dye-Sensitized Solar Cells (DSSC): DSSC [10-12] is potentially inexpensive alternatives to traditional semiconductor solar cells. The essential components of a DSSC are semiconductor metal oxides attached to sensitizing dyes (mostly,

ruthenium) and an electrolyte medium (iodine-based). A schematic of the interior and operating principle of a DSSC is shown in Figure 2.2. The typical basic configuration is as follows: at the heart of the device is the metal oxide layer (mostly ZnO/TiO_2), which is deposited on a fluorine doped tin oxide (FTO) coated glass substrate. Attached to the surface of the nanocrystalline film is a monolayer of the charge transfer dyes/QDs. Photoexcitation of the latter results in the injection of an electron into the conduction band of the oxide, leaving the dye in its oxidized state. The dye is restored to its ground state by electron transfer from the electrolyte, usually an organic solvent containing the iodide/triiodide (I^-/I_3^-) redox system. The regeneration of the sensitizer by iodide intercepts the recapturing of the conduction band electron by the oxidized dye. The I_3^- ions formed by oxidation of I^- diffuse a short distance (~ 60 μm) through the electrolyte to the cathode, which is coated with a thin layer of platinum catalyst, where the regenerative cycle is completed by electron transfer to reduce I_3^- to I^-.

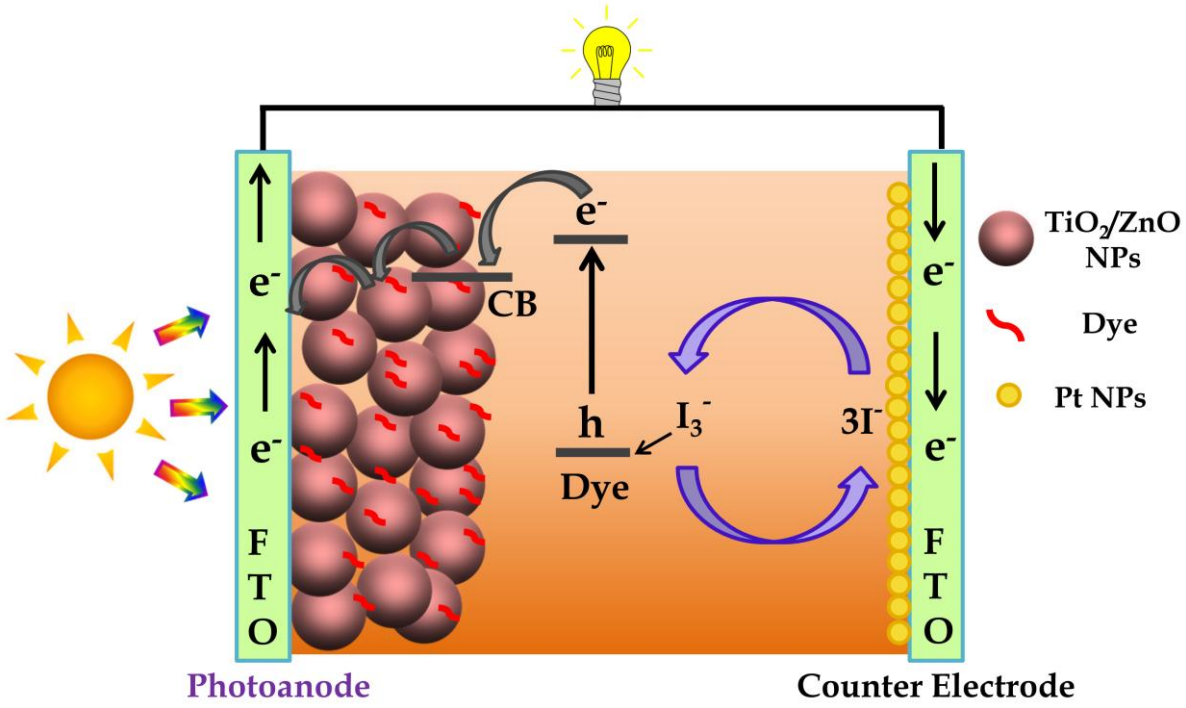

Figure 2.2. *Schematic representation of a DSSC showing different charge migration processes.*

In order to quantitatively measure the efficacy of a DSSC, photocurrent–voltage (*I*–*V* *or* *J*–*V*) measurements under simulated sunlight, incident photon-to-current conversion efficiency (IPCE) under monochromatic light and photovoltage decay measurement under dark condition following a brief illumination of light are important.

2.1.5.1. Photocurrent–Voltage (I–V) Measurements: Many solar cell parameters can be obtained from current-voltage (I-V) measurements of a cell. The I-V characteristics measurement can be done using a Source-Measure Units (SMUs), which can source and measure both current and voltage. A DSSC can be represented by an equivalent electric circuit shown in Figure 2.3, where, I_L is the photocurrent, R_S is the series resistance (describes the resistances of the materials) and R_{sh} the shunt resistance.

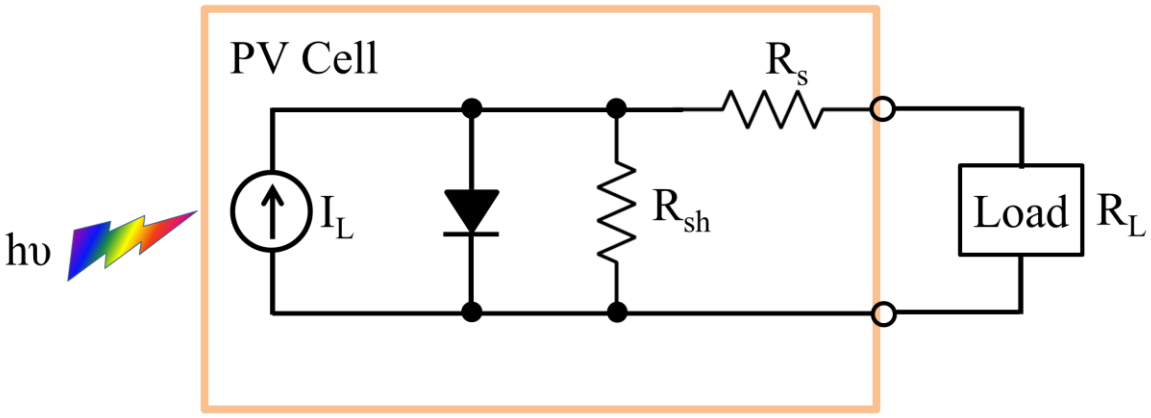

***Figure* 2.3.** *Idealized equivalent electric circuit of a DSSC.*

A. Short-Circuit Current (I_{SC} or J_{SC}): The current equals the short-circuit current when the applied bias potential is zero:

$$I = I_{ph} - I_S\left[\exp\left(\frac{V + I.R_S}{\eta.V_{th}}\right) - 1\right] \qquad (2.21)$$

B. Open-Circuit Voltage (V_{OC}): When no current is flowing through the cell the potential equals the open-circuit potential, using equation 2.21 one can find:

$$V_{OC} = \eta . V_{th} \ln\left(\frac{I_{ph}}{I_c} + 1\right) \tag{2.22}$$

C. Maximum Power Output (P_{max}): The power delivered from a solar cell at a certain potential equals the product of the current at this potential times the potential:

$$P(V) = I(V).V \tag{2.23}$$

To obtain a graphic representation of the power, one has to vary the potential between V_{OC} and 0. The point where the power is maximum (P_{max}) corresponds to the peak power point (PPP) for the $I-V$ curve. These are the optimal current and potential conditions (I_m, V_m) for the operating cell.

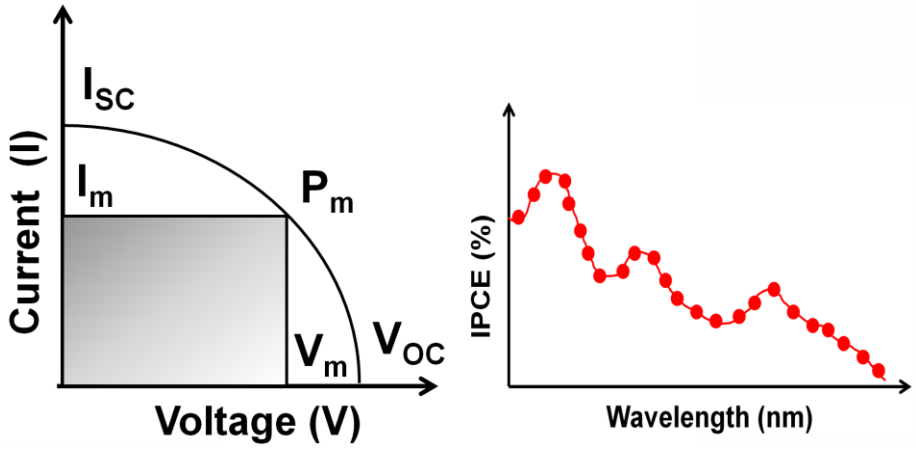

Figure 2.4. *Schematic representation of conventional I−V characteristic diagram (left). Typical IPCE characteristic diagram of a DSSC (right).*

D. Fill Factor (*FF*): The *FF* quantifies the quality of the solar cell, which is the ratio of actual power output ($V_m \times I_m$) versus its 'dummy' power output ($V_{OC} \times I_{SC}$) of a solar cell, as shown in equation 2.24:

$$FF = \frac{V_m I_m}{V_{OC} I_{SC}} \tag{2.24}$$

The *FF* lies between 0.6 and 0.85 for an efficient DSSC. These values are influenced by the values of the series and the shunt resistances. To obtain high *FF* values the shunt resistance has to be as small as possible and the series resistance as high as possible.

E. Photo-conversion Efficiency (η): The overall photo-conversion efficiency is given by the following equation:

$$\eta = \frac{V_m I_m}{P_{in}} = \frac{V_{OC} I_{SC} FF}{P_{in}} \tag{2.25}$$

It expresses the ratio of produced power and the incoming power (P_{in}). The experimental conditions have been fixed worldwide, in order to compare results coming from different places. A power density value of 100 mW/cm^2, at air mass 1.5 global (AM 1.5 G) condition has been set for the incident solar radiation, and the temperature of the cell should be 25 °C. The AM is the ratio of the path-length of incoming sunlight through the atmosphere when the sun is at an angle to the zenith, and the path-length when the Sun is at the zenith.

2.1.5.2. Incident Photon-to-Current Conversion Efficiency (IPCE) Measurements: The sensitivity of a solar cell varies with the wavelength of the incoming light. The IPCE value corresponds to the photocurrent density produced in the external circuit under monochromatic illumination of the cell divided by the photon flux that strikes the cell. From such an experiment the IPCE as a function of wavelength can be calculated from:

$$IPCE(\lambda) = \frac{n_{electrons}(\lambda)}{n_{photons}(\lambda)} = \frac{I(\lambda)/e}{P_{in}(\lambda)/h.\nu} = \frac{I(\lambda)}{\lambda.P_{in}(\lambda)} \cdot \frac{hc}{\nu} \tag{2.26}$$

$$\text{Or,} \qquad \text{IPCE\%} = \left[1240 \times J_{SC}\left(\text{A/cm}^2\right)\right] / \left[\lambda(\text{nm}) \times P\left(\text{W/cm}^2\right)\right] \times 100 \tag{2.27}$$

where, $I(\lambda)$ is the current given by the cell at wavelength λ, $P_{in}(\lambda)$ the incoming power at wavelength λ and I_p is the incident light power striking the device. IPCE values provide practical information about the monochromatic quantum efficiencies of a solar cell. Figure 2.4 (right) shows a typical IPCE spectrum of a standard DSSC.

2.1.5.3. Photovoltage Decay Measurement: The open circuit voltage of a DSSC generated under illumination is equivalent to the separation between the quasi-Fermi level of electrons in the TiO_2 film and the rest potential of the counter electrode, which remains in equilibrium with the redox couple. The forward electron injection from sensitizer to TiO_2 is terminated upon stopping the illumination, thus discharging of electrons occurs through the back electron transfer or recombination with the oxidized electrolytes. The open circuit voltage decay reflects the timescales for the recombination processes.

2.2. Systems:

2.2.1. Molecular Probes: In this section, we will discuss about the different probe molecules that have been used in the course of study.

2.2.1.1. Methylene Blue (MB): MB is a heterocyclic aromatic chemical compound with molecular formula: $C_{16}H_{18}ClN_3S$. It has many uses in a range of different fields. At room-temperature it appears as a solid and is odourless and a dark green powder, which yields a blue solution when dissolved in water. They are widely used as model water contaminant [13]. Its structure is given in Figure 2.5. When dissolved in water, the UV-visible spectrum of MB showed three absorption maxima. The first band was observed at 246 nm and then 291 nm and more intensely 663 nm. The absorption maxima wavelength of MB (λ_{max} = 663 nm) was used for the analysis during decolorization of MB dye.

2.2.1.2. 2,5-Cyclohexadiene-1,4-dione (*p*-Benzoquinone, BQ): BQ (Figure 2.5) is a well-known probe for electron accepting and shuttling for any electron rich material/compound, which readily accepts electron and adapted to be resonance species hydroquinone [14-15]. Large doses could induce local irritation, clonic convulsions, decreased blood pressure and death due to paralysis of the medullary centres.

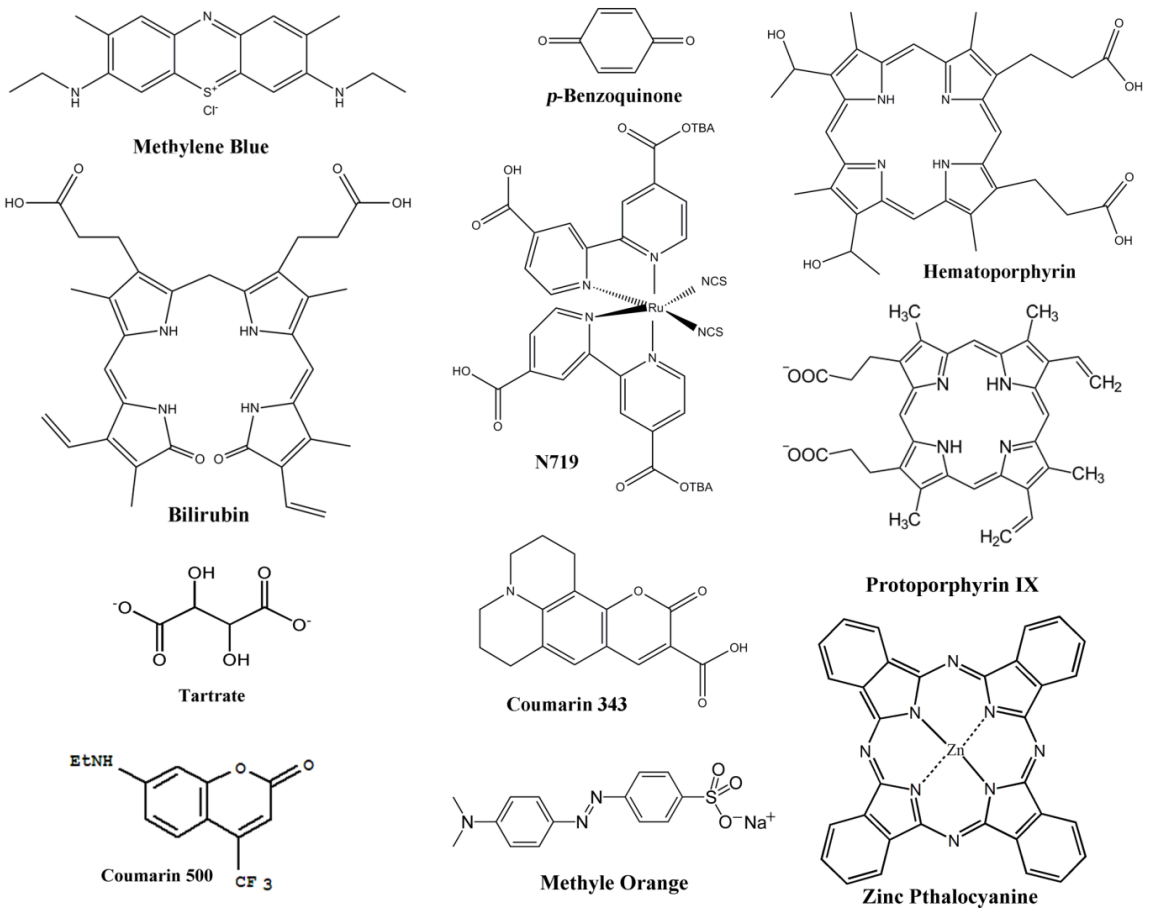

***Figure* 2.5.** *Schematic representation of the molecular probes used.*

2.2.1.3. Bilirubin (BR): BR, the yellow-orange breakdown product of normal heme catabolism in mammalian systems, introduces great biological and diagnostic values [16]. Both antioxidant and toxic properties have been attributed to BR [17], which is normally conjugated with glucuronic acid and then excreted in the bile. However, when its conjugation with glucuronic acid is inhibited, as in neonatal

jaundice and in hereditary forms of congenital jaundice, excess BR bind and deposit to various tissues, giving rise to severe hyperbilirubinemia and neurotoxicity. Phototherapy, the most effective treatment for jaundice to date, decreases the BR levels in the blood by changing the *ZZ*-BR isomer into water-soluble *ZE*-BR [18-20]. Because this reaction is readily reversible, equilibrium is established between native BR and the *ZE* isomer when BR is photoirradiated in a closed system. The second fastest reaction that occurs when BR is exposed to light is the production of lumirubin, a structural isomer of BR.

2.2.1.4. Di-tetrabutylammonium cis-bis(isothiocyanato)bis(2,2′-bipyridyl-4,4′-dicarboxylato)ruthenium(II) (N719): Metal complexes, in particular the Ru(II) complexes, have been investigated intensively for DSSC application because of their broad absorption spectra, large value of extinction coefficient (1.4×10^4 M^{-1} cm^{-1}) [21], and favorable photovoltaic properties. N719 (Figure 2.5) consists of a central Ru(II) ion with ancillary ligands having four anchoring groups (COOH). Light absorption in the visible part of the solar spectrum is due to a metal to ligand charge transfer (MLCT) process. The central metal ion is therefore a crucial part of the overall properties of the complexes. Ancillary ligands (bipyridines) can be tuned by different substituents (alkyl, aryl, heterocycle, etc.) to change the photophysical and electrochemical properties and thus improve the photovoltaic performance. Anchoring groups are employed to link the dye with the semiconductor and facilitate the injection of the excited electron into the conduction band of the semiconductor. One can modify any part of the complex to tune the energy levels of the MLCT states and to optimize electron injection and dye regeneration kinetics.

2.2.1.5. 8,13-Bis(1-hydroxyethyl)-3,7,12,17-tetramethyl-21H,23H-porphine-2,18-dipropionic acid (Hematoporphyrin, HP): Since the early 1960's, the hematoporphyrin derivative (HpD) has provided clinical investigators a sensitive means of diagnosis and a selective method for eradication of tumors [22]. Its

emerging importance in photoradiation therapy is evidenced by research efforts directed at the fundamental problems related to the mechanism of photosensitization and the increasing clinical applications for cancer therapy. They are also found to be a good alternative for Ru(II)-based solar cell dyes.

2.2.1.6. 3,7,12,17-Tetramethyl-8,13-divinyl-2,18-porphinedipropionic acid (Protoporphyrin IX, PP): PP is an important precursor to biologically essential prosthetic groups such as heme, cytochrome c, and chlorophylls. PP is a very well-known cancer drug and efficient hydrophobic photosensitizer (PS) for photodynamic therapies (PDT) [23]. The efficiency of PDT depends on the photoactivation of the photosensitizers accumulated at the target site and the pharmacokinetic properties of the photosensitizer to achieve the desired biological response.

2.2.1.7. Coumarin 343 (C343): C343 is an ideal system for studying electron transfer into metal oxides, as it is known to undergo fast electron injection [24-25] with ~80−90% efficiency [25-26]. C343 and its derivatives have been successfully used in organic DSSCs [27-29], where the carboxyl group of C343 binds directly to the metal ions on the surface of the nanoparticles [30]. They also have large extinction coefficient though absorption spectrum shows a sharp peak at ~442 nm (4.4×10^4 M^{-1} cm^{-1}) [31].

2.2.1.8. Coumarin 500 (C500): The derivatives of 1,2-benzopyrone, commonly known as the coumarin dyes, are the well-known laser dyes for the blue-green region [32]. The 7-aminocoumarin dyes are usually very strongly fluorescent, with their fluorescence quantum yields often close to unity. C500 is an ideal system for studying energy transfer into metal oxides. Coumarin is found naturally in many edible plants such as strawberries, black currants, apricots, and cherries.

2.2.1.9. Zinc Phthalocyanine (ZnPc): ZnPc is very well-known for its wide spread applications in the field of photodynamic therapy and solar energy harvesting

applications [33-34]. In DSSC, sensitizers with extended absorption in the near IR region of the sun emission spectra are paramount, and phthalocyanines are perfectly suited for their integration in light energy conversion systems. They exhibit very high extinction coefficients around 700 nm for efficient photon harvesting, as well as reversible redox properties and excellent photoconductivities.

2.2.1.10. Methyl Orange (MO): MO is an azo compound with molecular formula: $C_{14}H_{14}N_3NaO_3S$. It is a model dye which belongs to the class of synthetic organic compounds and is widely used in the textile industry [35]. The removal of these non-biodegradable organic chemicals from the environment is a crucial ecological problem. At room-temperature it appears as a solid and is odourless orange-yellow powder. MO shows orange colour in acidic medium and yellow colour in basic medium. Its structure is given in Figure 2.5. MO has strong absorption at λ_{max} = 460 nm which was used for the analysis during decolorization of MO dye.

References

[1] H. Spanggaard, F.C. Krebs, A Brief History of the Development of Organic and Polymeric Photovoltaics, *Sol. Energy Mater. Sol. Cells* 83 (2004) 125-146.

[2] Y. Shirota, H. Kageyama, Charge Carrier Transporting Molecular Materials and Their Applications in Devices, *Chem. Rev.* 107 (2007) 953-1010.

[3] H.B. Gray, J.R. Winkler, Electron Tunneling through Proteins, *Q. Rev. Biophys.* 36 (2003) 341-372.

[4] G. McLendon, R. Hake, Interprotein Electron Transfer, *Chem. Rev.* 92 (1992) 481-490.

[5] H. Bassler, Charge Transport in Disordered Organic Photoconductors: A Monte Carlo Simulation Study, *Phys. Status Solidi B* 175 (1993) 15-56.

[6] V.M. Kenkre, J.D. Andersen, D.H. Dunlap, C.B. Duke, Unified Theory of the Mobilities of Photoinjected Electrons in Naphthalene, *Phys. Rev. Lett.* 62 (1989) 1165-1168.

[7] J.H. Bang, P.V. Kamat, Quantum Dot Sensitized Solar Cells. A Tale of Two Semiconductor Nanocrystals: CdSe and CdTe, *ACS Nano* 3 (2009) 1467-1476.

[8] J.R. Lakowicz, Principles of Fluorescence Spectroscopy, 2nd ed., Kluwer Academic/Plenum, New York, 2006.

[9] D. Banerjee, S.K. Pal, Simultaneous Binding of Minor Groove Binder and Intercalator to Dodecamer DNA: Importance of Relative Orientation of Donor and Acceptor in FRET, *J. Phys. Chem. B* 111 (2007) 5047-5052.

[10] B. O'Regan, M. Grätzel, A Low-Cost, High-Efficiency Solar Cell Based on Dye-Sensitized Colloidal TiO_2 Films, *Nature* 353 (1991) 737-740.

[11] M. Grätzel, Conversion of Sunlight to Electric Power by Nanocrystalline Dye-Sensitized Solar Cells, *J. Photochem. and Photobiol. A* 164 (2004) 3-14.

[12] M. Grätzel, Photoelectrochemical Cells, *Nature* 414 (2001) 338-344.

[13] N. Xu, Z. Shi, Y. Fan, J. Dong, J. Shi, M.Z.C. Hu, Effects of Particle Size of TiO_2 on Photocatalytic Degradation of Methylene Blue in Aqueous Suspensions, *Ind. Eng. Chem. Res.* 38 (1999) 373-379.

[14] C. Burda, T.C. Green, S. Link, M.A. El-Sayed, Electron Shuttling across the Interface of CdSe Nanoparticles Monitored by Femtosecond Laser Spectroscopy, *J. Phys. Chem. B* 103 (1999) 1783-1788.

[15] A. Makhal, P. Kumar, P. Lemmens, S.K. Pal, Manipulation of Spontaneous Emission Dynamics of Organic Dyes in the Porous Silicon Matrix, *J. Fluorescence* 20 (2010) 283.

[16] J.D. Ostrow, Bile Pigments and Jaundice: Molecular, Metabolic and Medical Aspects, Marcel Dekker, New York, 1986.

[17] R. Stocker, A.N. Glazer, B.N. Ames, Antioxidant Activity of Albumin-Bound Bilirubin, *Proc. Natl. Acad. Sci. U.S.A.* 84 (1987) 5918-5922.

[18] D.A. Lightner, A.F. McDonagh, Molecular Mechanisms of Phototherapy for Neonatal Jaundice, *Acc. Chem. Res.* 17 (1984) 417-424.

[19] A.A. Lamola, W.E. Blumberg, R. McClead, A. Fanaroff, Photoisomerized Bilirubin in Blood from Infants Receiving Phototherapy, *Proc. Natl. Acad. Sci. U.S.A.* 78 (1981) 1882-1886.

[20] S.E. Braslavsky, A.R. Holzwarth, K. Schaffner, Solution Conformations, Photophysics, and Photochemistry of Bile Pigments; Bilirubin and Biliverdin, Dimethyl Esters and Related Linear Tetrapyrroles, *Angew. Chem. Int. Ed.* 22 (1983) 656-674.

[21] M.K. Nazeeruddin, F.D. Angelis, S. Fantacci, A. Selloni, G. Viscardi, P. Liska, S. Ito, B. Takeru, M. Grätzel, Combined Experimental and DFT-TDDFT Computational Study of Photoelectrochemical Cell Ruthenium Sensitizers, *J. Am. Chem. Soc.* 127 (2005) 16835-16847.

[22] R. Bonnett, R.J. Ridge, P.A. Scourides, M.C. Berenbaum, Haematoporphyrin Derivative, *Chem. Soc. Chem. Commun.* (1980) 1198-1199.

[23] W.E. Grant, A. MacRobert, S.G. Bown, C. Hopper, P.M. Speight, Photodynamic Therapy of Oral Cancer: Photosensitisation with Systemic Aminolaevulinic Acid, *Lancet* 342 (1993) 147-148.

[24] N.A. Anderson, T. Lian, Ultrafast Electron Transfer at the Molecule-Semiconductor Nanoparticle Interface, *Ann. Rev. Phys. Chem.* 56 (2005) 491-591.

[25] J.M. Rehm, G.L. McLendon, Y. Nagasawa, K. Yoshihara, J. Moser, M. Grätzel, Femtosecond Electron-Transfer Dynamics at a Sensitizing Dye−Semiconductor (TiO_2) Interface, *J. Phys. Chem.* 100 (1996) 9577-9578.

[26] O. Enea, J. Moser, M. Grätzel, Achievement of Incident Photon to Electric Current Conversion Yields Exceeding 80% in the Spectral Sensitization of Titanium Dioxide by Coumarin, *J. Electroanal. Chem.* 259 (1989) 59-65.

[27] K. Hara, K. Sayama, Y. Ohga, A. Shinpo, S. Suga, H. Arakawa, A Coumarin-Derivative Dye Sensitized Nanocrystalline TiO_2 Solar Cell Having a High Solar-Energy Conversion Efficiency up to 5.6%, *Chem. Commun.* (2001) 569-570.

[28] X. Zhang, J.J. Zhang, Y.Y. Xia, Molecular Design of Coumarin Dyes with High Efficiency in Dye-Sensitized Solar Cells, *J. Photochem. Photobiol. A* 194 (2008) 167-172.

[29] V. Kandavelu, H.S. Huang, J.L. Jian, T.C.K. Yang, K.L. Wang, S.T. Huang, Novel Iminocoumarin Dyes as Photosensitizers for Dye-Sensitized Solar Cell *Sol. Energy* 83 (2009) 574-581.

[30] W.R. Duncan, O.V. Prezhdo, Theoretical Studies of Photoinduced Electron Transfer in Dye-Sensitized TiO_2, *Annu. Rev. Phys. Chem.* 58 (2007) 143-184.

[31] G.A. Reynolds, K.H. Drexhage, New Coumarin Dyes with Rigidized Structure for Flashlamp-Pumped Dye Lasers, *Optics Commun.* 13 (1975) 222-225.

[32] S. Nad, H. Pal, Photophysical Properties of Coumarin-500 (C500): Unusual Behavior in Nonpolar Solvents, *J. Phys. Chem. A.* 107 (2003) 501-507.

[33] H.K. Moon, M. Son, J.E. Park, S.M. Yoon, S.H. Lee, H.C. Choi, Significant Increase in the Water Dispersibility of Zinc Phthalocyanine Nanowires and Applications in Cancer Phototherapy, *NPG Asia Mater.* 4 (2012) e12.

[34] S.D. Oosterhout, M.M. Wienk, S.S. van Bavel, R. Thiedmann, L. Jan Anton Koster, J. Gilot, J. Loos, V. Schmidt, R.A.J. Janssen, The Effect of Three-Dimensional Morphology on the Efficiency of Hybrid Polymer Solar Cells, *Nat. Mater.* 8 (2009) 818-824.

[35] S. Sardar, P. Kar, H. Remita, B. Liu, P. Lemmens, S.K. Pal, S. Ghosh, Enhanced Charge Separation and FRET at Heterojunctions between Semiconductor Nanoparticles and Conducting Polymer Nanofibers for Efficient Solar Light Harvesting, *Sci. Rep.* 5 (2015) 17313.

Chapter 3

Instrumentation and Sample Preparation

In this chapter, the details of instrumental setup and sample preparation techniques used in our studies have been described.

3.1. Instrumental Setups:

3.1.1. Steady-state UV-Vis Absorption and Emission Measurement: Steady-state UV-Vis absorption and emission spectra were measured with Shimadzu UV-2600 spectrophotometer and Horiba Fluorolog, respectively. Schematic ray diagrams of these two instruments are shown in Figures 3.1 and 3.2.

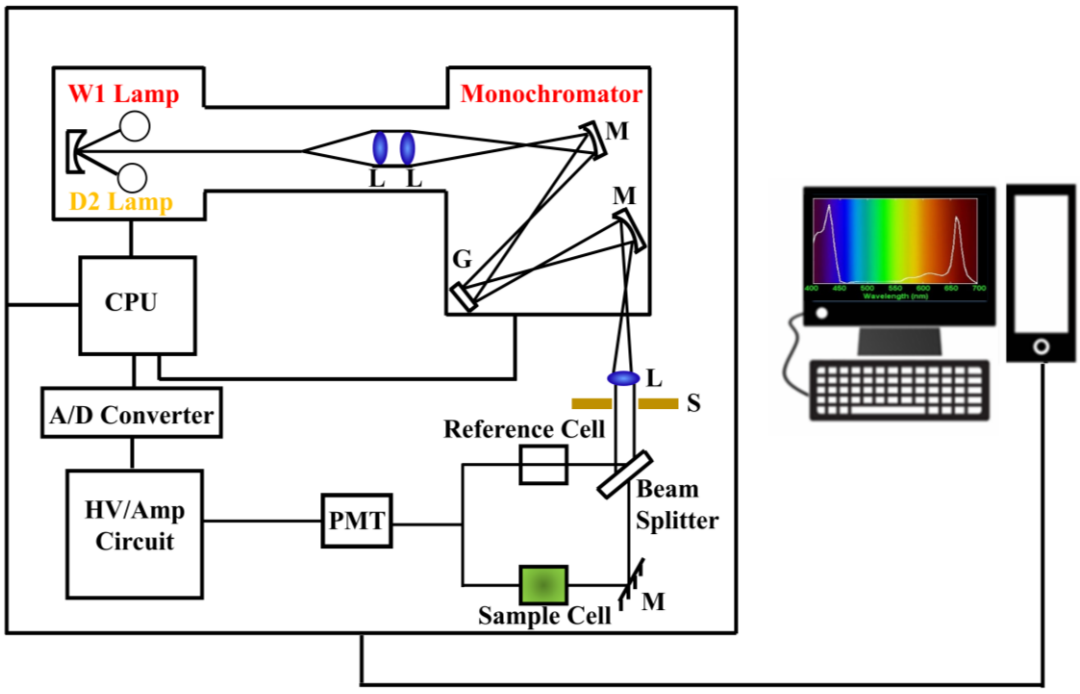

Figure 3.1. *Schematic ray diagram of an absorption spectrophotometer. Tungsten halogen (W1) and deuterium lamps (D2) are used as light sources in the visible and UV regions, respectively. M, G, L, S, PMT designate mirror, grating, lens, shutter and photomultiplier tube, respectively. CPU, A/D converter and HV/amp indicate central processing unit, analog to digital converter and high-voltage/amplifier circuit, respectively.*

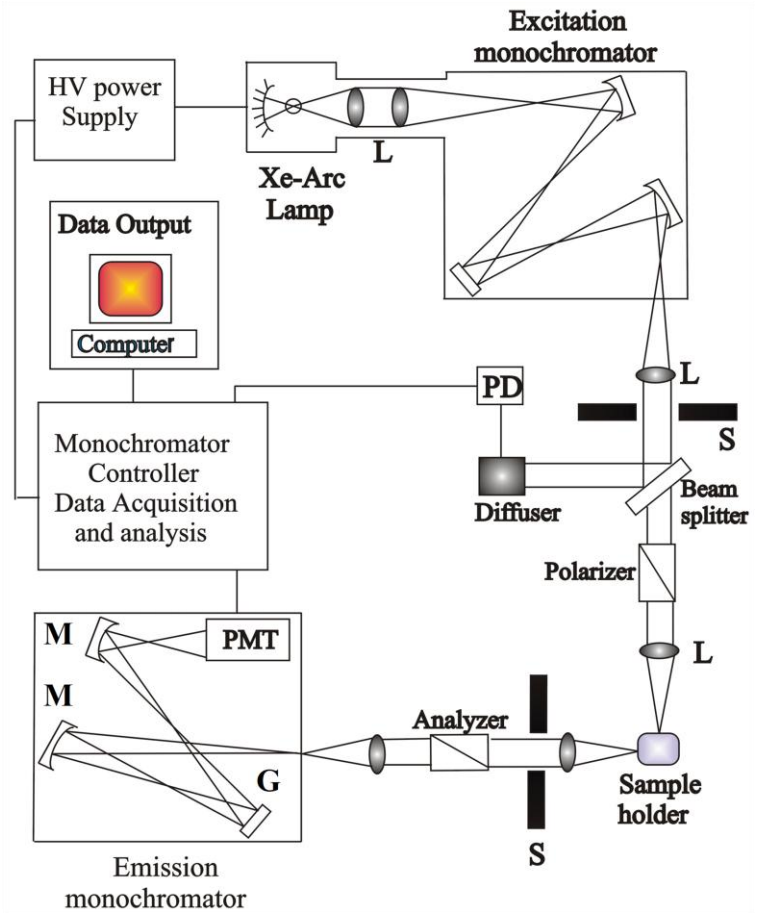

Figure 3.2. *Schematic ray diagram of an emission spectrofluorimeter. M, G, L, S, PMT and PD represent mirror, grating, lens, shutter, and photomultiplier tube and reference photodiode, respectively.*

3.1.2. Time-correlated Single Photon Counting (TCSPC) Technique: All the picosecond-resolved fluorescence transients were recorded using TCSPC technique. The schematic block diagram of a TCSPC system is shown in Figure 3.3. TCSPC setup from Edinburgh instruments, U.K., was used during fluorescence decay acquisitions. The instrument response functions (IRFs) of the laser sources at different excitation wavelengths varied between 70 ps to 80 ps. The fluorescence from the sample was detected by a photomultiplier after dispersion through a grating monochromator [1]. For all transients, the polarizer in the emission side was adjusted to be at 54.70 (magic angle) with respect to the polarization axis of excitation beam.

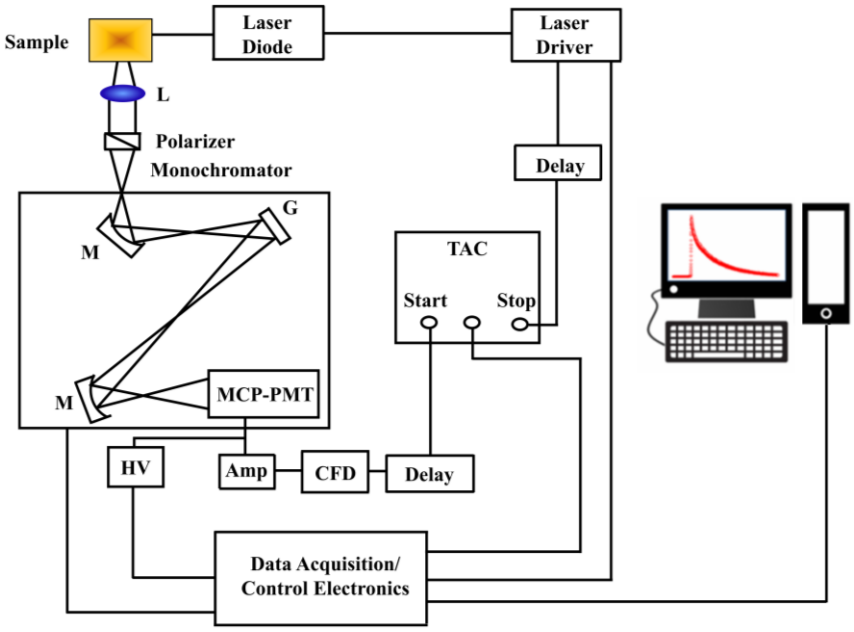

Figure 3.3. *Schematic ray diagram of a time correlated single photon counting (TCSPC) spectrophotometer. A signal from microchannel plate photomultiplier tube (MCP-PMT) is amplified (Amp) and connected to start channel of time to amplitude converter (TAC) via constant fraction discriminator (CFD) and delay. The stop channel of the TAC is connected to the laser driver via a delay line. L, M, G and HV represent lens, mirror, grating and high voltage source, respectively.*

3.1.3. Transmission Electron Microscopy (TEM): A FEI TecnaiTF-20 field-emission high-resolution TEM (Figure 3.4) equipped with energy dispersive X-ray

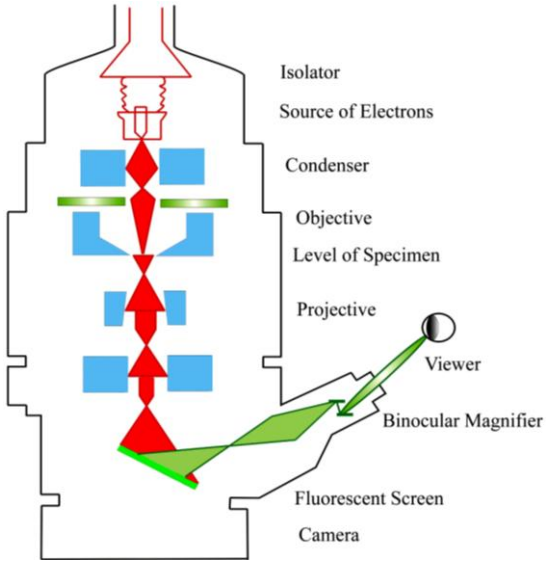

Figure 3.4. *Schematic diagram of a typical transmission electron microscope (TEM). After the transmission of electron beam through a specimen, the magnified image is formed either in the fluorescent screen or can be detected by a CCD camera.*

(EDAX) spectrometer was used to characterize the microscopic structures of samples and to analyze their elemental composition. The sizes of the nanostructures were determined from the TEM images obtained at 200 kV acceleration voltage of the microscope. Samples for TEM were prepared by placing a drop of the colloidal solution on a carbon-coated copper grid and allowing the film to evaporate overnight at room-temperature.

3.1.4. Scanning Electron Microscopy (SEM): Surface characterization of nanomaterials were done by scanning electron microscope FE (field emission)-SEM; JEOL. Ltd., JSM-6500F. An electron-gun is attached to SEM and the electrons from filament triggered by 0 KV to 30 KV voltages. These electrons go first through a condenser lens and then through an objective lens, then through an aperture and finally reach to the specimen. The high energy electrons go a bit in the sample and back again give secondary electrons. The signal from secondary electrons are detected by detector and amplified. The ray diagram of the SEM setup is shown in Figure 3.5.

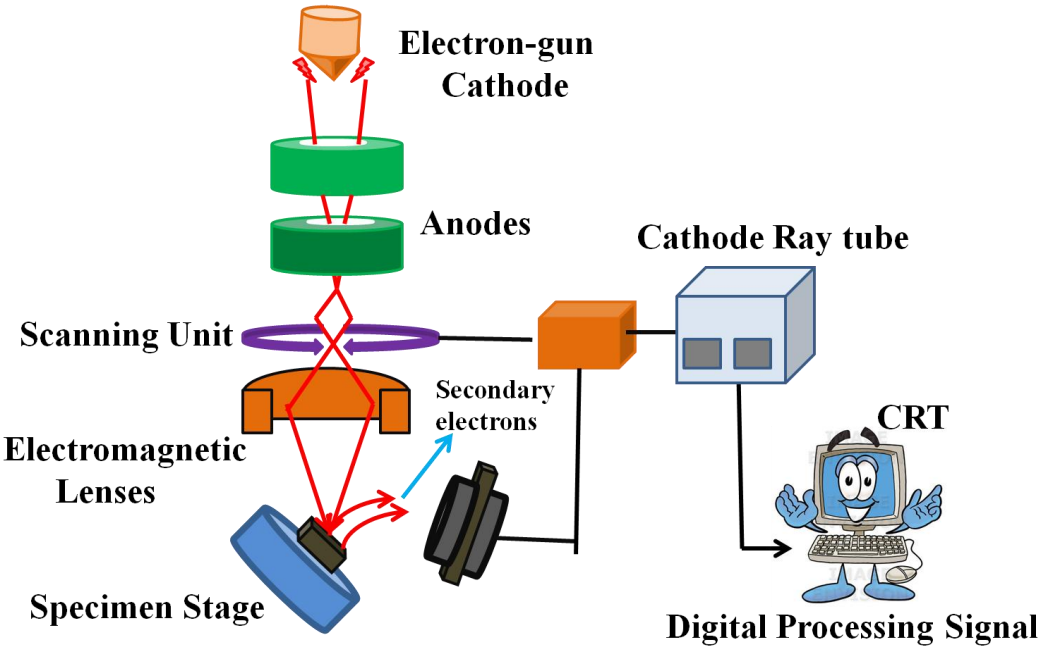

Figure 3.5. *Schematic diagram of typical scanning electron microscope (SEM).*

3.1.5. Dynamic Light Scattering (DLS): Dynamic light scattering (DLS), also known as Photon Correlation Spectroscopy (PCS) or Quasi-Elastic Light Scattering (QELS), is one of the most popular techniques used to determine the hydrodynamic size of the particle. DLS measurements were performed on a Nano S Malvern instruments, U.K. employing a 4 mW He-Ne laser (λ= 632.8 nm) and equipped with a thermostatted sample chamber. The instrument allows DLS measurements in which all the scattered photons are collected at 173˚ scattering angle (Figure 3.6). The instrument measures the time-dependent fluctuation in intensity of light scattered from the particles in solution at a fixed scattering angle. The ray diagram of the DLS setup is shown in Figure 3.6.

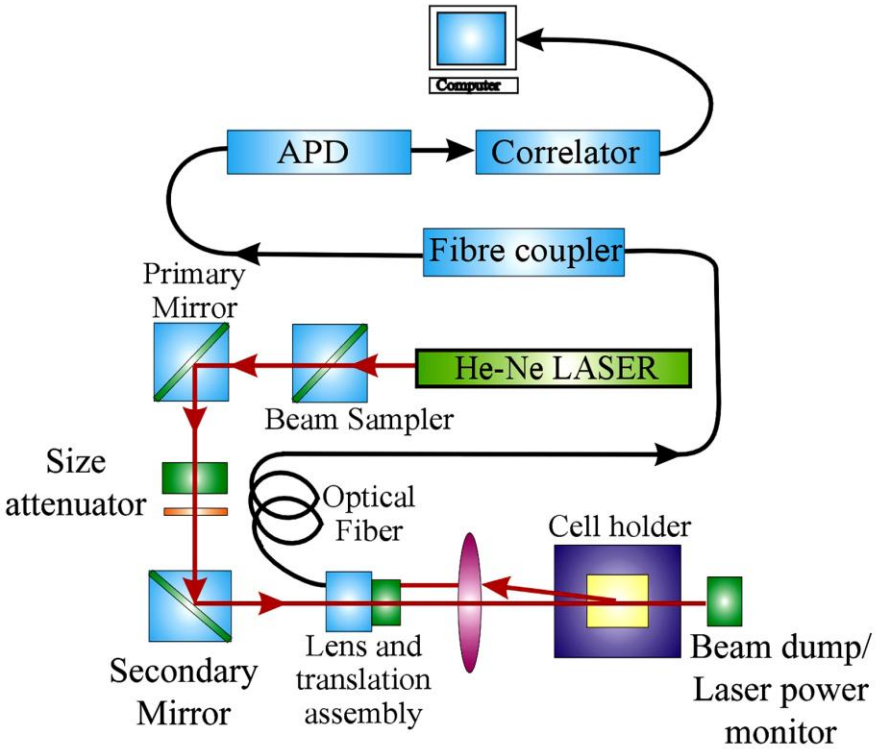

Figure 3.6. *Schematic ray diagram of dynamic light scattering (DLS) instrument. The avalanche photo diode (APD) is connected to preamplifier/amplifier assembly and finally to correlator. It has to be noted that lens and translational assembly, laser power monitor, size attenuator, laser are controlled by the computer.*

It has been seen that particles in dispersion are in a constant, random Brownian motion and this causes the intensity of scattered light to fluctuate as a

function of time. The correlator used in a DLS instrument constructs the intensity autocorrelation function G(τ) of the scattered intensity,

$$G(\tau) = \langle I(t)I(t+\tau)\rangle \tag{3.1}$$

where τ is the time difference (the sample time) of the correlator. For a large number of monodisperse particles in Brownian motion, the correlation function (given the symbol G) is an exponential decay function of the correlator time delay τ,

$$G(\tau) = A[1 + B\exp(-2\Gamma\tau)] \tag{3.2}$$

where A is the baseline of the correlation function, B is the intercept of the correlation function. Γ is the first cumulant and is related to the translational diffusion coefficient as, $\Gamma = Dq^2$, where q is the scattering vector and its magnitude is defined as,

$$q = \left(\frac{4\pi n}{\lambda_0}\right)\sin\left(\frac{\theta}{2}\right) \tag{3.3}$$

where n is the refractive index of dispersant, λ_0 is the wavelength of the laser and θ, the scattering angle. For polydisperse samples, the equation can be written as,

$$G(\tau) = A\left[1 + B\left|g^{(1)}(\tau)\right|^2\right] \tag{3.4}$$

where the correlation function $g^{(1)}(\tau)$ is no longer a single exponential decay and can be written as the Laplace transform of a continuous distribution G(Γ) of decay times,

$$g^{(1)}(\tau) = \int_0^\infty G(\Gamma)\exp(-\Gamma\tau)d\Gamma \tag{3.5}$$

The scattering intensity data in DLS are processed using the instrumental software to obtain the hydrodynamic diameter (d_H) and the size distribution of the scatterer in each sample. In a typical size distribution graph from the DLS measurement, X-axis shows a distribution of size classes in nm, while the Y-axis shows the relative intensity of the scattered light. The diffusion coefficient (D) can be calculated using the hydrodynamic diameter (d_H) of the particle by using the Stoke-Einstein relation,

$$D = \frac{k_B T}{3\pi\eta d_H} \tag{3.6}$$

where k_B, T, d_H, η are Boltzmann constant, temperature in Kelvin, hydrodynamic diameter and viscosity, respectively.

3.1.6. X-ray Diffraction (XRD) Measurement: XRD is a popular and a powerful technique for determining crystal structure of crystalline materials. By examining the diffraction pattern, one can identify the crystalline phase of the material. Small angle scattering is useful for evaluating the average interparticle distance while wide-angle diffraction is useful for refining the atomic structure of nanoclusters. The widths of the diffraction lines are closely related to strain and defect size and distribution in nanocrystals. As the size of the nanocrystals decreases, the line width is broadened due to loss of long-range order relative to the bulk. This XRD line width can be used to estimate the size of the particle by using the Debye-Scherrer formula,

$$D = \frac{0.9\lambda}{\beta \cos\theta} \tag{3.7}$$

where, D is the nanocrystal diameter, λ is the wavelength of light, β is the full-width half-maximum (FWHM) of the peak in radians, and θ is the Bragg angle. XRD measurements were performed on a PANalytical XPERT-PRO diffractometer (Figure 3.7) equipped with CuKα radiation (λ = 1.5418 Å at 40 mA, 40 kV). XRD

patterns were obtained by employing a scanning rate of 0.02° s^{-1} in the 2θ range from 15° to 75°.

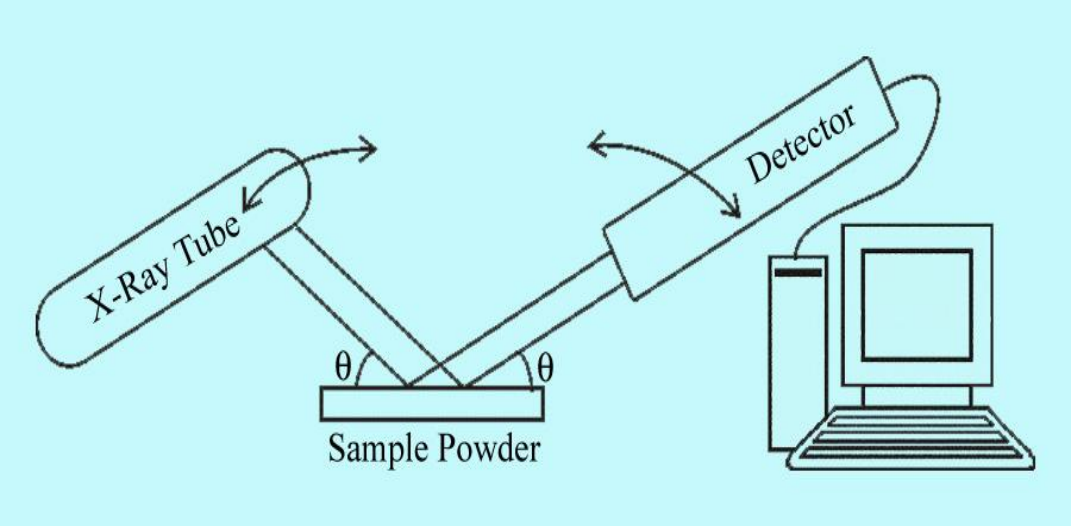

Figure 3.7. *Schematic diagram of X-ray Diffraction (XRD) instrument. By varying the angle θ, the Bragg's Law conditions, nλ=2dsinθ are satisfied by different d-spacings in polycrystalline materials. Plotting the angular positions and intensities of the resultant diffracted peaks of radiation produces a pattern, which is characteristic of the sample.*

3.1.7. Thermogravimetric-Differential Thermal Analyzer (TG-DTA) Setup: The thermogravimetric (TG) analysis was carried out using Diamond thermogravimetric (TG)-differential thermal analyzer (DTA) from Perkin Elmer. The TG determines the weight change of a sample whereas the DTA measures the change in temperature between a sample and the reference as a function of temperature and/or time. The schematic of the TG-DTA setup is shown in Figure 3.8. When a weight change occurs on the sample side, the beam holding the platinum pans is displaced. This movement is detected optically and the driving coil current is changed to return the displacement to zero. The detected driving coil current change is proportional to the sample weight change and the output is the TG signal. The DTA detects the temperature difference between the sample holder and the reference holder using the electromotive force of thermocouples, which are attached to the holders. This difference is measured as the DTA signal.

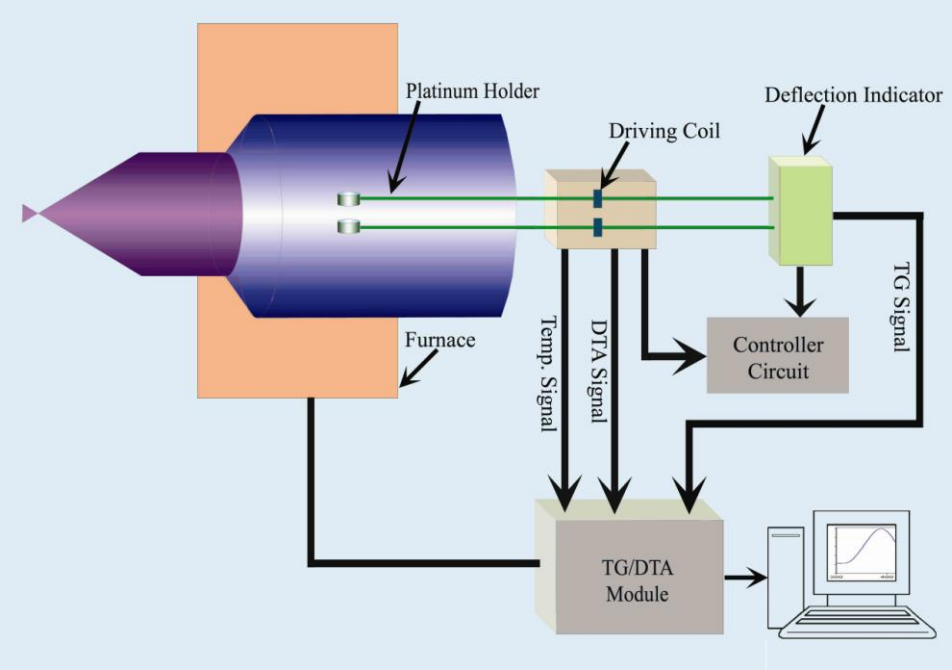

Figure 3.8. *The schematic representation of TG-DTA setup.*

3.1.8. Fourier Transform Infrared (FTIR) Measurement: FTIR spectroscopy is a technique that can provide very useful information about functional groups in a sample. An infrared spectrum represents the fingerprint of a sample with absorption peaks which correspond to the frequencies of vibrations between the bonds of the atoms making up the material. Because each different material is a unique combination of atoms, no two compounds produce the exact same infrared spectrum. Therefore, infrared spectroscopy can result in a positive identification (qualitative analysis) of every different kind of material. In addition, the size of the peaks in the spectrum is a direct indication of the amount of material present. The two-beam Michelson interferometer is the heart of FTIR spectrometer. It consists of a fixed mirror (M4), a moving mirror (M5) and a beam-splitter (BS1), as illustrated in Figure 3.9. The beam-splitter is a laminate material that reflects and transmits light equally. The collimated IR beam from the source is partially transmitted to the moving mirror and partially reflected to the fixed mirror by the beam-splitter. The two IR beams are then reflected back to the beam-splitter by the mirrors. The detector then sees the transmitted beam from the fixed mirror and

reflected beam from the moving mirror, simultaneously. The two combined beams interfere constructively or destructively depending on the wavelength of the light (or frequency in wavenumbers) and the optical path difference introduced by the moving mirror. The resulting signal is called an interferogram which has the unique property that every data point (a function of the moving mirror position) which makes up the signal has information about every infrared frequency which comes from the source. Because the analyst requires a frequency spectrum (a plot of the intensity at each individual frequency) in order to make identification, the measured interferogram signal cannot be interpreted directly. A means of "decoding" the individual frequencies is required. This can be accomplished *via* a well-known mathematical technique called the Fourier transformation. This transformation is performed by the computer which then presents the user with the desired spectral information for analysis. FTIR measurements were performed on a JASCO FTIR-6300 spectrometer (transmission mode). For the FTIR measurements, powdered samples were mixed with KBr powder and pelletized. The background correction was made using a reference blank of KBr pellet.

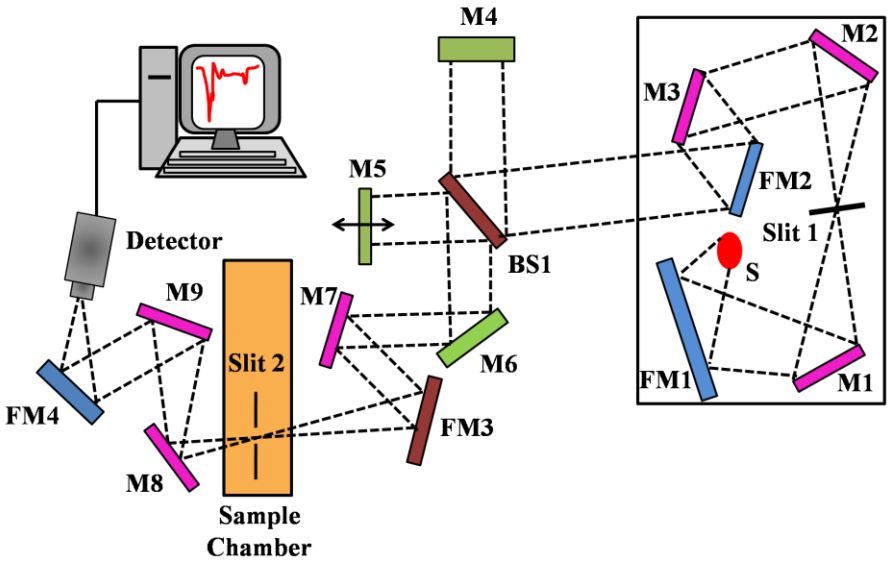

Figure 3.9. *Schematic of Fourier Transform Infrared (FTIR) spectrometer. It is basically a Michelson interferometer in which one of the two fully-reflecting mirrors is movable, allowing a variable delay (in the travel-time of the light) to be included in one of the beams. M, FM and BS1 represent the mirror, focussing mirror and beam splitter, respectively. M5 is a moving mirror.*

3.1.9. Laser Raman Spectroscopy: Raman spectroscopy is a useful technique for the identification of a wide range of substances− solids, liquids, and gases. It is a straightforward, non-destructive technique requiring no sample preparation. Raman spectroscopy involves illuminating a sample with monochromatic light and using a spectrometer to examine light scattered by the sample.

At the molecular level photons can interact with matter by absorption or scattering processes. Scattering may occur either elastically, or inelastically. The elastic process is termed Rayleigh scattering, whilst the inelastic process is termed Raman scattering. The electric field component of the scattering photon perturbs the electron cloud of the molecule and may be regarded as exciting the system to a 'virtual' state. Raman scattering occurs when the system exchanges energy with the photon and the system subsequently decays to vibrational energy levels above or below that of the initial state. The frequency shift corresponding to the energy difference between the incident and scattered photon is termed the Raman shift. Depending on whether the system has lost or gained vibrational energy, the Raman shift occurs either as an up or down-shift of the scattered photon frequency relative to that of the incident photon. The down-shifted and up-shifted components are called, respectively, the Stokes and anti-Stokes lines. A plot of detected number of photons versus Raman shift from the incident laser energy gives a Raman spectrum. Different materials have different vibrational modes, and therefore characteristic Raman spectra. This makes Raman spectroscopy a useful technique for material identification. There is one important distinction to make between the Raman spectra of gases and liquids, and those taken from solids− in particular, crystals. For gases and liquids it is meaningful to speak of the vibrational energy levels of the individual molecules which make up the material. Crystals do not behave as if composed of molecules with specific vibrational energy levels; instead the crystal lattice undergoes vibration. These macroscopic vibrational modes are called phonons.

In modern Raman spectrometers (LabRAM HR, Jobin Yvon), lasers are used as a photon source due to their highly monochromatic nature, and high beam fluxes (Figure 3.10). This is necessary as the Raman effect is weak, typically the Stokes lines are ~10^5 times weaker than the Rayleigh scattered component. In the visible spectral range, Raman spectrometers use notch filters to cut out the signal from a very narrow range centred on the frequency corresponding to the laser radiation. Most Raman spectrometers for material characterization use a microscope to focus the laser beam to a small spot (<1−100 μm diameter). Light from the sample passes back through the microscope optics into the spectrometer. Raman shifted radiation is detected with a charge-coupled device (CCD) detector, and a computer is used for data acquisition and curve fitting. These factors have helped Raman spectroscopy to become a very sensitive and accurate technique.

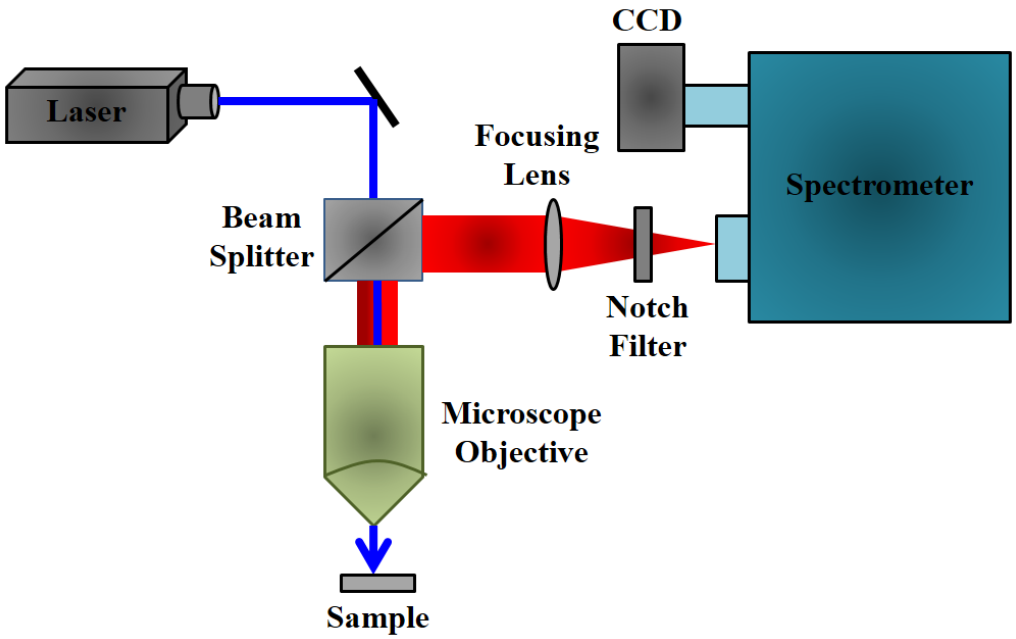

Figure 3.10. *Schematic diagram of a Raman spectrometer is shown.*

3.1.10. X-Ray Photoelectron Spectroscopy (XPS): XPS works on the principle of photoelectric effect discovered by Heinrich Hertz in 1887. When radiation of appropriate energy incident, electrons are emitted from the surface of the metal. The relation between the energy of the excitation radiation, work function of the

metal and the maximum kinetic energy of the emitted electron as proposed by Einstein in 1905 is:

$$h\upsilon = \phi + KE_{\max} \tag{3.8}$$

Φ is the work function of the metal, hυ is the energy of the radiation, KE_{max} is the maximum kinetic energy of the emitted electron. For analysing the core electronic structure (0 – 1300 eV) of elements, radiation of high energy were used like X-rays, hence the corresponding spectroscopy is termed X-ray Photoelectron Spectroscopy (XPS) (Figure 3.11).

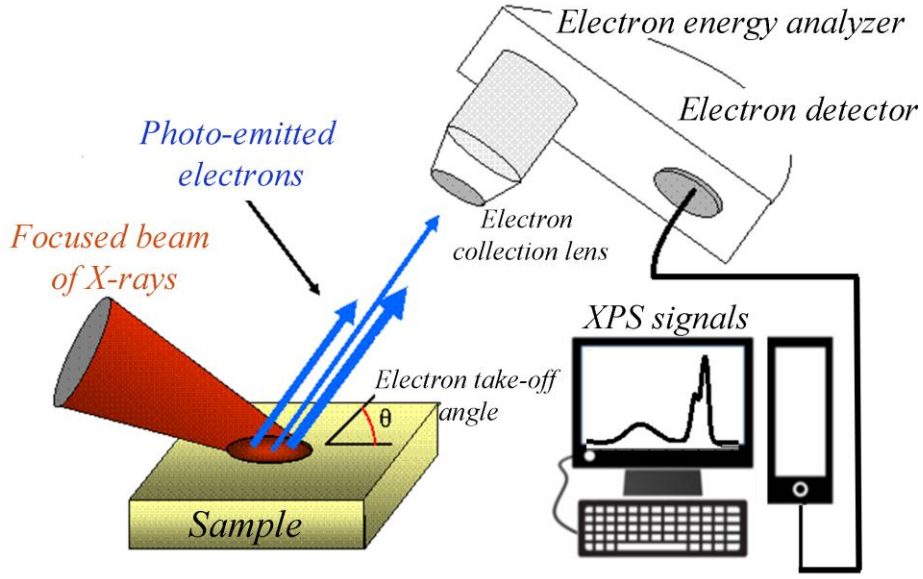

Figure 3.11. *Schematic diagram of a typical X-ray photoelectron spectroscopy (XPS).*

Surface analysis by XPS is accomplished by irradiating a sample with monoenergetic soft X-rays and analysing the energy of the detected electrons. Mg Kα (1253.6 eV), Al Kα (1486.6 eV), or monochromatic Al Kα (1486.7 eV) X-rays are usually used. These photons have limited penetrating power in a solid of the order of 1 – 10 μm. They interact with atoms in the surface region, causing electrons to be emitted by the photoelectric effect. The emitted electrons have measured kinetic energies given by:

$$KE = h\upsilon - BE - \phi_S \qquad (3.9)$$

where hυ is the energy of the photon, BE is the binding energy of the atomic orbital from which electron originates, Φ_S is the work function of the spectrometer. The binding energy may be regarded as the energy difference between the initial and final states after the photoelectron has left the atom. Because there is a variety of a possible final state of the ions from each type of atom, there is a corresponding variety of kinetic energies of the emitted electrons. Moreover, there is a different probability or cross section for each final state. Because each element has a unique set of binding energies, XPS can be used to identify and determine the concentration of the elements in the surface. Variation in the elemental binding energies (the chemical shifts) arise from differences in the chemical potential and polarizability of compounds. These chemical shifts can be used to identify the chemical state of the material being analysed. In our studies, XPS were performed on an Omicron ESCA probe spectrometer with polychromatic Mg Kα X-rays (hν = 1253.6 eV).

3.1.11. Cyclic Voltammetry (CV): CV is a useful technique for studying electrochemical reactions. In case of CV, the voltage is swept between two potential values (V_1 and V_2) at a fixed rate, however now when the voltage reaches V_2 from V_1, the scan is reversed and the voltage is swept back to V_1. The current response is plotted as a function of the applied potential. Electrochemical experiments were performed using a CH analyser potentiostat (CHI1110C). A three electrode system consisting of a platinum working electrode, a platinum counter electrode and a reference electrode were employed. All the potentials reported in this thesis are referenced to the Ag/Ag+ couple. Electrolyte is usually added to the sample solution to ensure sufficient conductivity. The solvent, electrolyte, and material composition of the working electrode will determine the potential range that can be accessed during the experiment. The schematic presentation of the CV set up is shown in Figure 3.12.

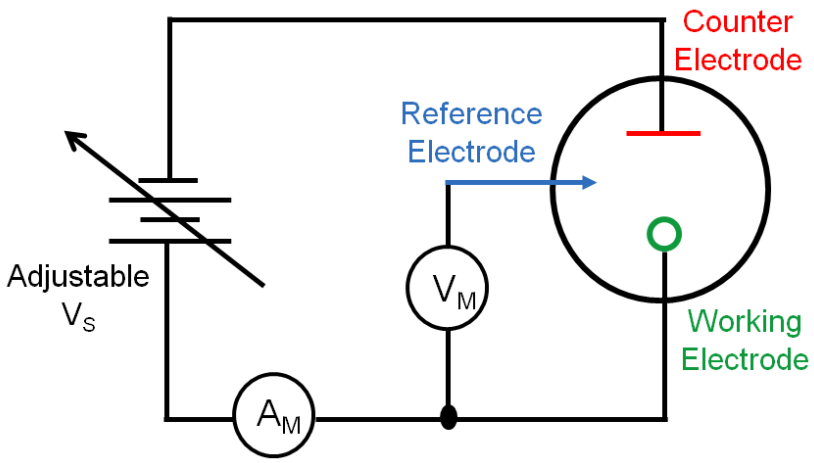

Figure 3.12. *Schematic diagram of a simplified measurement circuit for performing cyclic voltammetry (CV).*

A typical electrochemical measurement circuit made up of an electrochemical cell, an adjustable voltage source (V_S), an ammeter (A_M) and a voltmeter (V_M). The three electrodes of the electrochemical cell are the working electrode (WE), reference electrode (RE) and the counter (or auxiliary) electrode (CE). The voltage source (V_S) for the potential scan is applied between the working electrode and the counter electrode. The potential (E) between the reference electrode and the working electrode is measured with the voltmeter and the overall voltage (Vs) is adjusted to maintain the desired potential at the working electrode with respect to the reference electrode. The resulting current (i) flowing to or from the working electrode is measured with the ammeter (A_M).

3.1.12. Electrochemical Impedance Spectroscopy (EIS): Electrochemical Impedance Spectroscopy (EIS) is a powerful technique to investigate the electronic and ionic processes in dye sensitized solar cells (DSSC). Electrochemical impedance is usually measured by applying an ac potential to an electrochemical cell and then measuring the current through the cell. An important advantage of EIS over other techniques is the possibility of using tiny ac voltage amplitudes exerting a very small perturbation on the system. A Nyquist plot can be made by plotting the real part of the transfer function on the X-axis and the imaginary part

on the Y-axis. The Nyquist diagram for DSSC features typically three semicircles that in the order of increasing frequency are attributed to the Nernst diffusion within the electrolyte, the electron transfer at the oxide/electrolyte interface and the redox reaction at the platinum counter electrode. From applying appropriate equivalent circuits, the transport rate and lifetime of the electron in the mesoscopic film are derived. Electrochemical impedance spectroscopy (EIS) were performed on a electrochemical workstation CHI650E (CH instruments) with a frequency range from 100 kHz to 0.1 Hz in the open circuit condition. The schematic presentation of the EIS set up is shown in Figure 3.13. All impedance measurements were carried out under a bias illumination of 100mW/cm^2. The obtained spectra were fitted using the CHI650E software in terms of appropriate equivalent circuits.

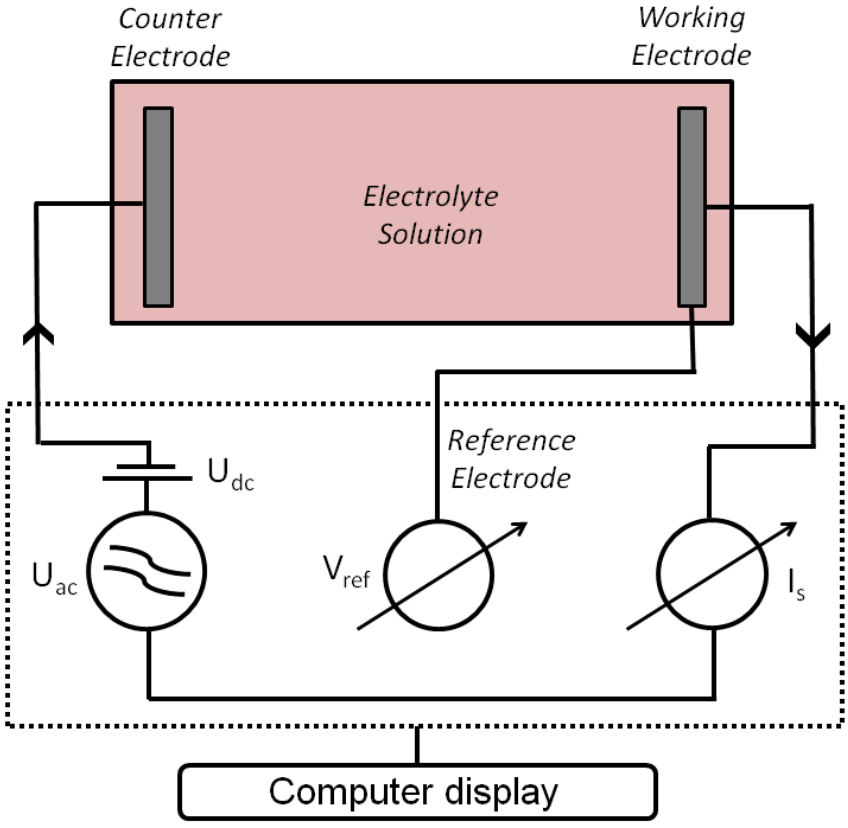

Figure 3.13. *Schematic diagram of a simplified measurement circuit for performing Electrochemical Impedance Spectroscopy (EIS).*

3.1.13. Solar Cell Characterization: The characterization of DSSCs involves the electrical current−voltage (I−V) characteristics, incident photon to current conversion efficiency (IPCE) measurements and photovoltage decay measurements. The current density-voltage characteristics of the cells were recorded by a keithley multimeter under irradiance of 100 mW cm^{-2} (AM 1.5 simulated illuminations, Photo Emission Tech). The electrical circuit used to measure the I−V characteristics of the solar cells is shown in Figure 3.14. The short-circuit current (I_{SC}) and open-circuit voltage (V_{OC}) of the solar cells were determined from their respective I−V characteristic curves. The fill factor (FF) and efficiency (η) of the solar cells were calculated by using equations 2.24 and 2.25, respectively.

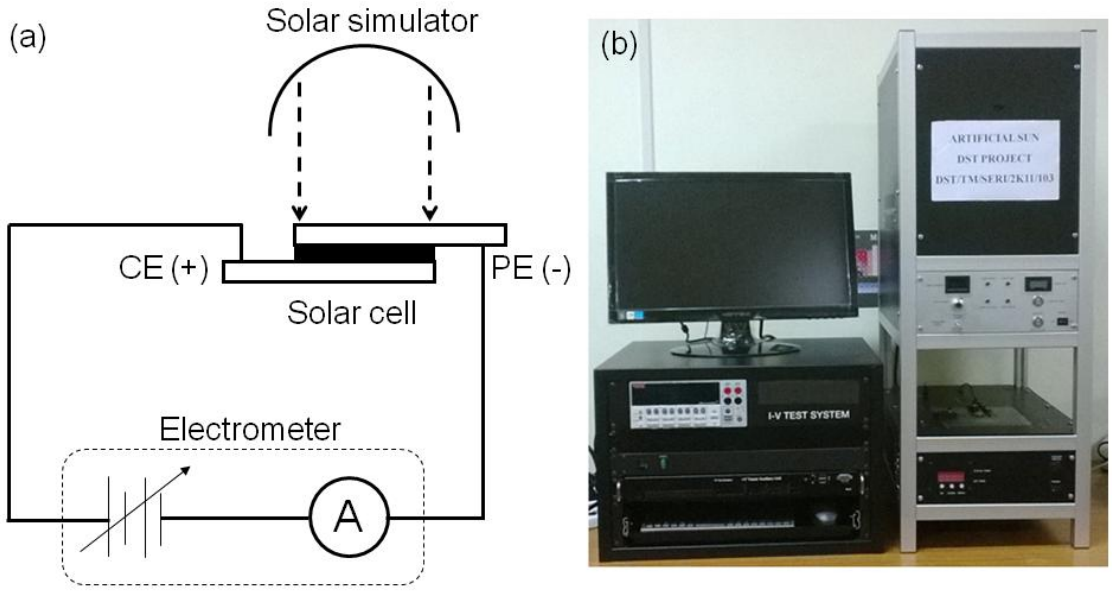

Figure 3.14. *(a) Electrical setup and (b) photograph of the solar simulator used for the solar cell characterization.*

The IPCE of the DSSCs was measured by using a homemade setup with a Bentham monochromator and dual light (deuterium and xenon) sources. The monochromatic light was allowed to fall on the solar cells and the respective current from the solar cell at every incident wavelength of light was measured.

Finally, the IPCE was calculated by using equation 2.27. The set up used to measure the IPCE of the solar cells is shown in Figure 3.15.

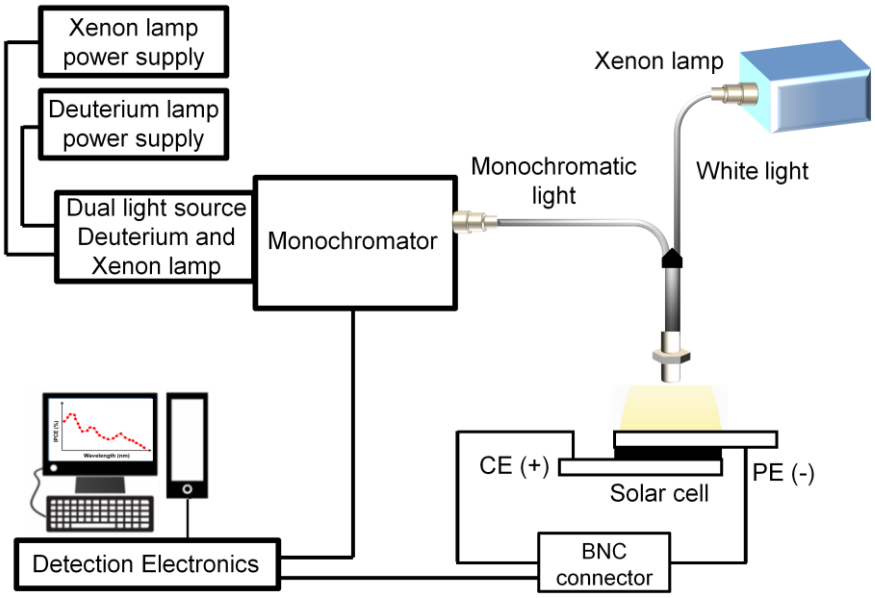

Figure 3.15. *Schematic diagram of a simplified measurement circuit for performing IPCE measurements.*

Photovoltage decay measurements were carried out after illuminating the cells under 1 Sun condition. The photovoltage decays after switching off the irradiation were monitored by an oscilloscope (Owon) through computer interface as shown in Figure 3.16. The decays were fitted with exponential decay functions using Origin software.

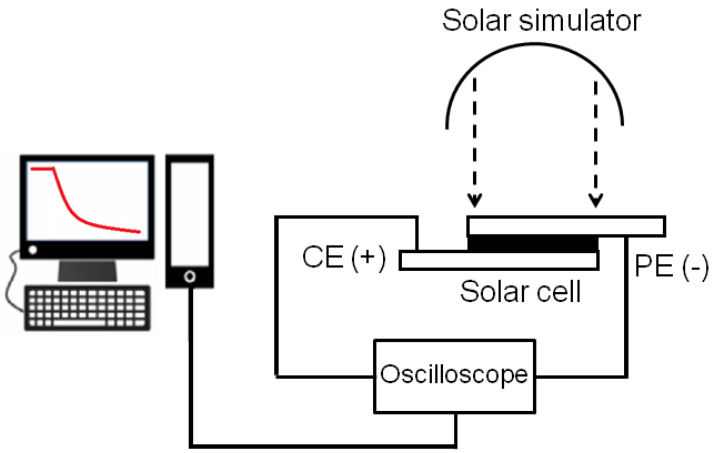

Figure 3.16. *Schematic diagram of the photovoltage decay measurement setup.*

3.1.14. Fiber-Optic Coupled System for Photocatalytic Measurements: Increased sensitivity in the signal detection in the presence of strong ambient light in our experimental setup lies on the confocal geometry of the excitation and detection sides [2]. As shown in the schematic ray-diagram of the experimental setup (Figure 3.17) the excitation fiber (400 µM core diameter) carrying laser light is connected to an optical coupler (Ocean Optics, USA, model: 74-UV) in order to focus excitation light at the middle of a sample holder, which is an all-side polished quartz-cuvette from Starna cells (U.S.A). The numerical aperture (NA) of

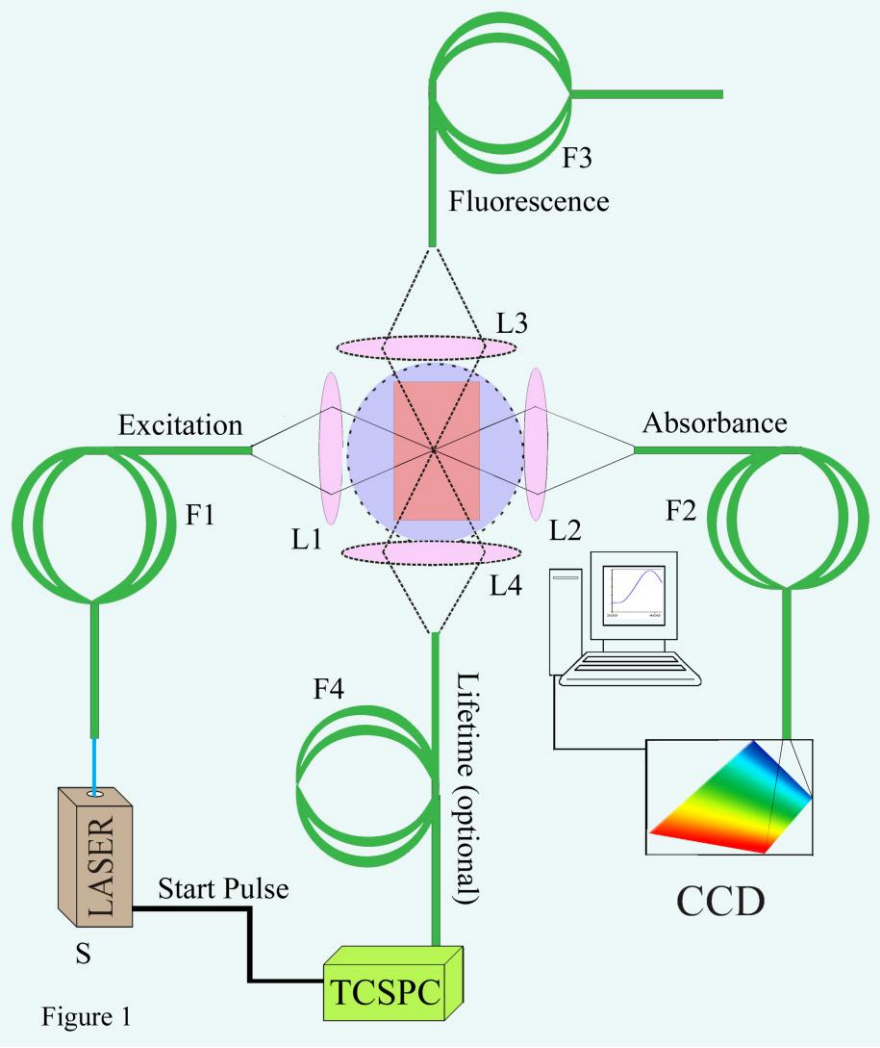

Figure 3.17. *Schematic diagram of the universal setup. S is the source, F1-F4 are the optical fibers, L1-L4 are the fiber coupler lenses, the violate circle represents the ambient light around the sample (reddish rectangle). CCD is the photo-signal detector, connected with computer.*

the excitation fiber (NA=0.45) and focal length of the optical coupling lens (0.5 cm) systems are to achieve out-of-focus rejection by two strategies: firstly by illuminating a single point of the specimen at any one time with a focused beam, so that illumination intensity drops off rapidly above and below the plane of focus and secondly by the use of optical fiber as a collecting unit with similar coupling lens so that light emitted away from the point in the specimen being illuminated is blocked from reaching the detector. The collection fiber is arranged in 'I' geometry and connected with the commercially available CCD based miniaturized spectrograph (Ocean Optics, USA, model: HR4000) in order to measure absorption of the sample of interest. More flexibility in the measurement can also be achieved by using Shimadzu spectrophotometer (UV-2600) or Jobin Yvon (Fluoromax-3) fluorimeter to measure absorption and photoluminescence, respectively. In order to establish the fact that the absorption of a sample can be measured in presence of strong ambient light effectively, we have placed the quartz cell containing test sample on a home-made UV bath (8W).

3.2. Sample Preparation:

In this section the different sample preparation methods have been discussed.

3.2.1. Chemicals Used: The chemicals and spectroscopic probes were procured from the following sources. Analytical-grade chemicals were used for synthesis without further purification. Deionized (DI) water, obtained from Millipore, was used to prepare all aqueous solutions. The probes methylene blue (Carlo Erba), methyl orange (Sigma Aldrich), bilirubin (Sigma Aldrich), benzoquinone (Alfa Aesar) and the dyes N719 (Solaronix, Switzerland), coumarin 343 (Sigma Aldrich), coumarin 500 (Sigma Aldrich), hematoporphyrin (Sigma Aldrich), protoporphyrin IX (Sigma Aldrich), zinc phthalocyanine (Sigma Aldrich) were used without any further purification. ZnO NPs (~ 30 nm), TiO_2 NPs (~ 21 nm), Al_2O_3 NPs (~ 40 nm) were purchased from Sigma Aldrich. PbS quantum dots were purchased from Evident Technology.

3.2.2. Sensitization of Hematoporphyrin (HP) and Fe(III)HP Dyes on TiO_2 NP Surface: A 0.5 mM HP C34H38N4O6 (Sigma) solution was prepared in anhydrous ethanol under constant stirring at room temperature for 1 h. The sensitization of TiO_2 NPs (Anatase P25) with HP dye was carried out in the dark and at room temperature by adding TiO_2 NPs into a 0.5 mM HP solution with continuous stirring for 12 h. After the sensitization process, the solution was centrifuged for a few minutes and the supernatant clear solution of unattached dyes was removed. Then the sensitized material was washed with ethanol several times to remove any unattached dye. The nanohybrid was then dried in a water bath and stored in the dark until further use. The Fe(III)HP was prepared by adding ferric chloride (Sigma) to the ethanolic solution of HP and stirred for 12 h. The sensitization was done by the same method as described above.

3.2.3. Synthesis of ZnO NPs: ZnO nanoparticles were synthesized in ethanol. In a typical synthesis process, a 2 mM $Zn(CH_3COO)_2.2H2O$ solution was prepared in 40 mL ethanol by mixing the solution at 60 °C until a clear solution was obtained. Separately, another 4 mM NaOH solution was prepared in 20 mL ethanol by refluxing the solution at 60 °C until a clear solution was obtained. Both the solutions were then allowed to cool down naturally to room temperature. Then the NaOH solution was slowly added to the zinc acetate solution and mixed properly. The glass beaker was then covered tightly with aluminum foil and placed in a pre-heated water bath at 60 °C for 2 hours to hydrolyze. After 2 hours, the resultant transparent ZnO nanoparticle colloidal solution was allowed to cool down naturally to room temperature and stored in a refrigerator for further use.

3.2.4. Sensitization of Zinc Phthalocyanine (ZnPc) on the ZnO NP Surface through Tartrate Ligands: A 0.5 mM ZnPc ($C_{32}H_{16}N_8Zn$) solution was prepared in dimethyl sulfoxide (DMSO) with constant stirring for 1 h. The functionalization of ZnO NPs with tartrate ligands was carried out at room temperature in dark ambience by adding ZnO NPs into a 0.5 mM tartrate aqueous solution (pH

adjusted to 9 by NaOH) with continuous stirring for 6 h. Then, the tartrate-functionalized ZnO NPs were added to the 0.5 mM ZnPc solution in a dimethyl sulfoxide (DMSO)–deionized (DI) water (1:1, v:v) mixture and stirred for 12 hours under dark conditions. After the sensitization process, the solution was centrifuged for a few minutes and the supernatant clear solution of unattached dyes was removed. Then, the sensitized material was washed with a DMSO–water mixture several times to remove any unattached dye. The nanohybrid was then dried in a water bath and stored in the dark until further use.

3.2.5. Synthesis of ZnO Nanorods (NRs): Zinc acetate dihydrate, $Zn(CH_3COO)_2$ $2H_2O$ (Merck), zinc nitrate hexahydrate, $Zn(NO_3)_2$, $6H_2O$ (Sigma-Aldrich), hexamethylenetetramine, and $C_6H_{12}N_4$ (Aldrich) were used as the starting materials for a low temperature hydrothermal synthesis of ZnO NRs on FTO substrates. Detailed processes for the hydrothermal growth of single-crystal ZnO NRs are described in our previous reports [3-5]. In brief, a ZnO seed layer was initially deposited on cleaned glass substrates by the spray-pyrolysis method at 100 ^{0}C using 10 mM zinc acetate solution in isopropanol. The seeded glass substrates were then annealed in air at 350 ^{0}C for 5 h and used for the hydrothermal growth of the ZnO NRs. An aqueous solution of zinc nitrate (20 mM) and hexamethylenetetramine (20 mM) was used as the precursor solution for the ZnO NR growth, which was carried out at 90 ^{0}C for 40 h. This led to the growth of ZnO NRs with a length of approximately 2–3 μm and diameter of 80–100 nm. To maintain a constant growth rate of the ZnO NRs during the hydrothermal process, the old precursor solution was replaced with a fresh solution every 1 h. The as-obtained ZnO NR samples were then taken out of the reaction vessel and rinsed thoroughly with DI water to remove unreacted residues. Finally, the samples were annealed in air at 350 ^{0}C for 1 h prior to the study.

3.2.6. Sensitization of ZnPc on the ZnO NR Surface Through Tartrate Ligands: The functionalization of ZnO NRs with tartrate ligands was carried out at room temperature in the dark by immersing the glass plates with ZnO NRs into a 0.5 mM tartrate aqueous solution (pH adjusted to 9 by NaOH) for 12 h. After that, the plates were washed with distilled water several times. For ZnPc sensitization, a 0.5 mM ZnPc solution, $C_{32}H_{16}N_8Zn$, was prepared in dimethyl sulfoxide (DMSO) with constant stirring for 1 h. The sensitization of the ZnO NRs with ZnPc dye was carried out in darkness and at room temperature by dipping the ZnO NR samples into the prepared dye solution for 12 h. After the sensitization process, the ZnO NRs were extracted from the dye solution, rinsed with a DMSO-water mixture thoroughly (to remove any physisorbed dye molecules), and stored in darkness for further use.

3.2.7. Sensitization of PbS QDs on ZnO NP Surface: TOPO capped colloidal PbS QDs in toluene were assembled to the ZnO NPs by constant stirring at room temperature in the dark for 12 h. After the sensitization process, the solution was centrifuged for a few minutes and the supernatant clear solution was removed. Then the sensitized material was washed with toluene several times. The nanocomposite was then dried in a water bath and stored in the dark until further use.

3.2.8. Synthesis of Polymer Nanostructures in Mesophases: The swollen hexagonal mesophases were prepared following the previously published method with some modifications [6-7]. Typically, 1 g of the surfactant (Sodium Dodecyl Sulfate) was dissolved in 2 mL of 0.3 $mol.L^{-1}$ NaCl in glass tubes. After a vigorous stirring at 30°C, the surfactant had completely dissolved leading to a transparent and viscous micellar solution. The subsequent addition of cyclohexane containing monomer 1, 4-diphenylbutadiyne (DPB) (10% of mass) and initiator benzoin methyl ether (BME) (1%) in the micellar solution under stirring leads to a white unstable emulsion. A cosurfactant, pentanol-1 (420 µL), was then added to the

mixture, which was then strongly stirred for a few minutes. This led to a perfectly colorless, translucent, birefringent and stable gel, a hexagonal mesophase. The doped mesophases were used as soft templates to synthesize polymer nanostructures induced by irradiation using UV light with an Oriel 300 W Xenon UV-Vis lamp at a distance of 5 cm for 12 hours. After reaction, the materials were extracted in a water-ethanol mixture, centrifuged and washed several times to eliminate the surfactant.

3.2.9. Preparation of PDPB-ZnO Nanoheterojunction (LHNH): PDPB–ZnO LHNH were prepared by dispersing ZnO (20 nm) into the ethanolic solution of as prepared PDPB nanofibers. The solutions were stirred for 48 h in the dark and then separated by centrifugation. The transparent supernatant was removed and the remaining yellowish powder was re-dispersed in ethanol for characterization. The LHNH was then dried in a water bath and stored in the dark until further use. During the synthesis of PDPB–ZnO nanoheterojunction, we used 5%, 10%, 20% and 50% of PDPB nanofibers with respect to ZnO nanoparticles (20 nm). We choose the lower concentration (5%) of PDPB nanofibers for further detailed study. The photocatalytic activity of PDPB–ZnO nanoheterojunction is found to be independent of the concentration of PDPB nanofibers (data not shown). The ~20 nm ZnO NPs does not have intrinsic defect state emission which is consistent with the literature. Hence, ZnO NPs (~5 nm) having intrinsic defect state emission have been employed for FRET study in order to confirm the molecular proximity between PDPB nanofibers and ZnO NPs within the LHNH.

For the direct *in situ* synthesis of ZnO NPs on PDPB nanofibers, we adopted a coprecipitation technique using ethanol as the solvent, following the previous reports from our group [8-10]. Briefly, 20 mL of 4 mM zinc acetate dehydrate solution was heated at 70 °C for 30 min in the presence of a fixed amount of PDPB nanofibers (1 mg). Then 20 mL of 4 mM sodium hydroxide solution in ethanol was

then added and the mixture was hydrolyzed for 2 h at 60 °C to obtain NPs of average diameters of ~5 nm.

3.2.10. Synthesis of Silver Modified TiO_2: The Ag-TiO_2 samples were obtained by radiolytic reduction of Ag^+ in the TiO_2 suspension following our previous report [11]. An ethanolic solution of $AgClO_4$ ($2x10^{-3}$ M) and TiO_2 (Evonik P25) suspension is sonicated for 3 min, then degassed with nitrogen and irradiated (under stirring) with a ^{60}Co panoramic gamma source (dose rate, 2.3 kGy h^{-1}). The silver ions were reduced by the solvated electrons and the alcohol radicals induced by solvent radiolysis under 1 h 20 min irradiation to reduce all the silver ions. The Ag-TiO_2 samples were centrifuged and dried at 60 °C.

3.2.11. Synthesis of Pt NPs Supported on Reduced Graphene Oxide: The graphene oxide (GO) was synthesized from graphite powder by the modified Hummers method as reported in our previous publication [12]. The GO (1 mg mL^{-1}) was then dispersed in 2-propanol and exfoliated in an ultrasonic bath for 20 min. Then 1 mM of platinum (II) acetylacetonate was added to the GO dispersion followed by deoxygenation under a N_2 flow. Then the mixture was irradiated under UV light for 6 h under a N_2 atmosphere [13]. Then as synthesized Pt-reduced graphene oxide nanohybrid was centrifuged and dried at 60 °C. The reduced GO was synthesized following the same procedure without adding the platinum salt.

3.2.12. Synthesis of TiO_2 Microspheres and Carbonate Doped TiO_2 Microspheres: The mesoporous TiO_2 microspheres were synthesized by following the modified previous reported literature [14-15]. In brief, 1 mL of titanium isopropoxide was mixed with 15 mL of anhydrous acetone and then stirred for 15 mins. Then the solution was transferred into a 20 mL Teflon lined stainless-steel autoclave and heated at 180 °C for 12 h. The precipitate was collected and washed with acetone and then with ethanol several times. The sample was dried at 60 °C.

Carbonate doped TiO_2 MS were synthesized by mixing the synthesized TiO_2 MS, urea and thiourea (1gm, 1.5 gm and 2 gm, respectively). The mixture was ground for 20 mins and then annealed at 400 °C for 5 h. After annealing the powder was washed with water for several times and then dried at 60 °C.

3.2.13. Sensitization of Protoporphyrin IX (PP) on ZnO NPs Surface: A 0.5 mM PP, $C_{34}H_{36}N_4O_5$, solution was prepared in dimethyl sulfoxide (DMSO)-deionized (DI) water (V/V) mixture under constant stirring for 1 h. The sensitization of ZnO NPs with PP dye was carried out at room temperature in the dark by adding ZnO NPs into a 0.5 mM PP solution with continuous stirring for 12 h. After the sensitization process, the solution was centrifuged for a few minutes and the supernatant clear solution of unattached dyes was removed. Then the sensitized material was washed with DMSO-water mixture several times to remove any unattached dye. The nanohybrid was then dried in a water bath and stored in the dark until further use.

3.2.14. Preparation of Dichlorofluorescein and ROS Measurements: DCFH was prepared [16-17] from DCFH-DA (dichlorofluorescin diacetate obtained from Calbiochem) by mixing 0.5 mL of 1.0 mM DCFH-DA in methanol with 2.0 mL of 0.01 N NaOH. This deesterification of DCFH-DA proceeded at room temperature for 30 min and the mixture was then neutralized with 10 mL of 25 mM NaH_2PO_4, pH 7.4. This solution was kept on ice in the dark until use. All the measurements were performed in a total volume of 2.0 mL water that contained 10 µL of DCFH solution, protoporphyrin (1 µM), ZnO (125 µM) and PP-ZnO (individual concentrations of PP and ZnO in the nanohybrid are 1 µM and 125 µM respectively).

3.2.15. Bacterial Strain and Culture Conditions: The viable count assay was performed with *E. coli* XL1-Blue cells. The cells were cultured at 37 °C in a liquid Luria-Bertani (LB) medium. When the optical density reached 0.6, the inoculum

was serially diluted ten thousand times with a Luria-Bertani (LB) medium and plated in LB agar plates containing protoporphyrin (0.2 µM), ZnO (25 µM) and PP-ZnO (individual concentration of PP and ZnO in the nanohybrid are 0.2 µM and 25 µM respectively). The amount of PP on ZnO surface was quantified from the absorption spectrum of PP-ZnO nanohybrids after the baseline correction. The PP concentration is calculated from the Q bands around 640 nm as ZnO has no absorbance above 380 nm. In order to study the effect of light, the plates were then incubated at 37 °C for three hrs and kept under green light (~500 Wm^{-2}) for one h. Finally, the colonies were counted after overnight incubation.

3.2.16. Fabrication of Dye-Sensitized Solar Cells: For the fabrication of DSSCs, platinum, Pt@RGO and RGO deposited on FTO substrates were used as counter electrodes. The platinum (Pt) was deposited on the FTO substrates by thermal decomposition of 5 mM platinum chloride (in isopropanol) at 385 °C for 30 min. The N719 coated TiO_2 and Ag-TiO_2 were used as the photo anodes and the two electrodes were placed on top of each other with a single layer of 60 µm thick Surlyn (Solaronix) as a spacer between the two electrodes. A liquid electrolyte composed of 0.5 M lithium iodide (LiI), 0.05 M iodine (I_2) and 0.5 M 4-tert-butylpyridine (TBP) in acetonitrile was used as the hole conductor and filled in the inter electrode space by using capillary force, through two small holes (diameter = 1 mm) predrilled on the counter electrode. Finally, the two holes were sealed by using another piece of Surlyn to prevent the leakage of electrolyte from the cell.

The N719 coated TiO_2 MS, doped TiO_2 MS and TiO_2 P25 were used as the active electrodes. The photoanodes were fabricated using the following procedure. Initially, TiO_2 was mixed in water and a small amount of acetyl acetonate was added. The mixer was stirred for 5 h. Then triton X-100 was added to the mixer and stirred for few minutes. Finally, the paste was coated on a conducting side of the ITO using the doctor-blade technique. The film was dried at room temperature, sintered at 450 °C for 1 h in a muffle furnace and then allowed to

cool naturally to room temperature. Then the plates were dipped into the ethanolic solution of N719 dye for 18 h at room temperature. The photoanodes were withdrawn from the solution and immediately rinsed with ethanol. The two electrodes were placed on top of each other with a single layer of 60 µm thick Surlyn (Solaronix) as a spacer between the two electrodes. I^-/I_3^- was used as an electrolyte. The liquid electrolyte as mentioned above was used as the hole conductor and filled in the inter electrode space by using capillary force, through two small holes predrilled on the counter electrode. In all our experiments, the active area of the DSSCs was fixed at 0.49 cm^2.

References

[1] D.V. O'Conner, D. Philips, Time Correlated Single Photon Counting, Academic Press, London, 1984.

[2] S.S. Sinha, P.K. Verma, A. Makhal, S.K. Pal, A Versatile Fiber-Optic Coupled System for Sensitive Optical Spectroscopy in Strong Ambient Light, *Rev. Sci. Instrum.* 80 (2009) 053109.

[3] S. Baruah, J. Dutta, pH-Dependent Growth of Zinc Oxide Nanorods, *J. Cryst. Growth* 311 (2009) 2549-2554.

[4] S. Baruah, J. Dutta, Effect of Seeded Substrates on Hydrothermally Grown ZnO Nanorods, *J. Sol-Gel Sci. Technol.* 50 (2009) 456-464.

[5] S. Sarkar, A. Makhal, K. Lakshman, T. Bora, J. Dutta, S.K. Pal, Dual-Sensitization Via Electron and Energy Harvesting in CdTe Quantum Dots Decorated ZnO Nanorod-Based Dye-Sensitized Solar Cells, *J. Phys. Chem. C* 116 (2012) 14248-14256.

[6] S. Ghosh, H. Remita, L. Ramos, A. Dazzi, A. Deniset-Besseau, P. Beaunier, F. Goubard, P.-H. Aubert, F. Brisset, S. Remita, PEDOT Nanostructures Synthesized in Hexagonal Mesophases, *New J. Chem.* 38 (2014) 1106-1115.

[7] E. Pena dos Santos, M.S. Tokumoto, G. Surendran, H. Remita, C. Bourgaux, P. Dieudonné, E. Prouzet, L. Ramos, Existence and Stability of New Nanoreactors: Highly Swollen Hexagonal Liquid Crystals, *Langmuir* 21 (2005) 4362-4369.

[8] A. Makhal, S. Sarkar, T. Bora, S. Baruah, J. Dutta, A.K. Raychaudhuri, S.K. Pal, Dynamics of Light Harvesting in ZnO Nanoparticles, *Nanotechnology* 21 (2010) 265703.

[9] S. Sardar, S. Chaudhuri, P. Kar, S. Sarkar, P. Lemmens, S.K. Pal, Direct Observation of Key Photoinduced Dynamics in a Potential Nano-Delivery Vehicle of Cancer Drugs, *Phys. Chem. Chem. Phys.* 17 (2015) 166-177.

[10] T. Bora, K.K. Lakshman, S. Sarkar, A. Makhal, S. Sardar, S.K. Pal, J. Dutta, Modulation of Defect-Mediated Energy Transfer from ZnO Nanoparticles for the Photocatalytic Degradation of Bilirubin, *Beilstein J. Nanotechnol.* 4 (2013) 714-725.

[11] E. Grabowska, A. Zaleska, S. Sorgues, M. Kunst, A. Etcheberry, C. Colbeau-Justin, H. Remita, Modification of Titanium(IV) Dioxide with Small Silver Nanoparticles: Application in Photocatalysis, *J. Phys. Chem. C* 117 (2013) 1955-1962.

[12] S. Ghosh, H. Remita, P. Kar, S. Choudhury, S. Sardar, P. Beaunier, P.S. Roy, S.K. Bhattacharya, S.K. Pal, Facile Synthesis of Pd Nanostructures in Hexagonal Mesophases as a Promising Electrocatalyst for Ethanol Oxidation, *J. Mater. Chem. A* 3 (2015) 9517-9527.

[13] F. Dehouche, P. Archirel, H. Remita, N. Brodie-Linder, A. Traverse, Alcohol to Water Catalyzed by Pt Nanoparticles: An Experimental and Computational Approach, *RSC Adv.* 2 (2012) 6686-6694.

[14] B. Liu, L.-M. Liu, X.-F. Lang, H.-Y. Wang, X.W. Lou, E.S. Aydil, Doping High-Surface-Area Mesoporous TiO_2 Microspheres with Carbonate for Visible Light Hydrogen Production, *Energy Environ. Sci.* 7 (2014) 2592-2597.

[15] Z.-Q. Li, Y.-P. Que, L.-E. Mo, W.-C. Chen, Y. Ding, Y.-M. Ma, L. Jiang, L.-H. Hu, S.-Y. Dai, One-Pot Synthesis of Mesoporous TiO_2 Micropheres and Its Application for High-Efficiency Dye-Sensitized Solar Cells, *ACS Appl. Mater. Interfaces* 7 (2015) 10928-10934.

[16] C.P. LeBel, H. Ischiropoulos, S.C. Bondy, Evaluation of the Probe 2',7'-Dichlorofluorescin as an Indicator of Reactive Oxygen Species Formation and Oxidative Stress, *Chem. Res. Toxicol.* 5 (1992) 227-231.

[17] R. Cathcart, E. Schwiers, B.N. Ames, Detection of Picomole Levels of Hydroperoxides Using a Fluorescent Dichlorofluorescein Assay, *Anal. Biochem.* 134 (1983) 111-116.

Chapter 4

Excited State Dynamics of a Light Harvesting Molecule in the Proximity of Wide Band Gap Semiconductor Nanostructures

4.1. Introduction: The conversion of solar energy to chemical energy during photosynthesis involves the transfer of electrons in porphyrin based chlorophyll chromophores embedded in the thylakoid membranes of chloroplast [1]. To clarify the complex mechanism of photosynthesis, the photochemistry of porphyrins and their metal complexes has long been an interesting subject of investigation [2-6]. Electron transfer-the most elementary chemical reaction, widely occurs in biological systems [7-9]. The complexity of electron transfer reactions in nature have led researchers to build up simplified model systems to understand the essential steps of enzyme mechanism in living organism [10-12]. A significant effort has also been devoted in recent times for the understanding of electron transfer mechanisms as a means of capturing and storing solar energy. The increasing demand for the complete photocatalytic mineralization of organic pollutants in water into harmless products through redox reactions necessitates the exploration of efficient catalysts able to mimic natural enzymatic systems.

Iron porphyrins under sunlight induce reversible redox processes of the metal centre, mimicking some significant biochemical sequences in the catalytic cycle of the cytochrome P-450 oxygenases [13-15]. To reveal the fundamental role of electron transfer processes in biological systems, photoredox reactions of iron porphyrins are very important. The metalloporphyrin excited states that show photochemistry are those involved in charge transfer transitions, either from the axial ligand to the metal centre or from the porphyrin itself to the metal. Due to

strong absorption of porphyrins in the region of 400-450 nm (Soret band or B) as well as 500-700 nm (Q bands), it finds applications in many fields such as photodynamic therapy for the treatment of cancer [16] and photovoltaic conversion of solar energy [17-23]. The reaction mechanism of porphyrin metallation in solution consists of the following steps: deformation of the porphyrin ring, outer sphere association of the solvated metal ion and the porphyrin, exchange of a solvent molecule with the first pyrrolenine nitrogen atom, chelate-ring closure with the expulsion of more solvent molecules followed by deprotonation of nitrogen atoms which leads to the formation of the metalloporphyrin [24]. The metallation reactions are generally slow process which can be attributed to the distortion of the porphyrin ring needed to form the first bonds to the metal [25-26].

Porphyrins anchored on nanocrystalline TiO_2 offer a number of advantages due to its isolation on a solid support: enhancement of its reactivity, inhibition of degradative intermolecular self reactions and mimicking the proteic environment of the hemeprotein. Colloidal TiO_2 suspensions have been reported extensively for environmental remediation under ultraviolet band light irradiation [27-29]. Bandgap excitations in TiO_2 occur only at wavelengths less than 380 nm, which prevents it from being a potential visible light harvester. Dye sensitization has been successfully applied to extend the spectral response of TiO_2 in the visible region. Organic dyes can serve as both a sensitizer and a substrate to be degraded [30-32]. Many dyes, however, do not sustain the oxidative stress generated on semiconductor surface [33]. For efficient photocatalysis, the dye has to be stable and regenerative. For example, Zhao et al. have reported the degradation of pollutant 4-chlorophenol by $Pt(dcbpy)Cl_2$ (dcbpy = 4,4′- dicarboxy-2,2′-bipyridine) incorporated titania under visible light [34]. Porphyrins and metalloporphyrins have been used for the visible light sensitization of TiO_2 and applied for the degradation of 4-nitrophenol, rhodamine B, acid chrome blue K, atrazine [35-40].

Though the photocatalysis using porphyrin and metalloporphyrin functionalized titania is well documented in the literature but the knowledge on the fundamental electron transfer dynamics are sparse. The key time scales for the photoinduced ultrafast electron transfer processes in iron porphyrin and its derivative have great importance due to their biological relevance and also the time scales are key factor for efficient solar energy conversion. Previously, Zewail & coworkers [41] have reported the femtosecond dynamics of Co(II) tetraphenylporphyrin (CoTPP) and ZnTPP where intramolecular electron transfer from porphyrin a_{2u} (π) to Co (d_{z2}) occurs as Co(II) (d^7) facilitates the existence of a low-lying charge transfer (CT) state but in case of Zn, there is no low-lying CT state as Zn has no unoccupied d orbitals. Oliveros et al. [39] have investigated the photodegradation of atrazine in aqueous solution and under visible light irradiation in the presence of tetra(4-carboxyphenyl)porphyrin (TcPP) with different metal centres (Fe(III), Cu(II), Zn(II) and metal free) adsorbed on TiO_2 surface. Photocatalytic activity was found only after the addition of hydrogen peroxide and complexes like TcPPFe and TcPPCu containing a central metal ion with unfilled d orbitals show higher photocatalytic activity. Wang et al. [42] have reported the efficient degradation of 4-nitrophenol by using 5,10,15,20-tetra-[4-(3-phenoxy)-propoxy]phenyl porphyrin and 5,10,15,20-tetra-[2-(3-phenoxy)-propoxy]-phenyl porphyrin with Cu(II) as central metal ion under visible irradiation. They have proposed that the excited electron at porphyrin LUMO goes to CB of TiO_2 and then it reduces Cu(II) to Cu(I) and Cu(I) can be reoxidized to Cu(II) by dioxygen species or by hydrogen peroxide produced in solution.

In the first work of this chapter, we have synthesized highly stable nanomaterials, hematoporphyrin-TiO_2 (HP-TiO_2) and Fe(III)-hematoporphyrin-TiO_2 (Fe(III)HP-TiO_2) nanohybrids. Steady-state and picosecond-resolved fluorescence measurements show the ultrafast charge transfer processes in HP-TiO_2 and Fe(III)HP-TiO_2 and we have explored the role of Fe(III) ions in

photoinduced electron transfer processes. The attachment of HP molecules to TiO_2 nanoparticles have been investigated by using FTIR, Raman scattering and XPS studies. The iron oxidation states and the attachment of iron to porphyrin through pyrrole nitrogen atoms have been investigated by cyclic voltametry and FTIR studies, respectively. The photocatalytic activity of these nanomaterials has been studied under wavelength dependent light irradiation. Photocurrent measurement shows the role of iron oxidation states in electron transfer processes.

The choice of photo-sensitizers in solar light-harvesting applications, including DSSC and visible light photocatalysis (VLP) is very important. In most cases, polypyridyl ruthenium complexes are likely choices for such applications [43-46]. While the complexes work reasonably well in visible light, the main drawback of such complexes is a lack of reasonable absorption in the near-IR region. Given that IR energy accounts for 49% of the solar spectrum, an extended red response of the sensitizers is necessary to improve the device efficiency [47]. Phthalocyanines (PCs) have been used in light-harvesting applications, including in polymer-based hybrid DSSC [48], to complement the optical absorption of the polymer in the red region of the solar spectrum. The chemical structures of the PCs are characterized by an aromatic monocyclic ligand carrying clouds of delocalized л-conjugated electrons and a central metallic atom with typically 2+ oxidation states playing the role of electron donor to the ligands. Zinc phthalocyanines (ZnPc) are a class of PCs whose main electronic features are explained in detail using DFT [49]. ZnPc is usually modified by the addition of anchoring groups for light-harvesting applications [50-55].

In another work in this chapter, a facile means to attach a biologically important ligand, tartrate, to the central metal of ZnPc using simple wet chemistry was employed. We have made nanohybrids of tartrate-functionalized ZnPc with ZnO of different morphologies (particles and nanorods) for light-harvesting applications or red light photocatalysis. Although titania (TiO_2) was reported to be

a more efficient charge separator from the excited sensitizer in light harvesting, recently DSSC based on ZnO have attained efficiency that is comparable to titania [48]. Moreover, ZnO has emerged more recently in the framework of light-harvesting devices as an alternative to titania because of its flexibility in materials synthesis and significant electron mobility [56]. While FTIR reveals attachment of the tartrate ligand through a carboxylate end to the ZnO NP, XRD confirms the intactness of the crystal structure of ZnO upon functionalization with tartrate. We have also studied the photocatalytic activity of the nanohybrid under red light illumination with a model water pollutant, methyl orange (MO), and found significant enhancement, which is found to be a manifestation of enhanced reactive oxygen species (ROS) formation from the nanohybrid in aqueous solution. To use the functional material (nanohybrid) in a flow device for the decontamination of polluted water, we have used ZnO nanorods (NR) functionalized with tartrate–ZnPc. The intrinsic emission of the ZnO NR and its spectral overlap with the absorbance of ZnPc reveals Förster resonance energy transfer (FRET) from the NR to the attached ZnPc, confirming the close proximity between ZnPc to the host ZnO NR. We have confirmed enhanced photocurrent under visible light and measured the wavelength-dependent photocurrent in the sensitized ZnO NR. A prototype of the flow device has also been made and tested for potential application in decontamination of the model water pollutant (MO).

4.2. Results and Discussion:

4.2.1. Role of Central Metal Ion in Hematoporphyrin-Functionalized Titania in Solar Energy Conversion Dynamics [57]:

A typical high-resolution transmission electron microscopic (HR-TEM) image of TiO_2 NPs showing the polycrystalline nature of the particles as in Figure 4.1a. Lattice fringe of a TiO_2 NP is illustrated which shows an interplanar distance of ~ 0.365 nm, corresponding to the spacing between two (101) planes of anatase

TiO_2 [58]. The particle sizes are estimated by fitting our experimental TEM data over 55 particles which provides the mean diameter of ~ 6 nm (Figure 4.1a, inset). In order to determine the complex formation between HP and semiconductor NPs, we have studied UV-Vis spectroscopy as shown in Figure 4.1b which shows visible light absorption between 400 to 700 nm in HP solution. A strong peak is observed at 397 nm for Soret band together with Q bands between 500-700 nm. The four weak Q bands have been assigned to the splitting of doubly degenerate states into the vibration components [59]. The HP-TiO_2 nanohybrid exhibits a 3 nm bathochromic shift of Soret band compared to absorption in HP. The bathochromic shift of the soret band is related with different physical and chemical changes in the porphyrin molecular structure when it is incorporated into solids or under specific conditions, in solution. Castillero et al. have proposed that the red shift with respect to the water solution can be attributed to a change in the environment of the monomeric porphyrin due to anchoring onto the TiO_2 surface [60]. Sarkar et al. have shown 12 nm bathochromic shift when HP attaches to ZnO NRs [21]. Thus the change in the absorption spectra indicates the formation of HP-TiO_2 complex.

As shown in Figure 4.1c, HP presents intense fluorescence emission from two pi orbitals, which encompass the basic tetrapyrrole structure upon excitation with 409 nm laser line. For HP-TiO_2 nanohybrid, there is a considerable decrease in the intensity of the emission peaks in the range of 600-710 nm as compared to bare HP. The decrease in emission intensities can be attributed to an efficient non-radiative photoinduced process from HP to the NPs. The inset of Figure 4.1c shows the quenching in the excitation spectra of HP upon binding to TiO_2 when monitored at the emission peak (625 nm). The decrease in emission and excitation intensities of HP is also seen in case of Fe(III)HP and Fe(III)HP-TiO_2 nanohybrid. In Fe(III)HP, intramolecular electron transfer occurs from excited HP to Fe(III) leading to the reduction of Fe(III) to Fe(II) [3].

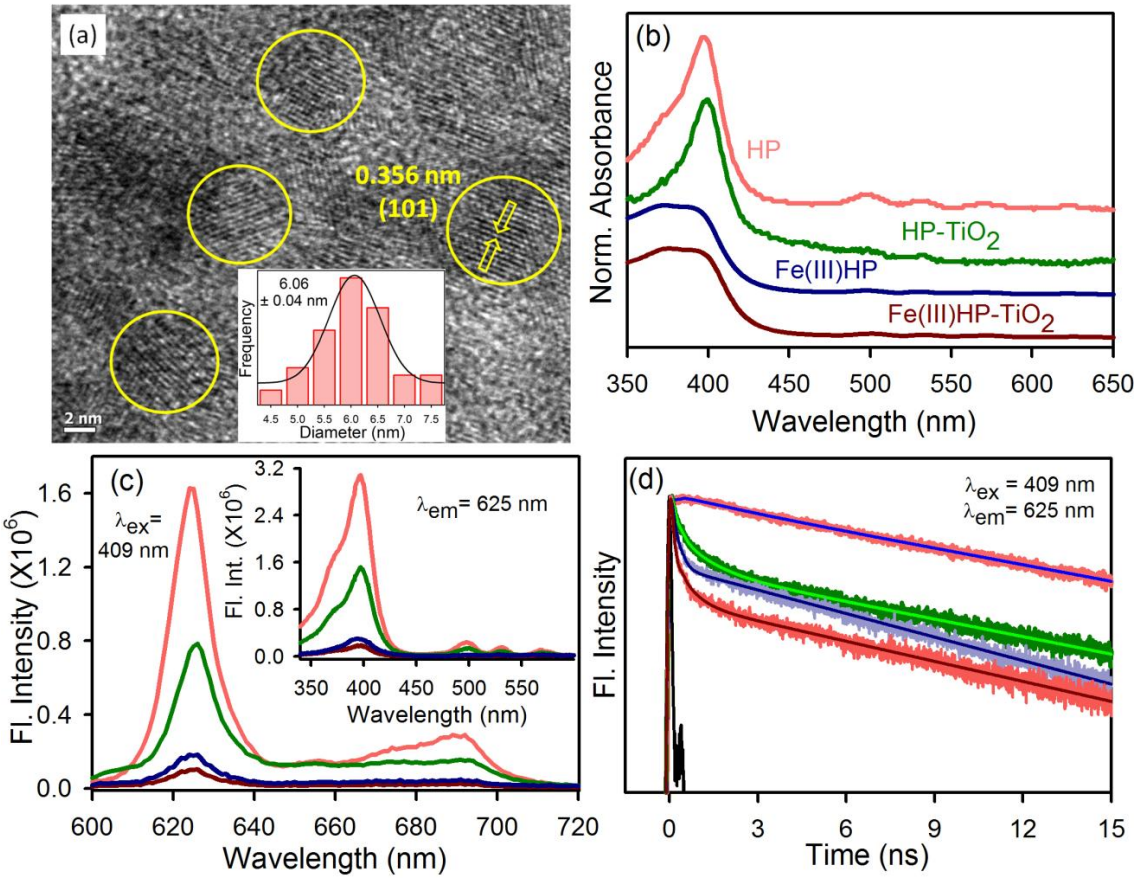

Figure 4.1. *(a) HRTEM image of TiO_2 NPs. Inset shows the size distribution of the TiO_2 NPs. (b) UV-Vis absorption of HP (red), HP-TiO_2 nanohybrids (dark green), Fe(III)HP (dark blue) and Fe(III)HP-TiO_2 nanohybrids (dark red) in ethanol. (c) Room temperature PL spectra (excitation wavelength was at 409 nm) of bare HP (red), HP-TiO_2 nanohybrids (dark green), Fe(III)HP (dark blue) and Fe(III)HP-TiO_2 nanohybrids (dark red) are shown. Inset shows the excitation spectra monitored at 625 nm. (d) Fluorescence decay profiles of HP (red), HP-TiO_2 nanohybrids (dark green), Fe(III)HP (dark blue) and Fe(III)HP-TiO_2 nanohybrids (dark red) in ethanol.*

Table 4.1. *Dynamics of picosecond-resolved luminescence transients of HP, Fe(III)HP, HP-TiO_2 and Fe(III)HP-TiO_2 nanohybrids*[a]

Sample	τ_1 (ns)	τ_2 (ns)	τ_3 (ns)	τ_{avg} (ns)	$k_{nr}\times10^8$ (sec^{-1})
HP (bare)	11.39±0.01 (100%)			11.39±0.01	
HP-TiO_2	0.40±0.003 (71%)	10.68±0.02 (29%)		3.38±0.01	2.08±0.010
Fe(III)HP	0.14±0.002 (78%)	8.43±0.02 (22%)		1.96±0.003	4.22±0.007
Fe(III)HP-TiO_2	0.09±0.002 (76.4%)	0.40±0.02 (12.5%)	9.74±0.03 (11.1%)	1.19±0.01	7.52±0.060

[a]*The emission (monitored at 625nm) was detected with 409 nm laser excitation. k_{nr} represents nonradiative rate constant. Numbers in the parenthesis indicate relative weightages.*

The fluorescence decay of free HP, Fe(III)HP, HP-TiO_2 and Fe(III)HP-TiO_2 in ethanol were obtained upon excitation of 409 nm laser and monitored at 625 nm (Figure 4.1d). The decay curve of free HP is fitted with single exponential decay with a lifetime of 11.39 ns (Table 4.1). In case of HP-TiO_2 nanohybrids, the decay curve of HP deviated from single exponential to bi-exponential showing a shorter lifetime 0.40 ns (71%) and longer lifetime 10.68 ns (29%) components. The observed decrease in lifetime could be correlated to the electron transfer process from HP molecules to TiO_2 NPs. The apparent non-radiative rate constant (k_{nr}) is determined by comparing the lifetimes of HP in the absence (τ_0) and in the presence (τ) of TiO_2, using the following equation:

$$k_{nr} = 1/\langle\tau\rangle - 1/\langle\tau_0\rangle \qquad (4.1)$$

The rate of electron transfer process from excited state of HP to the conduction band of semiconductor is estimated to be 2.08×10^8 s^{-1}. The k_{nr} value indicates that the electron transfer process is an ultrafast phenomenon, and it is quite similar to the values reported in the literature [61]. In case of Fe(III)HP, the decay curve of HP is composed of two components, one shorter 0.14 ns (78%) and one longer 8.43 ns (22%) lifetime components. The shorter life time could be correlated to the electron transfer process from HP to Fe(III) ions. In comparison, the decay curve for Fe(III)HP-TiO_2 has three components, two shorter and one longer component. The shortest component 0.09 ns (76.4%), which is comparable to the shorter component of the decay of Fe(III)HP, shows a preferable electron migration pathway from HP to Fe(III) and the second shorter component, 0.40 ns (12.5%), which is similar to that in the case of HP-TiO_2, could be correlated to the electron transfer process from HP to TiO_2 NPs. It is clear from the lifetime components that the photoinduced excited electrons in HP of Fe(III)HP-TiO_2 preferably transfer to the Fe(III) ions via nonradiative pathway as shown in Scheme 4.1 and the electron transfer rate is estimated to be 7.52×10^8 s^{-1}.

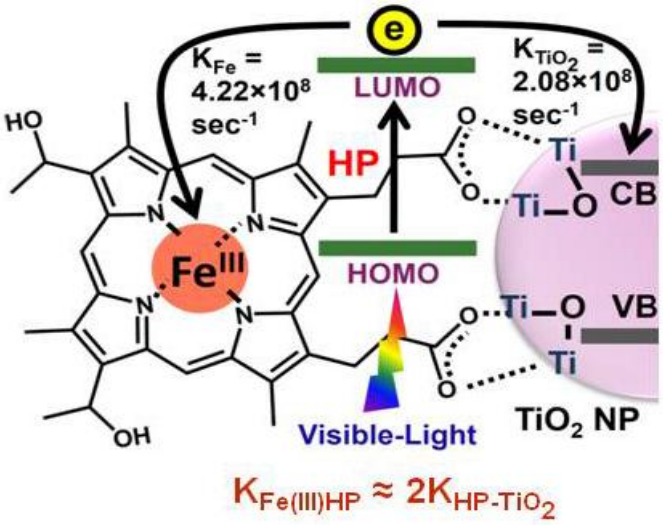

Scheme 4.1. *Schematic presentation of the electron transfer processes in the Fe(III)HP-TiO_2 nanohybrid upon photoexcitation.*

Fourier transform infra-red (FTIR) technique is used to investigate the binding mode of carboxylate group of HP on TiO_2 surface. For free HP, stretching frequencies of carboxylic group are at 1720 cm^{-1} and 1449 cm^{-1} for antisymmetric and symmetric stretching vibrations, respectively, as shown in Figure 4.2a. When HP is attached to TiO_2, the stretching frequencies of carboxylic group are located at 1656 and 1453 cm^{-1} for antisymmetric and symmetric stretching vibration, respectively. The difference between carboxylate stretching frequencies, $\Delta = \upsilon_{as} - \upsilon_{sym}$ is useful in identifying the bonding mode of carboxylate ligand [62]. The observed Δ value for the hybrid material is 203 cm^{-1} which is smaller than that for free HP (271 cm^{-1}). This suggests that the binding mode of HP on TiO_2 is predominantly bidentate. FTIR spectrum of Fe(III)HP-TiO_2 shows that in the presence of iron, HP binds to the TiO_2 NP through bidentate covalent bond. FTIR was also used to investigate the attachment of iron ion to HP molecule. For free HP, the stretching frequency of N-H bond is at 3435 cm^{-1}, as shown in Figure 4.2b. In case of HP-TiO_2 nanohybrid, the N-H stretching frequency of HP remains unperturbed as HP anchors onto the TiO_2 surface through carboxylic group. In the presence of iron, the N-H bond is perturbed and becomes broad which

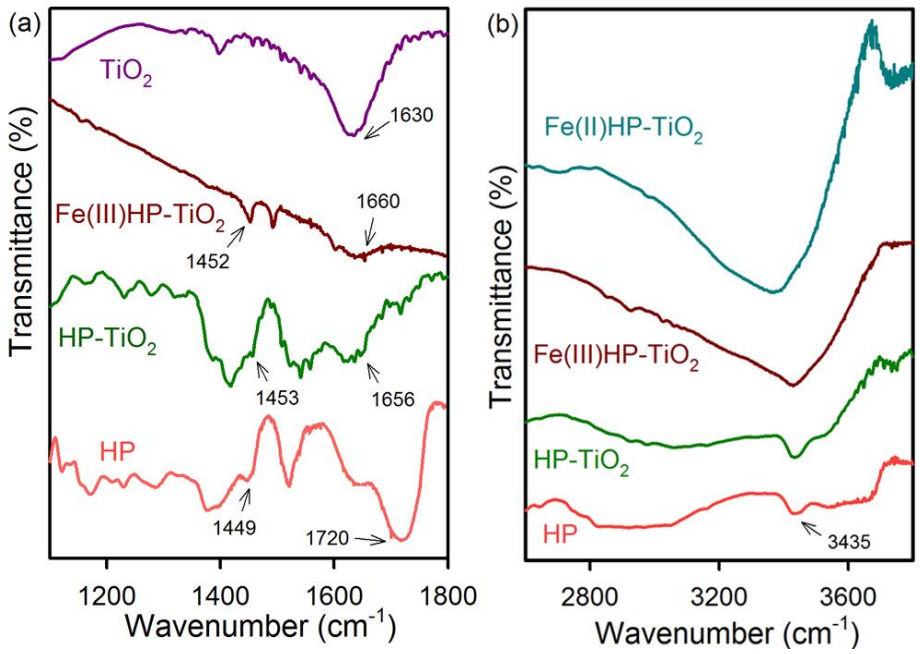

Figure 4.2. *(a) FTIR spectra of HP (red), TiO_2 NPs (dark pink), HP-TiO_2 (dark green) and Fe(III)HP-TiO_2 (dark red). The spectra of HP-TiO_2 and Fe(III)HP-TiO_2 nanohybrids are taken on TiO_2 background. (b) FTIR spectra of HP (red), HP-TiO_2 (dark green), Fe(III)HP-TiO_2 (dark red) and Fe(II)HP-TiO_2 (dark cyan).*

indicates that the Fe ion binds to the HP through the pyrrole nitrogen atoms of the porphyrin. After reduction of Fe(III) to Fe(II), FTIR spectra show that the N-H bond remain broad which indicates that Fe is still inside the porphyrin ring. The iron oxidation states are evaluated by cyclic voltametry experiments,

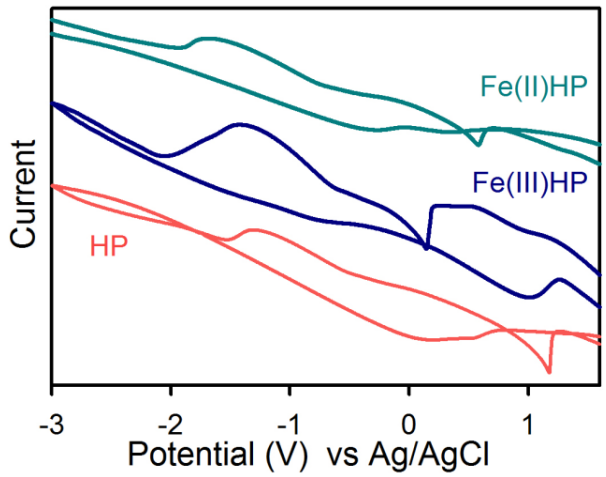

Figure 4.3. *Cyclic voltammograms of HP (red), Fe(III)HP (dark blue) and Fe(II)HP (dark cyan). The CVs were measured in aqueous solution at 0.1 V/s scan rate and Ag/AgCl as reference electrode.*

as shown in Figure 4.3. In the presence of Fe(III), a potential for Fe(III)/Fe(II) redox couple is observed at 0.99V vs Ag/AgCl reference electrode. After treating the Fe(III)HP by sodium borohydride, a reduction potential at - 0.35V was observed which can be attributed to the Fe(II)/Fe(0) redox couple. It is clear that the Fe(III) is reduced to Fe(II) after treating with sodium borohydride.

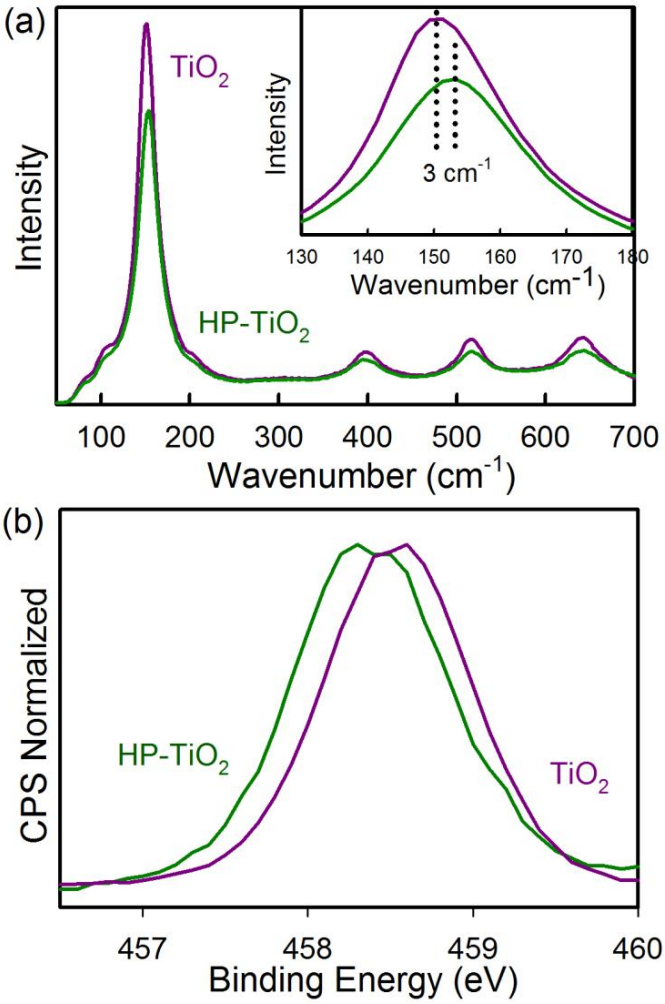

Figure 4.4. *(a) Raman spectra of TiO_2 NPs (dark pink) and HP-TiO_2 nanohybrids (dark green). Inset shows the peaks at 150 cm^{-1}. (b) XPS of the Ti (2p) regions of TiO_2 (dark pink) and HP-TiO_2 (dark green).*

According to factor group analysis, anatase TiO_2 has six Raman active modes (A_{1g} + $2B_{1g}$ + $3E_g$) [63]. As shown in Figure 4.4a, the Raman spectrum of anatase TiO_2 exhibits six peaks at 150 cm^{-1} (E_g), 198 cm^{-1} (E_g), 396 cm^{-1} (B_{1g}), 515 cm^{-1} (A_{1g}), 520 cm^{-1} (B_{1g}), 640 cm^{-1} (E_g). The Raman spectrum of HP does not show

any peak in the wavenumber range of 100-700 cm^{-1}. After binding of HP on TiO_2 surface, the characteristic bands of TiO_2 are all present but slightly blue shifted and broadened which is indicative of its good retention of the crystal structure and shape. In order to see the differences between the spectra more clearly, the wavenumbers and the full width at half maximum (FWHM) of the bands are given in Table 4.2. Figure 4.4a inset shows that the Raman band of TiO_2 at 150 cm^{-1} is shifted to 153 cm^{-1} after binding with HP. The blue shift and broadening of Raman bands of TiO_2 upon binding with HP can be attributed to the attachment of carboxylic group to Ti(IV) that are located at TiO_2 surface.

Table 4.2. *Raman bands and FWHM of TiO_2 and HP-TiO_2*

Sample	Raman band (cm^{-1})	FWHM (cm^{-1})
TiO_2	150	21
	396	33
	515	27
	640	38
HP-TiO_2	153	24
	397	36
	517	29
	642	42

The X-ray photoelectron spectra of the Ti (2p) regions for bare TiO_2 and HP sensitized TiO_2 are shown in Figure 4.4b. The Ti ($2p_{3/2}$) binding energy values of TiO_2 and HP-TiO_2 are 458.54 and 458.29 eV, respectively. The Ti ($2p_{3/2}$) peak for HP-TiO_2 is shifted to lower binding energy which suggests that Ti atom as the acceptor coordinates with oxygen atom in HP and that the oxygen atom provides electrons [37]. This suggests that HP molecules are adsorbed on the surface of TiO_2 with carboxyl as the coordinating group.

The irradiation of the HP and Fe(III)HP sensitized TiO_2 suspension with visible light ($\lambda > 395$ nm) led to the degradation of MB in aqueous solution as shown in Figure 4.5b. The sensitizer upon excitation with visible light injects electrons to the TiO_2 CB and the subsequent degradation of MB is initiated by

transferring CB electrons to MB. The CB electrons can be transferred to MB adsorbed on TiO_2 surface which lead to the reduction of MB to its leuco form. Thus proximity between MB and TiO_2 surface plays an important part in photodegradation. The CB electrons can also induce reactive oxygen species (ROS) formation. This sort of remote bleaching is well evidenced in the literature. For example Li et al. used porphyrin sensitized TiO_2 photocatalysts to degrade acid chrome blue K and the degradation mechanism was shown to follow ROS pathway [37].

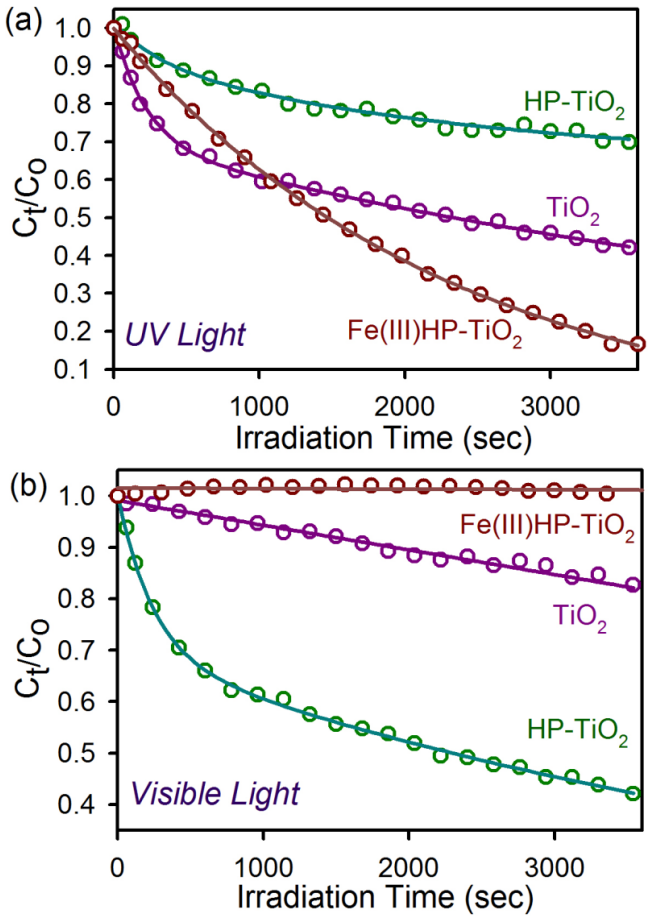

Figure 4.5. *Photocatalytic degradation of MB in the presence of TiO_2 NPs, HP-TiO_2 and Fe(III)HP-TiO_2 nanohybrids under (a) UV light and (b) visible light.*

The photocatalytic degradation of MB in the presence of HP-TiO_2 nanohybrids, Fe(III)HP-TiO_2 nanohybrids and TiO_2 under ultraviolet and visible light was investigated. Under ultraviolet irradiation, 58% MB is degraded in the

presence of TiO_2 whereas in the presence of HP-TiO_2 nanohybrids only 30% MB is degraded after 1 h irradiation of light, as shown in Figure 4.5a. Under UV irradiation, the TiO_2 valence band (VB) electrons are excited to the conduction band which can reduce dioxygen to superoxide, eventually leading to the production of hydroxyl radicals ($OH^{\bullet}$). The HP molecules that are attached to TiO_2 surface cannot simply withstand this severe oxidative stress and it is also degraded. HP acts as an electron scavenger and decreases the MB degradation rate. In the presence of Fe(III)HP-TiO_2 nanohybrids, 83% MB is degraded after 1 h of UV irradiation. The higher degradation rate can be attributed to the presence of Fe(III)HP which can improve the separation of photoinduced e^--h^+ pairs [38]. The Fe (III) ion plays an important role in the electron transfer process. Under UV light, TiO_2 VB electrons are excited to the CB and Fe (III) could be reduced to the Fe (II) by capturing the CB electrons of TiO_2. The reoxidation of Fe (II) to Fe (III) occurs by reducing oxygen to superoxide, eventually leading to the production of hydroxyl radicals ($OH^{\bullet}$). The following set of reactions explains the enhanced photocatalytic behavior in the presence of Fe (III).

$$\text{Fe(III)HP-TiO}_2 + h\upsilon \rightarrow \text{Fe(III)HP-TiO}_2\ (e^-_{cb}, h^+) \quad (4.2)$$

$$\text{Fe(III)HP-TiO}_2 + e^-_{cb} \rightarrow \text{Fe(II)HP-TiO}_2 \quad (4.3)$$

$$\text{Fe(II)HP-TiO}_2 + O_2 \rightarrow \text{Fe(III)HP-TiO}_2 + O_2^- \quad (4.4)$$

Under visible light irradiation, the HP-TiO_2 nanohybrid shows highly efficient photocatalytic activity. After 1 h irradiation it degrades 60% of MB, whereas under same condition bare TiO_2 degraded only 16% of MB. Visible light excites the HP molecules attached to TiO_2 and then the electrons from LUMO of the HP are injected to the CB of TiO_2. Since the rate of electron injection is much faster than the back electron transfer (from TiO_2 to HP) which leads to a null reaction, the electrons in the CB can be transferred to a substrate on TiO_2 surface. For example, Desilvestro et al reported that the rate of electron injection (k_{inj} = 3.2

× 10^7 s^{-1}) in the $Ru^{II}L_3/TiO_2$ system is 80 times faster than the back electron transfer (k_b = 4 × 10^5 s^{-1}) [64]. The regeneration of the sensitizer in the presence of suitable electron donors is a prerequisite for the development of practical photosensitization systems. Water in the media acts as an electron donor to regenerate the surface bound sensitizer molecules, which eliminate the need for any undesirable sacrificial electron donors. In the presence of Fe(III)HP-TiO_2, no MB degradation occurred after 1 h under visible light irradiation. In this case, the photoexcited electrons of HP are transferred to the Fe(III) ions instead of TiO_2, which is evident from the TCSPC studies as shown in Figure 4.1d. The back electron transfer from Fe(II) to HP takes only a few femtoseconds (~ 50 fs) [65]. Thus Fe(III)HP-TiO_2 shows no photocatalytic activity under visible light irradiation.

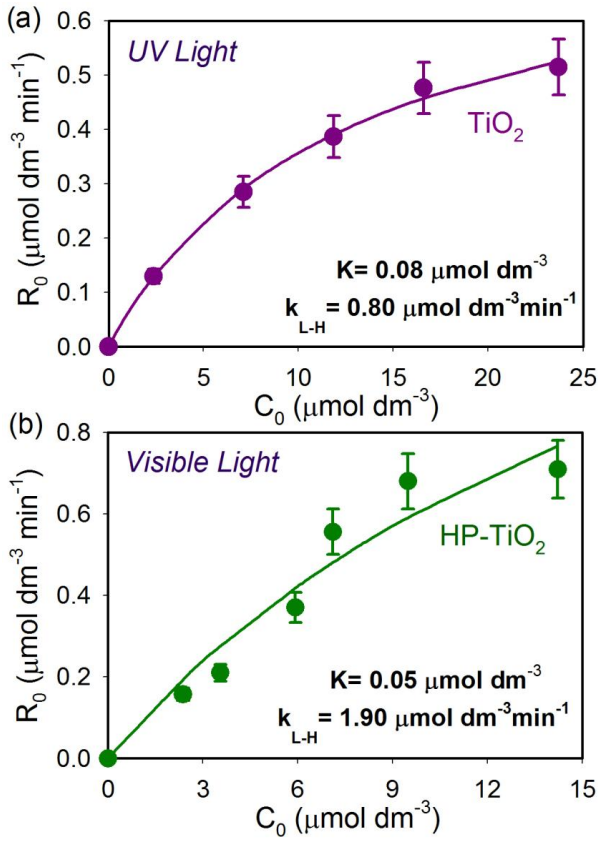

Figure 4.6. *Degradation rate (R_0) versus initial MB concentration (C_0) plots (with 10% error bar) (a) in the presence of TiO_2 NPs under UV light (b) in the presence of HP-TiO_2 nanohybrids under visible light.*

In Figure 4.6, MB degradation rate on the HP sensitized TiO_2 and bare TiO_2 surface under visible-light and UV-light, respectively, are investigated as a function of MB concentration. The R_0 versus C_0 curves are fitted using equation 2.18. The values of K and $k_{L\text{-}H}$ are given in Table 4.3. The Langmuir adsorption coefficient of MB molecules for bare TiO_2 (0.08 µmol dm^{-3}) is much higher than that for HP-TiO_2 nanohybrid (0.05 µmol dm^{-3}) which is obvious because in HP-TiO_2 nanohybrids, the TiO_2 surface sites are less available for MB attachment as HP is already attached to it. The Langmuir-Hinshelwood rate constant for HP-TiO_2 (1.90 µmol dm^{-3} min^{-1}) is higher compared to bare TiO_2 suspension (0.80 µmol dm^{-3} min^{-1}). This phenomenon can be attributed to the higher quantum yield of porphyrin sensitized TiO_2 than that of bare TiO_2 suspension [66-67].

Table 4.3. *Kinetic fitting parameters of Langmuir-Hinshelwood model*[b]

Sample	[MB] (µmol dm^{-3})	R_0 (µmol dm^{-3} min^{-1})	K (µmol dm^{-3})	$k_{L\text{-}H}$ (µmol dm^{-3} min^{-1})
Bare TiO_2	2.37	0.129	0.08	0.80
	7.11	0.285		
	11.85	0.387		
	16.59	0.476		
	23.70	0.515		
HP-TiO_2	2.37	0.157	0.05	1.90
	3.55	0.210		
	5.93	0.371		
	7.11	0.556		
	9.48	0.680		
	14.22	0.710		

[b]*R_0 is the degradation rate, $k_{L\text{-}H}$ is the Langmuir-Hinshelwood rate constant, and K is the Langmuir adsorption coefficient.*

The photocurrent measurement of HP-TiO_2 and (Fe)HP-TiO_2 nanohybrids were carried out in order to better understand the electron transfer processes in terms of short circuit current in a solar cell. Photocurrent measurements were done by using DSSC set up as shown in Figure 4.7a. The light source (10 mW cm^{-2}) was turned on and off every 20 sec and the obtained current values were continuously recorded. Figure 4.7b shows the photocurrent response of HP,

Fe(III)HP and Fe(II)HP sensitized TiO_2, where in the presence of Fe(III), photocurrent was found to decrease when compared to the electrodes sensitized with HP. This agrees well with our observations from the TCSPC and photocatalysis experiments. Photoexcited electrons from HP are transferred to Fe(III) instead of TiO_2 in case of Fe(III)HP sensitized TiO_2 which leads to a decrease in the photocurrent response. When Fe(III) is reduced to Fe(II), the photocurrent increases which indicates that the electrons from excited HP could be favorably transferred to TiO_2 CB.

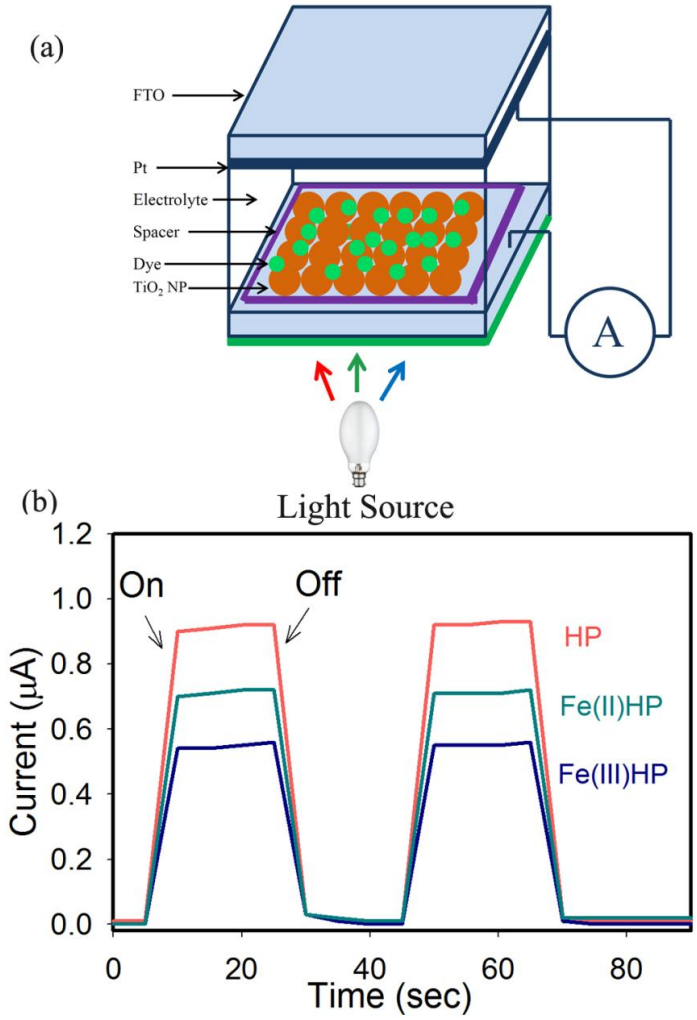

Figure 4.7. *(a) Schematic representation of photocurrent measurement set up using dye-sensitized solar cell geometry. (b) Photocurrent responses of HP (red), Fe(III)HP (dark blue) and Fe(II)HP (dark cyan) sensitized TiO_2 without any bias voltage under 10 mW cm^{-2} incident power irradiation from a light source.*

4.2.2. Ultrafast Dynamics at the Zinc Phthalocyanine/Zinc Oxide Nanohybrid Interface for Efficient Solar Light Harvesting in the near Red Region [68]:

The chemical structure of zinc phthalocyanine (ZnPc), tartrate ligand and a possible binding site for the formation of the nanohybrid are shown in Scheme 4.2.

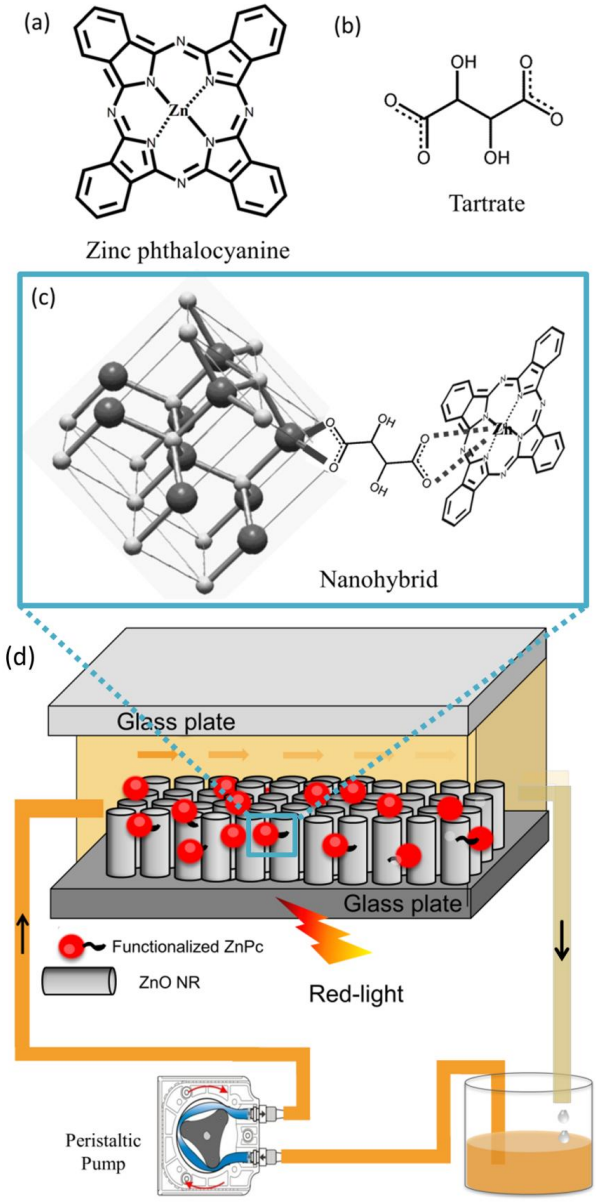

Scheme 4.2. *(a, b) Molecular structure of the sensitizer zinc phthalocyanine (ZnPc) and the ligand tartrate are shown. (c) The nanohybrid: possible molecular attachment of ZnPc with ZnO crystal through the tartrate ligand is indicated. (d) Schematic of the prototype flow device using the nanohybrid as the functional material is shown.*

A typical high-resolution transmission electron microscopic (HR-TEM) image of ZnO NPs is shown in Figure 4.8a. The lattice fringe of ZnO NP shows an interplanar distance of ~ 0.245 nm, corresponding to the spacing between two (002) planes [69]. The average particle size is estimated to be ~ 28 nm. Figure 4.8b shows the UV-Vis absorption spectra of ZnPc in DMSO and the nanohybrids. The absorption spectrum of the suspended ZnO NPs is also shown in Figure 4.8b as a reference. The intactness of the optical spectrum of ZnPc in the nanohybrid is confirmed from the studies.

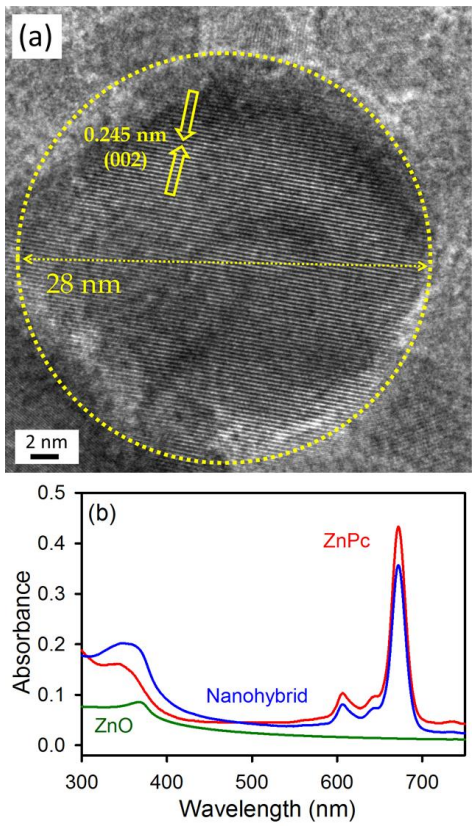

Figure 4.8. *(a) High-resolution transmission electron microscopy (HRTEM) of ZnO NP. Inter-fringe distance of 0.245 nm is consistent with (002) planes of the ZnO crystal. (b) UV-VIS absorption spectra of ZnPc in DMSO and the nanohybrid are shown. The absorption spectrum of the suspended NPs without sensitization is shown for comparison.*

In order to investigate the attachment of the tartrate ligand to the ZnPc, cyclic voltametry experiments were performed as shown in Figure 4.9a. Two observed redox processes are associated with ring based processes, $Zn(II)Pc^{2-}$

/Zn(II)Pc^{3-} and Zn(II)Pc^{3-}/Zn(II)Pc^{4-} as ZnPc complexes are not known to show redox activity at the central metal [70]. The redox potentials ($E_{1/2}$) of ZnPc are 0.62

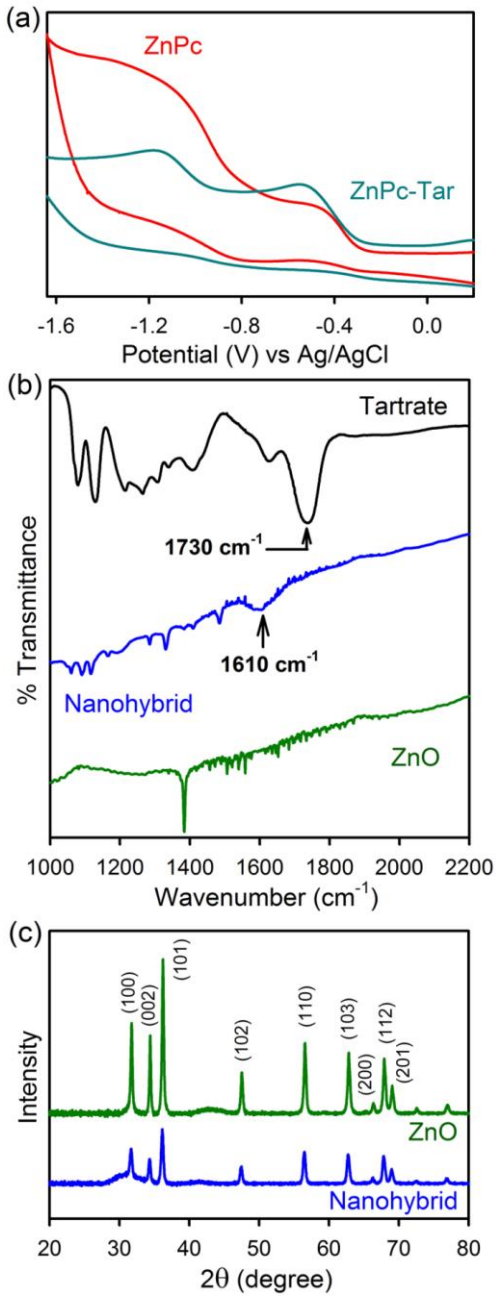

Figure 4.9. *(a) Cyclic voltammograms of ZnPc (red) and ZnPc attached to tartrate ligands (ZnPc-Tar, dark cyan). The CVs were measured in DMSO-aqueous KOH solution at 0.1 V s^{-1} scan rate and Ag/AgCl as reference electrode. (b) FTIR of the nanohybrid, ZnO NPs and tartrate are shown. A bidentate binding of the tartrate to the ZnO through the carboxylate end is evident (see text). (c) X-ray diffractograms of the nanohybrid and reference ZnO NPs are shown. Intactness of crystal structure of ZnO in the nanohybrid is evident (see text).*

V and 1.26 V vs Ag/AgCl in DMSO-1 (M) aqueous KOH solution for $Zn(II)Pc^{2-}$/$Zn(II)Pc^{3-}$, $Zn(II)Pc^{3-}$/$Zn(II)Pc^{4-}$ couples, respectively. Whereas the $E_{1/2}$ values of ZnPc attached to tartrate ligand (ZnPc-Tar) are shifted to 0.68 V and 1.30 V, respectively. The shift in the redox potentials can be attributed to the binding of tartrate ligand at the axial position of the ZnPc [71]. The Fourier transform infrared (FTIR) technique is used to investigate the binding mode of the carboxylate group of the tartrate on the ZnO NP surface because the attachment is very crucial for efficient binding of ZnPc and eventually for light-harvesting applications. For free tartrate, stretching frequencies of the carboxylic group are at 1730 cm^{-1} and 1412 cm^{-1} for antisymmetric and symmetric stretching vibrations, respectively, as shown in Figure 4.9b. When tartrate is attached to ZnO, the stretching frequencies of the carboxylic group are located at 1630 cm^{-1} and 1478 cm^{-1} for antisymmetric and symmetric stretching vibrations, respectively. The shifting of the stretching frequencies clearly indicates the formation of a covalent bond between the ligand tartrate and the host ZnO NPs [72]. The difference between the carboxylate stretching frequencies, $\Delta=\upsilon_{as} - \upsilon_{sym}$ is useful in identifying the bonding mode of the carboxylate ligand [62]. The observed Δ value for the hybrid material is 152 cm^{-1}, which is smaller than that of free tartrate (318 cm^{-1}). This observation reveals that the binding mode of tartrate on the ZnO surface is predominantly bidentate. The XRD study (Figure 4.9c) on the bare ZnO NPs (2θ range from 20^{o} to 70^{o}) and upon sensitization with tartrate-functionalized ZnPc shows characteristic planes of wurzite ZnO, (100), (002), (101), (102), (110), (103), (200), (112) and (201). The intactness of the crystal planes of ZnO upon sensitization with tartrate-ZnPc is also clear from the study. It has to be noted that (002) planes are more polar than (100) and (101) planes. Mclaren et al. [73] have shown that the terminal polar faces are more active surfaces for photocatalysis than the nonpolar surfaces perpendicular to them.

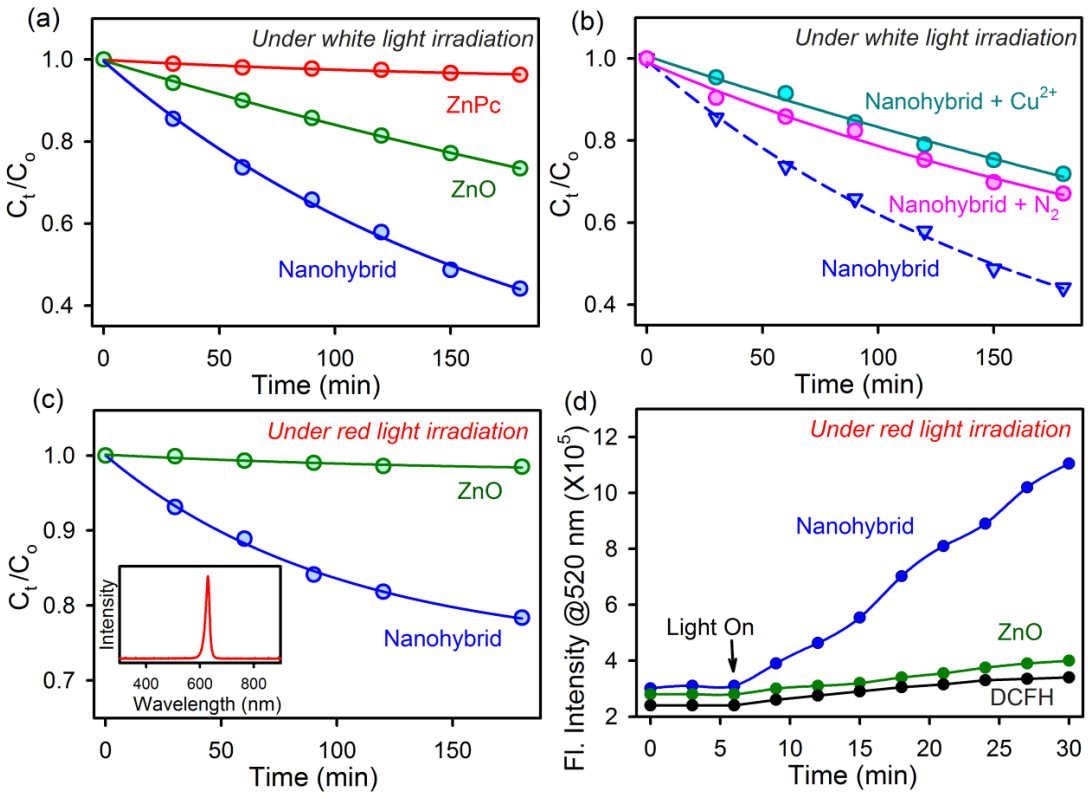

Figure 4.10. *(a) Methyl orange (MO) photodegradation in the presence of the nanohybrid and comparison with bare ZnO NP under white light illumination are shown. (b) Decrease in the rate of MO photodegradation in the presence of Cu^{2+} and after N_2 purging compared to that of the nanohybrid alone. (c) Photocatalytic activity of the nanohybrid under red light (optical irradiance spectrum is in the inset) illumination is shown. The reference for bare ZnO NPs does not show any activity under red light. (d) Red light-induced reactive oxygen species (ROS) generation in the nanohybrid and comparison with ZnO and control (DCFH) in aqueous solution are shown.*

Figure 4.10a shows the results of the investigation of photocatalytic efficiency of the nanohybrid under white light irradiation (λ›365 nm) in an aqueous environment. The test water under investigation contains methyl orange (MO), the model water contaminant. From the experimental data, a significant enhancement of the photocatalytic efficiency in the case of nanohybrids compared to that of the bare ZnO is clearly evident. During photocatalytic reactions, photoinduced electrons and holes escape recombination and migrate to the semiconductor surface which consequently generates (in the presence of oxygen and water) highly oxidative radicals, that can degrade the organic pollutants. In order to investigate the role of reactive oxygen species (ROS), the photocatalysis

experiments were performed after N_2 purging for 1 hr which drives out the dissolved oxygen. The decrease in the photocatalytic activity as shown in Figure 4.10b confirms that the mechanism is mainly through ROS [74]. The photocatalysis rate also decreases in the presence of Cu^{2+} which is a well-known scavenger of super oxides and photogenerated electrons [75-76]. The photocatalytic efficiency of the nanohybrid under red light illumination (620 nm) is also monitored, as shown in Figure 4.10c. The nanohybrid exhibits enhanced photocatalytic activity under red light as the sensitizer absorbs in the same region, whereas bare ZnO NPs show no activity under red light because of the lack of absorption in the visible or near infrared region. Comparison with the bare sensitizer ZnPc is difficult to make because the sensitizer is completely insoluble in water. The quantum yield (No of contaminant molecules reacted per incident photon) of the MO degradation reaction in the presence of nanohybrid under white and red light irradiation is found to be $7.0X10^{-6}$ and $4.6X10^{-6}$, respectively. The quantum yield values are consistent with the reported literature for MO degradation [77] by dye-sensitized TiO_2 nanoparticles under visible light irradiation through ROS pathway. Our observation is consistent with the enhanced photocatalytic activity of other nanohybrids reported in the literature [57, 78-79]. One of our earlier studies explored the higher efficiency of the photocatalytic activity of the protoporphyrin-IX-ZnO nanohybrid under green light irradiation through the formation of enhanced ROS in the medium [72]. The ROS generation in the present case is also monitored directly by the dichlorofluorescin-dichlorofluorecein (DCFH-DCF) conversion in an aqueous medium. DCFH is a well-known marker for ROS detection [80]. ROS oxidize non fluorescent DCFH to fluorescent DCF, and the emission intensity of the DCF was monitored with time as shown in Figure 4.10d. In the presence of nanohybrids, maximum enhancement in fluorescence intensity was observed under red light irradiation. In a control experiment, ZnO NPs show insignificant ROS generation under red light illumination because the NPs lack photon absorption in the red region of the

optical spectrum. It has to be noted that we cannot compare the efficacy of ROS generation of bare ZnPc as the sensitizer itself is insoluble in water. Time-dependent DCF emission in the absence of the ZnO/nanohybrid is also shown as a control experiment.

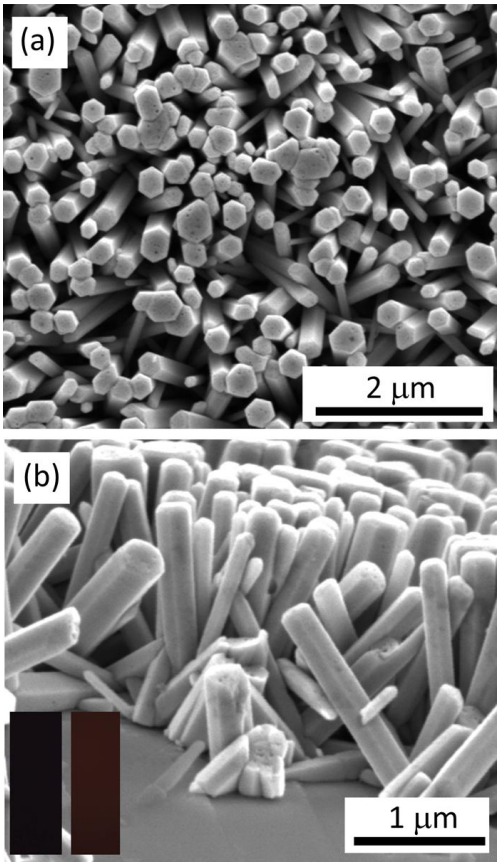

Figure 4.11. *(a, b) FEG-SEM of the ZnO nanorods (ZnO NR) on a glass plate for the prototype flow device is shown. Fluorescent micrographs of the plate before and after ZnPc sensitization are also shown in the inset of (b).*

To explore the application potentiality of the nanohybrids, we have sensitized ZnO nanorods (ZnO NR) with ZnPc through the tartrate ligand and formed a flow device as shown in Scheme 4.2c. The SEM images of ZnO NRs used in the flow device are shown in Figure 4.11a, top view and Figure 4.11b, side view. The ZnO NRs are found to be 2–3 μm in length and have diameters of 80–100 nm. The synthesized NR surfaces without sensitization were found to be emitting at 590 nm due to the intrinsic oxygen vacancy in the material [81].

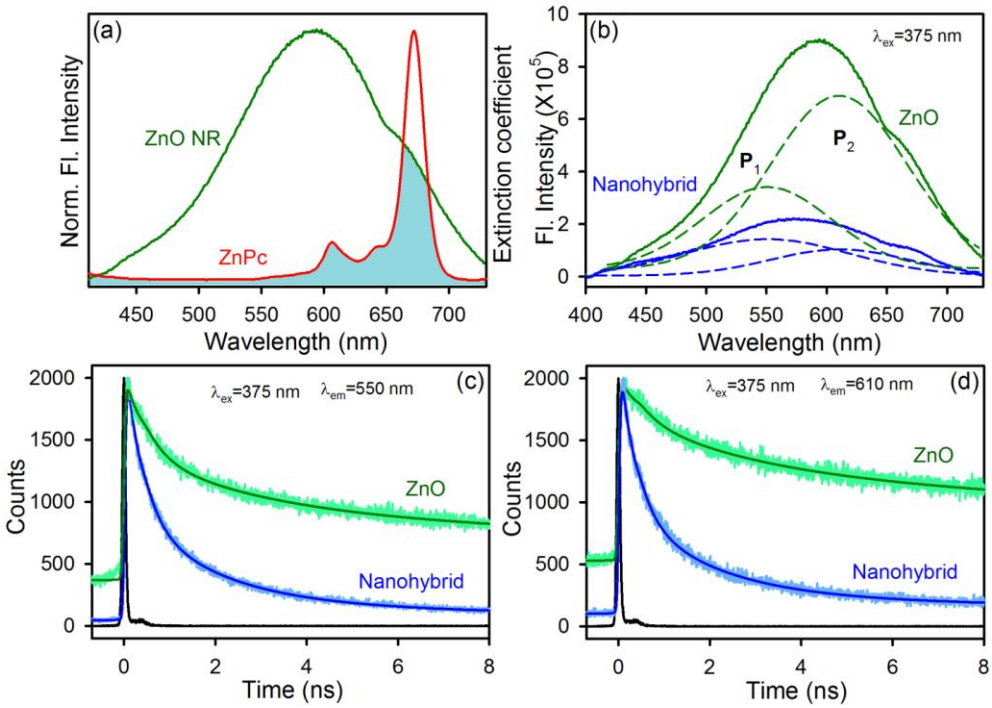

Figure 4.12. *(a) Spectral overlap of the emission of ZnO NR and the absorption spectrum of ZnPc is shown. (b) Emission from ZnO NRs. Deconvolution of the emission into two peaks (P_1 and P_2) is also shown. Relatively higher quenching of P_2 in the nanohybrid compared to bare ZnO NR is evident. (c, d) picosecond resolved emission transients of ZnO NR and nanohybrid detected at 550 nm (P_1 position) and 610 nm (P_2 position), respectively. Higher quenching efficiency for P_2 is consistent with steady-state spectra shown in (a).*

We have exploited FRET from the NR surface to the attached ZnPc due to their significant spectral overlap as shown in Figure 4.12a. A significant quenching of the NR emission is shown in Figure 4.12b. The broad NR emission is composed of two bands. One arises from the doubly charged vacancy center (V_o^{++}) located at 610 nm (P_2), and the other arises from the singly charged vacancy center (V_o^{+}) located at 550 nm (P_1) [82-83]. The emission intensity of ZnO NRs in the nanohybrid decreases considerably compared to that of free ZnO NRs, which can be attributed to the efficient non-radiative photo-induced processes from ZnO NRs to the ZnPc. Herein, we propose Förster Resonance Energy Transfer (FRET) from the donor ZnO NRs to the acceptor ZnPc. The assessment of molecular distances in numerous assemblies from FRET calculations has become a very useful tool [84-87]. The fluorescence decay profile of the donor ZnO NRs in the presence and absence of the acceptor ZnPc were obtained upon excitation with a

375 nm laser and monitored at 550 nm (P_1) and 610 nm (P_2) (Figure 4.12c and 4.12d, respectively). The excited-state lifetime of the ZnO NRs quenches in the nanohybrid compared to that of bare ZnO NRs. The details of the spectroscopic parameters and the fitting parameters of the fluorescence decays are tabulated in Table 4.4. From FRET calculations, the distance between the donor ZnO NRs and acceptor ZnPc is determined to be 3.3 nm and 3.1 nm for the P_1 and P_2 states, respectively. The energy transfer efficiency is calculated to be 86.2% and 89.3% from the P_1 and P_2 states, respectively. This observation is consistent with the fact that P_2 (V_o^{++}) states are closer to the surface of the ZnO NR [88]. The FRET distances confirm the proximity of the ZnPc to the ZnO NRs with molecular resolution.

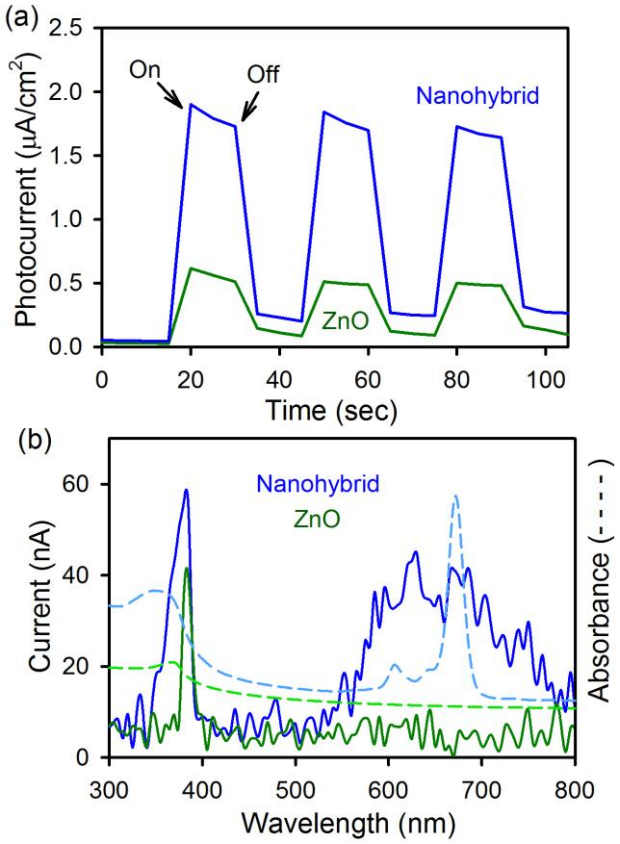

Figure 4.13. *(a) White light response of the nanohybrid and reference ZnO NR. A significant enhancement is observed for the nanohybrid. (b) Wavelength-dependent photocurrent spectra of the nanohybrid and bare ZnO NR (solid lines). The absorption spectra of the corresponding samples are also shown by dotted lines.*

The photoconductivity measurement [72] of the nanohybrid film was carried out to better understand the contribution of photo-induced charge separation to the net photocurrent in the device (Scheme 4.2c). Figure 4.13a shows the photocurrent response for the sensitized ZnO NR thin film under white light illumination. An improved photocurrent was observed for the nanohybrid thin film (~1.8 μA) under illuminated conditions compared to the ZnO NR thin film (~0.6 μA). The contribution of the ZnPc sensitizer to the charge separation for better light harvesting in the near red region is evident from Figure 4.13b. The wavelength-dependent photocurrents in the device format for the sensitized ZnO NR and the bare ZnO NR are consistent with the absorption spectra of the corresponding materials. In the case of the sensitized ZnO NRs, the additional peak at 650 nm in the photocurrent spectrum compared to that of the bare ZnO NR (peak at 370 nm) is in accordance with that of the 650 nm in the absorption spectrum of the nanohybrid. To investigate a molecular basis for the enhanced photocurrent in the red region of the excitation spectrum, which is close to the absorption of the sensitizer ZnPc, we have performed picosecond resolution studies. Figure 4.14a shows the steady-state emission spectra of the nanohybrid and free ZnPc in a DMSO solution. The concentration of ZnPc was maintained at the same level for both cases. A significant quenching of ZnPc emission upon red light excitation (633 nm) in the former case compared to the latter one is clearly evident from Figure 4.14a, revealing excited-state electron transfer from the LUMO of ZnPc to the host ZnO NR in the nanohybrid. Direct evidence of excited-state electron transfer is revealed from picosecond resolution fluorescence transients (excitation 633 nm, Figure 4.14b). One additional faster component of 30 ps (93%) in the nanohybrid emission, compared to the single exponential fluorescence decay of ZnPc in DMSO, clearly indicates an ultrafast photo-induced electron transfer from photoexcited ZnPc to the conduction band of the ZnO NR [89-90].

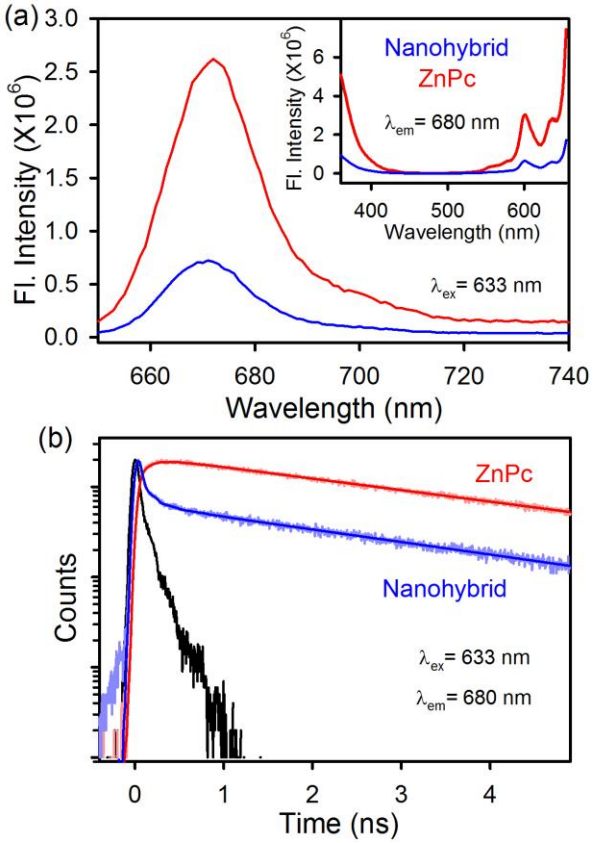

Figure 4.14. *(a) Steady-state emission spectra of ZnPc in DMSO and in the nanohybrids with the same concentration are shown. Fluorescence quenching of ZnPc in the nanohybrid upon 633 nm excitation is notable. Excitation spectra at a detection wavelength of 680 nm are also shown in the inset. (b) Picosecond-resolved fluorescence quenching of ZnPc in nanohybrid on glass plate compared to ZnPc in DMSO under red laser excitation (633 nm) and detected at 680 nm. Instrument response function is also shown as a reference (see text for details).*

To explore the potential application of the functional materials that have been developed here, we have made a prototype of a flow device as shown in Scheme 4.2c. The photocatalytic activity in the device under white light illumination (λ›365 nm) is shown in Figure 4.15a. A significant enhancement in the catalytic activity compared to that in bare ZnO NR is consistent with enhanced generation of photo-induced ROS in the device, as is evident from Figure 4.15b. If the nanorods are dipped in a solution of ZnPc without tartrate ligand then during washing the dyes which stick to the nanorods are washed out. The photocatalytic activity of the device without using tartrate ligand is found to be similar as ZnO NRs only.

Table 4.4. *Dynamics of picosecond-resolved luminescence transients of ZnPc and the nanohybrid*[c]

Sample	Excitation wavelength (nm)	Detection wavelength (nm)	τ_1 (ns)	τ_2 (ns)	τ_3 (ns)	τ_{avg} (ns)
ZnO NR	375	550	0.40 (42.5%)	2.70 (27.6%)	31.70 (29.9%)	10.40
Nanohybrid	375	550	0.30 (61.3%)	1.75 (32.3%)	10.60 (6.4%)	1.40
ZnO NR	375	610	0.40 (28.6%)	2.75 (30.9%)	31.70 (40.5%)	13.80
Nanohybrid	375	610	0.30 (62.7%)	1.80 (32.2%)	14.00 (5.1%)	1.50
ZnPc	633	680	3.40 (100%)			3.40
Nanohybrid	633	680	0.05 (93%)	3.10 (7%)		0.25

[c]*Numbers in parentheses indicate relative weights.*

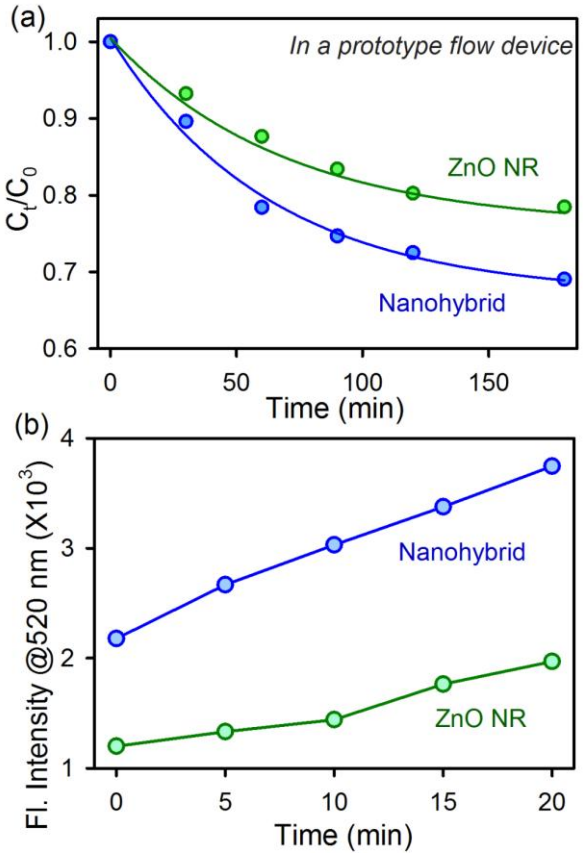

Figure 4.15. *Prototype performance: (a) photodegradation of MO under visible light illumination. (b) Enhanced generation of ROS in the presence of nanohybrid compared to bare ZnO NR is shown.*

4.3. Conclusion: In summary, we have investigated the efficacy of electron transfer processes in hematoporphyrin (HP) and iron hematoporphyrin ((Fe)HP) sensitized titania as a means of harvesting solar energy. The efficient quenching of HP fluorescence in the presence of Fe(III) ions and TiO_2 NPs suggest that photoinduced electron transfer takes place from LUMO of HP to the Fe(III) and CB of TiO_2 in Fe(III)HP-TiO_2 and HP-TiO_2 nanohybrids, respectively. Under UV light irradiation, Fe(III)HP-TiO_2 nanohybrid shows higher photocatalytic activity due to the cooperative functions of Fe(III)HP and TiO_2 in generating active species. HP-TiO_2 nanohybrids show higher photocatalytic activity under visible light due to the absence of Fe(III) ions which obstructs the electron transfer from HP to TiO_2. The bidentate covalent binding between TiO_2 and carboxylic groups of HP has been confirmed by the FTIR, Raman scattering and XPS studies. The iron oxidation states and the attachment of iron to porphyrin have been investigated by cyclic voltametry and FTIR studies, respectively. Photocurrent measurements show the role of iron oxidation states in electron transfer processes.

Additionally, we have sensitized ZnO NPs with ZnPc through a tartrate ligand for the light- harvesting application in the red region of the solar spectrum. A variety of spectroscopic and microscopic techniques have been employed to confirm the formation of a nanohybrid of ZnO with the organic ZnPc. We have used the nanohybrid for a potential application of red light-induced photocatalysis of a model water contaminant, namely MO. In a prototype, we have demonstrated that sensitized ZnO NRs in a flow device under red light illumination work reasonably well for decontamination of the model water pollutant MO. It was confirmed that the generation of enhanced ROS as a result of ultrafast photo-induced charge separation in the sensitized nanohybrid is the reason for the intrinsic catalytic activity of the flow device under red light. This work would find relevance in harvesting in the underutilized red region of the solar spectrum.

References

[1] K. Sauer, A Role for Manganese in Oxygen Evolution in Photosynthesis, *Acc. Chem. Res.* 13 (1980) 249-256.

[2] K.S. Suslick, R.A. Watson, The Photochemistry of Chromium, Manganese and Iron Porphyrin Complexes, *New J. Chem.* 16 (1992) 633-642

[3] A. Maldotti, R. Amadelli, C. Bartocci, V. Carassiti, E. Polo, G. Varani, Photochemistry of Iron-Porphyrin Complexes. Biomimetics and Catalysis, *Coord. Chem. Rev.* 125 (1993) 143-154.

[4] W.D. Edwards, B. Weiner, M.C. Zerner, Electronic Structure and Spectra of Various Spin States of (Porphinato)Iron(III) Chloride, *J. Phys. Chem.* 92 (1988) 6188-6197.

[5] Y. Ozaki, K. Iriyama, H. Ogoshi, T. Kitagawa, Ligand-Aided Photoreduction of Iron-Porphyrin Complexes Probed by Resonance Raman Spectroscopy, *J. Am. Chem. Soc.* 109 (1987) 5583-5586.

[6] C. Bartocci, F. Scandola, A. Ferri, V. Carassiti, Photoreduction of Hemin in Alcohol-Containing Mixed Solvents, *J. Am. Chem. Soc.* 102 (1980) 7067-7072.

[7] J.L. Dempsey, J.R. Winkler, H.B. Gray, Proton-Coupled Electron Flow in Protein Redox Machines, *Chem. Rev.* 110 (2010) 7024-7039.

[8] R.H. Holm, P. Kennepohl, E.I. Solomon, Structural and Functional Aspects of Metal Sites in Biology, *Chem. Rev.* 96 (1996) 2239-2314.

[9] P. de Rege, S. Williams, M. Therien, Direct Evaluation of Electronic Coupling Mediated by Hydrogen Bonds: Implications for Biological Electron Transfer, *Science* 269 (1995) 1409-1413.

[10] J.-M. Lehn, Supramolecular Chemistry—Scope and Perspectives Molecules, Supermolecules, and Molecular Devices (Nobel Lecture), *Angew. Chem. Int. Ed.* 27 (1988) 89-112.

[11] L. Que, W.B. Tolman, Biologically Inspired Oxidation Catalysis, *Nature* 455 (2008) 333-340.

[12] D. Astruc, Electron-Transfer Processes in Dendrimers and their Implication in Biology, Catalysis, Sensing and Nanotechnology, *Nat. Chem.* 4 (2012) 255-267.

[13] A. Maldotti, L. Andreotti, A. Molinari, V. Carassiti, Photochemically Driven Models of Oxygenases Based on the Use of Iron Porphyrins, *J. Biol. Inorg. Chem.* 4 (1999) 154-161.

[14] D. Ricard, M. L'Her, P. Richard, B. Boitrel, Iron Porphyrins as Models of Cytochrome C Oxidase, *Chem. Eur. J.* 7 (2001) 3291-3297.

[15] N. Hessenauer-Ilicheva, A. Franke, D. Meyer, W.-D. Woggon, R. van Eldik, Mechanistic Insight into Formation of Oxo-Iron(IV) Porphyrin Π-Cation Radicals from Enzyme Mimics of Cytochrome P450 in Organic Solvents, *Chem. Eur. J.* 15 (2009) 2941-2959.

[16] E.A. Lissi, M.V. Encinas, E. Lemp, M.A. Rubio, Singlet Oxygen O_2(1.Delta.g) Bimolecular Processes. Solvent and Compartmentalization Effects, *Chem. Rev.* 93 (1993) 699-723.

[17] A. Yella, H.-W. Lee, H.N. Tsao, C. Yi, A.K. Chandiran, M.K. Nazeeruddin, E.W.-G. Diau, C.-Y. Yeh, S.M. Zakeeruddin, M. Grätzel, Porphyrin-Sensitized Solar Cells with Cobalt (II/III)–Based Redox Electrolyte Exceed 12 Percent Efficiency, *Science* 334 (2011) 629-634.

[18] L.-L. Li, E.W.-G. Diau, Porphyrin-Sensitized Solar Cells, *Chem. Soc. Rev.* 42 (2013) 291-304.

[19] M.J. Griffith, K. Sunahara, P. Wagner, K. Wagner, G.G. Wallace, D.L. Officer, A. Furube, R. Katoh, S. Mori, A.J. Mozer, Porphyrins for Dye-Sensitised Solar Cells: New Insights into Efficiency-Determining Electron Transfer Steps, *Chem. Commun.* 48 (2012) 4145-4162.

[20] T. Bessho, S.M. Zakeeruddin, C.-Y. Yeh, E.W.-G. Diau, M. Grätzel, Highly Efficient Mesoscopic Dye-Sensitized Solar Cells Based on Donor–Acceptor-Substituted Porphyrins, *Angew. Chem.* 122 (2010) 6796-6799.

[21] S. Sarkar, A. Makhal, T. Bora, K. Lakhsman, A. Singha, J. Dutta, S.K. Pal, Hematoporphyrin–ZnO Nanohybrids: Twin Applications in Efficient Visible-Light

Photocatalysis and Dye-Sensitized Solar Cells, *ACS Appl. Mater. Interfaces* 4 (2012) 7027-7035.

[22] N. Masi Reddy, T.-Y. Pan, Y. Christu Rajan, B.-C. Guo, C.-M. Lan, E. Wei-Guang Diau, C.-Y. Yeh, Porphyrin Sensitizers with Π-Extended Pull Units for Dye-Sensitized Solar Cells, *Phys. Chem. Chem. Phys.* 15 (2013) 8409-8415.

[23] T. Hasobe, Supramolecular Nanoarchitectures for Light Energy Conversion, *Phys. Chem. Chem. Phys.* 12 (2010) 44-57.

[24] Y. Shen, U. Ryde, Reaction Mechanism of Porphyrin Metallation Studied by Theoretical Methods, *Chem. Eur. J.* 11 (2005) 1549-1564.

[25] M. Inamo, N. Kamiya, Y. Inada, M. Nomura, S. Funahashi, Structural Characterization and Formation Kinetics of Sitting-Atop (SAT) Complexes of Some Porphyrins with Copper(II) Ion in Aqueous Acetonitrile Relevant to Porphyrin Metalation Mechanism. Structures of Aquacopper(II) and Cu(II)−SAT Complexes as Determined by XAFS Spectroscopy, *Inorg. Chem.* 40 (2001) 5636-5644.

[26] S. Funahashi, Y. Inada, M. Inamo, Dynamic Study of Metal-Ion Incorporation into Porphyrins Based on the Dynamic Characterization of Metal Ions and on Sitting-Atop Complex Formation, *Anal. Sci.* 17 (2001) 917-927.

[27] O. Legrini, E. Oliveros, A.M. Braun, Photochemical Processes for Water Treatment, *Chem. Rev.* 93 (1993) 671-698.

[28] M.A. Fox, M.T. Dulay, Heterogeneous Photocatalysis, *Chem. Rev.* 93 (1993) 341-357.

[29] M.R. Hoffmann, S.T. Martin, W. Choi, D.W. Bahnemann, Environmental Applications of Semiconductor Photocatalysis, *Chem. Rev.* 95 (1995) 69-96.

[30] A. Mills, A. Belghazi, R.H. Davies, D. Worsley, S. Morris, A Kinetic Study of the Bleaching of Rhodamine 6G Photosensitized by Titanium Dioxide, *J. Photochem. Photobiol. A* 79 (1994) 131-139.

[31] C. Anderson, A.J. Bard, An Improved Photocatalyst of TiO_2/SiO_2 Prepared by a Sol-Gel Synthesis, *J. Phys. Chem.* 99 (1995) 9882-9885.

[32] K. Vinodgopal, D.E. Wynkoop, P.V. Kamat, Environmental Photochemistry on Semiconductor Surfaces: Photosensitized Degradation of a Textile Azo Dye, Acid Orange 7, on TiO_2 Particles Using Visible Light, *Environ. Sci. Technol.* 30 (1996) 1660-1666.

[33] H. Ross, J. Bendig, S. Hecht, Sensitized Photocatalytical Oxidation of Terbutylazine, *Sol. Energy Mater. Sol. Cells* 33 (1994) 475-481.

[34] W. Zhao, Y. Sun, F.N. Castellano, Visible-Light Induced Water Detoxification Catalyzed by Pt(II) Dye Sensitized Titania, *J. Am. Chem. Soc.* 130 (2008) 12566-12567.

[35] S. Rodrigues, K.T. Ranjit, S. Uma, I.N. Martyanov, K.J. Klabunde, Single-Step Synthesis of a Highly Active Visible-Light Photocatalyst for Oxidation of a Common Indoor Air Pollutant: Acetaldehyde, *Adv. Mater.* 17 (2005) 2467-2471.

[36] A.A. Ismail, D.W. Bahnemann, Metal-Free Porphyrin-Sensitized Mesoporous Titania Films for Visible-Light Indoor Air Oxidation, *ChemSusChem* 3 (2010) 1057-1062.

[37] D. Li, W. Dong, S. Sun, Z. Shi, S. Feng, Photocatalytic Degradation of Acid Chrome Blue K with Porphyrin-Sensitized TiO_2 under Visible Light, *J. Phys. Chem. C* 112 (2008) 14878-14882.

[38] H. Huang, X. Gu, J. Zhou, K. Ji, H. Liu, Y. Feng, Photocatalytic Degradation of Rhodamine B on TiO_2 Nanoparticles Modified with Porphyrin and Iron-Porphyrin, *Catal. Commun.* 11 (2009) 58-61.

[39] G. Granados-Oliveros, E.A. Páez-Mozo, F.M. Ortega, C. Ferronato, J.-M. Chovelon, Degradation of Atrazine Using Metalloporphyrins Supported on TiO_2 under Visible Light Irradiation, *Appl. Catal., B* 89 (2009) 448-454.

[40] M.-y. Duan, J. Li, G. Mele, C. Wang, X.-f. Lü, G. Vasapollo, F.-x. Zhang, Photocatalytic Activity of Novel Tin Porphyrin/TiO_2 Based Composites, *J. Phys. Chem. C* 114 (2010) 7857-7862.

[41] H.Z. Yu, J.S. Baskin, B. Steiger, C.Z. Wan, F.C. Anson, A.H. Zewail, Femtosecond Dynamics of Metalloporphyrins: Electron Transfer and Energy Redistribution, *Chem. Phys. Lett.* 293 (1998) 1-8.

[42] C. Wang, J. Li, G. Mele, G.-M. Yang, F.-X. Zhang, L. Palmisano, G. Vasapollo, Efficient Degradation of 4-Nitrophenol by Using Functionalized Porphyrin-TiO_2 Photocatalysts under Visible Irradiation, *Appl. Catal., B* 76 (2007) 218-226.

[43] M. Grätzel, Recent Advances in Sensitized Mesoscopic Solar Cells, *Acc. Chem. Res.* 42 (2009) 1788-1798.

[44] B. Oregan, M. Gratzel, A Low-Cost, High-Efficiency Solar-Cell Based on Dye-Sensitized Colloidal TiO_2 Films, *Nature* 353 (1991) 737-740.

[45] A. Makhal, S. Sarkar, T. Bora, S. Baruah, J. Dutta, A.K. Raychaudhuri, S.K. Pal, Role of Resonance Energy Transfer in Light Harvesting of Zinc Oxide-Based Dye-Sensitized Solar Cells, *J. Phys. Chem. C* 114 (2010) 10390-10395.

[46] C.-Y. Chen, J.-G. Chen, S.-J. Wu, J.-Y. Li, C.-G. Wu, K.-C. Ho, Multifunctionalized Ruthenium-Based Supersensitizers for Highly Efficient Dye-Sensitized Solar Cells, *Angew. Chem. Int. Ed.* 47 (2008) 7342-7345.

[47] M. Garcia-Iglesias, J.-J. Cid, J.-H. Yum, A. Forneli, P. Vazquez, M.K. Nazeeruddin, E. Palomares, M. Gratzel, T. Torres, Increasing the Efficiency of Zinc-Phthalocyanine Based Solar Cells through Modification of the Anchoring Ligand, *Energy Environ. Sci.* 4 (2011) 189-194.

[48] S.D. Oosterhout, M.M. Wienk, S.S. van Bavel, R. Thiedmann, L. Jan Anton Koster, J. Gilot, J. Loos, V. Schmidt, R.A.J. Janssen, The Effect of Three-Dimensional Morphology on the Efficiency of Hybrid Polymer Solar Cells, *Nat. Mater.* 8 (2009) 818-824.

[49] G. Mattioli, C. Melis, G. Malloci, F. Filippone, P. Alippi, P. Giannozzi, A. Mattoni, A. Amore Bonapasta, Zinc Oxide–Zinc Phthalocyanine Interface for Hybrid Solar Cells, *J. Phys. Chem. C* 116 (2012) 15439-15448.

[50] G. de la Torre, C.G. Claessens, T. Torres, Phthalocyanines: Old Dyes, New Materials. Putting Color in Nanotechnology, *Chem. Commun.* (2007) 2000-2015.

[51] L. Giribabu, C. Vijay Kumar, V. Gopal Reddy, P. Yella Reddy, C. Srinivasa Rao, S.-R. Jang, J.-H. Yum, M.K. Nazeeruddin, M. Grätzel, Unsymmetrical Alkoxy Zinc Phthalocyanine for Sensitization of Nanocrystalline TiO_2 Films, *Sol. Energ. Mat. Sol. Cells* 91 (2007) 1611-1617.

[52] S. Mori, M. Nagata, Y. Nakahata, K. Yasuta, R. Goto, M. Kimura, M. Taya, Enhancement of Incident Photon-to-Current Conversion Efficiency for Phthalocyanine-Sensitized Solar Cells by 3d Molecular Structuralization, *J. Am. Chem. Soc.* 132 (2010) 4054-4055.

[53] J. He, A. Hagfeldt, S.-E. Lindquist, H. Grennberg, F. Korodi, L. Sun, B. Åkermark, Phthalocyanine-Sensitized Nanostructured TiO_2 Electrodes Prepared by a Novel Anchoring Method, *Langmuir* 17 (2001) 2743-2747.

[54] G. Bottari, G. de la Torre, D.M. Guldi, T. Torres, Covalent and Noncovalent Phthalocyanine−Carbon Nanostructure Systems: Synthesis, Photoinduced Electron Transfer and Application to Molecular Photovoltaics, *Chem. Rev.* 110 (2010) 6768-6816.

[55] M.K. Nazeeruddin, R. Humphry-baker, M. Grätzel, D. Wöhrle, G. Schnurpfeil, G. Schneider, A. Hirth, N. Trombach, Efficient near-IR Sensitization of Nanocrystalline TiO_2 Films by Zinc and Aluminum Phthalocyanines, *J. Porphyrins Phthalocyanines* 3 (1999) 230-237.

[56] Ü. Özgür, Y.I. Alivov, C. Liu, A. Teke, M.A. Reshchikov, S. Doğan, V. Avrutin, S.-J. Cho, H. Morkoç, A Comprehensive Review of ZnO Materials and Devices, *J. Appl. Phys.* 98 (2005) 041301.

[57] S. Sardar, S. Sarkar, M.T.Z. Myint, S. Al-Harthi, J. Dutta, S.K. Pal, Role of Central Metal Ions in Hematoporphyrin-Functionalized Titania in Solar Energy Conversion Dynamics, *Phys. Chem. Chem. Phys.* 15 (2013) 18562-18570.

[58] V. Shklover, M.K. Nazeeruddin, S.M. Zakeeruddin, C. Barbé, A. Kay, T. Haibach, W. Steurer, R. Hermann, H.U. Nissen, M. Grätzel, Structure of Nanocrystalline TiO_2 Powders and Precursor to Their Highly Efficient Photosensitizer, *Chem. Mater.* 9 (1997) 430-439.

[59] R.C. Srivastava, V.D. Anand, W.R. Carper, A Fluorescence Study of Hematoporphyrin, *Appl. Spectrosc.* 27 (1973) 444-449.

[60] P. Castillero, J.R. Sánchez-Valencia, M. Cano, J.M. Pedrosa, J. Roales, A. Barranco, A.R. González-Elipe, Active and Optically Transparent Tetracationic Porphyrin/TiO_2 Composite Thin Films, *ACS Appl. Mater. Interfaces* 2 (2010) 712-721.

[61] A. Kathiravan, P.S. Kumar, R. Renganathan, S. Anandan, Photoinduced Electron Transfer Reactions between Meso-Tetrakis(4-Sulfonatophenyl)Porphyrin and Colloidal Metal-Semiconductor Nanoparticles, *Colloids Surf., A* 333 (2009) 175-181.

[62] G.B. Deacon, R.J. Phillips, Relationships between the Carbon-Oxygen Stretching Frequencies of Carboxylato Complexes and the Type of Carboxylate Coordination, *Coord. Chem. Rev.* 33 (1980) 227-250.

[63] H.C. Choi, Y.M. Jung, S.B. Kim, Size Effects in the Raman Spectra of TiO_2 Nanoparticles, *Vib. Spectrosc.* 37 (2005) 33-38.

[64] J. Desilvestro, M. Graetzel, L. Kavan, J. Moser, J. Augustynski, Highly Efficient Sensitization of Titanium Dioxide, *J. Am. Chem. Soc.* 107 (1985) 2988-2990.

[65] S. Franzen, L. Kiger, C. Poyart, J.-L. Martin, Heme Photolysis Occurs by Ultrafast Excited State Metal-to-Ring Charge Transfer, *Biophys. J .* 80 (2001) 2372-2385.

[66] L. Sun, J.R. Bolton, Determination of the Quantum Yield for the Photochemical Generation of Hydroxyl Radicals in TiO_2 Suspensions, *J. Phys. Chem.* 100 (1996) 4127-4134.

[67] A. Brune, G. Jeong, P.A. Liddell, T. Sotomura, T.A. Moore, A.L. Moore, D. Gust, Porphyrin-Sensitized Nanoparticulate TiO_2 as the Photoanode of a Hybrid Photoelectrochemical Biofuel Cell, *Langmuir* 20 (2004) 8366-8371.

[68] Z.S. Seddigi, S.A. Ahmed, S. Sardar, S.K. Pal, Ultrafast Dynamics at the Zinc Phthalocyanine/Zinc Oxide Nanohybrid Interface for Efficient Solar Light Harvesting in the Near Red Region, *Sol. Energ. Mat. Sol. Cells* 143 (2015) 63-71.

[69] S. Chaudhuri, S. Sardar, D. Bagchi, S.S. Singha, P. Lemmens, S.K. Pal, Sensitization of an Endogenous Photosensitizer: Electronic Spectroscopy of Riboflavin in the Proximity of Semiconductor, Insulator, and Metal Nanoparticles, *J. Phys. Chem. A* 119 (2015) 4162-4169.

[70] J. Obirai, N.P. Rodrigues, F. Bedioui, T. Nyokong, Synthesis, Spectral and Electrochemical Properties of a New Family of Pyrrole Substituted Cobalt, Iron, Manganese, Nickel and Zinc Phthalocyanine Complexes, *J. Porphyrins Phthalocyanines* 7 (2003) 508-520.

[71] M.-S. Liao, S. Scheiner, Electronic Structure and Bonding in Metal Phthalocyanines, Metal=Fe, Co, Ni, Cu, Zn, Mg, *J. Chem. Phys.* 114 (2001) 9780-9791.

[72] S. Sardar, S. Chaudhuri, P. Kar, S. Sarkar, P. Lemmens, S.K. Pal, Direct Observation of Key Photoinduced Dynamics in a Potential Nano-Delivery Vehicle of Cancer Drugs, *Phys. Chem. Chem. Phys.* 17 (2015) 166-177.

[73] A. McLaren, T. Valdes-Solis, G. Li, S.C. Tsang, Shape and Size Effects of ZnO Nanocrystals on Photocatalytic Activity, *J. Am. Chem. Soc.* 131 (2009) 12540-12541.

[74] A. Giri, N. Goswami, M. Pal, M.T. Zar Myint, S. Al-Harthi, A. Singha, B. Ghosh, J. Dutta, S.K. Pal, Rational Surface Modification of Mn_3O_4 Nanoparticles to Induce Multiple Photoluminescence and Room Temperature Ferromagnetism, *J. Mater. Chem. C* 1 (2013) 1885-1895.

[75] S. Ghosh, A. Priyam, S. Bhattacharya, A. Saha, Mechanistic Aspects of Quantum Dot Based Probing of Cu (II) Ions: Role of Dendrimer in Sensor Efficiency, *J. Fluoresc.* 19 (2009) 723-731.

[76] H.R. Ibrahim, M.I. Hoq, T. Aoki, Ovotransferrin Possesses Sod-Like Superoxide Anion Scavenging Activity That is Promoted by Copper and Manganese Binding, *Int. J. Biol. Macromolec.* 41 (2007) 631-640.

[77] A. Zyoud, N. Zaatar, I. Saadeddin, M.H. Helal, G. Campet, M. Hakim, D. Park, H.S. Hilal, Alternative Natural Dyes in Water Purification: Anthocyanin as

TiO_2-Sensitizer in Methyl Orange Photo-Degradation, *Solid State Sci.* 13 (2011) 1268-1275.

[78] S. Afzal, W.A. Daoud, S.J. Langford, Photostable Self-Cleaning Cotton by a Copper(II) Porphyrin/TiO_2 Visible-Light Photocatalytic System, *ACS Appl. Mater. Interfaces* 5 (2013) 4753-4759.

[79] S. Sardar, P. Kar, S.K. Pal, The Impact of Central Metal Ions in Porphyrin Functionalized ZnO/TiO_2 for Enhanced Solar Energy Conversion, *J. Mat. NanoSci.* 1 (2014) 12-30.

[80] C.P. LeBel, H. Ischiropoulos, S.C. Bondy, Evaluation of the Probe 2',7'-Dichlorofluorescin as an Indicator of Reactive Oxygen Species Formation and Oxidative Stress, *Chem. Res. Toxicol.* 5 (1992) 227-231.

[81] A.B. Djurišić, Y.H. Leung, K.H. Tam, L. Ding, W.K. Ge, H.Y. Chen, S. Gwo, Green, Yellow and Orange Defect Emission from ZnO Nanostructures: Influence of Excitation Wavelength, *Appl. Phys. Lett.* 88 (2006) 103107.

[82] K. Vanheusden, W.L. Warren, C.H. Seager, D.R. Tallant, J.A. Voigt, B.E. Gnade, Mechanisms Behind Green Photoluminescence in ZnO Phosphor Powders, *J. Appl. Phys.* 79 (1996) 7983-7990.

[83] A. van Dijken, E.A. Meulenkamp, D. Vanmaekelbergh, A. Meijerink, The Kinetics of the Radiative and Nonradiative Processes in Nanocrystalline ZnO Particles Upon Photoexcitation, *J. Phys. Chem. B* 104 (2000) 1715-1723.

[84] J.R. Lakowicz, Principles of Fluorescence Spectroscopy, 2nd ed., Kluwer Academic/ Plenum, New York, 1999.

[85] R.M. Clegg, [18] Fluorescence Resonance Energy Transfer and Nucleic Acids, in: J.E.D. David M.J. Lilley (Ed.) Methods in Enzymology, Academic Press 1992, 353-388.

[86] T. Bora, K.K. Lakshman, S. Sarkar, A. Makhal, S. Sardar, S.K. Pal, J. Dutta, Modulation of Defect-Mediated Energy Transfer from ZnO Nanoparticles for the Photocatalytic Degradation of Bilirubin, *Beilstein J. Nanotechnol.* 4 (2013) 714-725.

[87] S. Sarkar, S. Sardar, A. Makhal, J. Dutta, S. Pal, Engineering FRET-Based Solar Cells: Manipulation of Energy and Electron Transfer Processes in a Light Harvesting Assembly, in: X. Wang, Z.M. Wang (Eds.) High-Efficiency Solar Cells, Springer International Publishing 2014, pp. 267-318.

[88] A. Makhal, S. Sarkar, T. Bora, S. Baruah, J. Dutta, A.K. Raychaudhuri, S.K. Pal, Dynamics of Light Harvesting in ZnO Nanoparticles, *Nanotechnology* 21 (2010) 265703.

[89] D. Ino, K. Watanabe, N. Takagi, Y. Matsumoto, Electron Transfer Dynamics from Organic Adsorbate to a Semiconductor Surface: Zinc Phthalocyanine on TiO_2(110), *J. Phys. Chem. B* 109 (2005) 18018-18024.

[90] J. He, G. Benkö, F. Korodi, T. Polívka, R. Lomoth, B. Åkermark, L. Sun, A. Hagfeldt, V. Sundström, Modified Phthalocyanines for Efficient Near-IR Sensitization of Nanostructured TiO_2 Electrode, *J. Am. Chem. Soc.* 124 (2002) 4922-4932.

Chapter 5

Key Interfacial Carrier Dynamics in Inorganic-Inorganic Nanohybrids for Enhanced Light Harvesting Application

5.1. Introduction: Light harvesting via photocatalysis (PC) [1] and dye sensitized solar cells (DSSC) [2] are related to excited state charge transfer across nanostructured oxide surfaces. The former case consists of the absorption of photons at the oxide surfaces with the consequent generation of electron/hole pairs and eventual reduction/oxidation of adsorbed contaminant species. On the other hand in the latter case the photogenerated electron/hole pairs at the oxide surface migrate to the external circuit for photocurrent generation through an electrical load. Thus it is clear that a precise knowledge of excited state charge transfer across oxide surfaces, either naked or with adsorbed species, is important to fully understand the microscopic mechanism related to technologically important processes of PC and DSSC, both of which indeed have strong social impact. Technological advances in multiple areas from solar energy conversion (DSSC) to environmental remediation (PC) have been exploiting the exceptional properties of TiO_2 and ZnO [3-5]. However, one limitation of the oxide materials is the large band gap which renders clean solar energy driven processes inefficient. In order to sensitize the oxides in the visible light, several strategies have been studied. In photovoltaics, sensitization with visible light absorbing dyes is a prevalent solution [2]. In photocatalysis strategies include impurity doping [6-7] in addition to the dye sensitization [8-9] of the host oxide nanoparticles. In one of our recent studies, hematoporphyrin sensitized ZnO nanorods exhibit twin applications in efficient visible light photocatalysis (VLP) and DSSC [10]. As the stability of an organic dye on a wide band gap oxide material is an issue, another

approach beside the organic dye sensitization is to combine the material with a semiconductor that has a narrow band gap and an energetically high-lying conduction band [11]. In this direction, Kamat [12] and coworkers show photoinduced electron transfer from CdSe quantum dots (QDs) of different sizes to three unique metal oxide (TiO_2, ZnO and SnO_2) and suggest that in addition to electron transfer at the QD-metal oxide interface, other loss mechanisms play key roles in the determination of overall device efficiency.

Lead chalcogenides (mainly PbS and PbSe) are gaining research interest because of their unique photophysical properties such as tunable and broad spectral responses extending from the visible to near-IR regions, [13-14] high absorption coefficient, [15] long exciton lifetimes, [16-17] multiple exciton generation (MEG), [18-21] and hot carrier extraction [22]. In a survey of contemporary literature it appeared that PbS quantum dot sensitized solar cell are efficient to harvest light in the NIR region [23-24]. However, the works related to the use of the PbS sensitized nanomaterials for the photocatalysis application in the visible region, clearly indicate [25] that the material is sensitive in the visible (at light energy of 2.5 times higher than the band gap of QD) rather NIR region. Being in this regime, investigation of dynamical steps in the universality/limitation of such common applications of the nanomaterial in similar experimental conditions is the primary motive of the present study.

Here, we have synthesized and characterized the nanoscopic structure using high resolution transmission electron microscopy (HRTEM) of a well-known light-harvesting assembly (LHA), PbS QD sensitized ZnO nanoparticles (NPs) and their common applications in photocatalysis and solar cell. As both the parent materials ZnO and PbS have their intrinsic photoluminescence (PL) because of their defect states and band gap emission, respectively, [26-27] steady state spectroscopic studies on the LHA have been employed for the interfacial charge/energy migration. Picosecond-resolved PL-quenching of ZnO

nanoparticles shows Förster Resonance Energy Transfer (FRET) from donor ZnO to the acceptor PbS revealing nanoconjugate of the parent materials in the LHA. Picosecond-resolved photoluminescence (PL) study have been employed to investigate the ultrafast interfacial charge transfer dynamics in the LHA upon photoexcitation. We have also applied the LHA for the potential use in photocatalysis and photovoltaic applications under illumination of a number of excitation wavelengths ranging from UV to visible region. The difference in efficacies of the LHA in the PC and DSSC applications is rationalized from the crucial interfacial charge migration upon photoexcitation.

5.2. Results and Discussion:

5.2.1. Interfacial Carrier Dynamics in PbS-ZnO Light Harvesting Assemblies and their Potential Implication in Photovoltaic/ Photocatalysis Application [28]: As illustrated in Figure 5.1a, the representative high-resolution TEM (HRTEM) image of the PbS−ZnO LHA shows the average diameter is ~6 nm and ~3.2 nm for ZnO NPs and PbS QDs, respectively and confirms the proximity between PbS QDs and ZnO NPs. The synthesized ZnO NPs are spherical in shape and the NPs (diameter ~6 nm) do not show any quantum confinement effect as the Bohr radius of ZnO is ~ 3 nm. The lattice fringes of ZnO NPs and PbS QDs in PbS−ZnO LHAs are illustrated, which shows interplanar distances of ~0.314 and ~0.209 nm, corresponding to the spacing between two (100) planes [29] of ZnO NP and (220) planes [30] of PbS QD, respectively. In order to determine the complex formation between the TOPO-capped PbS QDs and ZnO NPs in the PbS−ZnO LHAs, we have also studied UV-vis spectroscopy, as shown in Figure 5.1b. The bare ZnO NPs show absorption peak at 326 nm corresponding to the band-gap excitation, which is found to be red-shifted to 337 nm in PbS−ZnO LHAs. A bathochromic shift of ~11 nm in the absorption spectra can be attributed to the ground-state complex formation between PbS QDs and ZnO NPs. The inset of Figure 5.1b shows the absorption spectra of TOPO-capped PbS QDs.

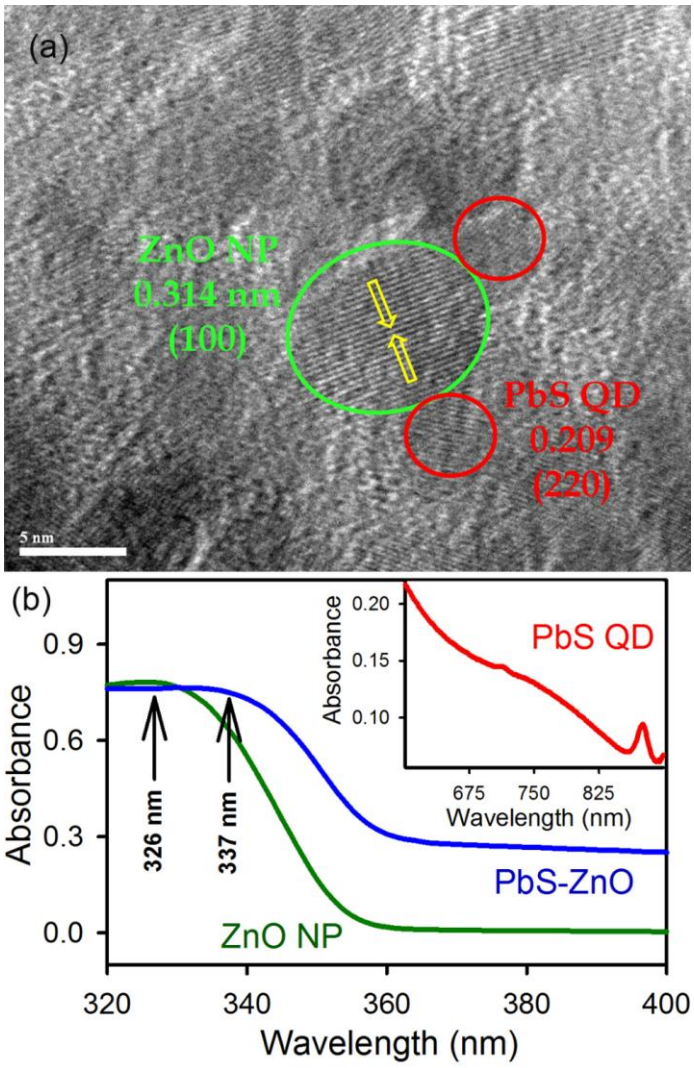

Figure 5.1. *(a) High-resolution TEM (HRTEM) image of PbS−ZnO LHA where PbS QD is attached to the ZnO NP surface. (b) UV-vis absorption spectra of bare ZnO NPs (dark green) and PbS−ZnO LHAs (blue). The inset shows the absorption spectra of PbS QDs (red).*

As shown in Figure 5.2a, the room temperature PL spectrum of ZnO NP is comprised of two emission bands upon excitation above the band-edge (λ_{ex} = 300 nm) [29]. The narrow UV band centered at 363 nm is due to the exciton recombination. The defect centers located near the surface are responsible for broad emission in blue green region which is composed of two bands, one arises from doubly charged vacancy center (V_o^{++}) located at 555 nm (P_2) and the other arises from singly charged vacancy center (V_o^{+}) located at 500 nm (P_1) [31-32]. For PbS−ZnO LHAs, there is a considerable decrease in the intensity of both the

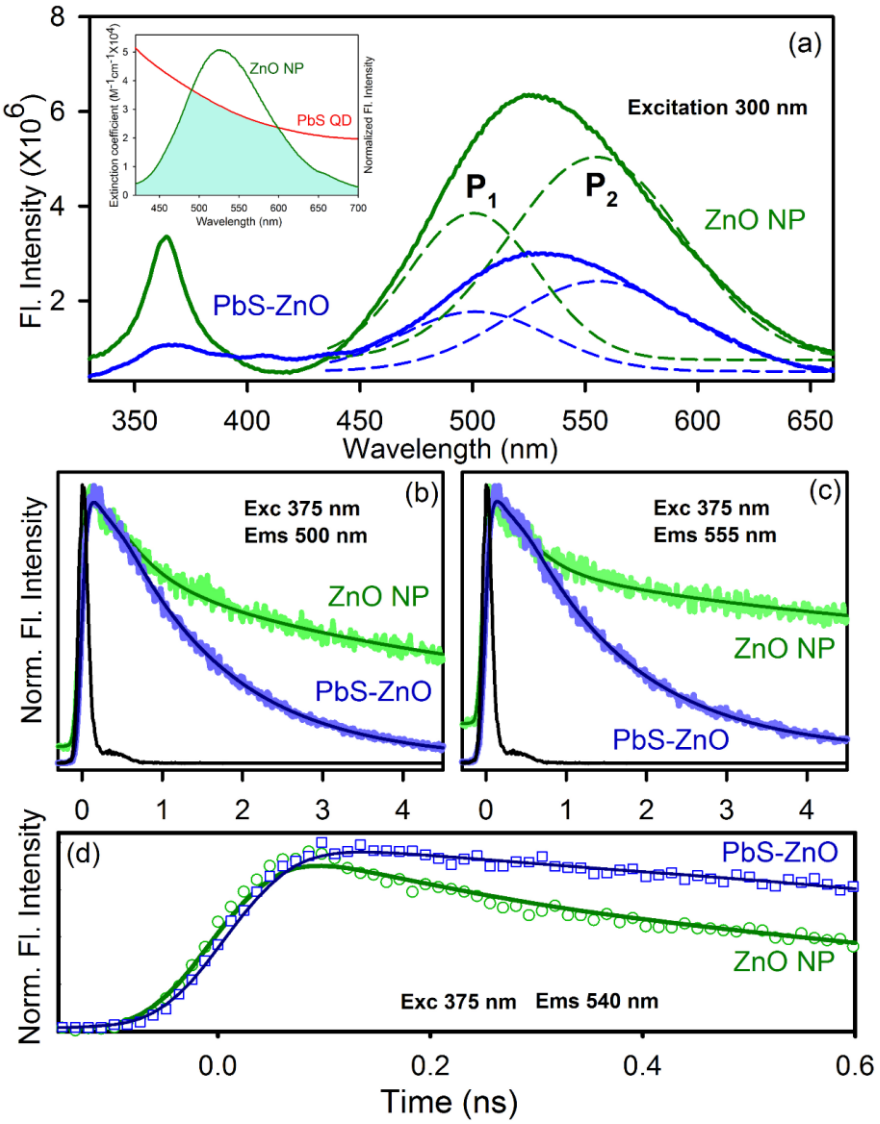

Figure 5.2. *(a) Room temperature PL spectra of ZnO NPs (dark green) and PbS−ZnO LHAs (blue) are shown. The excitation wavelength was at 300 nm. The broad emission band is composed of two components, P_1 (500 nm) and P_2 (555 nm). The inset shows the overlap of ZnO NP emission and PbS QD absorption. The picosecond-resolved fluorescence transients of ZnO NPs (excitation at 375 nm) in the absence (dark green) and in the presence of PbS QDs (red) collected at (b) 500 nm, (c) 555 nm and (d) 540 nm (shorter time window) are shown.*

emission peaks as compared to the bare ZnO NPs. The decrease in emission intensities can be attributed to the efficient non-radiative photoinduced processes in PbS−ZnO interface. Herein, we propose Förster Resonance Energy Transfer (FRET) from the donor ZnO NPs to the acceptor PbS QDs in PbS-ZnO LHAs, which is responsible for the observed inhibition of the emission bands. The spectral overlap of the defect-mediated PL band of ZnO NPs with that of the PbS

absorption is shown in Figure 5.2a, inset. The fluorescence decay of bare ZnO NPs and PbS−ZnO LHAs were obtained upon excitation of 375 nm laser and monitored at 500 nm and 555 nm (Figure 5.2b and 5.2c, respectively). The faster average excited state lifetime of the PbS-ZnO LHAs with respect to that of the ZnO NPs is clearly observed. The details of the spectroscopic parameters and the fitting parameters of the fluorescence decays are tabulated in Table 5.1. From FRET calculations, the distance between the donor and acceptor are determined to be 1.71 nm and 1.61 nm for P_1 and P_2 states, respectively. The calculated distances are consistent with the fact that the radius of the ZnO NPs used is ~3 nm and P_2 states are closer to the surface which leads to the shorter distance compare to the P_1 states. The energy transfer efficiency is calculated to be 81.6% and 86.3% from P_1 and P_2 states, respectively. The observation is in agreement with the reported literature that the P_2 state is in the proximity of the NP surface [33-34]. Further confirmation of non-radiative energy transfer from the ZnO NPs (donor) to the associated PbS QDs (acceptor) is evident from the emission characteristics of the acceptor as shown in Figure 5.3. The excitation spectrum of the LHAs at the detection wavelength of 820 nm (acceptor emission) as shown in Figure 5.3a clearly reveals a maximum at 360 nm, which is close to the absorption maximum of the ZnO NPs. The observation is consistent with the fact that the absorbed energy in the ZnO NPs migrate to the PbS QDs through a non-radiative pathway [35]. In the case of FRET, it is expected that emission transient from the acceptor shows buildup in the timescale comparable to the decay of the energy donor [35]. As shown in Figure 5.3b, the emission transient of the acceptor PbS QDs reveal no apparent rise component. However, the shorter component of the lifetime of acceptor PbS QDs is significantly retarded in PbS-ZnO LHAs as shown in Table 5.1 revealing an intrinsic buildup in the excited state due to FRET. We have estimated the buildup rate following the reported procedure [12] and found to be 1.45×10^7 sec^{-1}, which is close to the FRET rate from donor ZnO NPs to PbS QDs

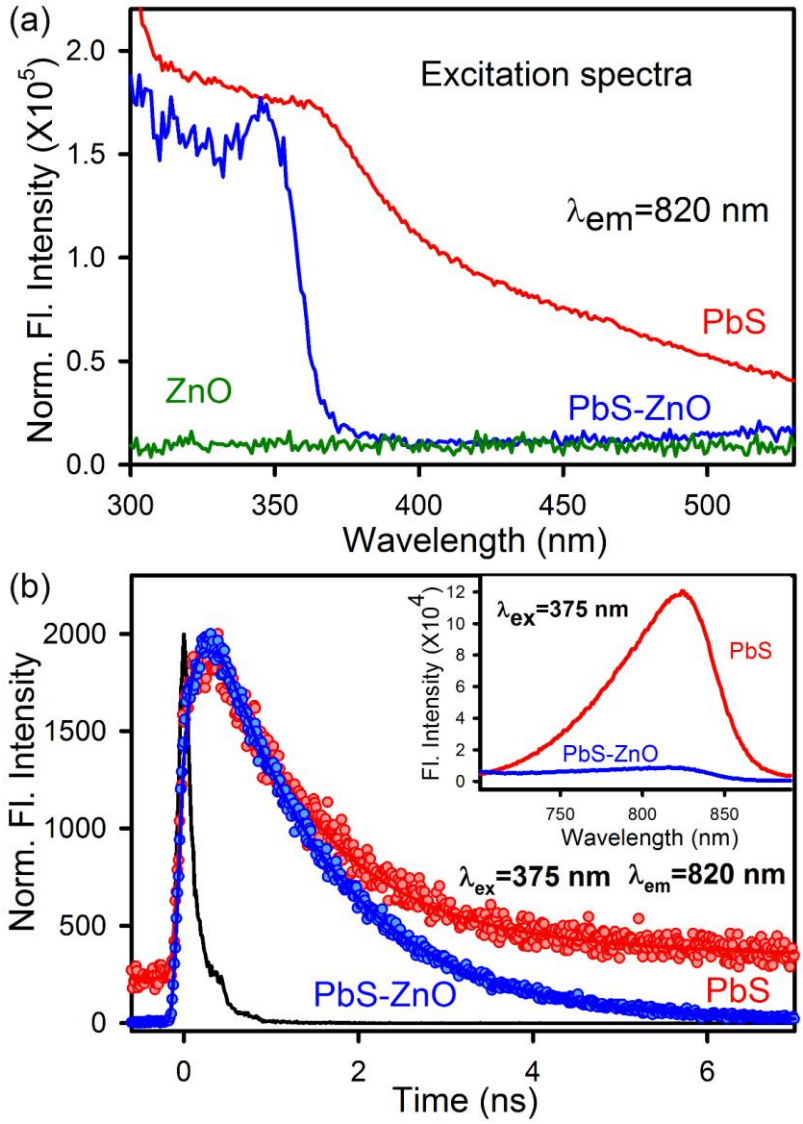

Figure 5.3. *(a) Excitation spectra of ZnO NPs (dark green), PbS QDs (red) and PbS−ZnO LHAs (blue) monitored at 820 nm. (b) The picosecond-resolved fluorescence transients of PbS QDs (excitation at 375 nm) in the absence (red) and in the presence of ZnO NPs (blue) collected at 820 nm. The inset shows the room temperature PL spectra of PbS QDs (red) and PbS−ZnO LHAs (blue) upon excitation at 375 nm.*

(1.47×10^7 sec^{-1}). The observation confirms the non-radiative energy transfer process from the donor ZnO NPs to the acceptor PbS QDs. As shown in Figure 5.3b, the overall quenching of the emission (steady state and transient) of PbS QDs in the LHAs clearly indicates that other non-radiative excited state events are associated following the energy transfer from the donor ZnO NPs. In order to investigate the non-radiative pathway of PbS QDs in the LHAs upon excitation,

we have excited the nanocomposite at 510 nm and followed the steady and time-resolved emission as shown in Figure 5.4. The quenching of the emission of the PbS QDs in the LHAs clearly reveals ultrafast (Table 5.1) electron transfer from the excited QDs to the CB of ZnO NPs through non-radiative pathway [36]. A non radiative ultrafast decay of 40 ps revealing the charge migration from the excited PbS to the host ZnO NPs is evident from Figure 5.4b. The manifestation of such charge transfer process in the emission of ZnO NPs at 540 nm upon excitation at 375 nm is also evident from Figure 5.2d.

Table 5.1. *Dynamics of picosecond-resolved luminescence transients of ZnO NP, PbS-ZnO LHA and PbS QD*[a]

Sample	Excitation wavelength (nm)	Detection wavelength (nm)	τ_1 (ns)	τ_2 (ns)	τ_3 (ns)	τ_{avg} (ns)
ZnO NP	375	500	0.46 (43.8%)	4.52 (41.6%)	37.39 (14.6%)	7.55
PbS-ZnO LHA	375	500	1.30 (95.5%)	3.46 (4.5%)		1.39
ZnO NP	375	555	0.37 (46.2%)	5.07 (25%)	44.93 (28.8%)	14.38
PbS-ZnO LHA	375	555	1.32 (94.3%)	5.22 (4.5%)	42.29 (1.2%)	1.98
ZnO NP	375	540	0.38 (75.3%)	3.36 (17.2%)	38.64 (7.5%)	3.76
PbS-ZnO LHA	375	540	1.31 (92.8%)	4.79 (5.1%)	45.95 (2.1%)	2.42
PbS QD	375	820	1.17 (91%)	13.21 (9%)		2.25
PbS-ZnO LHA	375	820	1.41 (100%)			1.41
PbS QD	510	820	130.35 (100%)			130.35
PbS-ZnO LHA	510	820	0.04 (99.33%)	138.34 (0.66%)		0.95

[a]*Numbers in the parenthesis indicate relative weightages.*

Table 5.1 reveals that the shorter component of the decay of bare ZnO NPs (0.46 ns and 0.37 ns for P_1 and P_2, states respectively) increases upon attaching to the PbS QDs (1.30 ns and 1.32 ns respectively). The lengthening of the faster relaxation times from the P_1 and P_2 states confirms the following two phenomena. Firstly, the quenching due to FRET is not operative in the timescale of ~400 ps. Secondly, the recombination processes in the ZnO defect states are heavily retarded in the proximity of PbS QDs as clearly shown in Figure 5.2d. The retardation of the recombination may be attributed to the quenching of the photoexcited holes of ZnO NPs by the PbS QDs. In an earlier study the proximity of a hole trapping molecule (4-amino-thiophenole) to CdSe QD is shown to increase the radiative recombination time of the QD at room temperature [37]. In our case the photo-generated hole in the valence band of the ZnO NPs is proposed to be quenched by an electron from the valence band of PbS QDs, which is expected to be recovered from the electron in the conduction band/P_1 state of the ZnO NPs (upper panel of scheme 5.1).

The room temperature PL spectra of PbS QDs shows emission peak at 820 nm upon the excitation at 510 nm, as shown in Figure 5.4a. The intensity of the emission peak decreases considerably when the QDs are attached to the ZnO NPs. This is attributed to the efficient charge migration from the conduction band of PbS QD to the ZnO NPs [16]. The fluorescence decays (Figure 5.4b) of PbS QDs and PbS−ZnO LHAs were measured upon excitation with 510 nm laser, and monitored at wavelength 820 nm. The emission decay curve of PbS QDs is fitted with single exponential function with a lifetime of 130.35 ns (Table 5.1). In case of PbS−ZnO LHA, the decay curve of PbS QD deviated from single exponential to bi-exponential showing one significant shorter lifetime 40 ps (99%) and a minor longer lifetime of 140 ns (1%). The observed decrease in lifetime could be correlated to the electron transfer process from PbS QDs to ZnO NPs [16, 38]. Plass et al. [36] have investigated the electron transfer in a solar cell structure made by

in situ growth of PbS QDs in a porous TiO_2 film, where initial charge separation occurs in 1 ps due to the electron trapping in PbS QD followed by electron injection into the conduction band of TiO_2 having a time constant of 20 ps. The band alignment of PbS QDs and ZnO NPs are well documented in the literature. The energy levels of photoexcited electrons and holes of 3.2 nm PbS QDs are at -3.7 and -5.1 eV [16] and the lowest unoccupied molecular orbital (LUMO) of ZnO NPs is −4.3 eV [39]. Eita et al. [40] have shown that the electron injection from photoexcited PbS QDs to ZnO NPs over ITO plate occurs on a time scale of a few hundred femtoseconds and the observation is supported by the interfacial electronic-energy alignment between the donor and acceptor moieties.

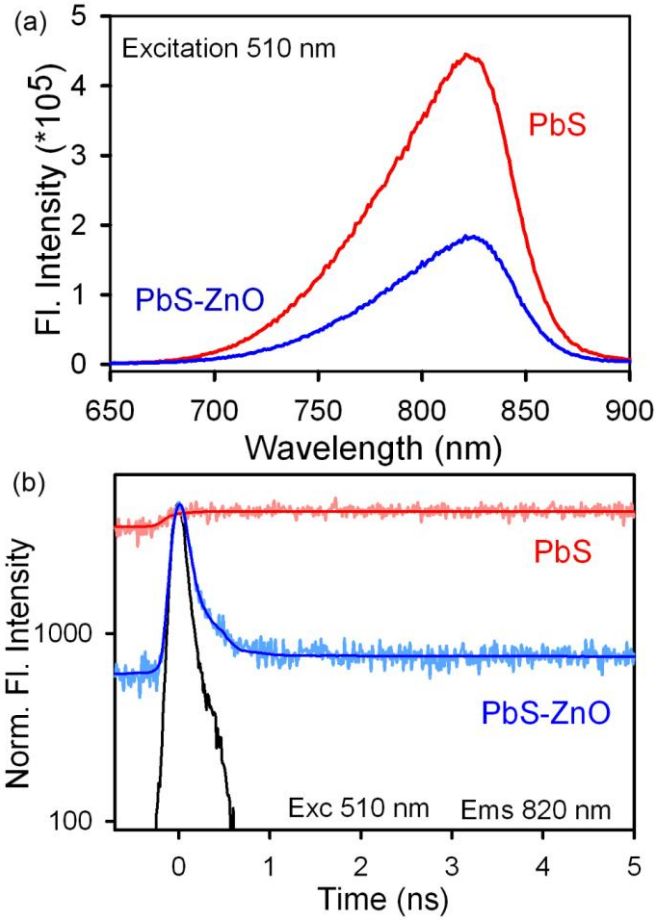

Figure 5.4. *(a) Room temperature PL spectra (excitation wavelength was at 510 nm) of PbS QDs (red) and PbS−ZnO LHAs (blue) are shown. (b) Fluorescence decay profiles of PbS QDs in the absence (red) and presence of ZnO NPs (blue) upon excitation at 510 nm and monitored at 823 nm.*

In order to investigate the interfacial charge transfer dynamics in photocatalysis application, we have probed the methylene blue (MB) reduction in presence of the LHA in aqueous solution. The results for the photoreduction of MB are shown in Figure 5.5a. The photoreduction of MB implies the generation of the colorless photoproduct Leuco-Methylene Blue (LMB). The maximum photoreduction is observed in the presence of ZnO NPs under UV irradiation while using 475 HP optical filter no photoreduction of MB is observed. This is obvious because ZnO being a wide band gap (3.37 eV) semiconductor, the band-gap excitation occurs only at wavelengths less than 380 nm. However, ZnO NPs in the proximity of PbS QDs in the LHAs show inefficient MB photoreduction both in presence and absence of the HP filter. We have attributed the de-excitation of ZnO NPs via FRET to be responsible for the less photocatalytic activity of the LHAs in UV light excitation (no filter) as shown in the upper panel of scheme 5.1. On the other hand visible light excitation (with filter) of the PbS QDs in the LHAs shuttles the photogenerated electron in the QDs through the conduction band of the ZnO NPs as shown in lower panel of scheme 5.1. Overall for white light excitation of the LHAs, the photogenerated electron is sparsely available for the reduction of MB in the solution due to the above mentioned two ultrafast mechanisms.

In order to investigate the efficacy of PbS-ZnO LHAs in photovoltaic application, we have performed photoelectrochemical measurements in a half cell geometry using the LHAs on ITO plate as anode and Pt as counter electrode [41]. For I-V measurement, the Ag/Ag^{+} couple are used as reference electrode. The photocurrent measurements were carried out in order to better understand the electron transfer processes in terms of short circuit current. The light source (100 mW cm^{-2}) was turned on and off every 60 sec and the obtained photocurrent values were continuously recorded. As shown in Figure 5.5b, under full light

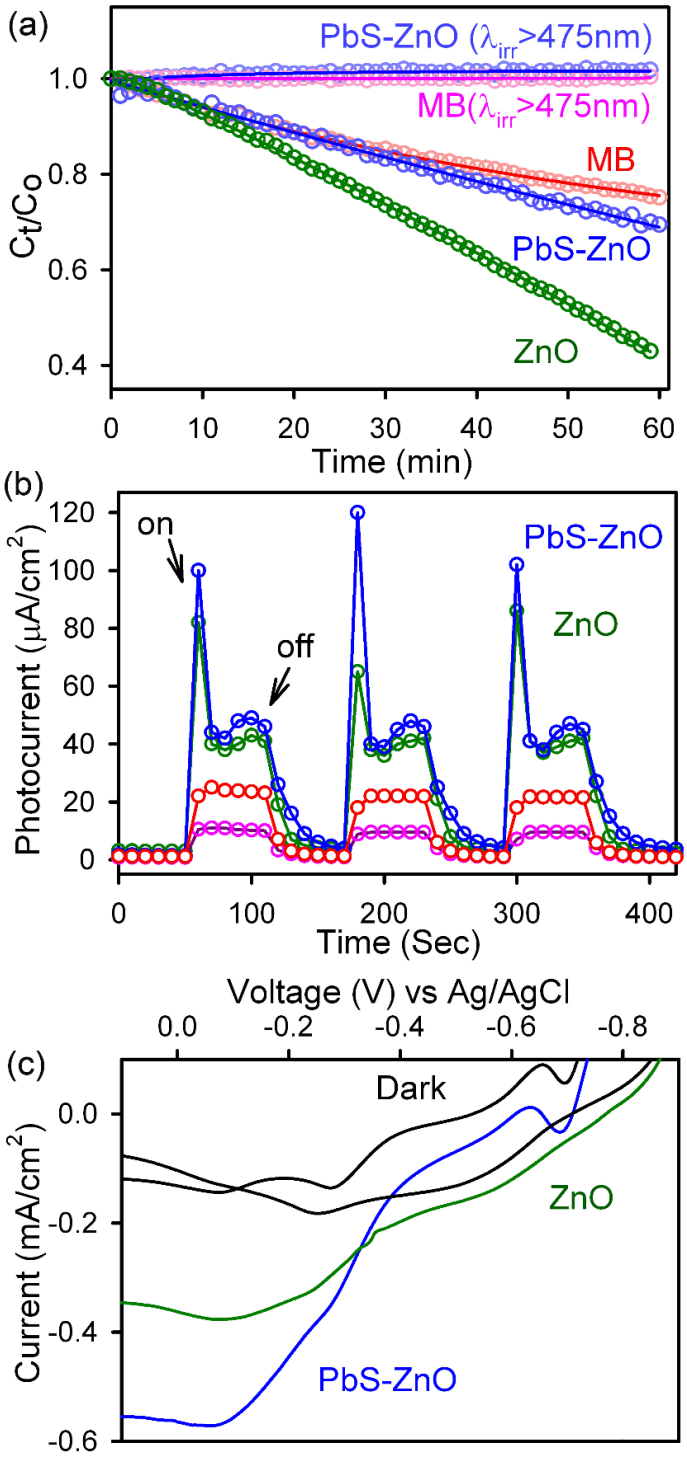

Figure 5.5. *(a) Photocatalytic degradation of MB in the presence of PbS QDs (blue), ZnO NPs (red and dark red) and PbS−ZnO LHA (dark green and pink) under different irradiation conditions (the optical filters used for the desired irradiation are indicated in the parentheses). (b) Photocurrent response of PbS-ZnO LHA (blue) and ZnO (green) under 100 mW cm^{-2} incident power irradiation and PbS-ZnO (red) and ZnO (pink) under visible light irradiation (using 400 nm filter) without any bias voltage. (c) Photocurrent-voltage (I-V) characteristics of PbS-ZnO LHA (blue) and ZnO (green) under 100 mW cm^{-2} incident power irradiation.*

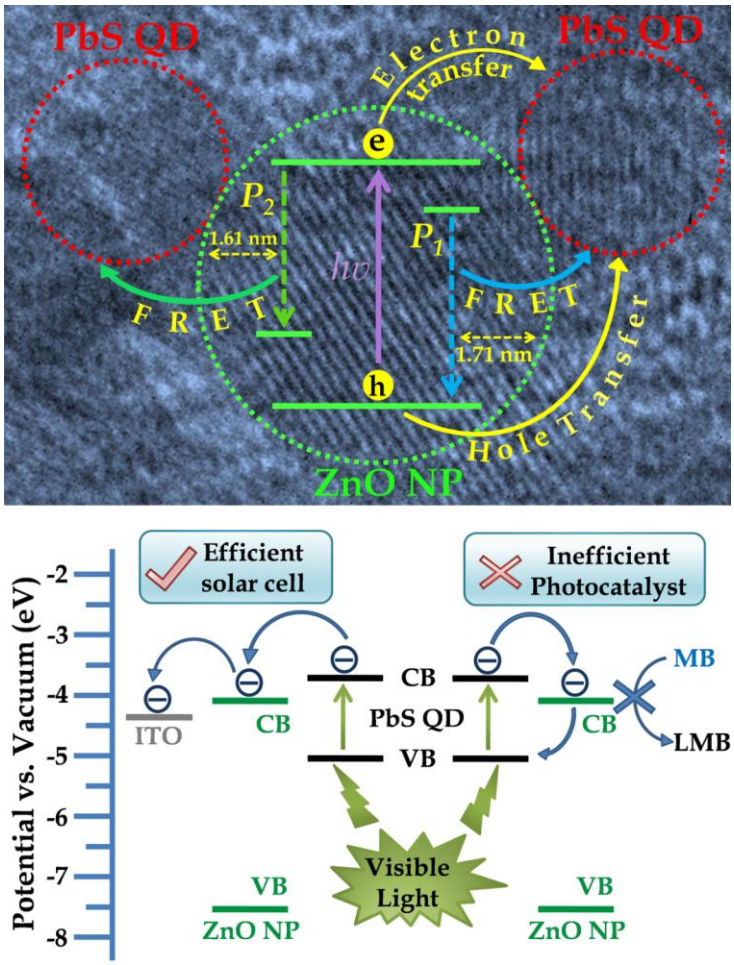

Scheme 5.1. *Schematic presentation of the interfacial carrier dynamics in PbS-ZnO LHAs (Upper panel). Lower panel shows the schematic energy level diagram and charge transfer processes for photocatalysis and photovoltaic applications.*

illumination PbS-ZnO has greater photocurrent response than ZnO NPs on the ITO plate. The observation is consistent with the fact that the LHAs would be able to harvest a wide band of light spectrum from UV to NIR in contrast to the ZnO NPs, which is expected to harvest only UV region of the incident white light. The initial spike is observed due to the slower recovery of the photoexcited holes from the electrolytes and is consistent with other studies reported in the literature [41]. Significant enhancement of the photocurrent in presence of PbS in the proximity of ZnO NPs in contrast to the retardation of photocatalysis activity of the LHAs is rationalized in the following way. The photogenerated electron in the PbS as well as ZnO NPs is expected to be channelized to the ITO plate because of the lower

potential as shown in lower panel of scheme 5.1. The I-V characteristics of the LHAs in presence of white light as shown in Figure 5.5c reveals significantly higher short-circuit current compared to those of the ZnO NPs. The observation clearly indicates the importance of the presence of ITO plate in the interfacial carrier dynamics of PbS-ZnO LHAs in photovoltaic application.

5.3. Conclusion: In summary, we have investigated dynamical processes in PbS-ZnO light harvesting assemblies (LHAs) upon photoexcitation and their common applications in photocatalysis and photovoltaics. The picosecond-resolved PL-quenching of ZnO nanoparticles (NPs) in the presence of PbS quantum dots (QDs) shows Förster Resonance Energy Transfer (FRET) from donor ZnO NPs to the acceptor PbS QDs and has been employed to confirm molecular proximity. Picosecond-resolved time correlated single photon counting (TCSPC) shows the ultrafast quenching of photoexcited holes in the ZnO NPs by PbS QDs. The photocatalytic activity of PbS−ZnO LHAs is probed by monitoring the photoreduction of the test contaminant methylene blue (MB). This shows that the LHA is inefficient as a photocatalyst because the photoexcited electrons shuttle across the semiconductor-semiconductor interface and are unavailable to the MB. The prospective use of the LHAs in photovoltaics is investigated by the photoelectrochemical studies where PbS-ZnO LHAs as working electrode shows higher photocurrent than that of bare ZnO NPs. This clearly indicates that the presence of ITO substrate provides directionality to the shuttling electrons at the PbS-ZnO interface. Thus PbS-ZnO LHAs are efficient in solar cell applications but are inefficient in heterogeneous catalysis. The exploration of interfacial carrier dynamics in PbS-ZnO LHAs will be helpful in improving the design and efficiency of the future solar energy harvesting devices.

References

[1] A. Fujishima, K. Honda, Electrochemical Photolysis of Water at a Semiconductor Electrode, *Nature* 238 (1972) 37-38.

[2] B. O'Regan, M. Gratzel, A Low-Cost, High-Efficiency Solar Cell Based on Dye-Sensitized Colloidal TiO_2 Films, *Nature* 353 (1991) 737-740.

[3] S. Sardar, S. Sarkar, M.T.Z. Myint, S. Al-Harthi, J. Dutta, S.K. Pal, Role of Central Metal Ions in Hematoporphyrin-Functionalized Titania in Solar Energy Conversion Dynamics, *Phys. Chem. Chem. Phys.* 15 (2013) 18562-18570.

[4] A. Hagfeldt, M. Grätzel, Molecular Photovoltaics, *Acc. Chem. Res.* 33 (2000) 269-277.

[5] M.R. Hoffmann, S.T. Martin, W. Choi, D.W. Bahnemann, Environmental Applications of Semiconductor Photocatalysis, *Chem. Rev.* 95 (1995) 69-96.

[6] C. Chen, X. Li, W. Ma, J. Zhao, H. Hidaka, N. Serpone, Effect of Transition Metal Ions on the TiO_2-Assisted Photodegradation of Dyes under Visible Irradiation: A Probe for the Interfacial Electron Transfer Process and Reaction Mechanism, *J. Phys. Chem. B* 106 (2001) 318-324.

[7] R. Asahi, T. Morikawa, T. Ohwaki, K. Aoki, Y. Taga, Visible-Light Photocatalysis in Nitrogen-Doped Titanium Oxides, *Science* 293 (2001) 269-271.

[8] W. Zhao, Y. Sun, F.N. Castellano, Visible-Light Induced Water Detoxification Catalyzed by Pt(II) Dye Sensitized Titania, *J. Am. Chem. Soc.* 130 (2008) 12566-12567.

[9] E. Bae, W. Choi, Highly Enhanced Photoreductive Degradation of Perchlorinated Compounds on Dye-Sensitized Metal/TiO_2 under Visible Light, *Environ. Sci. Technol.* 37 (2002) 147-152.

[10] S. Sarkar, A. Makhal, T. Bora, K. Lakhsman, A. Singha, J. Dutta, S.K. Pal, Hematoporphyrin–ZnO Nanohybrids: Twin Applications in Efficient Visible-Light Photocatalysis and Dye-Sensitized Solar Cells, *ACS Appl. Mater. Interfaces* 4 (2012) 7027-7035.

[11] P.V. Kamat, Quantum Dot Solar Cells. Semiconductor Nanocrystals as Light Harvesters, *J. Phys. Chem. C* 112 (2008) 18737-18753.

[12] K. Tvrdy, P.A. Frantsuzov, P.V. Kamat, Photoinduced Electron Transfer from Semiconductor Quantum Dots to Metal Oxide Nanoparticles, *Proc. Natl. Acad. Sci. USA* 108 (2011) 29-34.

[13] V.I. Klimov, A.A. Mikhailovsky, S. Xu, A. Malko, J.A. Hollingsworth, C.A. Leatherdale, H.-J. Eisler, M.G. Bawendi, Optical Gain and Stimulated Emission in Nanocrystal Quantum Dots, *Science* 290 (2000) 314-317.

[14] M.A. Hines, G.D. Scholes, Colloidal PbS Nanocrystals with Size-Tunable Near-Infrared Emission: Observation of Post-Synthesis Self-Narrowing of the Particle Size Distribution, *Adv. Mater.* 15 (2003) 1844-1849.

[15] L. Cademartiri, E. Montanari, G. Calestani, A. Migliori, A. Guagliardi, G.A. Ozin, Size-Dependent Extinction Coefficients of PbS Quantum Dots, *J. Am. Chem. Soc.* 128 (2006) 10337-10346.

[16] B.-R. Hyun, Y.-W. Zhong, A.C. Bartnik, L. Sun, H.D. Abruña, F.W. Wise, J.D. Goodreau, J.R. Matthews, T.M. Leslie, N.F. Borrelli, Electron Injection from Colloidal PbS Quantum Dots into Titanium Dioxide Nanoparticles, *ACS Nano* 2 (2008) 2206-2212.

[17] H.C. Leventis, F. O'Mahony, J. Akhtar, M. Afzaal, P. O'Brien, S.A. Haque, Transient Optical Studies of Interfacial Charge Transfer at Nanostructured Metal Oxide/PbS Quantum Dot/Organic Hole Conductor Heterojunctions, *J. Am. Chem. Soc.* 132 (2010) 2743-2750.

[18] J.J.H. Pijpers, R. Ulbricht, K.J. Tielrooij, A. Osherov, Y. Golan, C. Delerue, G. Allan, M. Bonn, Assessment of Carrier-Multiplication Efficiency in Bulk PbSe and PbS, *Nat. Phys.* 5 (2009) 811-814.

[19] J.A. McGuire, M. Sykora, J. Joo, J.M. Pietryga, V.I. Klimov, Apparent Versus True Carrier Multiplication Yields in Semiconductor Nanocrystals, *Nano Lett.* 10 (2010) 2049-2057.

[20] M.C. Beard, A.G. Midgett, M.C. Hanna, J.M. Luther, B.K. Hughes, A.J. Nozik, Comparing Multiple Exciton Generation in Quantum Dots to Impact Ionization in Bulk Semiconductors: Implications for Enhancement of Solar Energy Conversion, *Nano Lett.* 10 (2010) 3019-3027.

[21] A.O. El-Ballouli, E. Alarousu, A. Usman, J. Pan, O.M. Bakr, O.F. Mohammed, Real-Time Observation of Ultrafast Intraband Relaxation and Exciton Multiplication in PbS Quantum Dots, *ACS Photonics* 1 (2014) 285-292.

[22] W.A. Tisdale, K.J. Williams, B.A. Timp, D.J. Norris, E.S. Aydil, X.-Y. Zhu, Hot-Electron Transfer from Semiconductor Nanocrystals, *Science* 328 (2010) 1543-1547.

[23] H.J. Lee, P. Chen, S.-J. Moon, F. Sauvage, K. Sivula, T. Bessho, D.R. Gamelin, P. Comte, S.M. Zakeeruddin, S.I. Seok, M. Grätzel, M.K. Nazeeruddin, Regenerative PbS and CdS Quantum Dot Sensitized Solar Cells with a Cobalt Complex as Hole Mediator, *Langmuir* 25 (2009) 7602-7608.

[24] O.E. Semonin, J.M. Luther, M.C. Beard, Quantum Dots for Next-Generation Photovoltaics, *Mater. Today* 15 (2012) 508-515.

[25] C. Wang, K.-W. Kwon, M.L. Odlyzko, B.H. Lee, M. Shim, PbSe Nanocrystal/TiO_x Heterostructured Films: A Simple Route to Nanoscale Heterointerfaces and Photocatalysis, *J. Phys. Chem. C* 111 (2007) 11734-11741.

[26] T. Bora, K.K. Lakshman, S. Sarkar, A. Makhal, S. Sardar, S.K. Pal, J. Dutta, Modulation of Defect-Mediated Energy Transfer from ZnO Nanoparticles for the Photocatalytic Degradation of Bilirubin, *Beilstein J. Nanotechnol.* 4 (2013) 714-725.

[27] D. Deng, J. Xia, J. Cao, L. Qu, J. Tian, Z. Qian, Y. Gu, Z. Gu, Forming Highly Fluorescent Near-Infrared Emitting PbS Quantum Dots in Water Using Glutathione as Surface-Modifying Molecule, *J. Colloid Interface Sci.* 367 (2012) 234-240.

[28] S. Sardar, P. Kar, S. Sarkar, P. Lemmens, S.K. Pal, Interfacial Carrier Dynamics in PbS-ZnO Light Harvesting Assemblies and Their Potential Implication in Photovoltaic/ Photocatalysis Application, *Sol. Energ. Mat. Sol. Cells* 134 (2015) 400-406.

[29] S. Sarkar, A. Makhal, T. Bora, S. Baruah, J. Dutta, S.K. Pal, Photoselective Excited State Dynamics in ZnO-Au Nanocomposites and Their Implications in Photocatalysis and Dye-Sensitized Solar Cells, *Phys. Chem. Chem. Phys.* 13 (2011) 12488-12496.

[30] M. Flores-Acosta, M. Sotelo-Lerma, H. Arizpe-Chávez, F.F. Castillón-Barraza, R. Ramírez-Bon, Excitonic Absorption of Spherical PbS Nanoparticles in Zeolite A, *Solid State Commun.* 128 (2003) 407-411.

[31] A. van Dijken, E.A. Meulenkamp, D. Vanmaekelbergh, A. Meijerink, The Kinetics of the Radiative and Nonradiative Processes in Nanocrystalline ZnO Particles Upon Photoexcitation, *J. Phys. Chem. B* 104 (2000) 1715-1723.

[32] K. Vanheusden, W.L. Warren, C.H. Seager, D.R. Tallant, J.A. Voigt, B.E. Gnade, Mechanisms behind Green Photoluminescence in ZnO Phosphor Powders, *J. Appl. Phys.* 79 (1996) 7983-7990.

[33] A. Makhal, S. Sarkar, T. Bora, S. Baruah, J. Dutta, A.K. Raychaudhuri, S.K. Pal, Dynamics of Light Harvesting in ZnO Nanoparticles, *Nanotechnology* 21 (2010) 265703.

[34] S. Sarkar, S. Sardar, A. Makhal, J. Dutta, S. Pal, Engineering FRET-Based Solar Cells: Manipulation of Energy and Electron Transfer Processes in a Light Harvesting Assembly, in: X. Wang, Z.M. Wang (Eds.) High-Efficiency Solar Cells, Springer International Publishing 2014, 267-318.

[35] S.S. Narayanan, S.S. Sinha, S.K. Pal, Sensitized Emission from a Chemotherapeutic Drug Conjugated to CdSe/ZnS QDs, *J. Phys. Chem. C* 112 (2008) 12716-12720.

[36] R. Plass, S. Pelet, J. Krueger, M. Grätzel, U. Bach, Quantum Dot Sensitization of Organic−Inorganic Hybrid Solar Cells, *J. Phys. Chem. B* 106 (2002) 7578-7580.

[37] C. Burda, S. Link, M. Mohamed, M. El-Sayed, The Relaxation Pathways of CdSe Nanoparticles Monitored with Femtosecond Time-Resolution from the Visible to the IR: Assignment of the Transient Features by Carrier Quenching, *J. Phys. Chem. B* 105 (2001) 12286-12292.

[38] S.M. Willis, C. Cheng, H.E. Assender, A.A.R. Watt, The Transitional Heterojunction Behavior of PbS/ZnO Colloidal Quantum Dot Solar Cells, *Nano Letters* 12 (2012) 1522-1526.

[39] Y. Liang, T. Novet, J.E. Thorne, B.A. Parkinson, Photosensitization of ZnO Single Crystal Electrodes with PbS Quantum Dots, *Phys. Status Solidi. A* 211 (2014) 1954-1959.

[40] M. Eita, A. Usman, A.O. El-Ballouli, E. Alarousu, O.M. Bakr, O.F. Mohammed, A Layer-by-Layer ZnO Nanoparticle–PbS Quantum Dot Self-Assembly Platform for Ultrafast Interfacial Electron Injection, *Small* 11 (2014) 112-118.

[41] I. Robel, V. Subramanian, M. Kuno, P.V. Kamat, Quantum Dot Solar Cells. Harvesting Light Energy with CdSe Nanocrystals Molecularly Linked to Mesoscopic TiO_2 Films, *J. Am. Chem. Soc.* 128 (2006) 2385-2393.

Chapter 6

Ultrafast Carrier Dynamics in Inorganic-Organic Nanohybrid for Enhanced Solar Light Harvesting

6.1. Introduction: The development of novel functional materials to harvest and convert solar energy has been recognized as an important step to sustainable energy resources and to meet the rising energy demand [1-3]. In addition, demanding environmental pollution issues prompt for finding potential solutions via solar energy routes to clean up water and environmental pollutions. The key to the success of solar energy conversion is the development of high performance materials having a well matched photo absorption with the solar spectrum, an efficient photoexcited charge separation to prevent electron–hole recombination and an adequate energy of charges that carry out the desired chemical reactions (for example, photocatalysis) [4-7]. Although, oxide-based semiconductors, for example TiO_2, serve as the benchmark photo responsive materials, they are limited with respect to performance, e.g. in the absorption of ultraviolet light due to their wide band gap and their low-efficiency in charge separation [8-9]. The rapid recombination of photoexcited electron-hole pairs has been recognized as a key factor behind the observed small photon conversion efficiency [3, 10-11]. Therefore, a tremendous effort has been made to sensitize oxide based semiconductors in the visible spectral range *via* doping or surface-tuning [12-13]. Plasmonic photocatalysts have appeared as a very promising route to enhance solar light harvesting of TiO_2 [14-17]. Nevertheless, the high cost and low environmental stability of noble metal doped photocatalysts (i.e., Ag, Au) significantly limit their large-scale application. In fact, no single material can meet all stringent requirements as ideal solar energy converters. However, coupling of two materials as a semiconductor heterojunction has been demonstrated as an

effective strategy allowing both a broader range of solar light absorption as well as a significant promotion of photo generated charge separation, thereby considerably improving their solar light harvesting efficiency [18-22]. Along this way, we have studied ultrafast photoinduced charge separation and charge recombination processes at the semiconductor-semiconductor (PbS-ZnO) interface for efficient solar light harvesting [23].

Interestingly, the amalgamation of semiconductor nanocrystals and polymers is opening an efficient pathway for the development of multifunctional materials that demonstrate superior electrical, optical and mechanical properties [24-29]. Hence, incorporating semiconductor nanocrystals into conjugated polymers can complement the spectral absorption range of the polymers as well as allow to sensitize the semiconductor nanocrystals for renewable energy applications such as bulk heterojunction–type photovoltaics and photocatalysis [22, 30-34]. A series of semiconductor nanocrystals and bulk conjugated polymer based heterojunctions such as TiO_2-PANI, TiO_2-P3HT have been studied for the harvesting of visible light [35-37]. The integration of another potential semiconductor nanocrystal, ZnO to the conjugated polymer has shown an improved efficiency under solar light [38-39]. ZnO nanoparticles (NPs) are believed to be nontoxic and biocompatible and have been used in many applications in our daily life, such as drug carriers and cosmetics etc [40]. Although semiconductor and conducting polymer heterojunctions demonstrate certain visible-light activity, the reported photo-conversion efficiency is small [39]. Furthermore, as the interfacial area is critical in achieving the favorable charge separation, it is essential to involve nanoscale units in creating the heterojunctions. Thereby a large interface area and reduced charge transport length towards the heterojunction may be achieved. Hence, designing heterostructures with the appropriate morphological orientation and band position of the semiconductor and the polymer unit is challenging. Conjugated polymer nanostructures are

emerging materials for energy conversion and storage applications owing to their advantages of low cost facile synthesis, exceptional electrochemical activity and high carrier mobility [41-42]. The use of polymerizable organic moieties as sensitizers with a wide band gap semiconducting material has added the advantage of harvesting lower energy photons through the extension of conjugation to the polymeric form of the moiety. In this regard, we have recently reported the first experimental evidence of visible light responsive photocatalytic activity of conjugated polymer polydiphenylbutadiyne (PDPB) nanofibers for water depollution [43]. Moreover, we have shown that the polymer nanostructure is essential for the photoresponse in the visible spectral range [44].

In this chapter, we employ conjugated poly(diacetylene) based PDPB nanofibers with ZnO NPs for the formation of a unique nanoheterojunction to explore the effective charge separation from polymer to semiconductor nanocrystals. Notably, charge transfer or separation at the interface is a crucial aspect which determines the efficiency of light harvesting across the heterojunctions and consequently surface reactions. Nevertheless there is a common consensus that heterojunctions facilitate the migration of photoexcited electrons and holes across the interfaces in order to reduce charge recombination or enhance charge separation. However, very few direct experimental evidences or spectroscopic observations have been explored to establish the photoinduced charge transfer mechanism at the heterostructure interface [44-45]. Thus, investigations of the role of crystal defects, trapping sites and exciton-relaxation on the interfacial processes through spectroscopic studies towards the rational design of light harvesting nanoheterojunction (LHNH) are essential. By virtue of having intrinsic photoluminescence (PL) of ZnO from defect state emission as well as conducting polymer from different oligomeric and polymeric chains, ultrafast spectroscopic studies have been employed to investigate the interfacial charge/energy transfer dynamics. Furthermore, to ensure efficient charge

separation, as well as to address how nanoheterojunctions between PDPB and ZnO are beneficial for solar light harvesting, degradation of methyl orange as a model pollutant in water has been evaluated under visible light irradiation.

6.2. Results and Discussion:

6.2.1. Enhanced Charge Separation and FRET at Heterojunctions between Semiconductor Nanoparticles and Conducting Polymer Nanofibers for Efficient Solar Light Harvesting [46]: For the fabrication of nanoheterojunctions, the first step is to synthesize conjugated polymer nanostructures. We have developed a soft template mediated controlled synthesis of PDPB nanofibers in hexagonal mesophases by UV irradiation [42, 45]. The hydrophobic domain of the mesophases can accommodate high concentrations of 1, 4-diphenylbutadiyne (DPB) monomers, which can directly polymerize by photoirradiation in the presence of a free-radical initiator (benzoin methyl ether) [47]. The DPB monomers undergo polymerization *via* 1, 4-addition reaction to form alternating ene-yne polymer chains upon irradiation with UV light. The PDPB-ZnO LHNH was synthesized using ligand-free direct adsorption as well as *in situ* generation of ZnO NPs on polymer nanofibers by the coprecipitation method. A series of characterization techniques such as scanning electron microscope (SEM), transmission electron microscope (TEM), Fourier transform infrared spectroscopy (FTIR) and X-ray diffraction (XRD), UV–visible spectroscopy have been used to establish the formation of nanoheterojunctions. Figure 6.1 (a-b) illustrates the SEM images of PDPB nanofibers and PDPB-ZnO LHNH, respectively. The polymer nanofibers have high-density with average diameter of 22 nm and few micron lengths. For PDPB-ZnO, Figure 6.1b clearly shows the bright spots with the incorporation of 20 nm ZnO NPs, which cover the walls of PDPB nanofibers. Figure 6.1c illustrates a transmission electron microscopy image of PDPB nanofibers of uniform diameter of ~19 nm and a few micrometers long which are

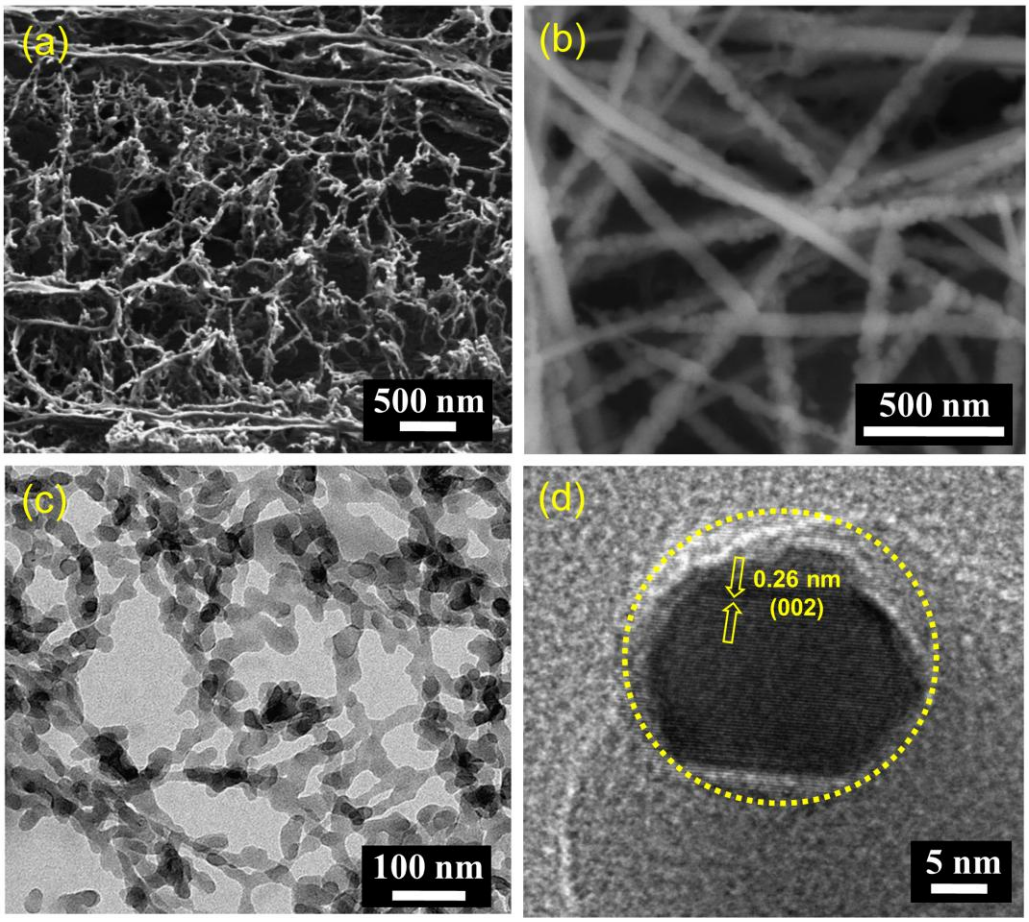

Figure 6.1. *Microscopic images of PDPB nanofibers and PDPB-ZnO light harvesting nanoheterojunction (LHNH). SEM images of (a) PDPB nanofibers and (b) PDPB-ZnO LHNH.TEM images of (c) PDPB nanofibers and (d) PDPB-ZnO LHNH.*

consistent with the SEM images. Notably, this one-dimensional structure reflects the geometry of the hydrophobic domains of the hexagonal mesophases. These polymer nanofibers are formed by л-stacking of PDPB oligomers [43]. A typical high-resolution TEM (HRTEM) image for PDPB-ZnO is shown in Figure 6.1d which demonstrates the presence of PDPB and crystalline ZnO NPs (~20 nm) in which nanocrystals are embedded in the PDPB nanofibers. The ZnO NPs possess a good degree of cystallinity as discernible from the lattice fringes in HRTEM and the interplanar distances of ~0.26 nm corresponding to the spacing between two (002) planes of ZnO [48]. Furthermore, the crystallinity of ZnO NPs within the nanoheterojunction is corroborated by XRD. Figure 6.2a illustrates XRD patterns of pure PDPB nanofibers, PDPB-ZnO and ZnO NPs. A comparably small

crystallinity is observed in the XRD pattern of PDPB nanofibers with a broad peak that may arise due to diffraction from polymeric chains. On the other hand, well-defined sharp peaks are observed at 2θ = 31.76°, 34.4°, 36.2°, 47.5°, 56.6°, 62.8°, 66.4°, 67.9°, and 69° which can be indexed as the (100), (002), (101), (102), (110), (103), (200), (112) and (201) diffraction planes of wurtzite structure (JCPDS card number: 36-1451), respectively, confirming the phase and crystallinity of ZnO NPs within the PDPB-ZnO LHNH. However, the broad peak originated from the PDPB nanofibers is not identified within the LHNH due to very low loading of polymer.

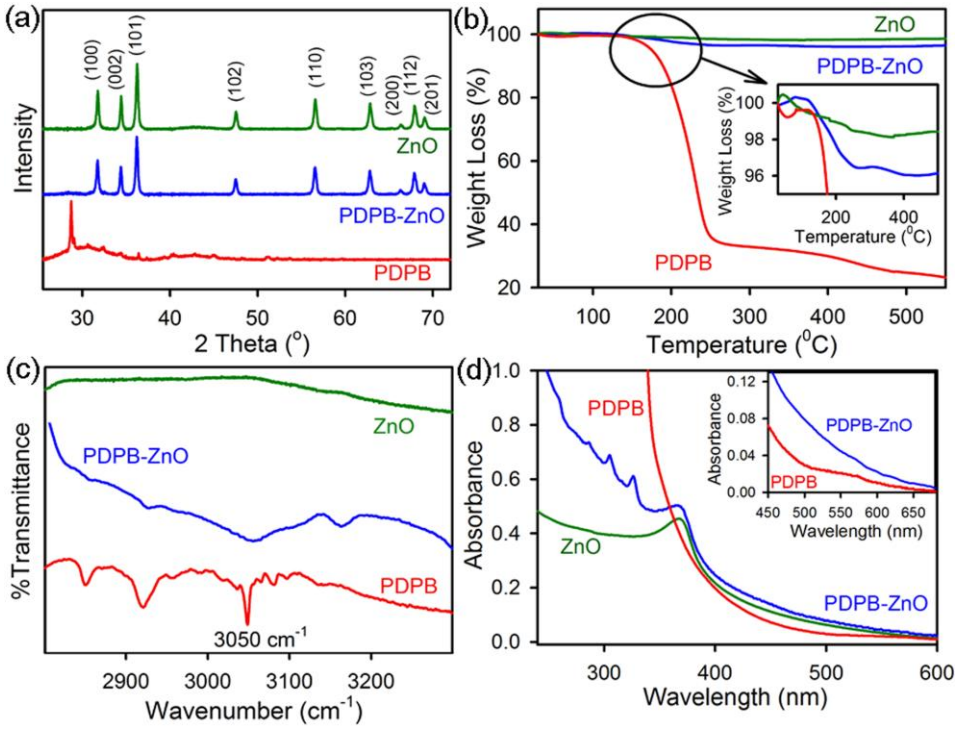

Figure 6.2. *Characterization of PDPB nanofibers and PDPB-ZnO light harvesting nanoheterojunction. (a) X-ray diffraction patterns (b) thermogravimetric analysis profile (c) FTIR spectra and (d) UV-Vis absorption spectra of ZnO (green), PDPB-ZnO (blue) and PDPB (red).*

The loading of polymer as well as the thermal stability of the PDPB-ZnO has been studied by thermogravimetric analysis (TGA). Figure 6.2b shows the thermogravimetric curves of each material. The TGA graph of PDPB nanofibers showed onset of decomposition at about 185°C until a major decomposition happens around ~250°C may be attributed to large-scale thermal degradation of polymeric chains. In contrast to polymer, pure ZnO NPs are very stable in air and

almost no decomposition takes place in the range of 30–600°C. The thermal decomposition of PDPB nanofibers in PDPB-ZnO LHNH is about 175°C, which is slightly lower than that of pure PDPB (185°C) may be associated with the interaction of inter-chains in PDPB macromolecule with ZnO NPs. The PDPB-ZnO LHNH exhibits a PDPB mass of as low as 4% determined from TGA curves (inset of Figure 6.2b). As the carbon based polymers having high surface area with nanofibers morphology, it is expected to accommodate large number of high density ZnO NPs on the polymer surface as shown in Figure 6.1b. Thus the weight percentage of polymer is lower compared to that of ZnO in the LHNH. This observation confirms the superlative formation of hybrid nanoheterojunction retaining the characteristic properties of each element. Additionally, chemical interaction between PDPB and ZnO has been monitored by Fourier transform infrared spectroscopy (FTIR) as shown in Figure 6.2c. The characteristic peaks of pure PDPB at 3050 cm^{-1} corresponds to the C–H vibration involving hydrogen atoms in the para and meta positions. Pure ZnO did not show any characteristic peak in this spectral region. In contrast to the pure PDPB, the absorption peaks corresponding to C–H vibration get shifted to the high wave number and also become wider in PDPB-ZnO. This observation confirms that the ZnO NPs are well incorporated into the PDPB nanofibers.

UV–Visible absorption spectra of pure PDPB, PDPB-ZnO and ZnO nanostructures are presented in Figure 6.2d. The PDPB nanofibers show a broad absorption in the visible range. The bare ZnO NPs demonstrate an absorption peak at 365 nm, corresponding to the band-gap excitation (E_g =3.37 eV). The PDPB-ZnO spectrum has the characteristics of both PDPB and ZnO, and it exhibits enhanced absorption intensity in the visible range. This suggest that PDPB-ZnO can efficiently absorb visible light which is attributed to the PDPB absorption (see inset of Figure 6.2d) and indicates that these heterojunctions could be useful in harvesting energy for optoelectronic applications.

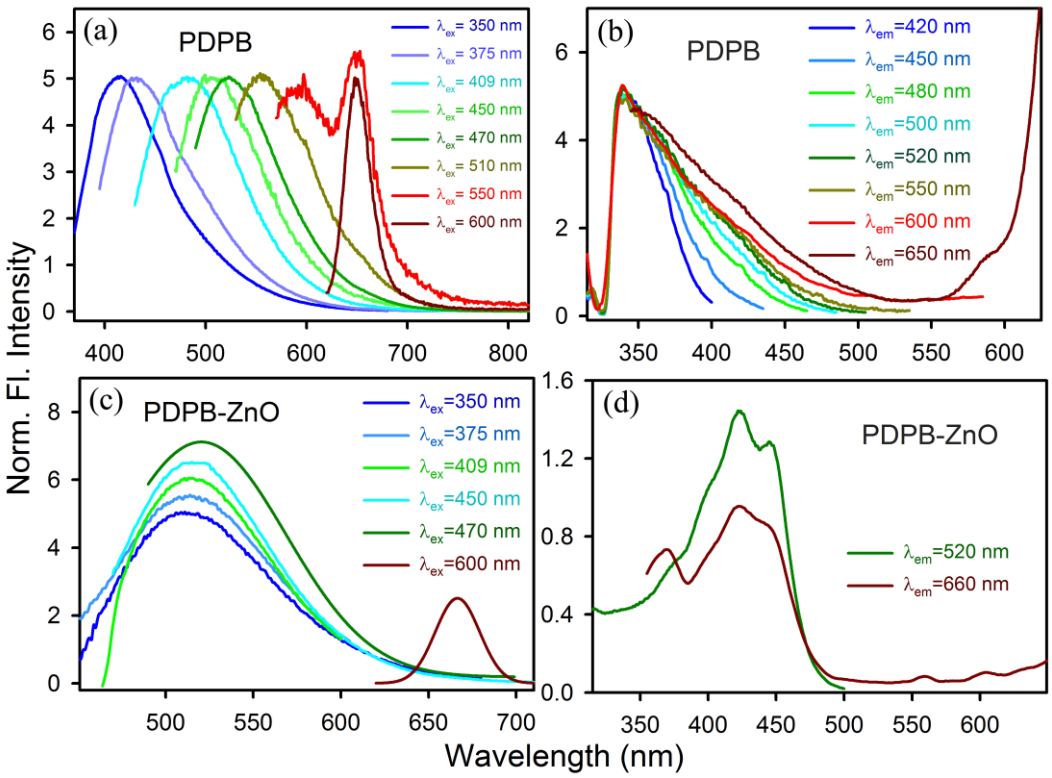

Figure 6.3. *Steady state emission and excitation of PDPB nanofibers and PDPB-ZnO light harvesting nanoheterojunction. Room temperature PL spectra of (a) PDPB (c) PDPB-ZnO at different excitation wavelengths. The excitation spectra of (b) PDPB (d) PDPB-ZnO monitored at different emission maxima are shown. All spectra were recorded in ethanol.*

In order to investigate the interfacial charge separation at the PDPB-ZnO nanoheterojunction which is the key step for efficient light harvesting, the photoinduced carrier dynamics is monitored by steady state and picosecond resolved fluorescence studies. Room temperature PL spectra of PDPB exhibit a strong dependency on the excitation wavelength as shown in Figure 6.3a. The emission peak is red shifted from 410 nm to 650 nm at different excitation wavelengths from 350 nm to 600 nm. This suggests the presence of multiple emitting states in the polymer nanofibers which are associated with the wide extend of conjugation in the different segments having various oligomeric and polymeric chains. This kind of phenomenon is well documented in the field of conjugated oligomers and polymers [49]. From the cyclic voltammetry measurement, we have estimated the bandgap to be 1.81 eV which is remarkably narrow for a polymer [43]. Additionally, these results are consistent with the

calculated value of the PDPB band gap, which is 1.95 eV, on the basis of density functional theory. The energy gaps (E_g) for PDPB oligomers and polymeric chains having numbers from 1 to 8, decrease as the length of the polymer chains increases (E_g = 3.99 eV for monomer whereas E_g = 1.96 eV for octamer) facilitating the greater charge delocalization. Thus the multiple photoluminescence of PDPB can be attributed to the various oligomers present in the system. It has to be noted that the emission at 650 nm for the excitation wavelengths above 510 nm is originated from the conjugated polymer chain which acts as molecular wire. The multiple photoluminescence are further investigated from the excitation spectra as shown in Figure 6.3b. The excitation spectra of PDPB at different detection wavelengths reveal a maximum at 340 nm which is consistent with the absorption spectra of PDPB as shown in Figure 6.2d. As the detection wavelength shifts from 420 nm to 600 nm, the tail of the excitation spectra extends to the visible region due to the extended conjugation in PDPB nanofibers. Moreover, the excitation spectra monitored at a wavelength of 650 nm shows a peak around 590 nm which can be attributed to the long conjugated polymeric chain. In contrast, the emission spectrum of the PDPB-ZnO LHNH is independent on the excitation wavelength from 350 nm to 470 nm due to oligomeric units of the polymer, as shown in Figure 6.3c. However, the emission spectrum of LHNH illustrates peak at 665 nm upon excitation at 600 nm, attributed to polymer chains. This observation clearly indicates the strong electronic interaction between semiconducting PDPB nanofibers and ZnO NPs. Due to the formation of nanoheterojunction with a large interfacial area the mobility of the excitons towards the interface is facilitated [44]. Consequently, the excited electrons from the polymer nanostructures instantly transfer to the ZnO NPs and eventually deexcite through defect centers located at the near surface that arise from oxygen vacancies [50]. The excitation spectrum of PDPB-ZnO as shown in Figure 6.3d at the detection wavelength 520 nm reveals two distinct peaks at 420 nm and 445 nm which are consistent with the band gap absorption of the oligomers.

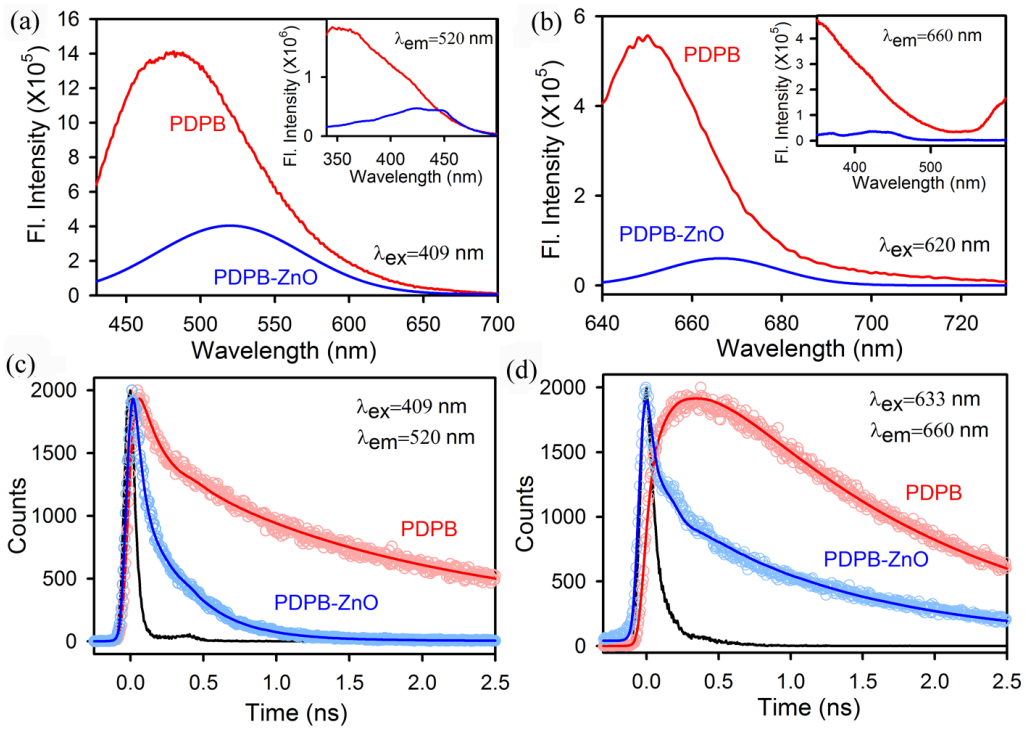

Figure 6.4. *Steady state and time resolve spectroscopy of PDPB nanofibers and PDPB-ZnO light harvesting nanoheterojunction. PL spectra of PDPB, PDPB-ZnO at excitation wavelengths (a) 409 nm and (b) 633 nm. The inset shows excitation spectra monitored at 520 nm and 660 nm, respectively. Fluorescence decay profiles of PDPB and PDPB-ZnO at (b) 520 nm (excitation at 409 nm) (d) 660 nm (excitation at 633 nm).*

The room temperature PL spectra of PDPB nanofibers show an emission peak at 485 nm upon the excitation at 409 nm, as shown in Figure 6.4a. The intensity of the emission peak decreases considerably and is red shifted to 520 nm when the polymers are attached to the ZnO NPs. The shift is due to the strong electronic interaction and energy level alignment at the nanoheterojunction. The inset of Figure 6.4a shows the corresponding excitation spectra. The picosecond resolved fluorescence decays (Figure 6.4c) of PDPB and PDPB-ZnO LHNH were measured upon excitation with 409 nm laser, and monitored at a wavelength of 520 nm. In case of PDPB-ZnO LHNH, the decay curve of PDPB shows significant shorter lifetime of 30 ps (74%) as compared to that of PDPB; 140 ps (45%) (Table 6.1). The observed decrease in lifetime can be correlated to the electron transfer process from PDPB oligomers to the ZnO NPs. The charge separation from polymeric chain of PDPB to ZnO NPs is also monitored from steady state and time

resolved spectroscopy, as shown in Figure 6.4b and 6.4d, respectively. The steady state emission peak decreases and is red shifted to 665 nm for PDPB-ZnO LHNH upon excitation at 620 nm. The inset of Figure 6.4b shows the corresponding excitation spectra. As shown in Figure 6.4d, the fluorescence decay curve for PDPB upon excitation at 633 nm shows an intrinsic buildup with a rise component of 290 ps (monitored at 660 nm) due to delocalization of electron in conjugated polymeric chain. The emission decay curve of PDPB is fitted with a rise followed by single exponential decay function with a lifetime of 1.58 ns. However, the decay curve of PDPB-ZnO LHNH deviates from single exponential to biexponential showing one significant shorter lifetime 30 ps (87%) and a longer lifetime of 1.24 ns (13%). Hence, the efficient photoinduced charge separation takes place at the nanoheterojunction where electrons are transferred from the conjugated polymer nanofibers to the ZnO NPs and holes remain in the polymers.

Table 6.1. *Dynamics of picosecond-resolved luminescence transients of PDPB and PDPB-ZnO LHNH*[a]

Sample	Excitation wavelength (nm)	Detection wavelength (nm)	τ_1 (ns)	τ_2 (ns)	τ_3 (ns)
PDPB	409	520	0.14 (45.4%)	1.40 (34.8%)	4.85 (19.8%)
PDPB-ZnO	409	520	0.03 (74.2%)	0.30 (23.8%)	2.21 (2.0%)
PDPB	633	650	0.29 (-21%)	1.58 (121%)	
PDPB-ZnO	633	650	0.03 (86.7%)	1.24 (13.3%)	

[a]*Numbers in the parenthesis indicate relative weightages.*

After studying the interfacial dynamics at the nanoheterojunction using ZnO NPs with approximate size ~20 nm which does not have intrinsic defect state emission, ZnO NPs (~5 nm) were synthesized in situ on PDPB nanofibers to investigate the role of defect states in the photoinduced charge transfer processes. Interestingly, during *in situ* synthesis of ZnO NPs on PDPB nanofibers, the average grain size of the ZnO is 5 nm which is similar to the size of ZnO NPs if formed alone.

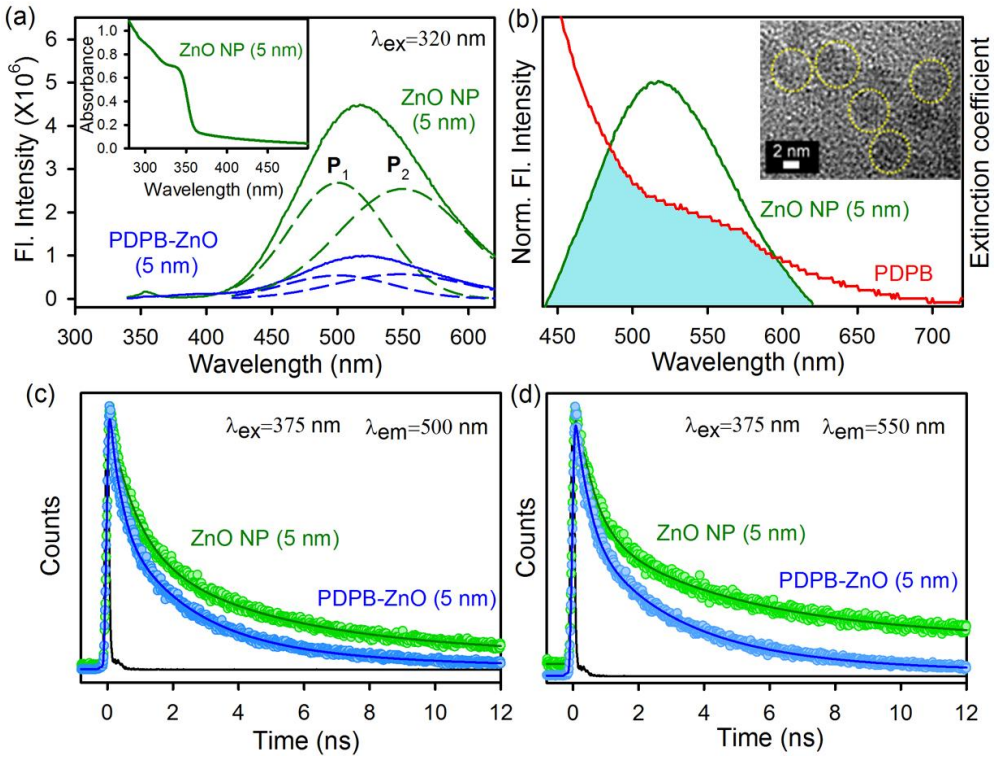

Figure 6.5. *FRET study between PDPB nanofibers and ZnO nanoparticles (5 nm). (a) Room temperature PL spectra of ZnO NPs (green) and PDPB-ZnO LHNH (blue) are shown. The excitation wavelength was at 320 nm. The broad emission band is composed of two components, P_1 (500 nm) and P_2 (555 nm). Inset shows the absorption spectrum of ZnO NPs (~5 nm). (b) Shows the overlap of the ZnO NP emission and PDPB absorption. Inset shows the HRTEM image of in situ synthesized ZnO NPs (~5 nm) on PDPB nanofibers. The picosecond-resolved fluorescence transients of ZnO NPs (excitation at 375 nm) in the absence (green) and in the presence of PDPB (blue) collected at (c) 500 nm and (d) 555 nm are shown.*

The ZnO NP (~5 nm) has an intrinsic defect state emission as shown in Figure 6.5a. Inset of Figure 6.5a illustrated the absorption spectrum of the corresponding ZnO NPs. The room temperature PL spectrum of ZnO NP is composed of two emission bands upon excitation above the band-edge (λ_{ex} = 320 nm). The narrow band at 360 nm in the emission spectra is due to the band gap emission. The broad emission band in the blue green region is associated with surface defect centers which is comprised of two bands: one arises from the doubly charged vacancy center (V_0^{++}) located at 550 nm (P_2) and the other one arises from the singly charged vacancy center (V_0^{+}) located at 500 nm (P_1) [50-52]. The emission intensity decreases when ZnO NPs are attached to the PDPB nanofibers (inset Figure 6.5b showed TEM image of PDPB-ZnO, 5 nm) which can

be attributed to photoinduced non-radiative processes from ZnO NPs to the PDPB nanofibers. There is significant spectral overlap between ZnO NP emission and PDPB absorption as shown in Figure 6.5b which leads to a probable energy transfer. Therefore, we propose Förster resonance energy transfer (FRET) from the donor ZnO NPs to the acceptor PDPB nanofibers [51]. The picosecond resolved fluorescence decay profile of the donor ZnO NPs in the presence and absence of the acceptor PDPB were obtained upon excitation with a 375 nm laser and monitored at 500 nm (P_1) and 550 nm (P_2) (Figure 6.5c and 6.5d, respectively). A shorter excited state lifetime of the ZnO NPs is clearly observed in the presence of PDPB. Details of the spectroscopic fitting parameters of the fluorescence transients are tabulated in Table 6.2. From FRET calculations, the distance between the donor ZnO NPs and acceptor PDPB nanofibers are determined to be 3.4 nm and 3.1 nm for P_1 and P_2 states, respectively. The FRET distance is consistent with the size of the ZnO NPs (radius = 2.5 nm). The energy transfer efficiency is calculated to be 64% and 70% from P_1 and P_2 states, respectively. This observation confirms the proximity between the PDPB and ZnO as well as UV light harvesting in the LHNH via energy transfer from ZnO to PDPB nanofibers.

Table 6.2. *Dynamics of picosecond-resolved luminescence transients of PDPB and PDPB-ZnO LHNH*[b]

Sample	Excitation wavelength (nm)	Detection wavelength (nm)	τ_1 (ns)	τ_2 (ns)	τ_3 (ns)	τ_{avg} (ns)
ZnO NP (5 nm)	375	500	0.82 (51.8%)	4.22 (40.7%)	29.30 (7.5%)	4.34
PDPB-ZnO	375	500	0.27 (53.3%)	2.15 (39.5%)	7.8 (7.2%)	1.55
ZnO NP (5 nm)	375	550	0.52 (51.3%)	4.01 (35.0%)	35.12 (13.7%)	6.48
PDPB-ZnO	375	550	0.34 (53.2%)	2.63 (39.8%)	9.89 (7%)	1.91

[b]*Numbers in the parenthesis indicate relative weightages.*

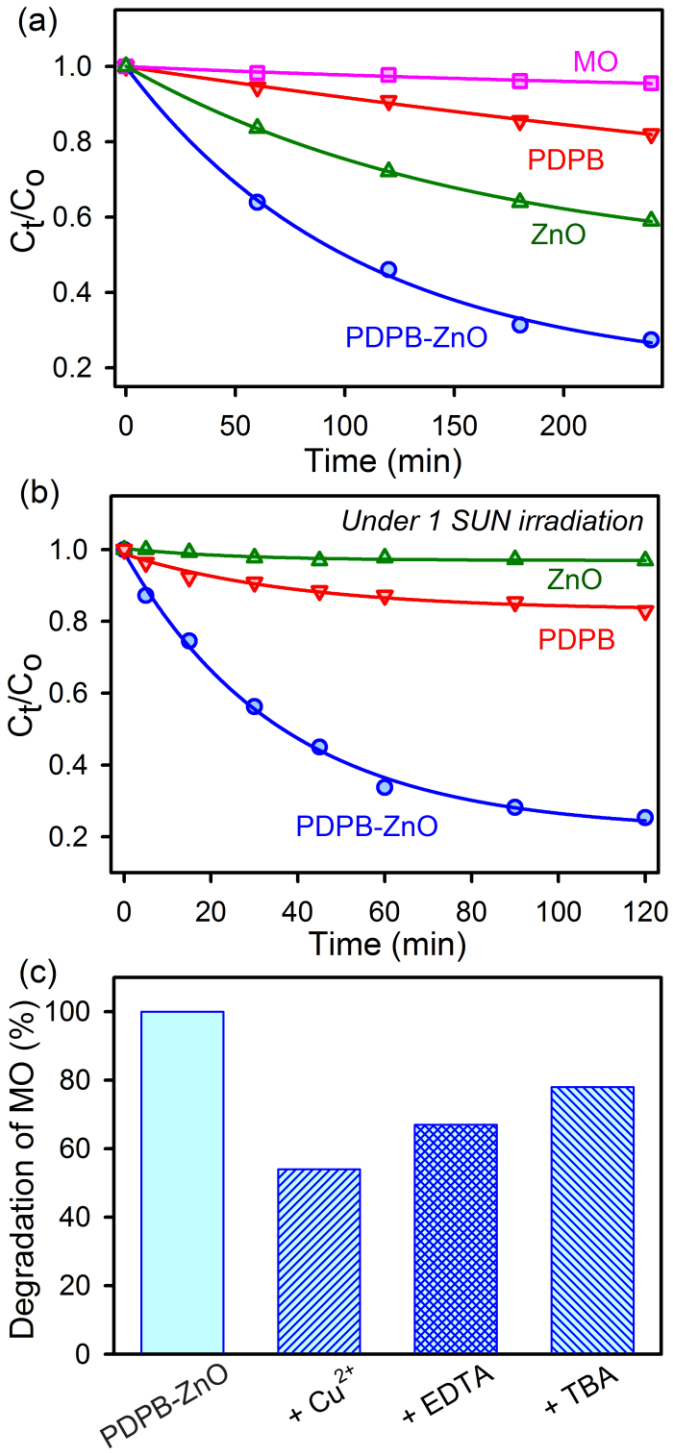

Figure 6.6. *Photocatalytic activity of PDPB nanofibers, ZnO nanoparticles and PDPB-ZnO light harvesting nanoheterojunction. Photocatalytic degradation of MO in the presence of PDPB (red), ZnO (green) and PDPB-ZnO (blue) under (a) UV light (b) Visible light (1 sun) irradiation. (c) Effect of Cu^{2+}, EDTA and TBA on the photocatalytic activity of PDPB-ZnO LHNH. The photodegradation reaction of MO (initial concentration $C_0 = 0.3\times10^{-4}$ M) was carried out in a 10 mm optical path quartz cell reactor containing 3.5 mL of a model solution with a concentration of 1 $g.L^{-1}$ of the PDPB-ZnO, PDPB nanofiber (0.2 $g.L^{-1}$) and ZnO NPs (1 $g.L^{-1}$).*

In order to investigate the manifestation of the interfacial charge transfer dynamics in PDPB-ZnO heterojunction, the photocatalytic activity has been studied using methyl orange (MO) as a model pollutant. Photocatalysis involves charge carrier generation and mobility from oxide based semiconductor nanomaterials and recognized as a green technology for the purification of water. Adsorption tests under dark condition showed that MO does not adsorb on the surface of the PDPB-ZnO LHNH. The photocatalytic activity of the LHNH for degradation of MO under UV-VIS and Visible light was compared with ZnO NPs and PDPB nanofibers as a control experiment (Figure 6.6a and 6.6b). Figure 6.6a demonstrates the efficient photocatalytic activity of PDPB-ZnO LHNH (74%) in comparison to both counter parts (PDPB, 18% and ZnO, 40%) under 240 min UV-VIS light irradiation ($\lambda \geq 365$ nm). Figure 6.6b shows that the PDPB-ZnO LHNH is also very active for photocatalytic degradation of MO under 120 min visible light irradiation. However, ZnO NPs having a wide band gap did not show any visible light activity. The activity of the polymer nanostructures is much lower ~17% in comparison to PDPB-ZnO LHNH (80%) under similar illumination conditions. These observations suggest that due to efficient charge separation at the interface between PDPB and ZnO, the PDPB-ZnO LHNH is suitable for solar light harvesting. This novel photocatalyst exhibits an additional advantage compared to unsupported ZnO or TiO_2 photocatalysts, it does not require any filtration step as it settles down quickly after use in the photocatalytic reactor. The ease of solution based synthesis and good photocatalytic activity of PDPB-ZnO LHNH make them promising nanostructures for environmental applications. During photocatalytic reaction, photoinduced electrons and holes escape recombination and migrate to the semiconductor surface which consequently generates (in the presence of oxygen and water) highly oxidative radicals, that can degrade the organic pollutants. A large number of reactive species including h^+, $^{\bullet}OH$, and $O_2^{\bullet -}$ are involved in the photocatalytic oxidation process [53]. Hence, the effects of free radical scavengers on the degradation of MO were examined to elucidate the

reaction mechanism. To investigate the role of the excess electrons, Cu^{2+} was used as a scavenger (it reacts with electron to yield Cu^{+}) [53]. Tertiary butyl alcohol (TBA) was introduced as the scavenger of $^{\bullet}OH$, and ethylenediaminetetraacetic acid (EDTA) was adopted to quench the holes (h^{+}) [54]. As a consequence of quenching, the photocatalytic oxidation reaction is partly suppressed. The effects of a series of scavengers on the degradation efficiency of MO are shown in Figure 6.6c. The degradation efficiency of PDPB-ZnO photocatalyst for MO is reduced to 44% after adding Cu^{2+}. A similar trend is observed after the addition of EDTA and TBA. The corresponding photodegradation efficiencies decreased to 49% and 55%, respectively. According to the above experimental results, it can be clearly seen that $O_2^{\bullet-}$ and h^{+} are the main reactive species in the photocatalytic oxidation process of MO, whereas $^{\cdot\bullet}OH$ has a minimal effect on this process.

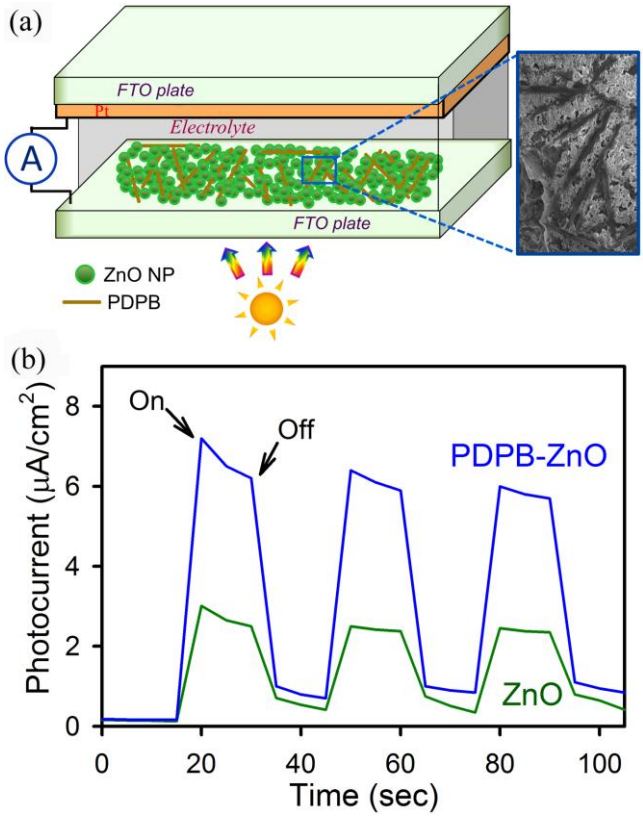

Figure 6.7. *Photocurrent response of ZnO nanoparticles and PDPB-ZnO light harvesting nanoheterojunction. (a) Schematic representation of photocurrent measurement set up using dye-sensitized solar cell geometry. (b) Photocurrent responses of PDPB-ZnO LHNH and ZnO NPs without any bias voltage under 1000 W m^{-2} incident power irradiation from a light source.*

A direct evidence of enhanced charge separation at the nanoheterojunction interface is followed by photocurrent measurements. Photocurrent generation of ZnO and PDPB-ZnO films deposited onto ITO electrodes were studied under white light irradiation (at 1000 W/m^2) in solar cell geometries, as shown in Figure 6.7a. A steady and rapid cathodic photocurrent response is obtained from the LHNH film when the irradiations is switched on and off, see Figure 6.7b. For PDPB-ZnO, the photocurrent response was 7.2 $\mu A/cm^2$, about 2.5 times higher than pure ZnO NPs which reflects higher separation and transfer efficiency of photo excited electrons from conjugated polymer to the conduction band of ZnO due to the formation of the heterostructure. The PDPB is a p-type, organic semiconductor; ZnO is an inorganic, n-type semiconductor and forming a donor-acceptor junction (heterojunction). When the PDPB-ZnO LHNH is illuminated under visible light, electrons are excited from the HOMO to the LUMO of PDPB, leaving holes behind in the HOMO of PDPB. The excited state electrons are readily injected into the conduction band of ZnO as schematically presented in Scheme 6.1a. Consequently, we have observed enhanced photocatalytic activity and photoresponse due to formation of the nanoheterojunction, as shown in Scheme 6.1b. In future, we will consider the optimization of the cell architecture, utilization of other types of semiconductors and conducting polymer nanostructures to obtain a significantly enhanced solar light harvesting.

6.3. Conclusion: In summary, we have successfully demonstrated that a simple adsorption of ZnO NPs on PDPB nanofiber surface leads to the effective sensitization of semiconductor nanocrystals for solar light harvesting. The formation of PDPB-ZnO LHNH has been confirmed by several microscopic and analytical techniques. Appropriate band gap alignment in combination with easy solution-processability, highlights this material as a promising candidate for energy harvesting applications. The interfacial carrier dynamics which is the key for efficient light harvesting has been unraveled by detailed steady state and

ultrafast spectroscopic studies, suggesting the co-sensitization of ZnO NPs by multiple states of polymer nanofibers originated from oligomeric and polymer chain unit. The efficient charge separation at the interface leads to enhanced photocatalytic activity and photoresponse. Our approach provides simple and economic ways to design hybrid nanoheterojunction with several functionalities which are suitable for solar cell, chemical sensors and optoelectronic device applications.

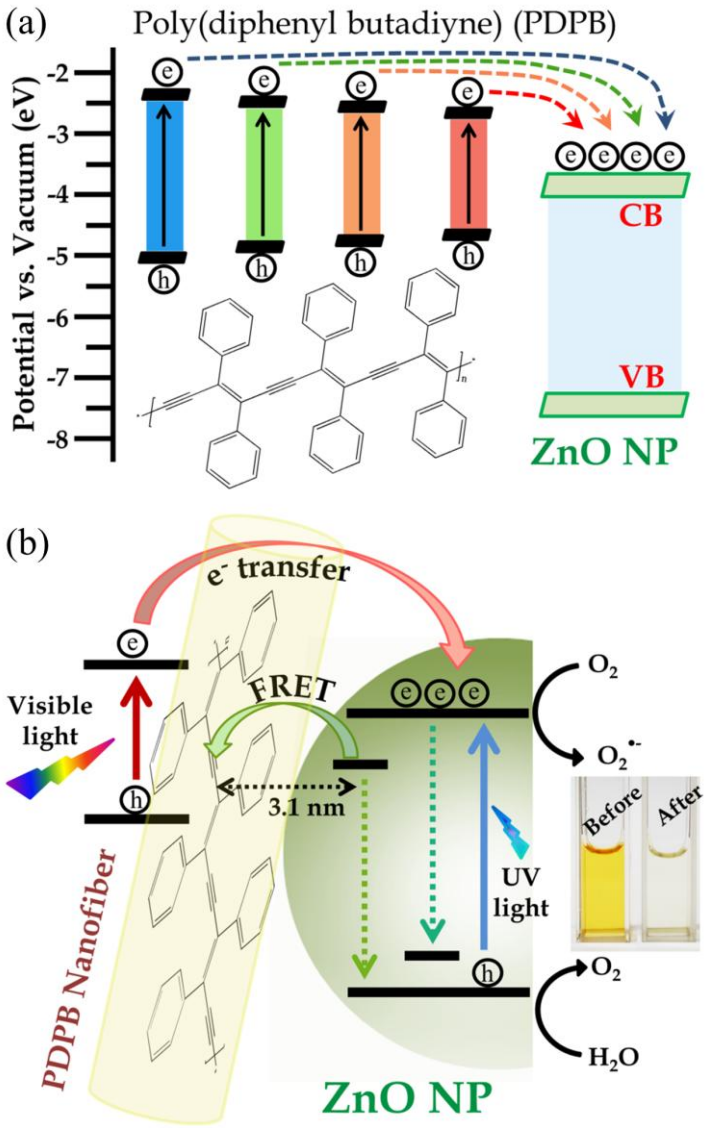

Scheme 6.1. *Schematic presentation of (a) the co-sensitization of different PDPB oligomers to ZnO NPs and molecular structure of PDPB polymer (b) the interfacial carrier dynamics at the heterojunction showing the photocatalytic degradation of MO in aqueous solution.*

References

[1] S. Chu, A. Majumdar, Opportunities and Challenges for a Sustainable Energy Future, *Nature* 488 (2012) 294-303.

[2] J.A. Turner, Sustainable Hydrogen Production, *Science* 305 (2004) 972-974.

[3] X. Chen, C. Li, M. Gratzel, R. Kostecki, S.S. Mao, Nanomaterials for Renewable Energy Production and Storage, *Chem. Soc. Rev.* 41 (2012) 7909-7937.

[4] N. Serpone, A.V. Emeline, Semiconductor Photocatalysis — Past, Present, and Future Outlook, *J. Phys. Chem. Lett.* 3 (2012) 673-677.

[5] Z. Hai, N. El Kolli, D.B. Uribe, P. Beaunier, M. Jose-Yacaman, J. Vigneron, A. Etcheberry, S. Sorgues, C. Colbeau-Justin, J. Chen, H. Remita, Modification of TiO_2 by Bimetallic Au-Cu Nanoparticles for Wastewater Treatment, *J. Mater. Chem. A* 1 (2013) 10829-10835.

[6] E. Kowalska, K. Yoshiiri, Z. Wei, S. Zheng, E. Kastl, H. Remita, B. Ohtani, S. Rau, Hybrid Photocatalysts Composed of Titania Modified with Plasmonic Nanoparticles and Ruthenium Complexes for Decomposition of Organic Compounds, *Appl. Catal., B* 178 (2015) 133-143.

[7] H. Nishi, T. Torimoto, T. Tatsuma, Wavelength- and Efficiency-Tunable Plasmon-Induced Charge Separation by the Use of Au-Ag Alloy Nanoparticles, *Phys. Chem. Chem. Phys.* 17 (2015) 4042-4046.

[8] M.D. Hernandez-Alonso, F. Fresno, S. Suarez, J.M. Coronado, Development of Alternative Photocatalysts to TiO_2: Challenges and Opportunities, *Energy Environ. Sci.* 2 (2009) 1231-1257.

[9] J. Schneider, M. Matsuoka, M. Takeuchi, J. Zhang, Y. Horiuchi, M. Anpo, D.W. Bahnemann, Understanding TiO_2 Photocatalysis: Mechanisms and Materials, *Chem. Rev.* 114 (2014) 9919-9986.

[10] R. Asahi, T. Morikawa, T. Ohwaki, K. Aoki, Y. Taga, Visible-Light Photocatalysis in Nitrogen-Doped Titanium Oxides, *Science* 293 (2001) 269-271.

[11] S.U.M. Khan, M. Al-Shahry, W.B. Ingler, Efficient Photochemical Water Splitting by a Chemically Modified N-TiO_2, *Science* 297 (2002) 2243-2245.

[12] J. Tao, T. Luttrell, M. Batzill, A Two-Dimensional Phase of TiO_2 with a Reduced Bandgap, *Nat. Chem.* 3 (2011) 296-300.

[13] X. Chen, L. Liu, P.Y. Yu, S.S. Mao, Increasing Solar Absorption for Photocatalysis with Black Hydrogenated Titanium Dioxide Nanocrystals, *Science* 331 (2011) 746-750.

[14] S. Linic, P. Christopher, D.B. Ingram, Plasmonic-Metal Nanostructures for Efficient Conversion of Solar to Chemical Energy, *Nat. Mater.* 10 (2011) 911-921.

[15] Y. Lu, H. Yu, S. Chen, X. Quan, H. Zhao, Integrating Plasmonic Nanoparticles with TiO_2 Photonic Crystal for Enhancement of Visible-Light-Driven Photocatalysis, *Environ. Sci. Technol.* 46 (2012) 1724-1730.

[16] L. Liu, S. Ouyang, J. Ye, Gold-Nanorod-Photosensitized Titanium Dioxide with Wide-Range Visible-Light Harvesting Based on Localized Surface Plasmon Resonance, *Angew. Chem. Int. Ed.* 52 (2013) 6689-6693.

[17] J. Scott, W. Irawaty, G. Low, R. Amal, Enhancing the Catalytic Oxidation Capacity of Pt/TiO_2 Using a Light Pre-Treatment Approach, *Appl. Catal., B* 164 (2015) 10-17.

[18] M.T. Mayer, Y. Lin, G. Yuan, D. Wang, Forming Heterojunctions at the Nanoscale for Improved Photoelectrochemical Water Splitting by Semiconductor Materials: Case Studies on Hematite, *Acc. Chem. Res.* 46 (2013) 1558-1566.

[19] J.S. Jang, H.G. Kim, J.S. Lee, Heterojunction Semiconductors: A Strategy to Develop Efficient Photocatalytic Materials for Visible Light Water Splitting, *Catal. Today* 185 (2012) 270-277.

[20] A. Kongkanand, K. Tvrdy, K. Takechi, M. Kuno, P.V. Kamat, Quantum Dot Solar Cells. Tuning Photoresponse through Size and Shape Control of CdSe−TiO_2 Architecture, *J. Am. Chem. Soc.* 130 (2008) 4007-4015.

[21] D.R. Baker, P.V. Kamat, Photosensitization of TiO_2 Nanostructures with CdS Quantum Dots: Particulate Versus Tubular Support Architectures, *Adv. Funct. Mater.* 19 (2009) 805-811.

[22] Y. Wang, Q. Wang, X. Zhan, F. Wang, M. Safdar, J. He, Visible Light Driven Type II Heterostructures and Their Enhanced Photocatalysis Properties: A Review, *Nanoscale* 5 (2013) 8326-8339.

[23] S. Sardar, P. Kar, S. Sarkar, P. Lemmens, S.K. Pal, Interfacial Carrier Dynamics in PbS-ZnO Light Harvesting Assemblies and their Potential Implication in Photovoltaic/ Photocatalysis Application, *Sol. Energ. Mat. Sol. Cells* 134 (2015) 400-406.

[24] A.C. Balazs, T. Emrick, T.P. Russell, Nanoparticle Polymer Composites: Where Two Small Worlds Meet, *Science* 314 (2006) 1107-1110.

[25] S. Ghosh, A.H. Khan, S. Acharya, Fabrication of Highly Stable, Hybrid PbS Nanocomposites in Pamam Dendrimer Matrix for Photodetection, *J. Phys. Chem. C* 116 (2012) 6022-6030.

[26] S. Ghosh, D. Ghosh, P.K. Bag, S.C. Bhattacharya, A. Saha, Aqueous Synthesis of ZnTe/Dendrimer Nanocomposites and their Antimicrobial Activity: Implications in Therapeutics, *Nanoscale* 3 (2011) 1139-1148.

[27] S. Ghosh, S.C. Bhattacharya, A. Saha, Probing of Ascorbic Acid by CdS/Dendrimer Nanocomposites: A Spectroscopic Investigation, *Anal. Bioanal. Chem.* 397 (2010) 1573-1582.

[28] S. Sinha Ray, Polylactide-Based Bionanocomposites: A Promising Class of Hybrid Materials, *Acc. Chem. Res.* 45 (2012) 1710-1720.

[29] L. Di Michele, A. Zaccone, E. Eiser, Analytical Theory of Polymer-Network-Mediated Interaction between Colloidal Particles, *Proc. Natl. Acad. Sci. USA* 109 (2012) 10187-10192.

[30] N. Zhang, S. Liu, Y.-J. Xu, Recent Progress on Metal Core@Semiconductor Shell Nanocomposites as a Promising Type of Photocatalyst, *Nanoscale* 4 (2012) 2227-2238.

[31] Y. Qu, X. Duan, Progress, Challenge and Perspective of Heterogeneous Photocatalysts, *Chem. Soc. Rev.* 42 (2013) 2568-2580.

[32] Q. Li, X. Jin, X. Yang, C. Chen, Z. Chen, Y. Qin, T.-h. Wei, W. Sun, Reducing the Excess Energy Offset in Organic/Inorganic Hybrid Solar Cells: Toward Faster Electron Transfer, *Appl. Catal., B* 162 (2015) 524-531.

[33] X. Jin, W. Sun, Z. Chen, T. Wei, C. Chen, X. He, Y. Yuan, Y. Li, Q. Li, Exciton Generation/Dissociation/Charge-Transfer Enhancement in Inorganic/Organic Hybrid Solar Cells by Robust Single Nanocrystalline LnP_xO_y (Ln = Eu, Y) Doping, *ACS Appl. Mater. Interfaces* 6 (2014) 8771-8781.

[34] G. Xing, N. Mathews, S. Sun, S.S. Lim, Y.M. Lam, M. Grätzel, S. Mhaisalkar, T.C. Sum, Long-Range Balanced Electron- and Hole-Transport Lengths in Organic-Inorganic $CH_3NH_3PbI_3$, *Science* 342 (2013) 344-347.

[35] D. Wang, J. Zhang, Q. Luo, X. Li, Y. Duan, J. An, Characterization and Photocatalytic Activity of Poly(3-Hexylthiophene)-Modified TiO_2 for Degradation of Methyl Orange under Visible Light, *J. Hazard. Mater.* 169 (2009) 546-550.

[36] G. Liao, S. Chen, X. Quan, H. Chen, Y. Zhang, Photonic Crystal Coupled TiO_2/Polymer Hybrid for Efficient Photocatalysis under Visible Light Irradiation, *Environ. Sci. Technol.* 44 (2010) 3481-3485.

[37] Q. Luo, L. Bao, D. Wang, X. Li, J. An, Preparation and Strongly Enhanced Visible Light Photocatalytic Activity of TiO_2 Nanoparticles Modified by Conjugated Derivatives of Polyisoprene, *J. Phys. Chem. C* 116 (2012) 25806-25815.

[38] Z.L. Wang, Nanostructures of Zinc Oxide, *Mater. Today* 7 (2004) 26-33.

[39] Z. Pei, L. Ding, M. Lu, Z. Fan, S. Weng, J. Hu, P. Liu, Synergistic Effect in Polyaniline-Hybrid Defective ZnO with Enhanced Photocatalytic Activity and Stability, *J. Phys. Chem. C* 118 (2014) 9570-9577.

[40] J. Zhou, N.S. Xu, Z.L. Wang, Dissolving Behavior and Stability of ZnO Wires in Biofluids: A Study on Biodegradability and Biocompatibility of ZnO Nanostructures, *Adv. Mater.* 18 (2006) 2432-2435.

[41] Z. Yin, Q. Zheng, Controlled Synthesis and Energy Applications of One-Dimensional Conducting Polymer Nanostructures: An Overview, *Adv. Energy Mater.* 2 (2012) 179-218.

[42] S. Ghosh, H. Remita, L. Ramos, A. Dazzi, A. Deniset-Besseau, P. Beaunier, F. Goubard, P.-H. Aubert, F. Brisset, S. Remita, PEDOT Nanostructures Synthesized in Hexagonal Mesophases, *New J. Chem.* 38 (2014) 1106-1115.

[43] S. Ghosh, N.A. Kouamé, L. Ramos, S. Remita, A. Dazzi, A. Deniset-Besseau, P. Beaunier, F. Goubard, P.-H. Aubert, H. Remita, Conducting Polymer Nanostructures for Photocatalysis under Visible Light, *Nat. Mater.* 14 (2015) 505-511.

[44] R. Liu, Hybrid Organic/Inorganic Nanocomposites for Photovoltaic Cells, *Materials* 7 (2014) 2747-2771.

[45] E. Pena dos Santos, M.S. Tokumoto, G. Surendran, H. Remita, C. Bourgaux, P. Dieudonné, E. Prouzet, L. Ramos, Existence and Stability of New Nanoreactors: Highly Swollen Hexagonal Liquid Crystals, *Langmuir* 21 (2005) 4362-4369.

[46] S. Sardar, P. Kar, H. Remita, B. Liu, P. Lemmens, S. Kumar Pal, S. Ghosh, Enhanced Charge Separation and FRET at Heterojunctions between Semiconductor Nanoparticles and Conducting Polymer Nanofibers for Efficient Solar Light Harvesting, *Sci. Rep.* 5 (2015) 17313.

[47] A. Matsumoto, [13] Control of Stereochemistry of Polymers in Free Radical Polymerization, Handbook of Radical Polymerization, John Wiley & Sons, Inc., 2003.

[48] S. Sarkar, A. Makhal, T. Bora, S. Baruah, J. Dutta, S.K. Pal, Photoselective Excited State Dynamics in ZnO-Au Nanocomposites and Their Implications in Photocatalysis and Dye-Sensitized Solar Cells, *Phys. Chem. Chem. Phys.* 13 (2011) 12488-12496.

[49] J.-L. Brédas, J. Cornil, D. Beljonne, D.A. dos Santos, Z. Shuai, Excited-State Electronic Structure of Conjugated Oligomers and Polymers: A Quantum-Chemical Approach to Optical Phenomena, *Acc. Chem. Res.* 32 (1999) 267-276.

[50] A. van Dijken, E.A. Meulenkamp, D. Vanmaekelbergh, A. Meijerink, The Kinetics of the Radiative and Nonradiative Processes in Nanocrystalline ZnO Particles upon Photoexcitation, *J. Phys. Chem. B* 104 (2000) 1715-1723.

[51] A. Makhal, S. Sarkar, T. Bora, S. Baruah, J. Dutta, A.K. Raychaudhuri, S.K. Pal, Dynamics of Light Harvesting in ZnO Nanoparticles, *Nanotechnology* 21 (2010) 265703.

[52] K. Vanheusden, W.L. Warren, C.H. Seager, D.R. Tallant, J.A. Voigt, B.E. Gnade, Mechanisms Behind Green Photoluminescence in ZnO Phosphor Powders, *J. Appl. Phys.* 79 (1996) 7983-7990.

[53] S. Ghosh, A. Priyam, S. Bhattacharya, A. Saha, Mechanistic Aspects of Quantum Dot Based Probing of Cu (II) Ions: Role of Dendrimer in Sensor Efficiency, *J. Fluoresc.* 19 (2009) 723-731.

[54] S.T. Martin, A.T. Lee, M.R. Hoffmann, Chemical Mechanism of Inorganic Oxidants in the TiO_2/UV Process: Increased Rates of Degradation of Chlorinated Hydrocarbons, *Environ. Sci. Technol.* 29 (1995) 2567-2573.

Chapter 7

Essential Dynamics in Plasmonic Nanostructure for Enhanced Solar Photovoltaic Application

7.1. Introduction: Solar energy is the most promising resource to meet future energy demands due to the depletion of fossil fuels. Among various technologies, dye-sensitized solar cells (DSSC) have attracted widespread attention as a solar energy conversion technology because of abundantly available low cost materials, ease of fabrication and relatively high photon to current conversion efficiency [1-7]. DSSC consist of a nanocrystalline porous semiconductor electrodes-sensitized with light absorbing dye as a photoanode, I^-/I_3^- or Co^{2+}/Co^{3+} redox couples as electrolytes and platinized conducting glass as counter electrode (CE) [1]. Extensive efforts have been made to improve the efficiency of DSSC by engineering all the components. For instance, nanocrystalline TiO_2 films with various morphologies [8-9] and dopants [10-11], synthesizing panchromatic dyes to absorb visible and near-infrared light effectively [12-13], synthesizing alternative redox electrolytes [14-15] and substituting platinized counter electrodes with low cost materials [16-18] have all been explored to enhance the photocurrent and photovoltage, in order to improve the efficiency of DSSC`.

Among all the factors, the photoanode is regarded as sovereign for improving the efficiency. In order to modulate the photoanode, thickness of the nanocrystalline titanium dioxide layer has been extensively studied to improve both the photocurrent and photovoltage [19-20]. Generally lowering the thickness of the active layer reduces the recombination at the interface between electrode and electrolyte which in turn increases the efficiency. However, the dye loading also decreases with decreasing thickness resulting in lower photocurrents. To combat this problem, surface modification of semiconductor nanoparticles (NPs)

with plasmonic metal nanostructures such as gold, silver and copper have been investigated recently [21-27]. Solar cells employing hybrid materials have revolutionized efficient solar energy conversion applications through cost-effective fabrication techniques [28-31]. Hupp et al. reported the enhancement of photocurrent in DSSC by the localized surface plasmon resonance (SPR) of silver NPs which increases the effective absorption cross section of dye molecules [21, 32]. The enhancement of photocurrents in DSSC by using silver doped semiconductor nanostructures are well documented in the literature [33-36]. But significant improvement of the photovoltage by surface modification with silver is reported sparsely in the literature. Recently, Kamat et al.[37] have reported significant photovoltage boosting of DSSC with thiolated gold nanocluster anchored on TiO_2 surface along with squaraine as a sensitizing dye. Gold nanoclusters increase the quasi-Fermi level of TiO_2 close to the conduction band which enhances the open circuit photovoltage. In the present study, we aimed to raise the photovoltage of DSSC by silver modification on TiO_2 surface.

Another aspect in order to realize the cost effective DSSC is the development of alternative counter electrode materials. In DSSC, the most prevailing CE is a platinum (Pt) thin film due to its exceptionally high electrochemical activity [38]. However, the high cost and corrosion of Pt in presence of the iodine electrolyte restricts it from large scale applications and long term use [39-40]. In this regard, carbon based materials such as carbon nanotube, graphene and reduced graphene oxide (RGO) as CE have induced current research interests as a substituent of Pt due to low cost, high charge carrier mobility [41] and reasonable performances [42-43]. However, the energy conversion efficiency is lower in case of graphene CE compared to that of Pt electrodes and also requires large quantities of graphene to achieve an acceptable catalytic activity [42, 44]. Thus hybridization of small amount of Pt with graphene or RGO can meet the requirements of low cost, long term stability as well as high

catalytic activity. Significant efforts have been made to fabricate Pt NPs on reduced graphene oxide film or substrate by using chemical reducing agents [45], photo-reduction [46], pulsed laser ablation method [47], dry plasma reduction [16], thermal decomposition [48-49] and hydrogen plasma [50] etc. However, in most cases, the energy conversion efficiency has not reached the expected level as well as the complex fabrication process limits its large scale application. The modification of both the active and counter electrode can provide both high efficiency and low cost requirements.

In the present chapter, we have modified both the active and counter electrodes to realize an energy efficient device using simple fabrication processes. We have synthesized and characterized small silver NPs embedded on the TiO_2 surface (Ag-TiO_2) as a photoanode material which exhibits significant enhancement in the photovoltage. On the other hand, the CE has been modified with the Pt NPs supported on RGO (Pt@RGO) using a facile photo-reduction method without any reducing or stabilizing agents where Pt loading is very low compared to that of the standard Pt CE. This reduces the cost and also increases the catalytic activity to regenerate the electrolyte more efficiently. The combination of both factors enhances the efficiency of the device as high as 8%. The open circuit photovoltage decay in the presence of Ag-TiO_2 photoanode unravels slow back electron transfer from the active layer to the electrolyte or oxidized dye molecules.

7.2. Results and Discussion:

7.2.1. Enhanced Photovoltage in DSSC: Synergistic Combination of Silver Modified TiO_2 Photoanode and Low Cost Counter Electrode [51]: The formation of silver modified TiO_2 (Ag-TiO_2) by radiolysis and detailed characterization are reported previously [52]. The silver ions were reduced by the free radicals such as solvated electrons and alcohol radicals generated due to high energy radiation.

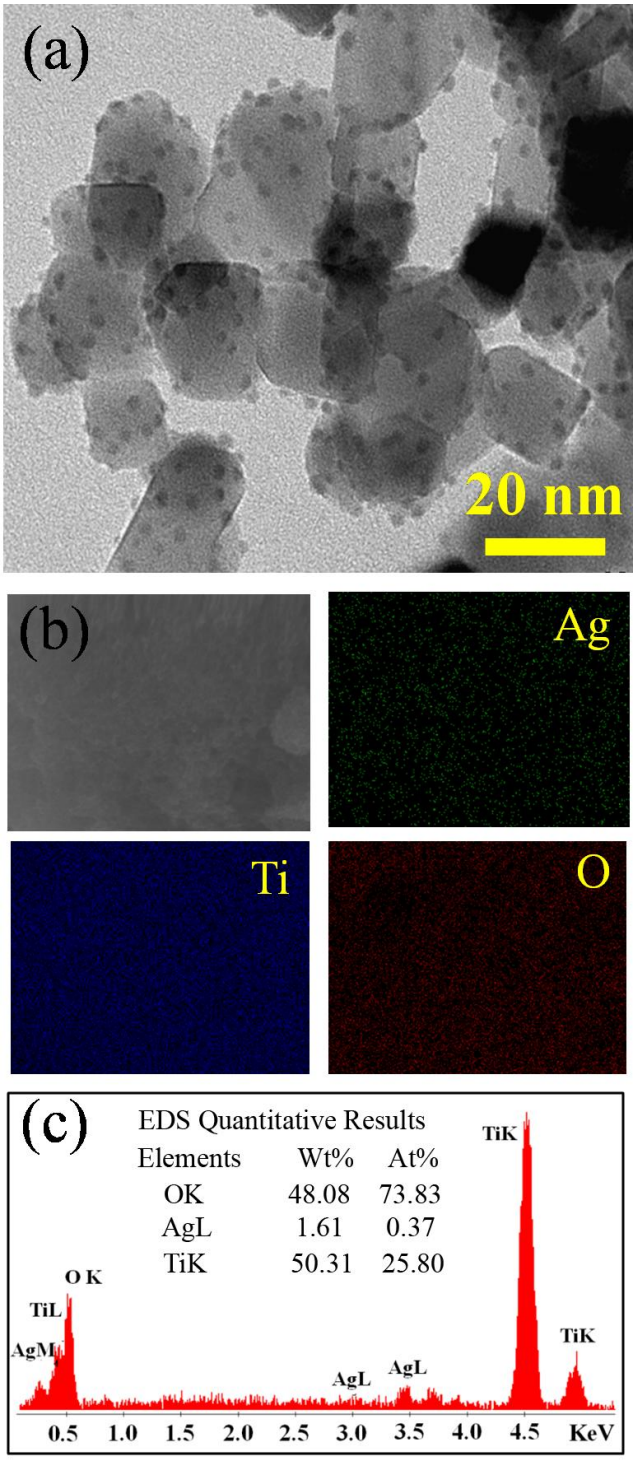

Figure 7.1. *Characterization of Ag-TiO_2 nanocomposites. (a) TEM image of silver modified TiO_2. (b) SEM image and Ag, Ti, O elemental mapping images of Ag-TiO_2 nanocomposites. (c) EDAX spectrum of Ag-TiO_2 nanocomposites.*

The silver nanoparticles (NPs) (2% metal loading) are homogeneously distributed on P25 TiO_2 NPs as shown in a Transmission Electron Microscopic image (Figure

7.1a). The average size of the silver NPs is 2 nm. The elemental distribution of the Ag-TiO_2 was further characterized by energy dispersive spectroscopic (EDS) mapping. The EDS elemental mapping clearly confirmed the presence and homogeneous distribution of Ag, Ti, and O elements in the Ag-TiO_2 as shown in Figure 7.1b. The EDS spectrum indicates the presence of 1.61% Ag in the material (Figure 7.1c).

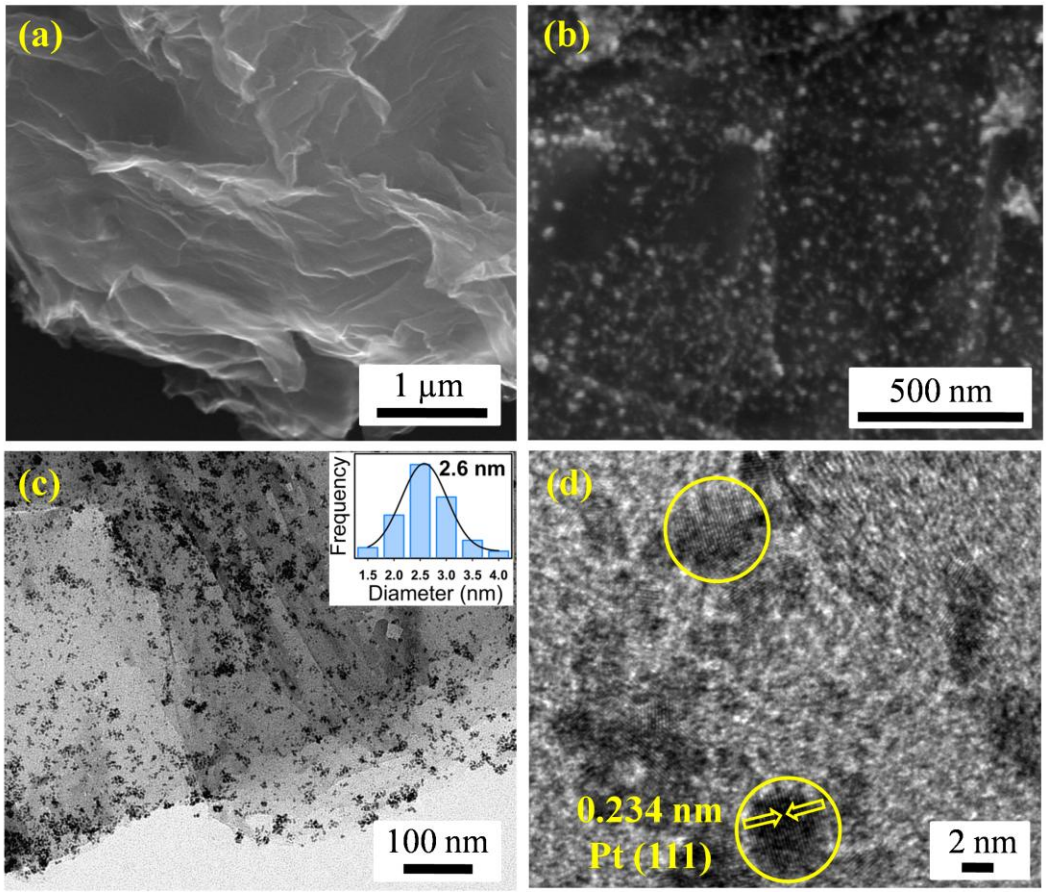

Figure 7.2. *Electron microscopic images of the Pt@RGO nanocomposites. SEM images of (a) RGO nanosheets and (b) Pt@RGO nanocomposites. (c) TEM and (d) HRTEM images of Pt@RGO nanocomposites. Inset of (c) shows the size distribution of the Pt NPs on RGO nanosheets.*

In order to lower the Pt content in CE which in turn decreases the cost, small amount of Pt has been hybridized with RGO (Pt@RGO). The simultaneous photo-reduction of GO and Pt salt under UV light irradiation without any chemical reducing or stabilizing agents results in the successful formation of the nanohybrid. In hydrogen-donating solvents, $Pt(acac)_2$ undergoes efficient

photodegradation to yield colloidal platinum. The photoreduction mechanism of $Pt(acac)_2$ in alcohol solution has been established previously [53]. Figure 7.2a and 7.2b illustrate the scanning electron microscopic (SEM) images of RGO and Pt NPs on the RGO, respectively. The homogeneous distribution of Pt NPs all over the RGO nanosheet is clearly evident from the TEM image as shown in Figure 7.2c. The average particle size of Pt NPs is estimated by fitting the experimental TEM data over 200 particles and it is found to be 2.6 nm as shown in the inset of Figure 7.2c. From high resolution TEM (HR-TEM) image of Pt@RGO, the inter-planar distance between the fringes of Pt NPs is found to be 0.234 nm which is consistent with (111) planes (Figure 7.2d) [47]. The crystal planes of the RGO nanosheets are also evident from the HR-TEM image. The Pt content in Pt@RGO nanocomposite is estimated from the ICP-MS and it is found to be 20.7%.

The X-ray diffraction patterns (XRD) of GO, RGO and Pt@RGO are presented in Figure 7.3a. The GO sample shows characteristic diffraction peaks at 25.9^o and 42.3^o which can be assigned to the (002) and (100) crystal planes, respectively. In case of RGO and Pt@RGO, the peak at 25.9^o moved slightly to a higher angle which indicates the partial reduction of GO to the conjugated crystalline graphene network (sp^2) [54]. The peak at 42.3^o corresponding to the (100) planes diminishes after the deposition of Pt on RGO nanosheets due to the surface coverage by Pt NPs [55]. In addition, the peaks of the Pt@RGO nanocomposites at 39.8^o, 46.5^o and 67.5^o can be assigned to the (111), (200) and (220) crystal planes of face centered-cubic (fcc) Pt NPs, respectively. The results confirm the successful formation of Pt NPs over the RGO nanosheets. To further characterize the nanocomposites, Raman spectra of GO, RGO and Pt@RGO have been collected as shown in Figure 7.3b. The Raman spectra show two major peaks, a G band at 1590 cm^{-1} and a D band at 1352 cm^{-1}. The G band corresponds to the in plane bond stretching motion of pairs of C sp^2 atoms (E_{2g} mode), while D band

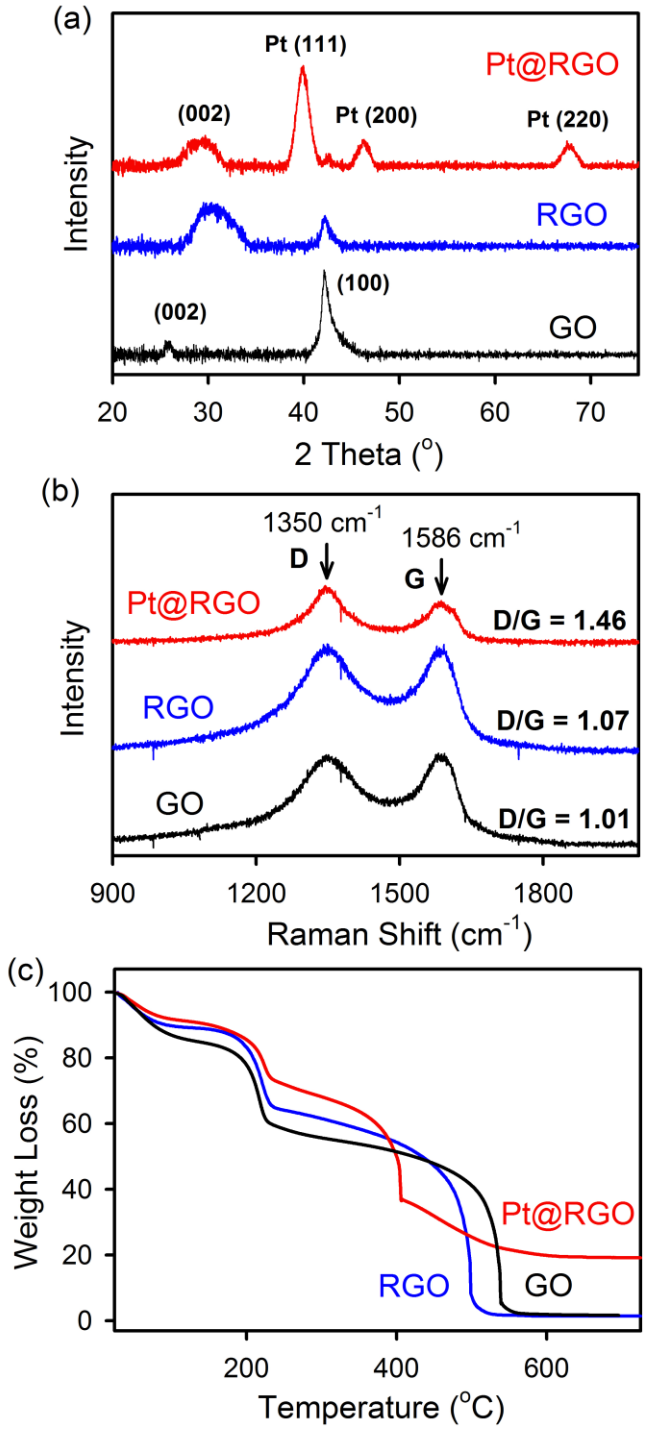

Figure 7.3. *Characterization of the Pt@RGO nanocomposites. (a) X-ray diffraction patterns (b) Raman spectra and (c) thermogravimetric analysis profiles of Pt@RGO (red), RGO (blue) and GO (black).*

corresponds to the disordered structures, such as bond angle disorders and asymmetric lattices in the graphite [16, 45]. The intensity ratio of D band to G band

(D/G) increases after reduction of GO to RGO and further increases after the formation of the nanocomposite. The increase in D/G intensity ratio can be attributed to (a) an increase in the quantity of amorphous carbon, (b) a higher density of defects on the structure, or (c) a reduction in the crystallite size or domains [56]. In the present case, the increase in the intensity ratio may be due to the increase in the density of defects on the graphene structures. In case of Pt@RGO, a strong D′ peak at 1615 cm^{-1} is observed, which can be assigned to the nonzero phonon density of the states at energies above the energy of the G band. These phonons are usually Raman-inactive but become active due to phonon confinement caused by the defects [57]. Moreover, thermogravimetric analysis has been carried out to assess the thermal stability of the nanocomposite as shown in Figure 7.3c. For the GO sample, a weight loss of ~40% occurs between 180 to 230 ^{o}C due to a pyrolysis of the labile oxygen-containing functional groups, yielding CO, CO_2 and steam [58]. The weight loss in the similar temperature range for the RGO and Pt@RGO decreases to ~33% and 27%, respectively. This observation indicates the decrease of functional groups in the RGO and Pt@RGO samples after reduction. The complete decomposition of the GO and RGO samples occurs around 500 ^{o}C, while the carbonaceous material present in the Pt@RGO decomposes around 400 ^{o}C. The lower decomposition temperature can be attributed to an increase in the interlayer distance of the nanosheets due to the presence of Pt NPs. A residue of ~20% remains at high temperature in case of Pt@RGO due to the presence of Pt NPs which is well consistent with the ICP-MS data.

In order to demonstrate practical applications utilizing Ag-TiO_2 at active electrode and Pt@RGO at counter electrode, a series of DSSC were fabricated. Figure 4a shows the photocurrent-voltage characteristics of DSSC fabricated with different active and counter electrodes. The corresponding values of the

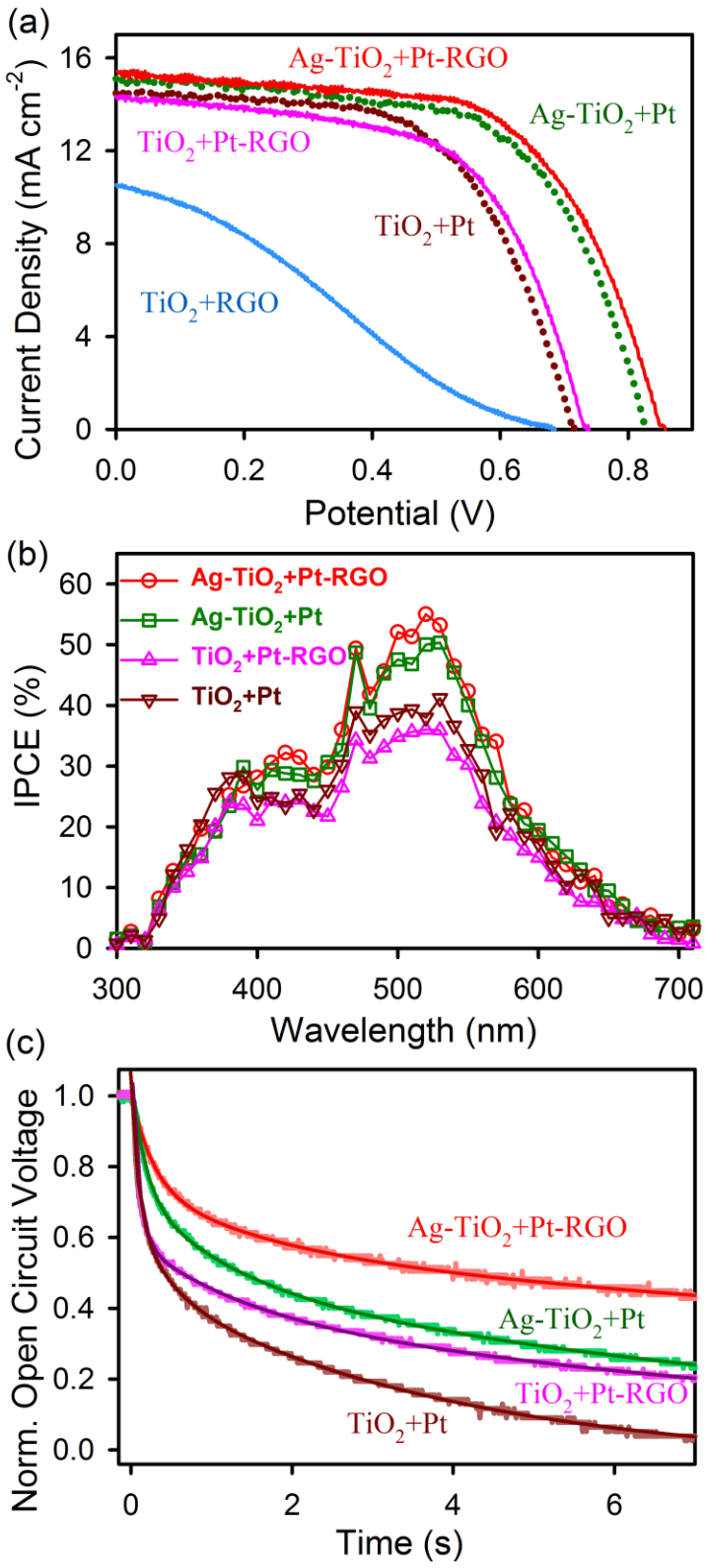

Figure 7.4. *Device performance. (a) J-V characteristics, (b) incident photon to current conversion efficiency (IPCE) spectra and (c) open circuit voltage decay profiles of different DSSCs.*

Table 7.1. *Solar cell performance using different active and counter electrodes*[a]

Photoanode	Counter electrode	Best Values				Average Value η (%)
		J_{sc} (mA cm^{-2})	V_{oc} (V)	Fill Factor (FF)	η (%)	
TiO_2	Pt-RGO	14.3	0.74	59.5	6.37	5.64
	Pt	14.5	0.72	59.1	6.21	5.58
	RGO	10.5	0.69	26.8	1.95	1.50
Ag-TiO_2	Pt-RGO	15.4	0.86	60.8	8.02	7.22
	Pt	15.1	0.84	61.4	7.73	6.80

[a]*Short-circuit photocurrent densities (J_{SC} cm^{-2}), open-circuit voltage (V_{OC}) and efficiency (η).*

photovoltaic parameters, such as the short circuit photocurrent density (J_{sc}), open circuit voltage (V_{oc}), fill factor (FF), power conversion efficiency (η) for the best cells along with the average efficiency values are presented in Table 7.1. An increase of around 16% (from 0.72 to 0.84 V) in the photovoltage (V_{oc}) is observed in case of Ag-TiO_2 at photoanode compared to that of the bare TiO_2 along with Pt at the counter electrode. During steady state illumination, V_{oc} is the difference in potential between the quasi-Fermi level of the TiO_2 film and the rest potential of the counter electrode, which remains in equilibrium with the redox couple. Semiconductor and metal NPs undergo electron equilibration under light illumination. In the Ag-TiO_2 nanocomposites, due to the larger work function of Ag (4.5-4.7 eV) [59] compared to the electron affinity of TiO_2 (1.59 eV) [60], a schottky barrier exists at their interface [61]. The possible electron transfer pathways and formation of schottky barrier are shown in Scheme 7.1. Under light illumination, the electrons from excited N719 dyes are injected to the Ag NPs on TiO_2 surface which results in accumulation of electrons in Ag NPs. As a result, the Fermi level of the Ag NPs shifted closer to the conduction band (CB) of TiO_2 in the Ag-TiO_2 nanocomposites which is responsible for the increase in V_{oc}. To the best of our knowledge, such a significant enhancement in the V_{oc} in presence of Ag NPs has not been reported earlier. Time resolved microwave conductivity (TRMC) studies have shown that electrons can be injected from Ag NPs to the CB of TiO_2 [52] in order to establish charge equilibrium in the system. In contrast, the

electrons at the CB of the TiO_2 cannot reverse their path to recombine with the oxidized dye or electrolyte due to the presence of schottky barrier which results in enhanced efficiency of the device. In addition to the enhancement in V_{oc}, photocurrent also increases (14.5 to 15.1 mA cm^{-2}) in case of Ag-TiO_2 nanocomposite which is well documented in the literature [32, 34]. This is due to an increase in effective absorption cross section of the dye (N719) and a modest increase in the framework surface area.

After the successful demonstration of Ag-TiO_2 as a photoanode, the counter electrode has been modified with Pt@RGO to reduce the Pt loading as well as optimization of the catalytic activity. The amount of Pt in the Pt@RGO nanocomposite is 10 times smaller than that of the standard Pt counter electrode which lowers the cost and makes it viable for large scale commercial utilization. Although the amount of Pt decreases, the catalytic activity of Pt@RGO is comparable or slightly higher than the Pt only. The DSSC with Ag-TiO_2 photoanode along with Pt@RGO and Pt counter electrode show energy conversion efficiency of 8.02% and 7.73%, respectively. The effect of CE on DSSC performance is dictated by the electrical conductivity and electrocatalytic activity in the reduction of triiodide to iodide [62]. In case of Pt@RGO, the catalytic activity of Pt and high electron conductivity of the stable support material RGO are synergistically combined owing to more interfacial active sites. The combination of Pt@RGO with bare TiO_2 as photoanode also exhibits slightly higher efficiency (η = 6.37%) than the Pt alone as CE (η = 6.21%). However, using control RGO as CE with TiO_2 as photoanode showed lower efficiency of 1.95%. In order to investigate the light harvesting by the N719 dye, the incident photon to current conversion efficiency (IPCE) of the cells were monitored as shown in Figure 7.4b. The spectra collected from different cells show good agreement between the wavelength of photocurrent maximum and N719 absorption maximum (λ_{max} = 520nm), signifying that the N719 sensitizers on the photoanode surface are indeed

responsible for photocurrent generation. The trend in the photocurrent responses is consistent with the short circuit currents of the corresponding cells as shown in Figure 7.4a.

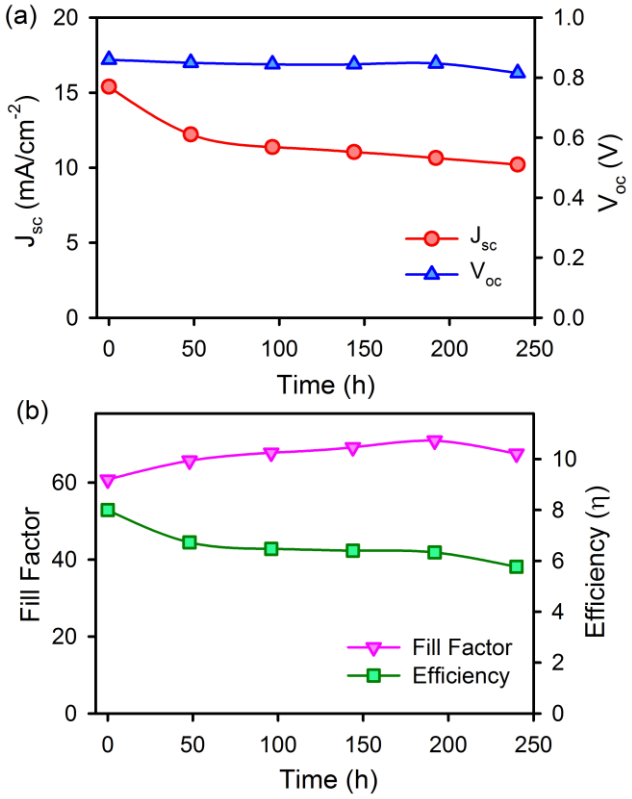

Figure 7.5. *Stability of the device. Plot of (a) J_{sc} and V_{oc}, (b) Fill factor and efficiency of the DSSC fabricated using Ag-TiO_2 photoanode and Pt@RGO CE with time.*

In order to investigate the lifetime of accumulated charges at the photoanode, the decay of open circuit voltage has been monitored for different cells in the dark following a brief period of illumination. Upon visible light illumination, the excited sensitizers inject electrons into TiO_2 electrode. The accumulated electrons in the TiO_2 drives the Fermi level to the more negative potential which reflects in the photovoltage enhancement. The forward electron injection from sensitizer to TiO_2 is terminated upon stopping the illumination, thus discharging of electrons occurs through the back electron transfer or recombination with the oxidized electrolytes. The open circuit voltage decay reflects the timescales for the recombination processes. Figure 7.4c shows the

decay profiles of different DSSC fabricated using Ag-TiO_2 and TiO_2 as photoanode, Pt@RGO and Pt as CE. The fitted timescales are presented in Table 7.2. The Ag-TiO_2 photoanode in combination with Pt@RGO CE exhibit a remarkably slow rate of voltage decay (15.68 s) compared to the bare TiO_2 photoanode (3.74 s). This is due to the storage of electrons in Ag NPs [52] which prevents recombination with the oxidized electrolytes. This observation is consistent with the enhanced photovoltage in the presence of Ag-TiO_2 as a photoanode. The Pt@RGO CE in combination with TiO_2 photoanode shows slower decay with a lifetime of 3.74 s compare to the Pt CE (1.91 s). This can be attributed to the higher catalytic activity of Pt@RGO than Pt only at the CE in regenerating the oxidized electrolyte which in turn reduces the recombination processes. The stability of the DSSC fabricated using Ag-TiO_2 photoanode and Pt@RGO CE, the photocurrent-voltage characteristics were monitored for 240 h. Figure 7.5a depicts the change in short circuit current and open circuit voltage with time. Initially the J_{sc} decreases but after few days it is stable for a long period. The V_{oc} is very stable during the experimental time window which can be attributed to the stability of the Ag-TiO_2 photoanode. It is reported that the Ag NPs are easily damaged under oxidizing conditions [63]. However, our observation suggests that the Ag modified TiO_2 photoanode are stable which is consistent with the reported literature [32-33]. The fill factor and overall efficiency of the DSSC are also consistent with time as shown in Figure 7.5b.

Table 7.2. *Dynamics of photovoltage transients of DSSCs fabricated using different active and counter electrodes*[b]

Active Electrode	Counter Electrode	τ_1 (S)	τ_2 (S)	τ_3 (S)	τ_{avg} (S)
TiO_2	Pt-RGO	0.09 (48.5%)	1.28 (16.9%)	10.08 (34.6%)	3.74
	Pt	0.08 (32.4%)	0.39 (19.9%)	3.78 (47.7%)	1.91
Ag-TiO_2	Pt-RGO	0.26 (25.7%)	1.67 (19.2%)	27.77 (55.1%)	15.68
	Pt	0.16 (30.2%)	1.17 (24.3%)	9.99 (45.5%)	4.87

[b]*Numbers in the parenthesis indicate relative weightages.*

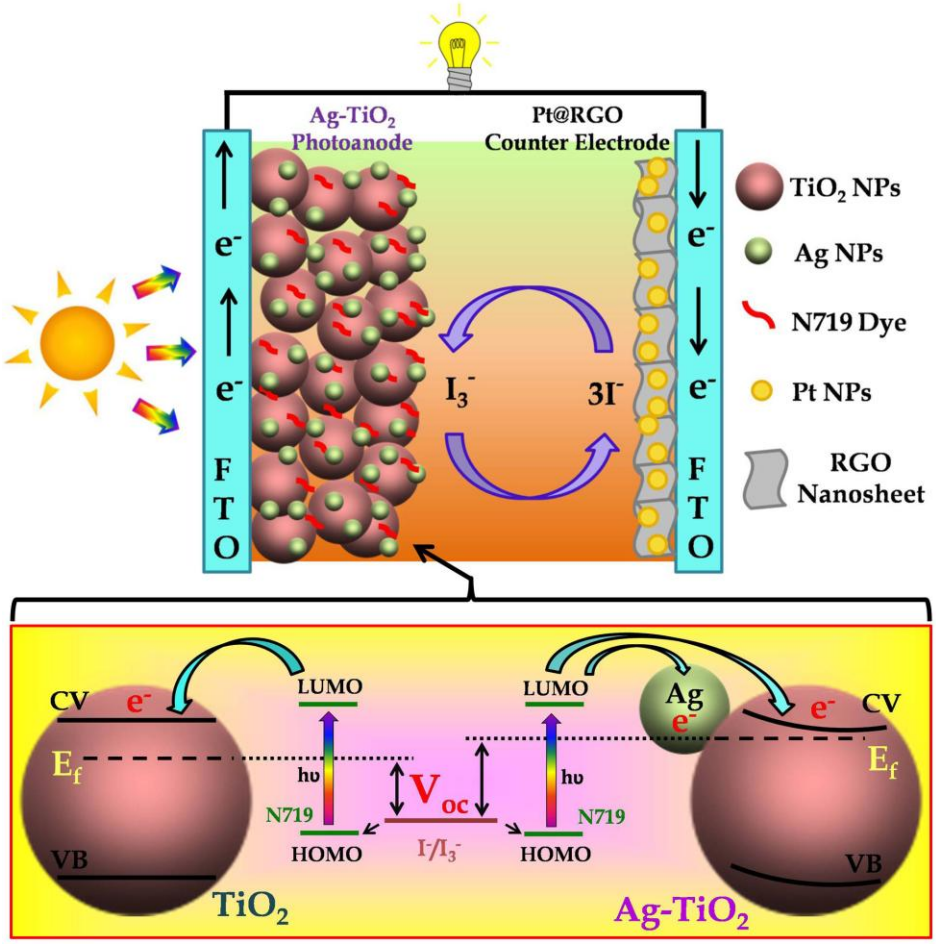

Scheme 7.1. *Schematic presentation of the dye-sensitized solar cell consists of Ag-TiO_2 photoanode and Pt@RGO counter electrode. Lower panel shows the energy level diagram.*

In order to investigate the electronic and ionic processes in DSSC, electrochemical impedance spectroscopy (EIS) were performed. As shown in Figure 7.6a, the Nyquist plot features two semicircles, one in the high frequency region and the other one in the intermediate frequency region. The semicircle in the high frequency region can be attributed to the charge transfer at counter electrode while the semicircle in the intermediate frequency region is associated with the electron transport in the mesoscopic TiO_2 film and back reaction at the TiO_2/electrolyte interface. The Nyquist plots are fitted using the equivalent circuit shown in Figure 7.6b and the parameters are summarized in Table 7.3. The R_2 value represents the interfacial recombination resistance at TiO_2/electrolyte

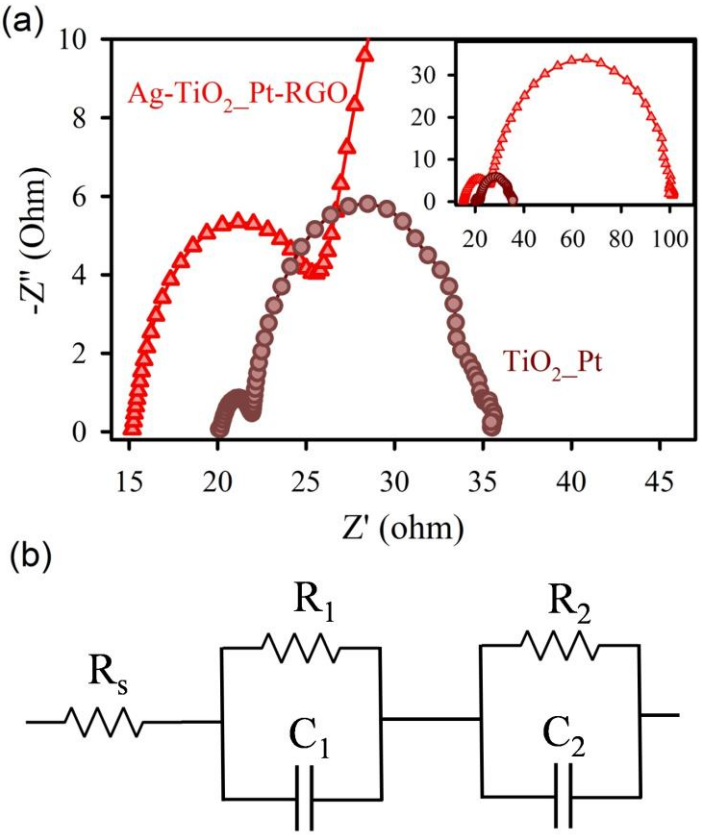

Figure 7.6. *EIS of the device. (a) Nyquist plots of different cells. Inset shows the full region. (b) Equivalent circuit model that was used to fit the EIS spectra.*

interface. The R_2 value for Ag-TiO_2 photoanode (72.1 Ω) is greater than that of the bare TiO_2 photoanode (12.6 Ω) which can be attributed to the less charge recombination from Ag-TiO_2 photoanode to the triiodide ions in the electrolyte [33]. The observation is consistent with the slower photovoltage decay of the DSSC with Ag-TiO_2 photoanode as shown in Figure 7.4c. This confirms that Ag NPs act as electron-hole separator due to the formation of schottky barrier at the Ag-TiO_2 interface which prevents recombination with the oxidized electrolytes [61]. The R_1

Table 7.3. *EIS parameters of DSSCs fabricated using different active and counter electrodes.*

Active Electrode	Counter Electrode	R_s (Ω)	R_1 (Ω)	R_2 (Ω)
Ag-TiO_2	Pt-RGO	15.5	11.0	72.1
TiO_2	Pt	20.3	1.9	12.6

value represents the charge transfer resistance at the CE interface i.e. the catalytic activity of the electrode for reducing triiodide ions. The R_1 value for Pt CE (1.9 Ω) is less than that of the Pt@RGO CE (11.0 Ω). Thus the Pt CE prepared by drop casting method exhibits slightly higher catalytic activity than that of the Pt@RGO CE as observed from EIS spectra [48] which can be attributed to the 10 times lower Pt content in Pt@RGO CE than that of the Pt CE. However, the device performance of the Pt@RGO CE is comparable or slightly higher than Pt CE as shown in Figure 7.4a which decreases the cost of CE significantly.

7.3. Conclusion: In summary, we have successfully utilized Ag modified TiO_2 (Ag-TiO_2) as photoanode material in dye sensitized solar cell. On the other hand, we have demonstrated a facile synthesis of Pt NPs supported on RGO (Pt@RGO) surface by simple photo-reduction method without using chemical reducing or stabilizing agents. The quantity of Pt in the Pt@RGO nanocomposite is 10 times lower than that of the Pt counter electrode which reduces the cost and makes it viable for large scale commercial utilization. The combination of Ag-TiO_2 as photoanode and Pt@RGO as counter electrode leads to a light to electrical energy conversion with an overall efficiency of 8%. An enhancement of around 16% in the photovoltage (V_{oc}) is observed in case of Ag-TiO_2 at photoanode compared to that of the bare TiO_2, which can be attributed to the shifting of the quasi-Fermi level of the TiO_2 photoanode close to the conduction band in the presence of Ag NPs due to the formation of schottky barrier at Ag-TiO_2 interface. Moreover, Pt@RGO is found to be more efficient than Pt only as CE due to the catalytic activity of Pt and high electron conductivity of the stable support material RGO. These advantages are synergistically combined owing to the large number of active interfacial sites. The open circuit voltage decay profiles show remarkably slow rate of electron recombination from Ag-TiO_2 photoanode to the oxidized electrolyte. The present study holds great promise for low cost, large scale fabrication of efficient solar devices.

References

[1] B. O'Regan, M. Gratzel, A Low-Cost, High-Efficiency Solar Cell Based on Dye-Sensitized Colloidal TiO_2 Films, *Nature* 353 (1991) 737-740.

[2] A. Yella, H.-W. Lee, H.N. Tsao, C. Yi, A.K. Chandiran, M.K. Nazeeruddin, E.W.-G. Diau, C.-Y. Yeh, S.M. Zakeeruddin, M. Grätzel, Porphyrin-Sensitized Solar Cells with Cobalt (II/III)–Based Redox Electrolyte Exceed 12 Percent Efficiency, *Science* 334 (2011) 629-634.

[3] S. Mathew, A. Yella, P. Gao, R. Humphry-Baker, F.E. CurchodBasile, N. Ashari-Astani, I. Tavernelli, U. Rothlisberger, K. NazeeruddinMd, M. Grätzel, Dye-Sensitized Solar Cells with 13% Efficiency Achieved through the Molecular Engineering of Porphyrin Sensitizers, *Nat. Chem.* 6 (2014) 242-247.

[4] M. Grätzel, Dye-Sensitized Solar Cells, *J. Photochem. Photobiol. C* 4 (2003) 145-153.

[5] M. Grätzel, Recent Advances in Sensitized Mesoscopic Solar Cells, *Acc. Chem. Res.* 42 (2009) 1788-1798.

[6] M. Graetzel, R.A.J. Janssen, D.B. Mitzi, E.H. Sargent, Materials Interface Engineering for Solution-Processed Photovoltaics, *Nature* 488 (2012) 304-312.

[7] K. Lee, S.W. Park, M.J. Ko, K. Kim, N.-G. Park, Selective Positioning of Organic Dyes in a Mesoporous Inorganic Oxide Film, *Nat. Mater.* 8 (2009) 665-671.

[8] H. Wang, B. Wang, J. Yu, Y. Hu, C. Xia, J. Zhang, R. Liu, Significant Enhancement of Power Conversion Efficiency for Dye Sensitized Solar Cell Using 1D/3D Network Nanostructures as Photoanodes, *Sci. Rep.* 5 (2015) 9305.

[9] S.S. Mali, C.A. Betty, P.N. Bhosale, P.S. Patil, C.K. Hong, From Nanocorals to Nanorods to Nanoflowers Nanoarchitecture for Efficient Dye-Sensitized Solar Cells at Relatively Low Film Thickness: All Hydrothermal Process, *Sci. Rep.* 4 (2014) 5451.

[10] Y. Duan, N. Fu, Q. Liu, Y. Fang, X. Zhou, J. Zhang, Y. Lin, Sn-Doped TiO_2 Photoanode for Dye-Sensitized Solar Cells, *J. Phys. Chem. C* 116 (2012) 8888-8893.

[11] X. Zhang, S.-T. Wang, Z.-S. Wang, Effect of Metal-Doping in TiO_2 on Fill Factor of Dye-Sensitized Solar Cells, *Appl. Phys. Lett.* 99 (2011) 113503.

[12] J.-W. Shiu, Y.-C. Chang, C.-Y. Chan, H.-P. Wu, H.-Y. Hsu, C.-L. Wang, C.-Y. Lin, E.W.-G. Diau, Panchromatic Co-Sensitization of Porphyrin-Sensitized Solar Cells to Harvest Near-Infrared Light Beyond 900 nm, *J. Mater. Chem. A* 3 (2015) 1417-1420.

[13] C.-L. Wang, J.-Y. Hu, C.-H. Wu, H.-H. Kuo, Y.-C. Chang, Z.-J. Lan, H.-P. Wu, E. Wei-Guang Diau, C.-Y. Lin, Highly Efficient Porphyrin-Sensitized Solar Cells with Enhanced Light Harvesting Ability Beyond 800 nm and Efficiency Exceeding 10%, *Energ. Environ. Sci.* 7 (2014) 1392-1396.

[14] H.N. Tsao , C. Yi , T. Moehl, J.-H. Yum, S.M. Zakeeruddin, M.K. Nazeeruddin, M. Grätzel, Cyclopentadithiophene Bridged Donor–Acceptor Dyes Achieve High Power Conversion Efficiencies in Dye-Sensitized Solar Cells Based on the Tris-Cobalt Bipyridine Redox Couple, *ChemSusChem* 4 (2011) 591-594.

[15] H. Nusbaumer, S.M. Zakeeruddin, J.-E. Moser, M. Grätzel, An Alternative Efficient Redox Couple for the Dye-Sensitized Solar Cell System, *Chem. Eur. J.* 9 (2003) 3756-3763.

[16] V.-D. Dao, N.T.Q. Hoa, L.L. Larina, J.-K. Lee, H.-S. Choi, Graphene-Platinum Nanohybrid as a Robust and Low-Cost Counter Electrode for Dye-Sensitized Solar Cells, *Nanoscale* 5 (2013) 12237-12244.

[17] G.-r. Li, F. Wang, Q.-w. Jiang, X.-p. Gao, P.-w. Shen, Carbon Nanotubes with Titanium Nitride as a Low-Cost Counter-Electrode Material for Dye-Sensitized Solar Cells, *Angew. Chem. Int. Ed.* 49 (2010) 3653-3656.

[18] P. Joshi, Y. Xie, M. Ropp, D. Galipeau, S. Bailey, Q. Qiao, Dye-Sensitized Solar Cells Based on Low Cost Nanoscale Carbon/TiO_2 Composite Counter Electrode, *Energ. Environ. Sci.* 2 (2009) 426-429.

[19] K. Hara, T. Horiguchi, T. Kinoshita, K. Sayama, H. Sugihara, H. Arakawa, Highly Efficient Photon-to-Electron Conversion with Mercurochrome-Sensitized

Nanoporous Oxide Semiconductor Solar Cells, *Sol. Energ. Mat. Sol. Cells* 64 (2000) 115-134.

[20] S. Ito, T. Kitamura, Y. Wada, S. Yanagida, Facile Fabrication of Mesoporous TiO_2 Electrodes for Dye Solar Cells: Chemical Modification and Repetitive Coating, *Sol. Energ. Mat. Sol. Cells* 76 (2003) 3-13.

[21] S.D. Standridge, G.C. Schatz, J.T. Hupp, Distance Dependence of Plasmon-Enhanced Photocurrent in Dye-Sensitized Solar Cells, *J. Am. Chem. Soc.* 131 (2009) 8407-8409.

[22] Y. Li, H. Wang, Q. Feng, G. Zhou, Z.-S. Wang, Gold Nanoparticles Inlaid TiO_2 Photoanodes: A Superior Candidate for High-Efficiency Dye-Sensitized Solar Cells, *Energ. Environ. Sci.* 6 (2013) 2156-2165.

[23] C. Andrei, E. Lestini, S. Crosbie, C. de Frein, T. O'Reilly, D. Zerulla, Plasmonic Enhancement of Dye Sensitized Solar Cells Via a Tailored Size-Distribution of Chemically Functionalized Gold Nanoparticles, *PLoS One* 9 (2014) e109836.

[24] S. Linic, P. Christopher, D.B. Ingram, Plasmonic-Metal Nanostructures for Efficient Conversion of Solar to Chemical Energy, *Nat. Mater.* 10 (2011) 911-921.

[25] S. Sarkar, A. Makhal, T. Bora, S. Baruah, J. Dutta, S.K. Pal, Photoselective Excited State Dynamics in ZnO-Au Nanocomposites and Their Implications in Photocatalysis and Dye-Sensitized Solar Cells, *Phys. Chem. Chem. Phys.* 13 (2011) 12488-12496.

[26] T. Bora, H.H. Kyaw, S. Sarkar, S.K. Pal, J. Dutta, Highly Efficient ZnO/Au Schottky Barrier Dye-Sensitized Solar Cells: Role of Gold Nanoparticles on the Charge-Transfer Process, *Beilstein J. Nanotechnol.* 2 (2011) 681-690.

[27] Z. Hai, N. El Kolli, D.B. Uribe, P. Beaunier, M. Jose-Yacaman, J. Vigneron, A. Etcheberry, S. Sorgues, C. Colbeau-Justin, J. Chen, H. Remita, Modification of TiO_2 by Bimetallic Au-Cu Nanoparticles for Wastewater Treatment, *J. Mater. Chem. A* 1 (2013) 10829-10835.

[28] S. Sardar, P. Kar, S. Sarkar, P. Lemmens, S.K. Pal, Interfacial Carrier Dynamics in PbS-ZnO Light Harvesting Assemblies and Their Potential Implication in

Photovoltaic/ Photocatalysis Application, *Sol. Energ. Mat. Sol. Cells* 134 (2015) 400-406.

[29] S. Sardar, S. Sarkar, M.T.Z. Myint, S. Al-Harthi, J. Dutta, S.K. Pal, Role of Central Metal Ions in Hematoporphyrin-Functionalized Titania in Solar Energy Conversion Dynamics, *Phys. Chem. Chem. Phys.* 15 (2013) 18562-18570.

[30] S. Sardar, P. Kar, S.K. Pal, The Impact of Central Metal Ions in Porphyrin Functionalized ZnO/TiO_2 for Enhanced Solar Energy Conversion, *J. Mat. NanoSci.* 1 (2014) 12-30.

[31] S. Ghosh, A.H. Khan, S. Acharya, Fabrication of Highly Stable, Hybrid PbS Nanocomposites in PAMAM Dendrimer Matrix for Photodetection, *J. Phys. Chem. C* 116 (2012) 6022-6030.

[32] N.C. Jeong, C. Prasittichai, J.T. Hupp, Photocurrent Enhancement by Surface Plasmon Resonance of Silver Nanoparticles in Highly Porous Dye-Sensitized Solar Cells, *Langmuir* 27 (2011) 14609-14614.

[33] K. Guo, M. Li, X. Fang, X. Liu, B. Sebo, Y. Zhu, Z. Hu, X. Zhao, Preparation and Enhanced Properties of Dye-Sensitized Solar Cells by Surface Plasmon Resonance of Ag Nanoparticles in Nanocomposite Photoanode, *J. Power Sources* 230 (2013) 155-160.

[34] S.-J. Lin, K.-C. Lee, J.-L. Wu, J.-Y. Wu, Plasmon-Enhanced Photocurrent in Dye-Sensitized Solar Cells, *Sol. Energy* 86 (2012) 2600-2605.

[35] M. Sun, W. Fu, H. Yang, Y. Sui, B. Zhao, G. Yin, Q. Li, H. Zhao, G. Zou, One-Step Synthesis of Coaxial Ag/TiO_2 Nanowire Arrays on Transparent Conducting Substrates: Enhanced Electron Collection in Dye-Sensitized Solar Cells, *Electrochem. Com.* 13 (2011) 1324-1327.

[36] S.H. Hwang, H. Song, J. Lee, J. Jang, Multifunctional Ag-Decorated Porous TiO_2 Nanofibers in Dye-Sensitized Solar Cells: Efficient Light Harvesting, Light Scattering, and Electrolyte Contact, *Chem. Eur. J.* 20 (2014) 12974-12981.

[37] H. Choi, Y.-S. Chen, K.G. Stamplecoskie, P.V. Kamat, Boosting the Photovoltage of Dye-Sensitized Solar Cells with Thiolated Gold Nanoclusters, *J. Phys. Chem. Lett.* 6 (2015) 217-223.

[38] L. Bay, K. West, B. Winther-Jensen, T. Jacobsen, Electrochemical Reaction Rates in a Dye-Sensitised Solar Cell—the Iodide/Tri-Iodide Redox System, *Sol. Energ. Mat. Sol. Cells* 90 (2006) 341-351.

[39] N. Robertson, Optimizing Dyes for Dye-Sensitized Solar Cells, *Angew. Chem. Int. Ed.* 45 (2006) 2338-2345.

[40] E. Olsen, G. Hagen, S. Eric Lindquist, Dissolution of Platinum in Methoxy Propionitrile Containing LiI/I_2, *Sol. Energ. Mat. Sol. Cells* 63 (2000) 267-273.

[41] K.S. Novoselov, A.K. Geim, S.V. Morozov, D. Jiang, Y. Zhang, S.V. Dubonos, I.V. Grigorieva, A.A. Firsov, Electric Field Effect in Atomically Thin Carbon Films, *Science* 306 (2004) 666-669.

[42] H. Wang, Y.H. Hu, Graphene as a Counter Electrode Material for Dye-Sensitized Solar Cells, *Energ. Environ. Sci.* 5 (2012) 8182-8188.

[43] S.G. Hashmi, J. Halme, Y. Ma, T. Saukkonen, P. Lund, A Single-Walled Carbon Nanotube Coated Flexible PVC Counter Electrode for Dye-Sensitized Solar Cells, *Adv. Mater. Interfaces* 1 (2014) 1300055.

[44] X. Xu, D. Huang, K. Cao, M. Wang, S.M. Zakeeruddin, M. Grätzel, Electrochemically Reduced Graphene Oxide Multilayer Films as Efficient Counter Electrode for Dye-Sensitized Solar Cells, *Sci. Rep.* 3 (2013) 1489.

[45] M.-Y. Yen, C.-C. Teng, M.-C. Hsiao, P.-I. Liu, W.-P. Chuang, C.-C.M. Ma, C.-K. Hsieh, M.-C. Tsai, C.-H. Tsai, Platinum Nanoparticles/Graphene Composite Catalyst as a Novel Composite Counter Electrode for High Performance Dye-Sensitized Solar Cells, *J. Mater. Chem.* 21 (2011) 12880-12888.

[46] V. Tjoa, J. Chua, S.S. Pramana, J. Wei, S.G. Mhaisalkar, N. Mathews, Facile Photochemical Synthesis of Graphene-Pt Nanoparticle Composite for Counter Electrode in Dye Sensitized Solar Cell, *ACS Appl. Mater. Interfaces* 4 (2012) 3447-3452.

[47] R. Bajpai, S. Roy, P. Kumar, P. Bajpai, N. Kulshrestha, J. Rafiee, N. Koratkar, D.S. Misra, Graphene Supported Platinum Nanoparticle Counter-Electrode for Enhanced Performance of Dye-Sensitized Solar Cells, *ACS Appl. Mater. Interfaces* 3 (2011) 3884-3889.

[48] F. Gong, H. Wang, Z.-S. Wang, Self-Assembled Monolayer of Graphene/Pt as Counter Electrode for Efficient Dye-Sensitized Solar Cell, *Phys. Chem. Chem. Phys.* 13 (2011) 17676-17682.

[49] H. Gong, S. Park, S.-S. Lee, S. Hong, Facile and Scalable Fabrication of Transparent and High Performance Pt/Reduced Graphene Oxide Hybrid Counter Electrode for Dye-Sensitized Solar Cells, *Int. J. Precis. Eng. Man.* 15 (2014) 1193-1199.

[50] Q. Wang, M. Song, C. Chen, W. Hu, X. Wang, Plasma Synthesis of Surface-Functionalized Graphene-Based Platinum Nanoparticles: Highly Active Electrocatalysts as Electrodes for Direct Methanol Fuel Cells, *ChemPlusChem* 77 (2012) 432-436.

[51] S. Sardar, S. Ghosh, H. Remita, P. Kar, B. Liu, C. Bhattacharya, P. Lemmens, S.K. Pal, Enhanced Photovoltage in DSSC: Synergistic Combination of Silver Modified TiO_2 Photoanode and Low Cost Counter Electrode, *RSC Adv.* 6 (2016) 33433-33442.

[52] E. Grabowska, A. Zaleska, S. Sorgues, M. Kunst, A. Etcheberry, C. Colbeau-Justin, H. Remita, Modification of Titanium(IV) Dioxide with Small Silver Nanoparticles: Application in Photocatalysis, *J. Phys. Chem. C* 117 (2013) 1955-1962.

[53] F. Dehouche, P. Archirel, H. Remita, N. Brodie-Linder, A. Traverse, Alcohol to Water Catalyzed by Pt Nanoparticles: An Experimental and Computational Approach, *RSC Adv.* 2 (2012) 6686-6694.

[54] A. Grinou, Y. Yun, S. Cho, H. Park, H.-J. Jin, Dispersion of Pt Nanoparticle-Doped Reduced Graphene Oxide Using Aniline as a Stabilizer, *Materials* 5 (2012) 2927-2936.

[55] C. Zhang, X. Zhu, Z. Wang, P. Sun, Y. Ren, J. Zhu, J. Zhu, D. Xiao, Facile Synthesis and Strongly Microstructure-Dependent Electrochemical Properties of Graphene/Manganese Dioxide Composites for Supercapacitors, *Nanoscale Res. Lett.* 9 (2014) 490.

[56] P. Hasin, M.A. Alpuche-Aviles, Y. Wu, Electrocatalytic Activity of Graphene Multilayers toward I^-/I_3^-: Effect of Preparation Conditions and Polyelectrolyte Modification, *J. Phys. Chem. C* 114 (2010) 15857-15861.

[57] K.N. Kudin, B. Ozbas, H.C. Schniepp, R.K. Prud'homme, I.A. Aksay, R. Car, Raman Spectra of Graphite Oxide and Functionalized Graphene Sheets, *Nano Lett.* 8 (2008) 36-41.

[58] S. Stankovich, D.A. Dikin, R.D. Piner, K.A. Kohlhaas, A. Kleinhammes, Y. Jia, Y. Wu, S.T. Nguyen, R.S. Ruoff, Synthesis of Graphene-Based Nanosheets via Chemical Reduction of Exfoliated Graphite Oxide, *Carbon* 45 (2007) 1558-1565.

[59] W. Nie, R.C. Coffin, D.L. Carroll, Silver Nanoparticle-Doped Titanium Oxide Thin Films for Intermediate Layers in Organic Tandem Solar Cell, *Int. J. Photoenergy* 2013 (2013) 829463.

[60] H. Wu, L.S. Wang, Electronic Structure of Titanium Oxide Clusters: TiO_y ($y= 1-3$) and $(TiO_2)_n$ ($n = 1-4$), *J. Chem. Phys.* 107 (1997) 8221-8228.

[61] Z. Zhang, J.T. Yates, Band Bending in Semiconductors: Chemical and Physical Consequences at Surfaces and Interfaces, *Chem. Rev.* 112 (2012) 5520-5551.

[62] N. Papageorgiou, Counter-Electrode Function in Nanocrystalline Photoelectrochemical Cell Configurations, *Coordin. Chem. Rev.* 248 (2004) 1421-1446.

[63] S.D. Standridge, G.C. Schatz, J.T. Hupp, Toward Plasmonic Solar Cells: Protection of Silver Nanoparticles Via Atomic Layer Deposition of TiO_2, *Langmuir* 25 (2009) 2596-2600.

Chapter 8

Facile Carbonate Doping in Mesoporous TiO_2 Microspheres for Dye Sensitized Solar Cell with Enhanced Efficiency

8.1. Introduction: The marathon race for the ultimate goal of commercialization of an alternative silicon-free solar cell technology to achieve lower cost-per-watt level with grid parity versus fossil fuel technologies, started with the seminal demonstration of a prototype dye sensitized solar cell (DSSC) in last century with 7% efficiency [1]. Since then many efforts are dedicated to enhance the efficiency of the cells by a variety of following ways [2]: (i) selection of strongly absorbing donor-pi-acceptor sensitizing dyes [3-5] (ii) use of redox couples to achieve higher open circuit voltage [6-8] (iii) better thin film (composition and morphology) on the photoanode [9-11]. Apparently first two points look independent of the third one. However, given the amount of dye adsorption, electron injection from the dye to the photoanode and redox coupling, the parameters are found to be key factors for the optimum DSSC efficiency. Successful design of the photoanode again relies on the four key parameter: (a) light trapping via scattering of incident solar radiation (b) very high surface area of the oxide film in the photoanode for dye adsorption (c) ultrafast electron injection from excited dye to the oxide layer (d) efficient transport of charge carriers with minimal recombination loss of electrons [2].

A mammoth of literature on the various ways of controlling above four parameters for the efficient DSSC is existing [2, 12-13]. For example, plasmonic nanoparticles (Ag, Au) are integrated into photovoltaic devices for light trapping [14-16]. However, use of plasmonic nanoparticles on the photoanode is reported to

generate a negative influence named Fano effect due to destructive interference between scattered and unscattered light below the plasmon resonance of nanostructure causing reduced light absorption in DSSC at short wavelength [17]. Application of Aluminum (Al) nanoparticles is reported to overcome such limitation due to Fano effect [17]. Use of porous oxide layer in the photoanodes are reported to be efficient strategy for the layer with higher surface area [18]. Ultrafast electron injection in the DSSC were achieved by doping plasmonic metals [15, 19] and atomic layer deposition (ALD) of TiO_2/Al_2O_3 after dye adsorption [20]. The use of unidirectional nanotube arrays is shown to exhibit a faster electron diffusion time (τ_d) along the tube axis [21]. In principle, charge collection efficiency (η_{cc}) can be enhanced by reducing τ_d [22]. However, it has been shown that the nanostructure based photoanodes exhibit an undesired porous structure and thereby offer poor solar light harvesting [23]. Alternatively, a particular submicron sized TiO_2 structure called beads was used in photoanode or as scattering layer in order to increase charge collection efficiency [9].

From the brief overview of different synthesis strategies for the optimization of photoanode to account different important parameters for the betterment of the DSSC efficiency, it is most likely that optimization of one parameter may compromise others. Thus finding one-shot optimization strategy of all the parameters for the betterment of solar cell efficiency is "most wanted" and is the motive of the present study. In this work, we have used a particular TiO_2 structure called carbonate doped mesoporous microstructure (doped MS) in photoanode of a N719 dye containing solar cell. The doped MS prepared using two step non-aqueous solvothermal method in the photoanode essentially satisfies all the key requirements for the enhancement of efficiency of the DSSC. While scattering and electronic band modification increase light trapping, porosity enhances the dye adsorption. The ultrafast electron injection and minimization of

electron recombination leading to better solar cell efficiency compared to DSSC with photoanode using undoped MS are also demonstrated.

8.2. Results and Discussion:

8.2.1. Carbonate Doping in TiO_2 Microsphere: The Key Parameter Influencing Others for Efficient Dye Sensitized Solar Cell [24]: The control TiO_2 MS and doped MS were prepared according to modified procedures reported earlier [25-27]. The positive influences of the doped MS in DSSC performance are schematically shown in Scheme 8.1. Figure 8.1-A-a shows scanning electron

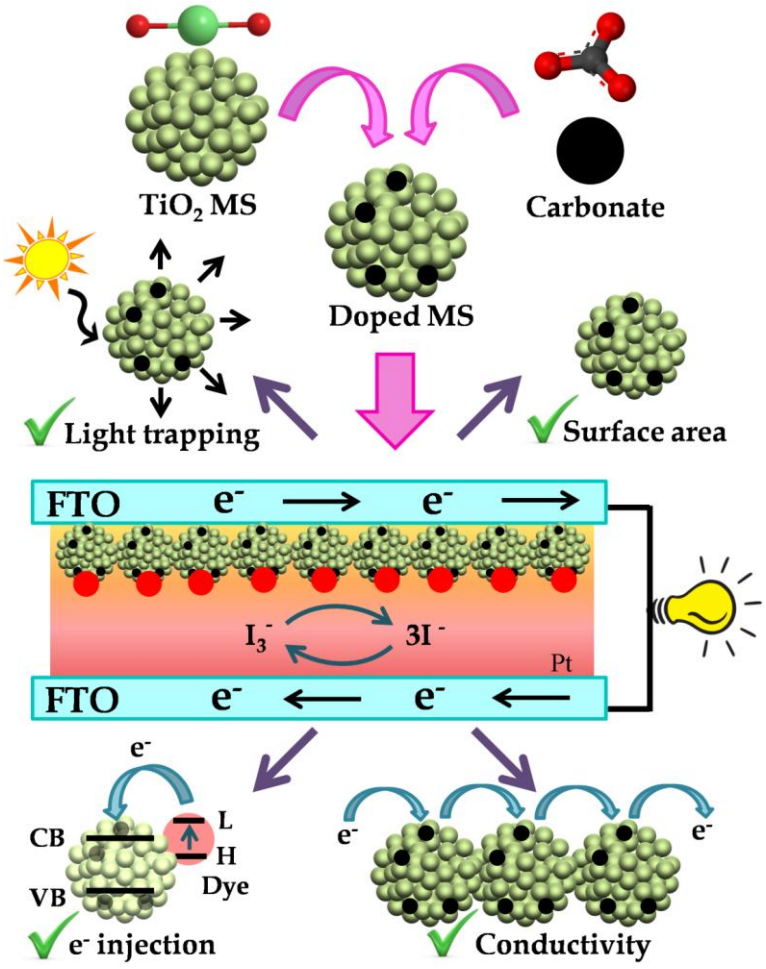

Scheme 8.1. *Schematic presentation. Synthesis of doped TiO_2 MS and their advantages in the dye-sensitized solar cells.*

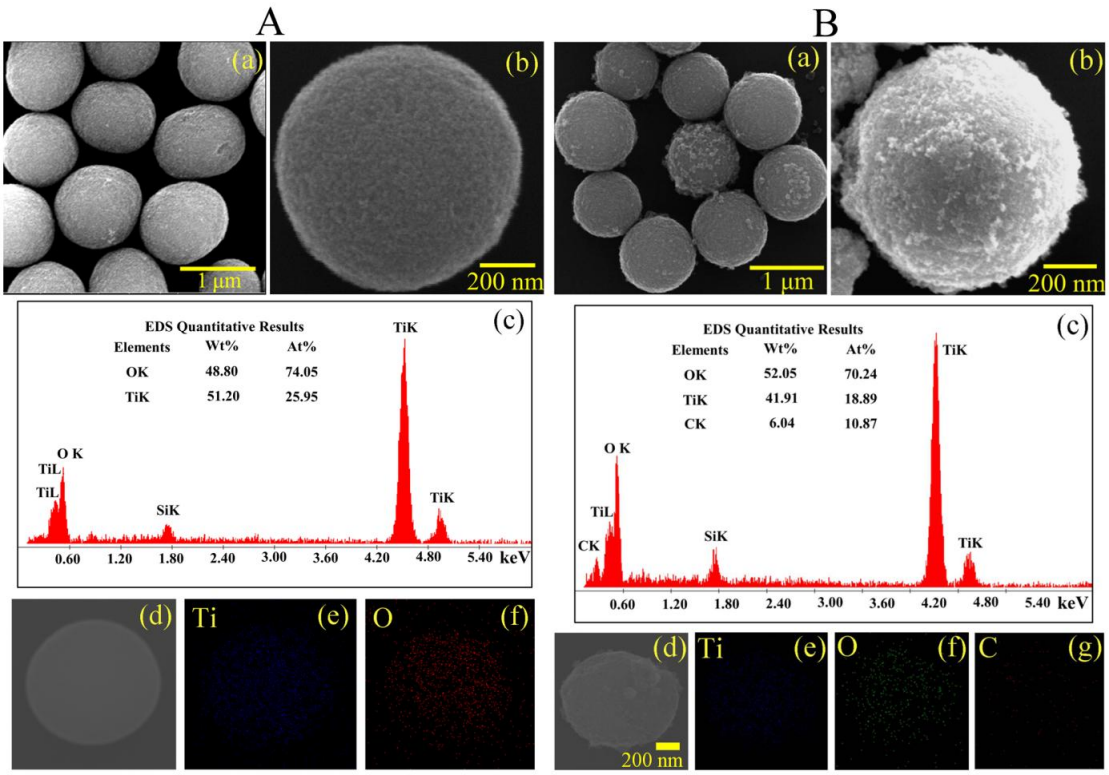

Figure 8.1. *Characterization of TiO_2 MS and doped TiO_2 MS. (A) SEM images (a and b); EDAX spectrum (c); SEM image of a single particle (d) and Ti, O elemental mapping images of that particle (e, f) of TiO_2 MS. (B) SEM images (a and b); EDAX spectrum (c); SEM image of a single particle (d) and Ti, O, C elemental mapping images of that particle (e, f, g) of doped TiO_2 MS.*

microscopy (SEM) image of TiO_2 MS with a diameter range 1-1.1 µm obtained by solvothermal treatment at 180 ^oC for 12 h. Densely-packed, interconnected TiO_2 nanocrystals are clearly visible in the high resolution image as shown in Figure 8.1-A-b. Figure 8.1-A-c shows EDAX spectrum of the microspheres with the relative distribution of oxygen and titanium. The elemental EDAX mapping of the microspheres for Ti and O and their distribution in a microsphere are shown in Figure 8.1-A-(d-f), consistent with uniform distribution of the element in the sample. No signature of carbon in this sample is evident. In Figure 8.1-B-a, we have shown SEM images of the doped MS. The distribution lies in the range of 0.9-1 µm, which is slightly smaller than that of the undoped MS. Similar interconnection of the TiO_2 nanocrystals with a bit higher porosity is evident from Figure 8.1-B-b. The EDAX spectrum (Figure 8.1-B-c), the elemental mapping for Ti,

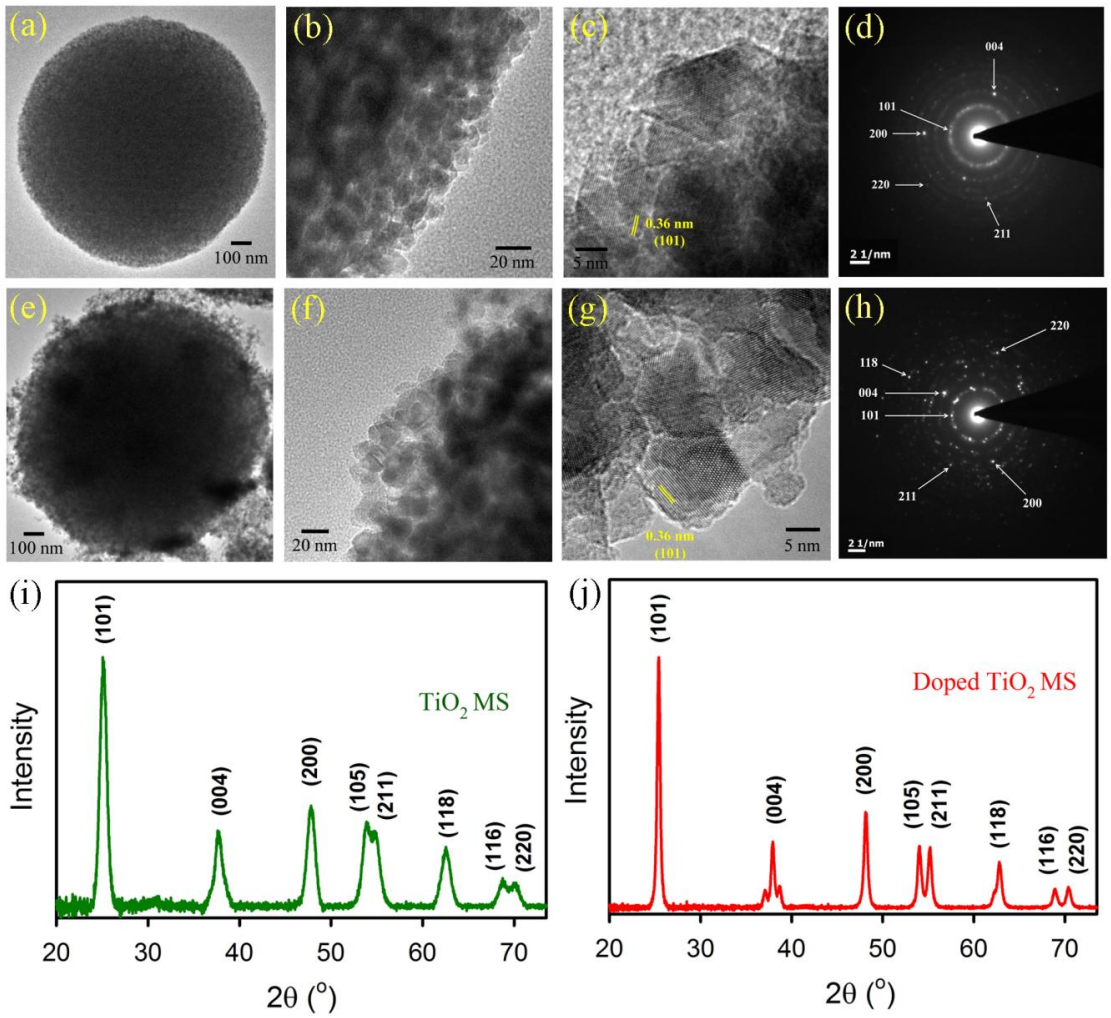

Figure 8.2. *Characterization of TiO_2 MS and doped TiO_2 MS. TEM and HRTEM images (a-c), SAED patterns (d), powder XRD patterns (i) of TiO_2 MS. TEM and HRTEM images (e-g), SAED patterns (h), powder XRD patterns (j) of doped TiO_2 MS.*

O and C (Figure 8.1-B-(d-g)) and their atomic percentages clearly show uniform C-doping in the microsphere. In an earlier report on the synthesis of such C-doped nanoparticles, X-ray photoelectron spectroscopy (XPS) was performed and obtained two distinct peaks at 284 eV and 288 eV consistent with C 1s binding energy. While the peak at 284 eV was assigned to carbon adsorbed on the TiO_2 surface as contaminant, the later peaking at around 288 eV was concluded to be the result of Ti-C bonds [27]. Although high resolution microscopy on the samples was out of the scope of the report, the absorption spectrum of the C-doped samples is consistent with our result (see later). The high resolution transmission

electron microscopy (HRTEM) images of the MS before and after doping are shown in Figure 8.2. Relatively higher porosity and similar nanoparticle size of 10-20 nm in the case of doped MS compared to undoped counterpart are clear. The additional porosity and surface roughness in the case of doped MS could be result of surface adsorbed carbon as concluded in the earlier XPS study [27]. As the materials were annealed at 450 ^{o}C for the preparation of working electrode of the DSSC, we have examined the crystalline condition of the materials after the annealing as shown in Figure 8.2 (i, j). We have obtained negligibly small difference in the diffractograms after and before annealing. The diffraction peaks of the undoped and doped samples are not only consistent with that reported in the literature [28], also consistent with the selected area electron diffraction (SAED) patters of the corresponding samples as shown in Figure 8.2 (d, h).

The absorption spectrum of the doped MS is found to be significantly different from that of undoped counterpart as shown in Figure 8.3a. The main electronic band of TiO_2 at ~360 nm is found to be red-shifted to 410 nm upon carbonate doping in addition to significant scattering across the absorption spectrum of N719 in the entire visible solar spectrum. In a recent computational study the density of states (DOS) of undoped and carbonate doped TiO_2 have been performed [26]. The study showed that the carbonate-doping produced band tail states near the valence and conduction band edges of TiO_2 decreasing the band gap by about 0.2 eV. The calculation also demonstrated that the band gap in doped TiO_2 is smaller than that of the undoped one. As shown in Figure 8.3b, the red-shift in the absorption spectrum of the doped MS has significant spectral overlap with green light (~500 nm) emission from two coumarin dyes namely C343 and C500 covalently and non-covalently adsorbed at the TiO_2 surfaces. The ability of absorbing direct sunlight and contributing to the total photoinduced charge carrier in the doped MS are additional advantages over its undoped

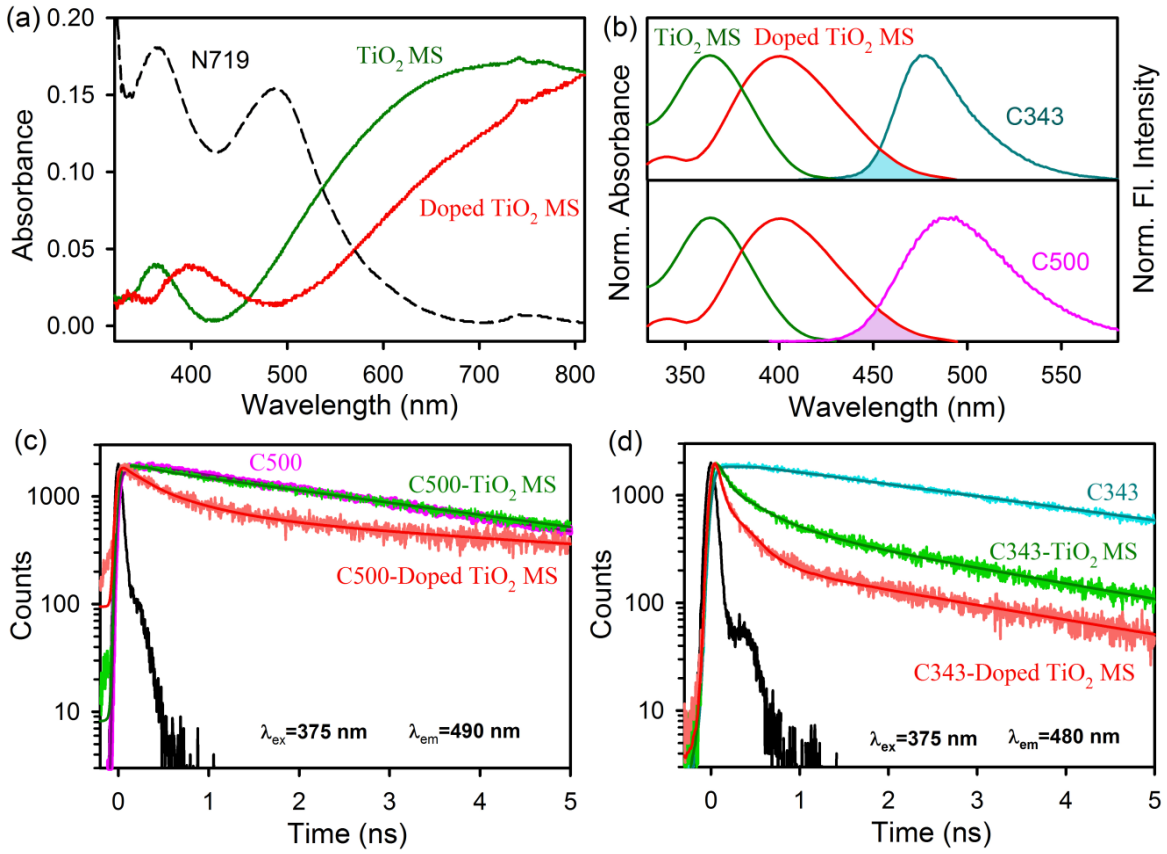

Figure 8.3. *Optical studies of TiO_2 MS and doped TiO_2 MS attached to C343 and C500 dyes. (a) UV-VIS absorption spectra of TiO_2 MS and doped TiO_2 MS. (b) Shows the overlap of C343, C500 emission and doped TiO_2 MS absorption. (c) The picosecond-resolved fluorescence transients of C500 (excitation at 375 nm) in the absence (pink) and in the presence of TiO_2 MS (green) and doped TiO_2 MS (red) collected at 490 nm. (d) The picosecond-resolved fluorescence transients of C343 (excitation at 375 nm) in the absence (cyan) and in the presence of TiO_2 MS (green) and doped TiO_2 MS (red) collected at 480 nm.*

counterpart. N719 dye does not have emission, thus the coumarin dyes are used to study the electron and energy transfer processes. We have quantified the light absorption in terms of Förster resonance energy transfer (FRET) from the green emitting dye C500 adsorbed to the host surface of the MS. As shown in Figure 8.3c, the dye C500 at the doped MS shows faster fluorescence decay compared to C500 at the undoped MS surface revealing resonance energy transfer in the former case [29]. The estimated distance between the dye and the host surface of doped TiO_2 is found to be 1.53 nm, consistent with the surface adsorption of the dye C500. The ultrafast electron injection of the covalently attached coumarin dye

C343 is evident from Figure 8.3d. The spectroscopic and fitting parameters are shown in Table 8.1. It is well known that the covalently adsorbed dye C343 undergoes electron transfer to host TiO_2 upon photoexcitation [30]. The apparent rate constant, k_{nr}, is determined for the nonradiative processes by comparing the lifetimes of C343 in the absence (τ_0) and the presence (τ) of MS, using the following equation [31]:

$$k_{nr} = 1/\langle\tau\rangle - 1/\langle\tau_0\rangle \qquad (8.1)$$

we have estimated that electron transfer rate of the dye C343 at the doped MS ($2.8X10^9$ s^{-1}) is much faster than that at the undoped MS ($1.1X10^9$ s^{-1}). Although a significant spectral overlap of the C343 emission with the absorption band of the doped MS is evident from Figure 8.3b, the possibility of FRET in this case can be ruled out for the interference of much faster electron transfer dynamics.

Table 8.1. *Dynamics of picosecond-resolved luminescence transients of C343, C500 and nanohybrids*[a]

Sample	Excitation wavelength (nm)	Detection wavelength (nm)	τ_1 (ns)	τ_2 (ns)	τ_3 (ns)	τ_{avg} (ns)
C343	375	480	3.88 (100%)			3.88
C343-TiO_2 MS	375	480	0.19 (80.7%)	3.04 (19.3%)		0.74
C343-doped TiO_2 MS	375	480	0.08 (78.3%)	0.35 (16.3%)	3.88 (5.4%)	0.33
C500	375	490	3.25 (100%)			3.25
C500-TiO_2 MS	375	490	3.25 (100%)			3.25
C500-doped TiO_2 MS	375	490	0.35 (66.7%)	3.25 (33.3%)		1.31

[a]*Numbers in the parenthesis indicate relative weightages.*

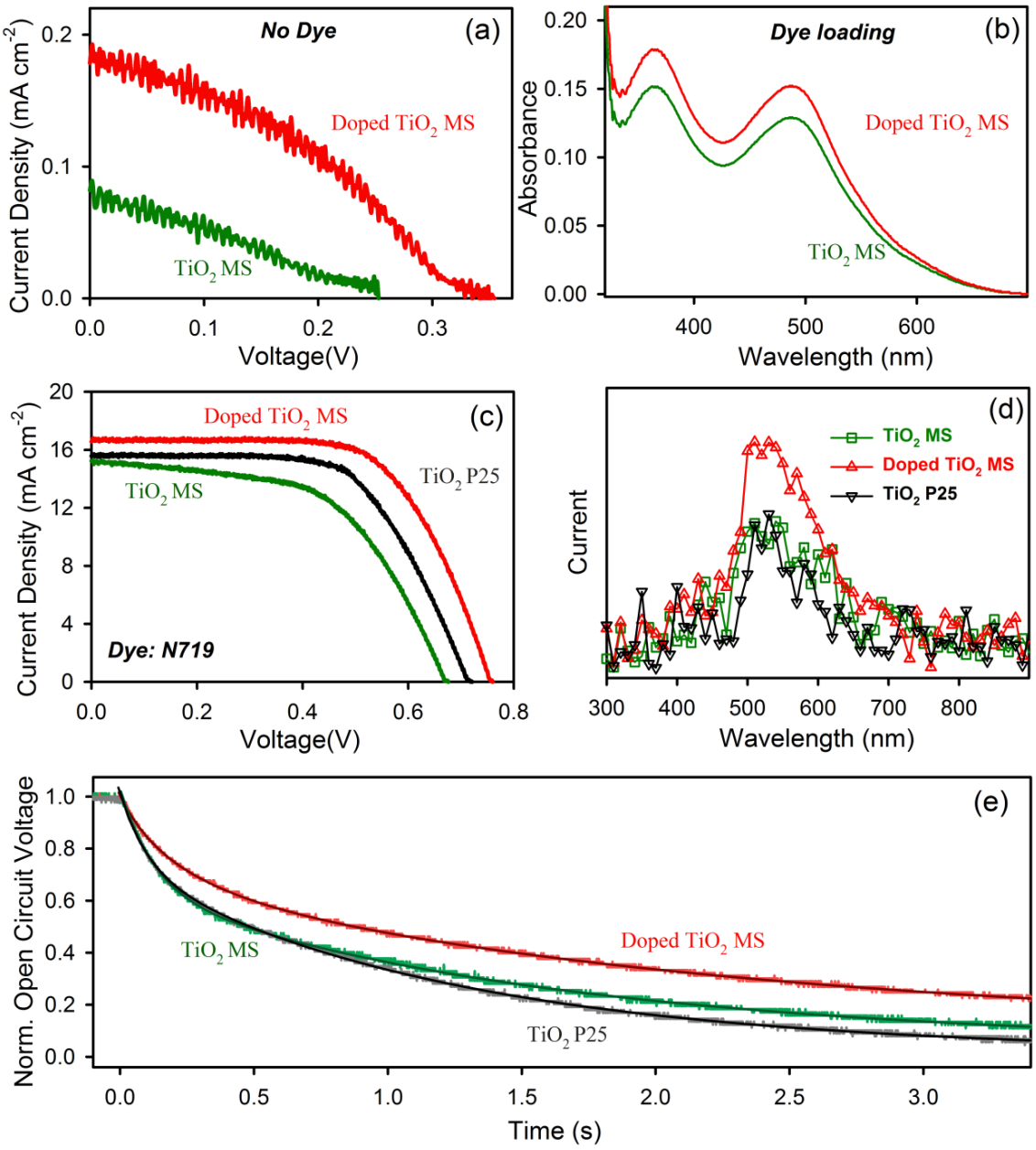

Figure 8.4. *Device performance. I-V characteristics without dye (a) and with N719 dye (c); (b) dye loading; (d) wavelength dependent photocurrent response curves and (e) open circuit voltage decay profiles of different DSSCs fabricated with TiO_2 MS and doped TiO_2 MS.*

The direct light harvesting ability and the better photoconductivity of the doped MS compared to those in its undoped counterpart is evident from I-V characteristics of the solar cell without sensitizing dye (Figure 8.4a). Figure 8.4b shows enhanced dye loading capability of the doped MS because of its better

Table 8.2. *Solar cell performance using different active electrodes*[b]

Photoanode	Dye	J_{sc} (mA cm^{-2})	V_{oc} (V)	Fill Factor	η (%)
TiO_2 MS	No dye	0.08	0.27	38.7	0.01
Doped TiO_2 MS	No dye	0.18	0.35	38.5	0.02
TiO_2 MS	N719	15.2	0.68	54.8	5.16
Doped TiO_2 MS	N719	16.6	0.76	65.6	7.65
TiO_2 NP P25	N719	15.6	0.72	63.2	6.49

[b]*Short-circuit photocurrent densities (J_{SC} cm^{-2}), open-circuit voltage (V_{OC}) and efficiency (η).*

porosity as discussed earlier. The betterment of all the key parameters ultimately enhances the solar cell efficiency as shown in Figure 8.4c. The corresponding values of the photovoltaic parameters, such as the short circuit photocurrent density (J_{sc}), open circuit voltage (V_{oc}), fill factor (FF), power conversion efficiency (η) values are presented in Table 8.2. The DSSC with doped TiO_2 MS shows higher energy conversion efficiency of 7.6% compared to that of the undoped MS (5.2%). The enhancement of photocurrent at the peak absorption of the dye N719 is also studied and shown in Figure 8.4d. The spectra collected from different cells show good agreement between the wavelength of photocurrent maximum and N719 absorption maximum (λ_{max} = 520nm). The temporal decay of the open circuit voltage has been monitored for different cells in the dark following a brief period of illumination as shown in Figure 8.4e, revealing reduced recombination in the case of DSSC with doped MS. The fitted timescales are presented in Table 8.3. The open circuit voltage decay reflects the timescales for the recombination processes of the electron at the conduction band of the semiconductor with the oxidized electrolytes [32]. The increase in V_{oc} as evident from Figure 8.4c is a consequence of reduction in the back electron transfer [33].

Table 8.3. *Dynamics of photovoltage transients of DSSCs fabricated using different active electrodes*[c]

Active Electrode	τ_1 (S)	τ_2 (S)	τ_{avg} (S)
TiO_2 MS	0.13 (38.8%)	1.60 (61.2%)	1.03
Doped TiO_2 MS	0.21 (33.7%)	2.21 (66.3%)	1.54
TiO_2 NP P25	0.11 (28.8%)	1.25 (71.2%)	0.92

[c]*Numbers in the parenthesis indicate relative weightages.*

8.3. Conclusion: Carbonate doped TiO_2 microspheres were synthesized via two step facile solvothermal routes and used as photoanode of a N719 based dye sensitized solar cell (DSSC). Our single-shot modification in the solar cell design is shown to take care of several key parameters including porosity for dye loading, scattering for light trapping, electron injection for photocurrent and less electron recombination with redox coupling for the enhancement of the efficiency of the solar cell as schematically shown in Scheme 8.1. We have compared the efficiency of the DSSC with undoped TiO_2 microsphere and conventional TiO_2 nanoparticle (P25) and found significant improvement in the light harvesting efficiency upon doping. To our knowledge the realization of carbonate doping solar cells provides a novel pathway to control conversion efficiency in DSSC. Future investigations will focus on tailoring the absorption wavelengths of the sensitizing dye for the light trapping in the NIR region of solar radiation, where 49% power remains un-harvested.

References

[1] B. Oregan, M. Gratzel, A Low-Cost, High-Efficiency Solar-Cell Based on Dye-Sensitized Colloidal TiO_2 Films, *Nature* 353 (1991) 737-740.

[2] B.E. Hardin, H.J. Snaith, M.D. McGehee, The Renaissance of Dye-Sensitized Solar Cells, *Nat. Photon.* 6 (2012) 162-169.

[3] J.-W. Shiu, Y.-C. Chang, C.-Y. Chan, H.-P. Wu, H.-Y. Hsu, C.-L. Wang, C.-Y. Lin, E.W.-G. Diau, Panchromatic Co-Sensitization of Porphyrin-Sensitized Solar Cells to Harvest Near-Infrared Light beyond 900 nm, *J. Mater. Chem. A* 3 (2015) 1417-1420.

[4] C.-L. Wang, J.-Y. Hu, C.-H. Wu, H.-H. Kuo, Y.-C. Chang, Z.-J. Lan, H.-P. Wu, E. Wei-Guang Diau, C.-Y. Lin, Highly Efficient Porphyrin-Sensitized Solar Cells with Enhanced Light Harvesting Ability beyond 800 nm and Efficiency Exceeding 10%, *Energy Environ. Sci.* 7 (2014) 1392-1396.

[5] S. Mathew, A. Yella, P. Gao, R. Humphry-Baker, F.E. CurchodBasile, N. Ashari-Astani, I. Tavernelli, U. Rothlisberger, K. NazeeruddinMd, M. Grätzel, Dye-Sensitized Solar Cells with 13% Efficiency Achieved through the Molecular Engineering of Porphyrin Sensitizers, *Nat. Chem.* 6 (2014) 242-247.

[6] A. Yella, H.-W. Lee, H.N. Tsao, C. Yi, A.K. Chandiran, M.K. Nazeeruddin, E.W.-G. Diau, C.-Y. Yeh, S.M. Zakeeruddin, M. Grätzel, Porphyrin-Sensitized Solar Cells with Cobalt (II/III)–Based Redox Electrolyte Exceed 12 Percent Efficiency, *Science* 334 (2011) 629-634.

[7] H.N. Tsao, C. Yi , T. Moehl, J.-H. Yum, S.M. Zakeeruddin, M.K. Nazeeruddin, M. Grätzel, Cyclopentadithiophene Bridged Donor–Acceptor Dyes Achieve High Power Conversion Efficiencies in Dye-Sensitized Solar Cells Based on the Tris-Cobalt Bipyridine Redox Couple, *ChemSusChem* 4 (2011) 591-594.

[8] H. Nusbaumer, S.M. Zakeeruddin, J.-E. Moser, M. Grätzel, An Alternative Efficient Redox Couple for the Dye-Sensitized Solar Cell System, *Chem. Eur. J.* 9 (2003) 3756-3763.

[9] L.-P. Heiniger, F. Giordano, T. Moehl, M. Grätzel, Mesoporous TiO_2 Beads Offer Improved Mass Transport for Cobalt-Based Redox Couples Leading to High Efficiency Dye-Sensitized Solar Cells, *Adv. Energy Mater.* 4 (2014) 1400168.

[10] F. Sauvage, D. Chen, P. Comte, F. Huang, L.-P. Heiniger, Y.-B. Cheng, R.A. Caruso, M. Graetzel, Dye-Sensitized Solar Cells Employing a Single Film of Mesoporous TiO_2 Beads Achieve Power Conversion Efficiencies over 10%, *ACS Nano* 4 (2010) 4420-4425.

[11] Z.-Q. Li, W.-C. Chen, F.-L. Guo, L.-E. Mo, L.-H. Hu, S.-Y. Dai, Mesoporous TiO_2 Yolk-Shell Microspheres for Dye-Sensitized Solar Cells with a High Efficiency Exceeding 11%, *Sci. Rep.* 5 (2015) 14178.

[12] M. Grätzel, Recent Advances in Sensitized Mesoscopic Solar Cells, *Acc. Chem. Res.* 42 (2009) 1788-1798.

[13] M. Grätzel, Dye-Sensitized Solar Cells, *J. Photochem. Photobiol. C* 4 (2003) 145-153.

[14] N.C. Jeong, C. Prasittichai, J.T. Hupp, Photocurrent Enhancement by Surface Plasmon Resonance of Silver Nanoparticles in Highly Porous Dye-Sensitized Solar Cells, *Langmuir* 27 (2011) 14609-14614.

[15] S.D. Standridge, G.C. Schatz, J.T. Hupp, Distance Dependence of Plasmon-Enhanced Photocurrent in Dye-Sensitized Solar Cells, *J. Am. Chem. Soc.* 131 (2009) 8407-8409.

[16] T. Bora, H.H. Kyaw, S. Sarkar, S.K. Pal, J. Dutta, Highly Efficient ZnO/Au Schottky Barrier Dye-Sensitized Solar Cells: Role of Gold Nanoparticles on the Charge-Transfer Process, *Beilstein J. Nanotechnol.* 2 (2011) 681-690.

[17] X. Chen, B. Jia, Y. Zhang, M. Gu, Exceeding the Limit of Plasmonic Light Trapping in Textured Screen-Printed Solar Cells Using Al Nanoparticles and Wrinkle-Like Graphene Sheets, *Light Sci. Appl.* 2 (2013) e92.

[18] Y.P. Lin, S.Y. Lin, Y.C. Lee, Y.W. Chen-Yang, High Surface Area Electrospun Prickle-Like Hierarchical Anatase TiO_2 Nanofibers for Dye-Sensitized Solar Cell Photoanodes, *J. Mater. Chem. A* 1 (2013) 9875-9884.

[19] N. Guijarro, Q. Shen, S. Giménez, I. Mora-Seró, J. Bisquert, T. Lana-Villarreal, T. Toyoda, R. Gómez, Direct Correlation between Ultrafast Injection and Photoanode Performance in Quantum Dot Sensitized Solar Cells, *J. Phys. Chem. C* 114 (2010) 22352-22360.

[20] H.-J. Son, C.H. Kim, D.W. Kim, N.C. Jeong, C. Prasittichai, L. Luo, J. Wu, O.K. Farha, M.R. Wasielewski, J.T. Hupp, Post-Assembly Atomic Layer Deposition of Ultrathin Metal-Oxide Coatings Enhances the Performance of an Organic Dye-Sensitized Solar Cell by Suppressing Dye Aggregation, *ACS Appl. Mater. Interfaces* 7 (2015) 5150-5159.

[21] K. Zhu, N.R. Neale, A. Miedaner, A.J. Frank, Enhanced Charge-Collection Efficiencies and Light Scattering in Dye-Sensitized Solar Cells Using Oriented TiO_2 Nanotubes Arrays, *Nano Lett.* 7 (2007) 69-74.

[22] J. van de Lagemaat, N.G. Park, A.J. Frank, Influence of Electrical Potential Distribution, Charge Transport and Recombination on the Photopotential and Photocurrent Conversion Efficiency of Dye-Sensitized Nanocrystalline TiO_2 Solar Cells: A Study by Electrical Impedance and Optical Modulation Techniques, *J. Phys. Chem. B* 104 (2000) 2044-2052.

[23] K.D. Benkstein, N. Kopidakis, J. van de Lagemaat, A.J. Frank, Influence of the Percolation Network Geometry on Electron Transport in Dye-Sensitized Titanium Dioxide Solar Cells, *J. Phys. Chem. B* 107 (2003) 7759-7767.

[24] Z.S. Seddigi, S.A. Ahmed, S. Sardar, S. Kumar Pal, Carbonate Doping in TiO_2 Microsphere: The Key Parameter Influencing Others for Efficient Dye Sensitized Solar Cell, *Sci. Rep.* 6 (2016) 23209.

[25] Z.-Q. Li, Y.-P. Que, L.-E. Mo, W.-C. Chen, Y. Ding, Y.-M. Ma, L. Jiang, L.-H. Hu, S.-Y. Dai, One-Pot Synthesis of Mesoporous TiO_2 Microperes and Its Application for High-Efficiency Dye-Sensitized Solar Cells, *ACS Appl. Mater. Interfaces* 7 (2015) 10928-10934.

[26] B. Liu, L.-M. Liu, X.-F. Lang, H.-Y. Wang, X.W. Lou, E.S. Aydil, Doping High-Surface-Area Mesoporous TiO_2 Microspheres with Carbonate for Visible Light Hydrogen Production, *Energy Environ. Sci.* 7 (2014) 2592-2597.

[27] T. Ohno, T. Tsubota, K. Nishijima, Z. Miyamoto, Degradation of Methylene Blue on Carbonate Species-Doped TiO_2 Photocatalysts under Visible Light, *Chem. Lett.* 33 (2004) 750-751.

[28] X. Wei, G. Zhu, J. Fang, J. Chen, Synthesis, Characterization, and Photocatalysis of Well-Dispersible Phase-Pure Anatase TiO_2 Nanoparticles, *Int. J. Photoenergy* 2013 (2013) 6.

[29] P. Majumder, R. Sarkar, A.K. Shaw, A. Chakraborty, S.K. Pal, Ultrafast Dynamics in a Nanocage of Enzymes: Solvation and Fluorescence Resonance Energy Transfer in Reverse Micelles, *J. Colloid Interface Sci.* 290 (2005) 462-474.

[30] J.M. Rehm, G.L. McLendon, Y. Nagasawa, K. Yoshihara, J. Moser, M. Grätzel, Femtosecond Electron-Transfer Dynamics at a Sensitizing Dye−Semiconductor (TiO_2) Interface, *J. Phys. Chem.* 100 (1996) 9577-9578.

[31] K. Tvrdy, P.A. Frantsuzov, P.V. Kamat, Photoinduced Electron Transfer from Semiconductor Quantum Dots to Metal Oxide Nanoparticles, *Proc. Natl. Acad. Sci. USA* 108 (2011) 29-34.

[32] H. Choi, Y.-S. Chen, K.G. Stamplecoskie, P.V. Kamat, Boosting the Photovoltage of Dye-Sensitized Solar Cells with Thiolated Gold Nanoclusters, *J. Phys. Chem. Lett.* 6 (2015) 217-223.

[33] J.G. Doh, J.S. Hong, R. Vittal, M.G. Kang, N.G. Park, K.J. Kim, Enhancement of Photocurrent and Photovoltage of Dye-Sensitized Solar Cells with TiO_2 Film Deposited on Indium Zinc Oxide Substrate, *Chem. Mater.* 16 (2004) 493-497.

Chapter 9

Key Light Harvesting Dynamics in Various Nanostructures for Biomedical Application

9.1. Introduction: In recent years, use of nanotechnology in medical science is gaining a lot of attention across the world. Research focusing on the use of various nanostructured materials in different areas, such as for drug delivery [1], cancer treatments [2-3] etc. is underway. Out of the numerous nanostructured materials, zinc oxide (ZnO) is one of the most promising materials for the applications in the medical fields due to its biocompatibility, biodegradability and non-toxicity [4]. Moreover, ZnO can degrade various organic compounds efficiently through photocatalysis [5-6]. It has been reported that the native defects in the ZnO lattice, mostly the oxygen vacancy sites, play an important role in the photocatalytic activity of the nanostructures [6]. Oxygen vacancies have been reported as the cause of the characteristic green luminescence of ZnO [7-9], which exist in three charged states: singly charged (V_O^+), doubly charged (V_O^{++}) and neutral (V_O^x). The presence of the oxygen vacancies and other native defects in the ZnO lattice reduces the direct e^-/h^+ recombination process thus increasing the quantum yield of ZnO nanocrystalline photocatalysts. Furthermore, defect mediated energy emitted from the ZnO nanostructures can also effectively degrade various organic compounds in water through Förster Resonance Energy Transfer (FRET) [10]. Hence, for an efficient ZnO nanostructure based photocatalysis system, the control of such defect sites is a crucial factor. One of the effective ways to modulate the concentration of defect density in the ZnO lattices is to anneal the ZnO nanostructures in an oxygen rich atmosphere. The effect of post-annealing treatment on the native defects of ZnO has been studied extensively and it has been demonstrated that the crystallinity of ZnO can be improved by annealing the

samples at a higher temperature, typically above 500 °C [11-15]. However, some studies show that annealing at higher temperatures can also introduce defects, such as oxygen interstitials in the ZnO lattice [16-17].

In the first work of this chapter, we have explored the potential use of ZnO NPs as a phototherapy agent, by controlling the surface defect states of the nanoparticles through a post-annealing treatment in oxygen rich atmosphere, in order to efficiently degrade BR molecules through photocatalysis. Bilirubin (BR) is a yellow-orange pigment which is a byproduct of normal heme catabolism in mammals. In human body, 250–400 mg BR is produced every day [18], that can exist both as a free molecule and as an albumin complex in the body. The unconjugated ZZ-BR isomer is water insoluble, which is converted to water soluble ZE-BR isomer in the liver with the assistance of glucuronic acid following which most are extracted in the bile while a small portion passes through urine [19]. Excess bilirubin in blood can lead to deposits on tissues, giving rise to neurotoxicity and hyperbilirubinemia or yellowish pigmentation of the skin, a disease commonly known as Jaundice. According to World Health Organization, almost 30,000 people suffering from jaundice die every year [20]. Jaundice is most commonly seen in newly born babies, known as Neonatal Jaundice, which typically develops within a few weeks of birth. There can be many sources for neonatal jaundice, like weak liver function, high level of red blood cells in blood and deficiency in the important enzymes in the body [21]. At present, phototherapy, a technique used to treat various diseases under light irradiation, is the most widely used treatment for neonatal jaundice in the medical field, where unconjugated ZZ-BR isomers are converted to water soluble ZE-BR isomers using a light source. Under the light radiation, the unconjugated ZZ-BR isomer undergoes rearrangement of its molecular structure forming either structural or configurational water soluble isomers. Additionally, upon absorption of light, the ZZ-BR isomers can also react with oxygen in the blood forming colorless oxidation

products, which are typically extracted via urine [19]. However, the photo-oxidation of ZZ-BR is a slow process and isomerization of ZZ-BR occurs much faster than the photo-oxidation [22]. In one of our recent studies, it was demonstrated that upon surface adsorption of BR molecules on ZnO nanostructures, defect mediated energy from the photo-excited ZnO nanostructures resonantly transfers to the BR molecules inducing their photodegradation [10]. It was also demonstrated that the system can effectively degrade BR when it is bound to albumin. Although literature related to the molecular transformation of water insoluble BR via photocatalysis process is limited, a few studies are available on the photocatalytic degradation of BR adsorbed on nanostructured hydroxyapatite coating [23] or molecularly imprinted titania film [24], amongst others. The current study focuses on the efficient utilization of the defect mediated emission from the ZnO NPs, modulated through post-annealing of the nanoparticles, in order to improve the overall efficiency of the FRET process and hence to expedite the photocatalytic degradation of BR molecules. By using steady state and picosecond-resolved fluorescence spectroscopy techniques, we have explored the influence of the surface defect states (mainly the oxygen vacancies) of the various annealed and as-synthesized ZnO NPs on the photocatalytic degradation process of BR.

The use of nanoscale materials in delivering drugs precisely and safely to the target site at the right time and with maximum impact provides great opportunity in the area of drug delivery. These nanoscale materials facilitate high drug loading due to their large surface to volume ratio and consequently minimize the toxicity by their preferential accumulation at the target site. Nanoparticle-based drug delivery systems have many other advantages such as, improving solubility of hydrophobic drugs and also prolonging the half-life of drug systemic circulation by reducing immunogenicity [25-26]. A number of nanoparticle-based therapeutic and diagnostic agents have been successfully

introduced in the treatment of diabetes, pain, cancer and infectious diseases [27-32]. However, most of the nanoparticles are toxic to animals and very less biocompatible in vivo [33-35]. Among them ZnO NPs have shown promising potential as drug delivery vehicles due to their low cost, good biocompatibility and low toxicity [36-38]. Unfortunately, because of its large band gap of 3.3 eV, the popular ZnO can be activated only by UV light of wavelength <375 nm. UV light is not suitable for most in vivo experiments because it can only penetrate the skin by several millimeters and is harmful to the human body. However, ZnO NPs as efficient drug carriers in photodynamic therapies (PDT) which avoid non-significant accumulation of the drug at the target site have attracted considerable research interest [39].

Photodynamic therapy (PDT) is a promising noninvasive treatment for cancer which involves the uptake of a photosensitizer by cancer tissue followed by photoirradiation [40-42]. Protoporphyrin IX (PP) is a very well-known cancer drug and efficient hydrophobic photosensitizer (PS) for PDT [43]. The efficiency of PDT depends on photoactivation of the photosensitizers accumulated at the target site and the pharmacokinetic properties of the photosensitizer to achieve the desired biological response. Due to very low water solubility of hydrophobic drugs like PP, several strategies have been employed to prepare stable formulations, including conjugation to water-soluble polymers or encapsulation in colloidal carriers such as oil-in-water emulsions, [44] gold NPs, [45-46] polymer NPs [47-48], microspheres [49] and block copolymer micelles [50-51]. Majid and co-workers [39] have shown that PEGylated ZnO NPs coated with PP exhibit an excellent anticancer effect due to countable localization of the drug in the targeted area in the presence of a suitable light dose. ZnO NPs loaded with drugs can penetrate cancer cells through specific ligand-receptor recognition or non-specific binding forces based on hydrophobic or coulombic interactions [36]. The stability of the combination of the ZnO and the drug molecules is very important. The guest drug

molecules should not leak from the host surface during blood circulation in vivo, so strong interactions with ZnO carriers are necessary, e.g., covalent bonds. The drug molecules have to be released from these carriers easily at the target site. The tumor and cancer cells have acidic environments and ZnO NPs are decomposed completely at pH 5 in aqueous solution, therefore drugs can be released easily by ZnO nanocarriers at the target site [52].

The photochemical and photophysical processes in the PS during PDT are the key for the generation of reactive oxygen species (ROS). When a PS in its ground state is exposed to light of a specific wavelength, it absorbs a photon and is promoted to an excited singlet state. The singlet state is eventually decayed to triplet excited state via intersystem crossing (ISC) and then the triplet state energy is transferred to ground state molecular oxygen to produce singlet oxygen. It is the cytotoxicity of the singlet oxygen which can cause oxidation of biomolecules and, finally, cell death. The enhancement in the ROS generation can essentially increase the overall activity of a PS, thereby reducing the concentration of the essential photosensitizer. Therefore, the electron−hole separation in PS, immediately after the photoexcitation, is a key-step to enhance the average ROS concentration. In this context, photoinduced electron transfer between drugs and colloidal semiconductors plays a vital role where the rapid charge injection from sensitizer molecules to the conduction band (CB) of the semiconductor followed by the generation of ROS may enhance the activity of the PS. This necessitates the exploration of photoinduced ultrafast dynamics in PP-ZnO nanohybrid as a potential photodynamic agent.

In this chapter, we have also exploreed the key photoinduced dynamics in ZnO upon complexation with a model cancer drug PP, which eventually leads to the enhanced efficiency in PDT and successful realization of ZnO NPs as drug delivery vehicle of cancer drugs. To study the nanohybrid formation at the molecular level, picosecond-resolved FRET from the defect emission of ZnO to PP

has been used. Picosecond-resolved fluorescence studies on PP−ZnO nanohybrid also reveal efficient electron migration from photoexcited PP to ZnO, eventually enhancing the ROS activity in the PP-ZnO nanostructures. In addition, we have used a well-known electron acceptor, p-benzoquinone (BQ) to emphasize the electron-donating efficiency of PP upon photo-excitation. The dichlorofluorescin (DCFH) oxidation and no oxidation of luminol in PP/PP-ZnO nanohybrids upon green light illumination indicate that the nature of ROS is essentially singlet oxygen rather superoxide anions. PP-ZnO nanohybrids were employed to construct photoelectrode that lead to enhanced photocurrent. We have also used the nanohybrid in a model photodynamic therapy application in bacteriological culture experiment.

9.2. Results and Discussion:

9.2.1. Modulation of Defect Mediated Energy Transfer from ZnO Nanoparticles for the Photocatalytic Degradation of Bilirubin [53]: Figure 9.1a shows the UV/Vis optical absorption spectra of the as-synthesized ZnO NPs and the particles annealed in air at different temperatures. The as-synthesized ZnO NPs show a sharp absorbance onset at about 340 nm indicating almost uniform size of the NPs. However, upon annealing at higher temperatures, a slight red-shift in the absorption spectra of the nanoparticles was observed indicating a marginal increase in the size of the ZnO NPs after annealing [54]. The changes in the crystallite size of the NPs after annealing were estimated from their respective XRD patterns (Figure 9.1b) using Scherrer equation. The crystallite size of the as-synthesized ZnO NPs was found to be about 7.3 nm that marginally increases upon annealing to 7.8 nm at 250 °C. The changes in the sizes of ZnO NPs annealed at different temperatures were further verified by transmission electron microscopy (TEM). Figure 9.2a shows the typical TEM of the fairly monodispersed ZnO NPs annealed at 250 °C. As shown in Figure 9.2b, the lattice fringe

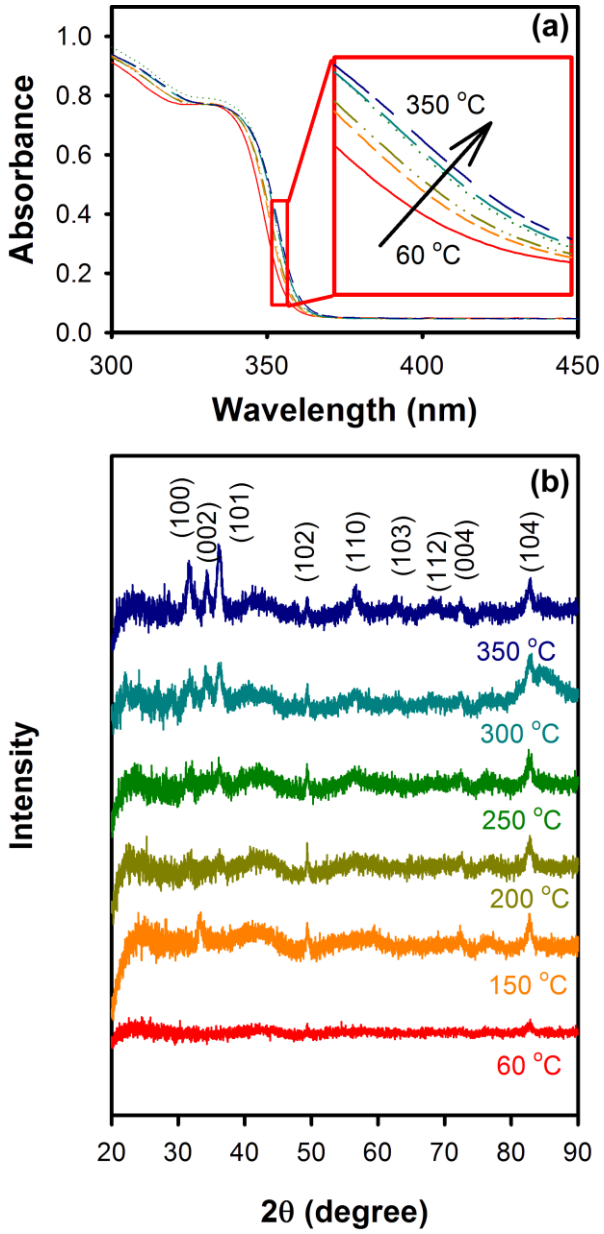

Figure 9.1. *(a) UV/Vis optical absorption and (b) X-ray diffraction pattern of ZnO NPs annealed at various temperatures in air for 1 hour. The 60 °C sample indicates the non-annealed as-synthesized ZnO NPs.*

width of 0.26 nm indicates the (002) plane of the wurtzite structure of ZnO NPs, demonstrating polycrystalline nature confirmed from their corresponding selected area electron diffraction (SAED) pattern (Figure 9.2c). The particle size distribution of all the ZnO NP samples obtained from their respective TEM micrographs are also shown in Figure 9.2d to 9.2i. For the as-synthesized ZnO NPs the mean

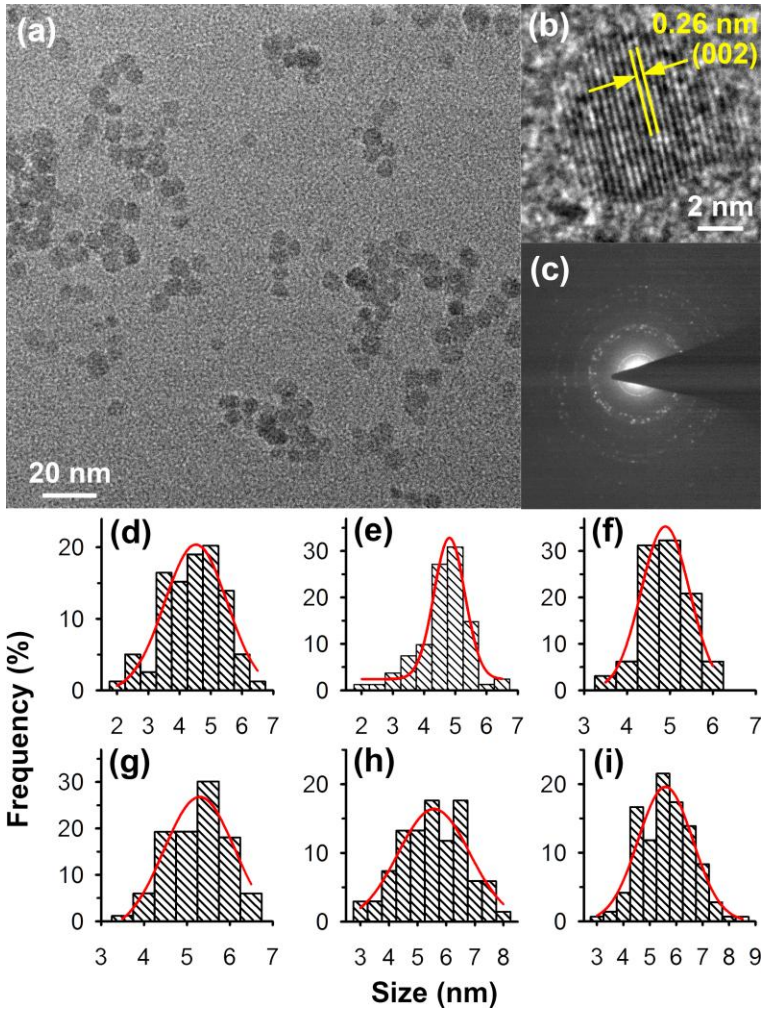

Figure 9.2. *(a) Transmission electron micrograph, (b) high resolution TEM image of a single ZnO NP and (c) SAED pattern of the ZnO NPs annealed at 250 °C. The particle size distribution of the (d) as-synthesized, (e) 150 °C, (f) 200 °C, (g) 250 °C, (h) 300 °C and (i) 350 °C annealed ZnO NPs are also shown.*

particle size was found to be 4.5 nm, while the NPs increased in size upon annealing at higher temperatures corroborating well with our previous observations from XRD analysis. The mean size for the ZnO NPs annealed at 250 °C was obtained as 5.5 nm, and the maximum particle size was obtained in case of the NPs annealed at 350 °C showing a mean particle size of 5.9 nm. Here, it should be noted that the size of the NPs estimated by using Scherrer equation yielded larger crystallite sizes than the size obtained from TEM images. This discrepancy arises due to band broadening in XRD patterns primarily from the inhomogeneous strain on the samples as well as instrumental effect apart from the

actual size of the sample [55]. As a result, size estimation from XRD peaks using Scherrer's equation typically yields larger sizes than the actual sample size that can be obtained from TEM more accurately.

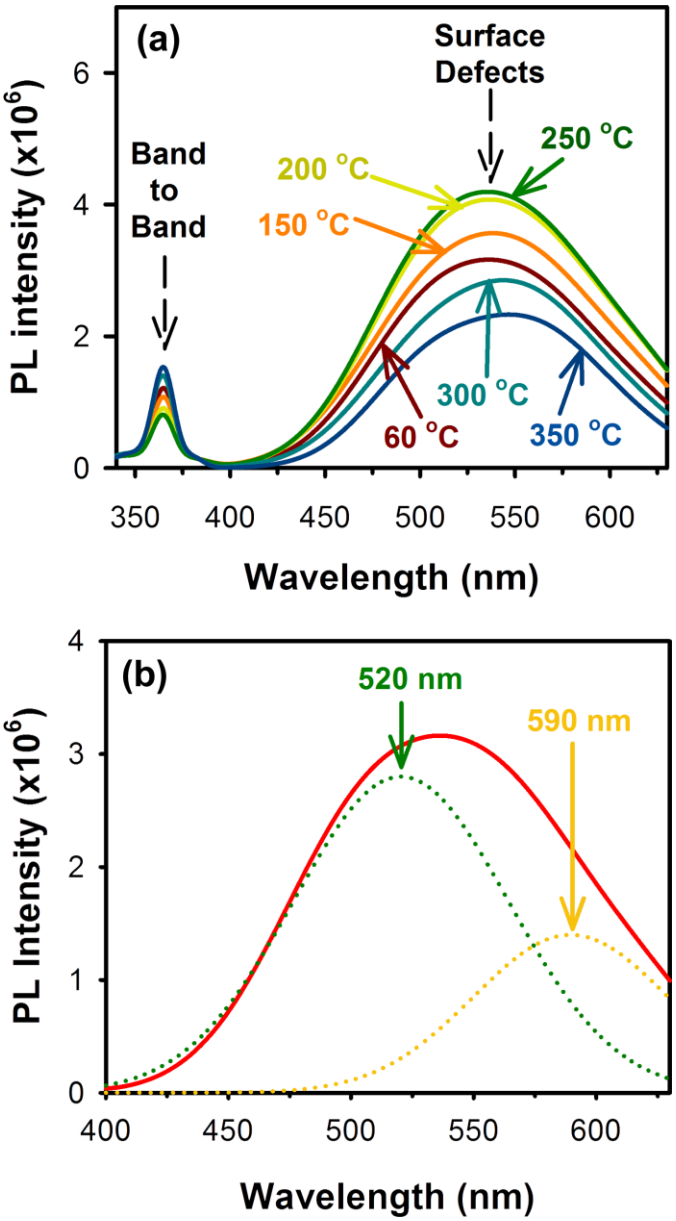

Figure 9.3. *(a) Room temperature photoluminescence (PL) spectra of the ZnO NPs annealed at various temperatures in air for 1 hour (Excitation wavelength: 320 nm) and (b) defect mediated green-yellow emission from ZnO NPs showing the two individual emission bands peaking at 520 nm and 590 nm wavelengths, which are contributed by the singly charged and doubly charged oxygen vacancy states respectively.*

The room temperature photoluminescence (PL) spectra of annealed ZnO NPs are shown in Figure 9.3a. All the NP samples show a small UV emission at ~355 nm, attributed to the near band edge transitions in the ZnO NPs and a large and broad green-yellow emission centered at around 530 nm, attributed to the oxygen vacancy defect states (mostly present at the surface of the NPs) [56]. A. van Dijken et al. [57] has proposed the transition of a photoexcited electron from the conduction band of ZnO to a deep level trap state (V_O^{++}) as the origin of the green luminescence; whereas, Vanheusden et al. [58] reported that the recombination of an electron from V_O^{+} state to a valence band hole lead to the green luminescence peak. In contrast, J. D. Ye et al. [56] has reported that both the above assumptions are correct and demonstrated that the broad green-yellow luminescence from ZnO is mainly composed of two individual emission bands centered at ~ 520 and 590 nm respectively, as shown in Figure 9.3b. It was observed that with increasing annealing temperature the green-yellow emission from the ZnO NPs also increases representing the rise in the surface defect states responsible for the broad green-yellow emission from ZnO. Maximum defect originated emission was observed from ZnO NPs annealed at 250 °C. These observations show that upon annealing the ZnO NPs up to 250 °C in air, the concentration of the surface defect sites in the NPs gradually increases. Previously it was observed that the ZnO NPs grow slowly along with the annealing temperatures demonstrating gradual improvement in their crystallinity, as can be evidenced from TEM and XRD analysis, respectively. However, at the same time, they also show higher defect densities near their surface for annealing temperatures up to 250 °C. In case of the as synthesized ZnO NPs, initially defects are randomly created within the particles as they grow and hence defects are located randomly from the core to the surface of the particles. As the particles are subjected to high temperature annealing, the defects within the particles start to diffuse inside out, i.e. from the core of the particles towards the surface, increasing the defect densities near the surface of the particles. This results in a gradual increase of the surface defect

mediated green-yellow emission peak of the ZnO NPs annealed up to 250 °C. It should be noted that during the process the core of the particles gets annealed first; however, the total defect concentration within the particle volume remains almost similar since no sintering of the particles were observed upon annealing at such low temperatures. Although the ZnO NPs annealed at 250 °C demonstrated slightly higher crystallite size (5.5 nm) than the as synthesized NPs (4.5 nm), only a marginal improvement in the crystallinity of the NPs were observed from the XRD pattern compared to the as synthesized particles due to the relatively unchanged total defect concentration within the particle volume. For the ZnO NPs annealed at temperatures above 250 °C, significant drop in the surface defect mediated emission band was observed indicating reduction in the oxygen vacancy states. In this regard, recently Wei et al. [59] has reported that at annealing temperatures above 300 °C, oxygen vacancies can be eliminated from the ZnO crystal lattice as well as the Zn–O bonding can be enhanced, which further confirms the observed reduction in the intensity of the green-yellow emission band from samples annealed at temperatures above 250 °C. Improvement in the ZnO crystal stoichiometry upon annealing at temperatures above 250 °C can also be evident from the higher band to band emission of the annealed NPs (Figure 9.3a) as well as from their respective XRD spectra (Figure 9.1b).

Following the optical characterization of the ZnO NP samples annealed at various temperatures, we have explored the effect of the concentration of the surface defects in the ZnO NPs on the efficient photocatalytic degradation of BR using the NPs as a photocatalyst medium. The photocatalytic degradation of BR was conducted by using a 7 μM BR solution prepared in chloroform, which shows an absorption peak at 450 nm (inset of Figure 9.4). Under UV light irradiation, the photocatalytic degradation of BR in the presence and absence of different ZnO NP samples were studied by constantly monitoring the absorption spectra of BR

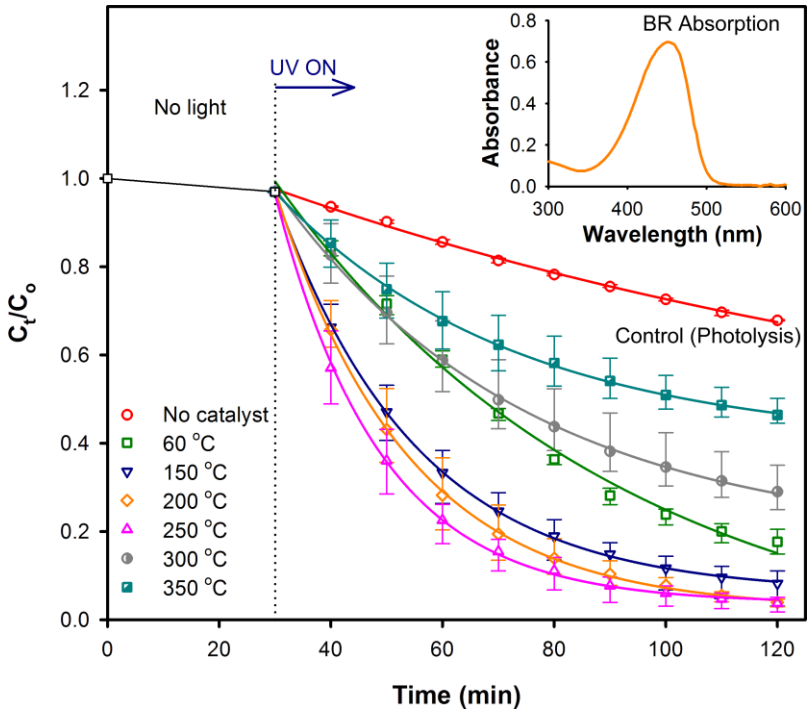

Figure 9.4. *Relative concentration (C_t/C_o) of BR with varying UV irradiation time during photocatalytic degradation (monitored for BR peak absorbance at 450 nm) in the absence (control) and presence of ZnO np catalysts air annealed at different temperatures. Adsorption of BR on ZnO surface under no light condition was carried out for 30 minutes prior to the UV light irradiation. Inset shows the UV-Vis absorption spectrum of the BR solution.*

solution at 450 nm wavelength over a period of 90 minutes. The BR adsorption on ZnO surface in dark was studied over a period of 1 hour and it was found that irrespective of the annealing temperatures of the ZnO NPs an equilibrium adsorption reaches in about 30 minutes. All the adsorption curves were found to be Langmuir type. Figure 9.4 shows the relative concentration (C_t/C_o) of BR with respect to UV irradiation time in the absence and presence of ZnO NPs, with a BR adsorption period in dark of 30 minutes. A control experiment was performed in the absence of ZnO NPs and the photolytic degradation of BR was monitored. In the absence of a catalyst, about 30% degradation in BR concentration was observed upon UV light irradiation for 90 minutes. However, in the presence of the ZnO NPs as the catalyst medium, much faster degradation of BR was observed. In this context, it has been previously shown that the defect mediated energy transfer from the surface defects of ZnO NPs to the BR molecules via

Förster Resonance Energy Transfer (FRET) mechanism is the pre-dominant reason for the faster degradation of BR molecules under UV irradiation in the presence of ZnO NPs [10]. Upon inclusion of the as-synthesized ZnO NPs (hydrolyzed at ~60 °C) in BR, almost 50% degradation was observed to occur within 40 minutes of UV irradiation, leading to about 70% faster photocatalytic reduction of BR compared to the degradation of BR in 40 minutes when no catalyst was used. The reduction in the BR concentration increased further when annealed ZnO NPs (up to 250 °C) were employed as the photocatalysts due to their higher concentrations of surface defects compared to the as-synthesized NPs, resulting in higher energy transfer between the donor ZnO and acceptor BR molecules. The course of BR photocatalytic degradation were found to follow a first-order exponential equation, showing maximum photocatalytic activity for the ZnO NPs annealed at 250 °C, attributed to the increased surface defect states. However, when the surface defects were reduced by annealing the ZnO NPs at temperatures above 250 °C, significant drop in the catalytic activity was observed suggesting the vital role of the surface defects in the photocatalytic degradation of BR. It should be noted that since the FRET process between the ZnO NPs and the BR molecules does not interfere in the normal phototherapy process of BR under UV irradiation. Hence, the photoproducts formed after the photocatalysis of BR in the presence of ZnO NPs should mainly contain the structural (Z-lumirubin) and configurational (ZE-BR) isomers of water insoluble BR, which are the usual photoproducts of BR phototherapy [19]. In addition, the presence of Methylvinylmaleimide (MVM) as an outcome of the photocatalytic degradation of BR in the presence of ZnO NPs has also been evidenced in our previous study [10].

In order to obtain further insight on the influence of defect concentration of the ZnO NP samples on the BR photocatalytic degradation rate (R_o), we conducted photocatalysis experiments with different initial concentrations (C_o) of BR,

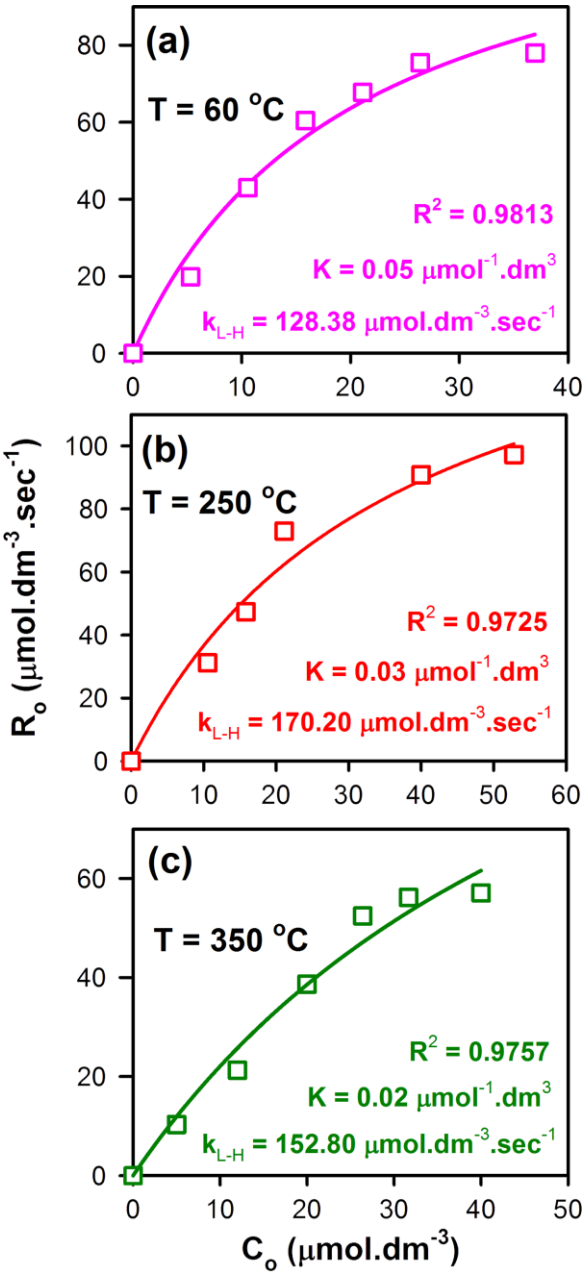

Figure 9.5. *Langmuir-Hinshelwood (L-H) plot showing the Langmuir–Hinshelwood rate constant ($k_{L\text{-}H}$), Langmuir adsorption coefficient (K) and regression coefficients (R^2) for the photocatalytic reactions conducted by using (a) the as-synthesized, (b) 250 °C and (c) 350 °C annealed ZnO NPs as catalysts.*

keeping the ZnO concentration constant. For these experiments, we selected the as-synthesized ZnO NPs, the ZnO NPs annealed at 250 °C having the maximum surface defect states and the ZnO NPs annealed at 350 °C demonstrating minimum surface defect states. The rate of photocatalytic degradation of BR (R_o)

was then fitted by using Langmuir-Hinshelwood (L-H) kinetic model, which typically explains the bimolecular reaction of two species upon surface adsorption [60]. Upon fitting the rate constant (R_o) vs. initial concentration of BR (C_o) curves using equation 2.18, we observe that the photocatalytic degradation of BR on the surface of the ZnO NPs with three different concentrations of surface defect states exactly follows the phenomenon explained by the L-H model (Figure 9.5). In case of the as-synthesized ZnO NPs, the value of the L-H rate constant (k_{L-H}) was found to be 128.38 $\mu mol.dm^{-3}.sec^{-1}$; which then improved to 170.20 $\mu mol.dm^{-3}.sec^{-1}$ for the 250 °C annealed ZnO NPs, owing to the maximum surface defect concentrations resulting in faster photocatalytic activity. For the ZnO NPs with minimum surface defect states, the values of k_{L-H} and K were found to reduce again to 152.80 $\mu mol.dm^{-3}.sec^{-1}$ and 0.02 $\mu mol^{-1}.dm^3$, respectively.

The energy transfer process (FRET) between the acceptor BR molecules and the donor ZnO NPs having various surface defect concentrations was then probed by studying the FRET dynamics process using picosecond-resolved fluorescence technique. For efficient FRET process it is important to have a significant spectral overlap between the emission spectrum of the donor and the absorption spectrum of the acceptor species. There are generally two mechanisms used to describe the transfer of excitations between a donor and an acceptor species, Dexter and Förster mechanisms. In both these mechanisms, the energy transfer rate is dependent on the distance between the donor and acceptor as well as the spectral overlapping of the emission from donor and the absorption of acceptor molecules. However, the basic difference between the two mechanisms is that in Dexter mechanism the donor and the acceptor exchange their electron, whereas in Förster mechanism energy (not electron) is exchanged between the donor and acceptor. Therefore, wavefunction overlapping or molecular orbital overlapping between the donor and acceptor is very crucial in case of Dexter mechanism so that

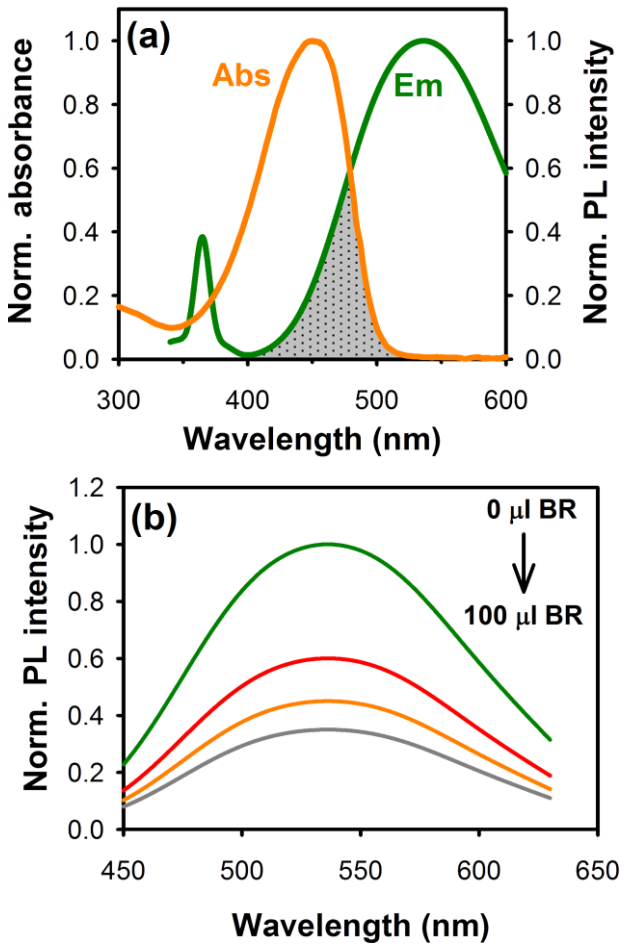

Figure 9.6. *(a) Spectral overlap (shaded area) between the defect mediated ZnO NP emission and the BR absorption spectra and (b) quenching of the steady state defect mediated PL of the ZnO NPs with gradual addition of BR into the system.*

the electrons can occupy the other's molecular orbital. The energy transfer rate also decays exponentially in Dexter mechanism with the distance between the donor and acceptor molecules and the exchange normally occurs when the distance is smaller than 1 nm or 10 Å. On the other hand, the energy transfer in Förster mechanism is highly influenced by the Förster distance (R_o) and the relative space orientation of the transition dipoles of the donor and acceptor. Furthermore, in Förster mechanism the energy exchange occurs within a minimal donor-acceptor distance of 1–10 nm. Therefore, here in this study, the consideration of Dexter mechanism (orbital overlap) via an exchange process associated with the transfer of single charge carriers can be excluded, as it is a

short-range mechanism. Figure 9.6a shows the spectral overlap of the defect mediated ZnO emission and BR absorption spectra, responsible for the energy exchange process between donor ZnO and acceptor BR. As represented in Figure 9.6b, the defect mediated green-yellow emission of the ZnO nanoparticles was found to be suppressed upon gradual addition of BR into the system, clearly indicating that an energy exchange process takes place through FRET when the two species are in close proximity (typically 1–10 nm).

The fluorescence decay kinetics of the as-synthesized and annealed ZnO NPs in the presence and in the absence of BR were then studied by using picosecond-resolved TCSPC technique. The emissions from ZnO NPs were detected at 540 nm with a laser excitation wavelength at 375 nm. As shown in Figure 9.7, upon addition of BR into the system, a faster fluorescence decay component was observed, attributed to the energy transfer process via FRET between the donor ZnO and acceptor BR. The various decay transients of the ZnO NPs in the presence and absence of BR, obtained after the deconvolution of the fluorescence decay curves with IRF (fitted globally by keeping the time scale fixed) are tabulated in Table 9.1.

In case of the as-synthesized ZnO NPs (hydrolyzed at 60 °C), it was observed that the fraction of electrons following the faster nonradiative decay path (τ_1 in Table 9.1) increased significantly from 33% to 72% upon the addition of BR into the NP system, validating the FRET process between donor ZnO and acceptor BR. Using picosecond resolved spectroscopy techniques we have recently demonstrated that both singly charged (V_O^+) and doubly charged (V_O^{++}) oxygen vacancy centers contribute to the energy transfer process with efficiencies of about 78% and 89% respectively [10]. In the present study, the average lifetime (τ_{avg}) of the fluorescence decay of the as-synthesized ZnO NPs was found to reduce by an order of magnitude, from 8.78 ns to 0.79 ns, upon the addition of BR, with energy transfer efficiency (E) of 91.53%.

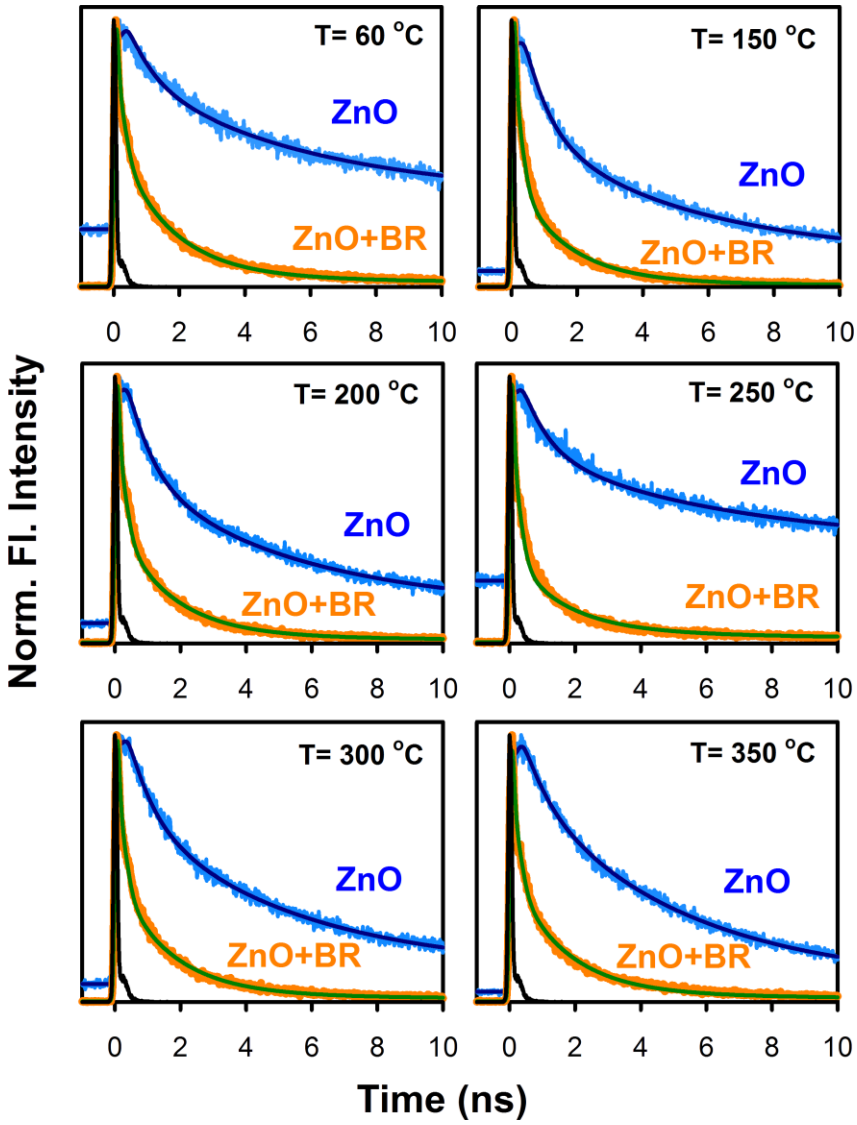

Figure 9.7. *The picosecond resolved fluorescence transients of the as-synthesized (hydrolyzed at 60 °C) and annealed ZnO NPs in the presence and in the absence of BR. The fluorescence decay was monitored at 540 nm with an excitation wavelength of 375 nm.*

However, upon annealing the nanoparticles, the τ_{avg} was observed to reduce in presence of the BR molecules with higher number of electrons following the faster decay path (τ_1), reaching a maximum of 85% in case of the NPs annealed at 250 °C having maximum surface defects. This suggests that in nanoparticles with higher amount of surface defect states, more number of photoexcited electrons lose their energy through a nonradiative path. This loss of energy through the nonradiative path can be directly correlated to the FRET

Table 9.1. *Picosecond resolved fluorescence transients of the as-synthesized and annealed ZnO NPs in the presence and in the absence of BR*[a]

Annealing temperature (°C)	Samples	τ_1 (ns)	τ_2 (ns)	τ_3 (ns)	τ_{avg} (ns)	E (%)
60	ZnO only	0.71 (33%)	4.69 (46%)	39.20 (21%)	8.78	-
	ZnO + BR	0.13 (72%)	1.60 (26%)	14.20 (2%)	0.79	91.53
150	ZnO only	0.71 (50%)	4.69 (43%)	39.20 (7%)	5.11	-
	ZnO + BR	0.13 (81%)	1.60 (18%)	14.20 (1%)	0.53	88.63
200	ZnO only	0.71 (47%)	4.69 (45%)	39.20 (8%)	5.58	-
	ZnO + BR	0.13 (78%)	1.60 (21%)	14.20 (1%)	0.58	86.20
250	ZnO only	0.71 (42%)	4.69 (33%)	39.20 (25%)	11.64	-
	ZnO + BR	0.13 (85%)	1.60 (14%)	14.20 (1%)	0.48	93.79
300	ZnO only	0.71 (41%)	4.69 (52%)	39.20 (7%)	5.47	-
	ZnO + BR	0.13 (78%)	1.60 (21%)	14.20 (1%)	1.85	88.18
350	ZnO only	0.71 (28%)	4.69 (67%)	39.20 (5%)	5.30	-
	ZnO + BR	0.13 (75%)	1.60 (23%)	14.20 (2%)	0.75	87.25

[a]*The emissions from ZnO NPs were detected at 540 nm with a laser excitation wavelength at 375 nm. Numbers in parentheses indicate relative weightages.*

process, in which the energy associated with the surface defects of the NPs transfers resonantly to the acceptor BR molecules, resulting in faster photocatalytic degradation of the BR. The population of the trap state electrons, indicated by the number in parenthesis in the slower time component (τ_3) of the fluorescence decay curves, was also found maximum (25%) in case of the 250 °C annealed ZnO NPs pointing the highest concentration of surface defect states in these NPs. It was observed that the energy transfer efficiency increases with increasing surface defect states. For the ZnO NPs annealed at 250 °C, demonstrating maximum surface defect states, highest energy transfer efficiency of 93.79% was observed,

which reduces gradually to 87.25% in samples annealed at 350 °C, due to the reduction in the surface defects in the NPs. From the steady-state photoluminescence study of the annealed ZnO NPs (Figure 9.3a), it was observed earlier that the defect mediated green-yellow luminescence from oxygen vacancies is maximum for the NPs annealed at 250 °C in air, which justifies the highest energy transfer efficiency observed here. As a result, the ZnO NPs annealed at 250°C in air demonstrated highest photocatalytic degradation of BR compared to the NPs annealed at other temperatures. Therefore, it is clear from our results that efficient BR degradation can be achieved through photocatalysis using ZnO NPs as the catalyst medium by careful utilization of the surface defect states of the ZnO NPs.

9.2.2. Direct Observation of Key Photoinduced Dynamics in a Potential Nano-delivery Vehicle of Cancer Drugs [61]: A typical high-resolution transmission electron microscopic (HR-TEM) image of ZnO NPs is shown in Figure 9.8a. The lattice fringe of ZnO NP shows an interplanar distance of ~0.26 nm, corresponding to the spacing between two (002) planes. The average particle size is estimated by fitting our experimental TEM data over 60 particles and it is found to be ~5 nm. As characterized by UV-Vis spectroscopy, the soret band peak of drug PP resides at 405 nm while the Q-band peaks are observed in the range between 500 nm and 650 nm as shown in Figure 9.8b. The Soret band of PP−ZnO is red-shifted by ~5 nm as compared to that of free PP. The bathochromic shift of the Soret band is related with different physical and chemical changes in the porphyrin molecular structure when it is incorporated into solids or under specific conditions, in solution. This observation suggests successful anchoring of PP to the ZnO surface. The efficiency of the ZnO NPs as nano delivery vehicles is also evident from our UV-Vis spectroscopic studies. The absorption spectra of ZnO NPs as shown in Figure 9.8b has baseline upliftment due to the scattering of colloidal ZnO NPs.

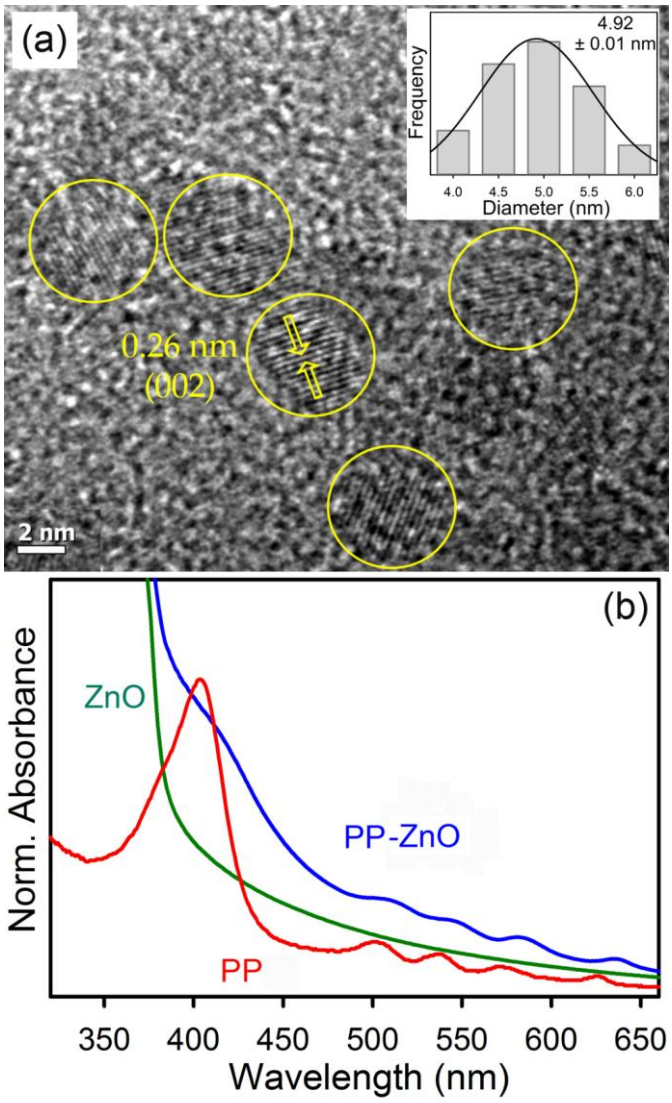

Figure 9.8. *(a) HRTEM images of ZnO NPs. Inset shows the size distribution of the ZnO NPs. (b) UV-Vis absorption of ZnO NPs (green), PP (red) and PP−ZnO (blue) in DMSO-ethanol mixture.*

The ZnO NPs have no molecular absorption beyond 380 nm. According to the Rayleigh scattering, the scattering intensity is inversely proportional to the fourth order of wavelength offering higher scattering cross section of the colloidal samples at lower wavelength. Thus the baseline upliftment in the absorption spectra (Figure 9.8b) decreases with increase in wavelength. We have estimated that 74 µM and 20 µM of PP are associated with 9.6 nM and 4.2 nM of 5 nm and 30 nm ZnO NPs, respectively[62]. In other words ~7800 and ~5000 PP are found to be attached with each 5 nm and 30 nm ZnO NPs, respectively.

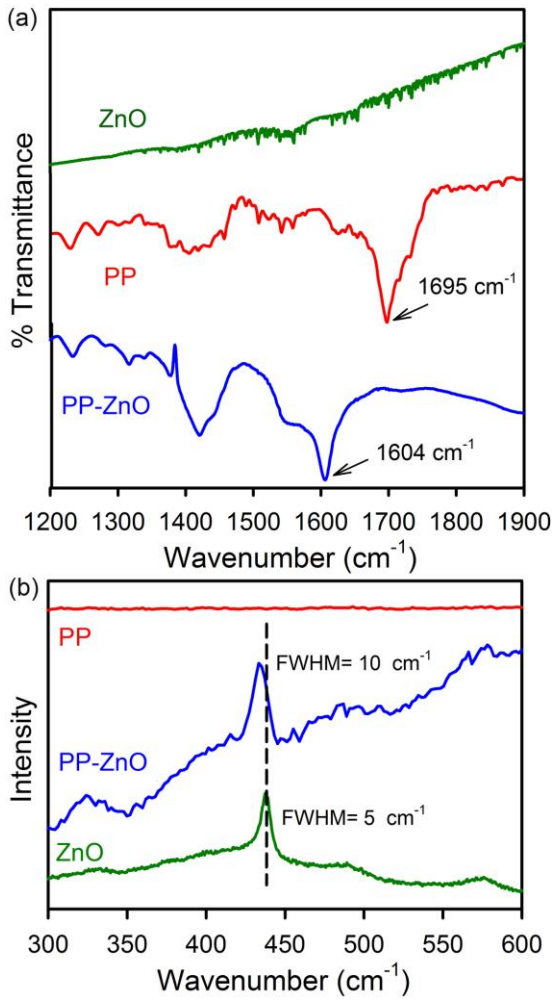

Figure 9.9. *(a) FTIR and (b) Raman spectra of PP (red), ZnO NPs (green) and PP−ZnO composites (blue).*

The Fourier transform infra-red (FTIR) technique is used to investigate the binding mode of the carboxylate group of PP on the ZnO surface as the attachment is very crucial for precise and safe delivery of the drug. For free PP, stretching frequencies of the carboxylic group are at 1695 cm^{-1} and 1406 cm^{-1} for antisymmetric and symmetric stretching vibrations, respectively, as shown in Figure 9.9a. When PP is attached to ZnO, the stretching frequencies of the carboxylic group are located at 1604 cm^{-1} and 1418 cm^{-1} for antisymmetric and symmetric stretching vibrations, respectively. The shifting of the stretching frequencies clearly indicates the formation of a covalent bond between the drug PP and the carrier ZnO NPs [63-65]. The difference between carboxylate stretching

frequencies, $\Delta=\upsilon_{as}$ - υ_{sym} is useful in identifying the bonding mode of the carboxylate ligand [66]. The observed Δ value for the hybrid material is 186 cm^{-1} which is smaller than that of free PP (289 cm^{-1}). This observation is consistent with the fact that the binding mode of PP on ZnO surface is predominantly bidentate. To further investigate the binding between drug and delivery vehicle, Raman spectra were collected from PP, ZnO NPs and PP-ZnO nanohybrids as shown in Figure 9.9b. The Raman spectrum of PP does not show any peak in the wavenumber range of 300–600 cm^{-1}. However, four vibration peaks at 328, 378, 438, and 577 cm^{-1} are observed in the Raman spectrum of ZnO NPs, indicating the presence of a wurtzite structure. After binding of PP on the ZnO surface, the characteristic bands of ZnO are all present but slightly blue shifted and broadened which is indicative of its good retention of the crystal structure and shape. The strong peak at 438 cm^{-1} is assigned to the nonpolar optical phonon, E_2 mode of the ZnO NPs at high frequency, which is associated with oxygen deficiency. Noticeably, the E_2 mode's characteristic band of ZnO shifts toward lower wavenumbers and its linewidth is larger upon its attachment to PP. The observation can be attributed to the attachment of the carboxylic group to Zn (II) that is located at the ZnO surface.

The emission spectrum of ZnO NP is comprised of two emission bands upon excitation above the band-edge (λ_{ex} = 300 nm) as shown in Figure 9.10a. The narrow UV band centered at 363 nm in the emission spectra of ZnO NPs is due to the band gap emission. The broad emission is composed of two bands, one arises from doubly charged vacancy center (V_o^{++}) located at 555 nm (P_2) and the other arises from singly charged vacancy center (V_o^{+}) located at 500 nm (P_1) [8-9]. The emission intensity of ZnO NPs in the PP-ZnO nanohybrid decreases considerably than that of free ZnO NPs which can be attributed to the efficient non-radiative photoinduced processes from ZnO NPs to the PP. Herein, we propose FRET

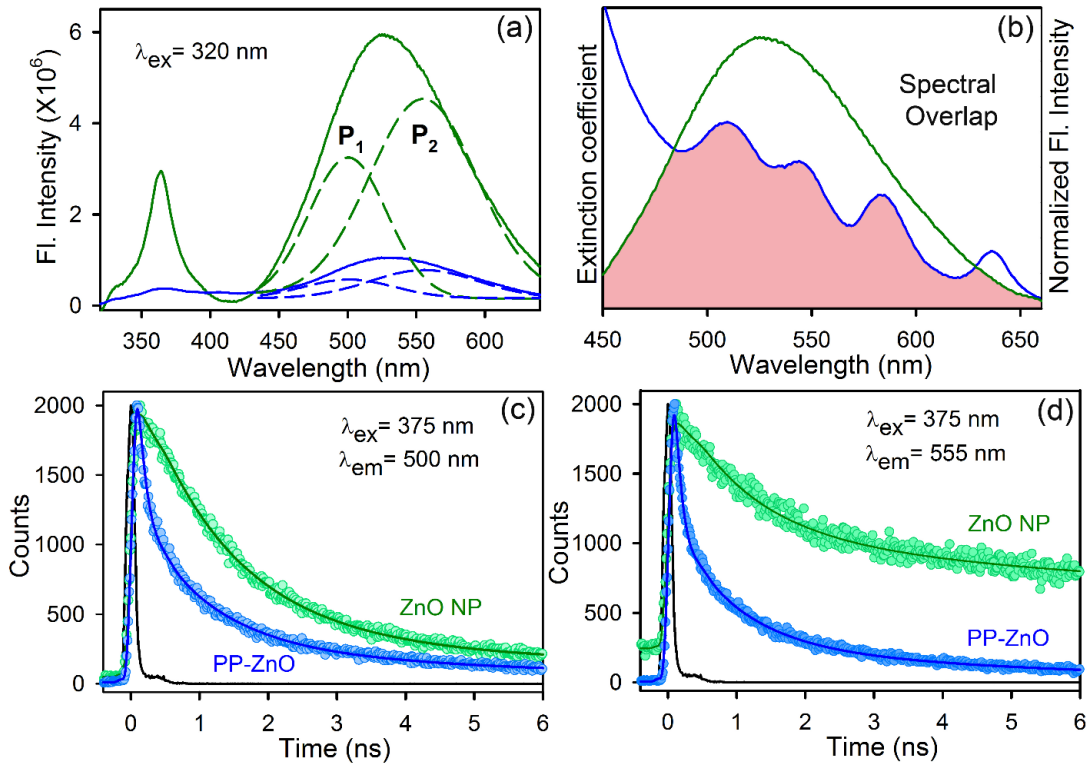

Figure 9.10. *(a) Room temperature PL spectra of ZnO NPs (green) and PP−ZnO composites (blue) are shown. The excitation wavelength was at 320 nm. The broad emission band is composed of two components, P1 (500 nm) and P2 (555 nm). (b) Shows the overlap of ZnO NP emission and PP absorption. The picosecond-resolved fluorescence transients of ZnO NPs (excitation at 375 nm) in the absence (green) and in the presence of PP (blue) collected at (c) 500 nm and (d) 555 nm are shown.*

from the donor ZnO NPs to the acceptor PP. The assessment of molecular distances in numerous biomolecular assemblies from FRET calculations has become a very useful tool [53, 67-68]. The spectral overlap of the donor ZnO NPs emission with that of the PP absorption is shown in Figure 9.10b. The fluorescence decay profile of the donor ZnO NPs in the presence and absence of the acceptor PP were obtained upon excitation of 375 nm laser and monitored at 500 nm (P_1) and 555 nm (P_2) (Figure 9.10c and 9.10d, respectively). The excited state lifetime of the ZnO NPs quenches in PP-ZnO nanohybrid compared to that of bare ZnO NPs. The details of the spectroscopic parameters and the fitting parameters of the fluorescence decays are tabulated in Table 9.2. From FRET calculations, the distance between the donor ZnO NPs and acceptor PP drug are determined to be 1.59 nm and 1.16 nm for P_1 and P_2 states respectively. The energy transfer

efficiency is calculated to be 77.7% and 95.7% from P_1 and P_2 states, respectively. The FRET distances confirm the proximity of the PP drugs to the ZnO NPs delivery vehicle.

Table 9.2. *Dynamics of picosecond-resolved luminescence transients of PP and PP-ZnO composites*[b]

Sample	Excitation wavelength (nm)	Detection wavelength (nm)	τ_1 (ns)	τ_2 (ns)	τ_3 (ns)	τ_{avg} (ns)
ZnO NP	375	500	1.14 (67.4%)	2.41 (27.0%)	38.94 (5.6%)	3.60
PP-ZnO nanohybrid	375	500	0.11 (65.7%)	1.04 (27.1%)	6.27 (7.2%)	0.80
ZnO NP	375	555	0.95 (50.7%)	3.90 (21.3%)	44.76 (28.0%)	13.84
PP-ZnO nanohybrid	375	555	0.08 (71.3%)	0.87 (21.3%)	4.81 (7.4%)	0.60

[b]*Numbers in parentheses indicate relative weightages.*

In order to explore the PP as an efficient source of electrons, a well-known electron acceptor benzoquinone (BQ) is attached to PP and the possible excited-state electron donor−acceptor interactions in PP-BQ composite is investigated by a series of time-resolved fluorescence measurements with increasing BQ concentration. The fluorescence decay profile for PP−BQ and free PP were obtained upon photoexcitation at 409 nm in DMSO and monitored at 630 nm as shown in Figure 9.11a. The time profile of the fluorescence decay at 630 nm for the singlet excited-state of reference PP showed single exponential decay, with a lifetime of 16.09 ns. The lifetime components of the transients are tabulated in Table 9.3. As evident from Table 9.3, time components of ~1.50 ns and ~0.14 ns appear in the fluorescence transients of PP in the presence of the quencher. These components were found to be enhanced with increase in BQ concentration. The fast-decaying component of ~140 ps in the PP−BQ composite accounts for the ultrafast charge transfer process from PP to electron acceptor BQ molecules. The time component of ~1.50 ns appears probably due to the formation of PP

aggregates in the experimental solution [69]. The PL quenching, as evident from the time-resolved PL studies, shows the affinity of PP dyes to BQ molecules. A detailed Stern Volmer (SV) analysis on the quenching of the PP PL (Figure 9.11b)

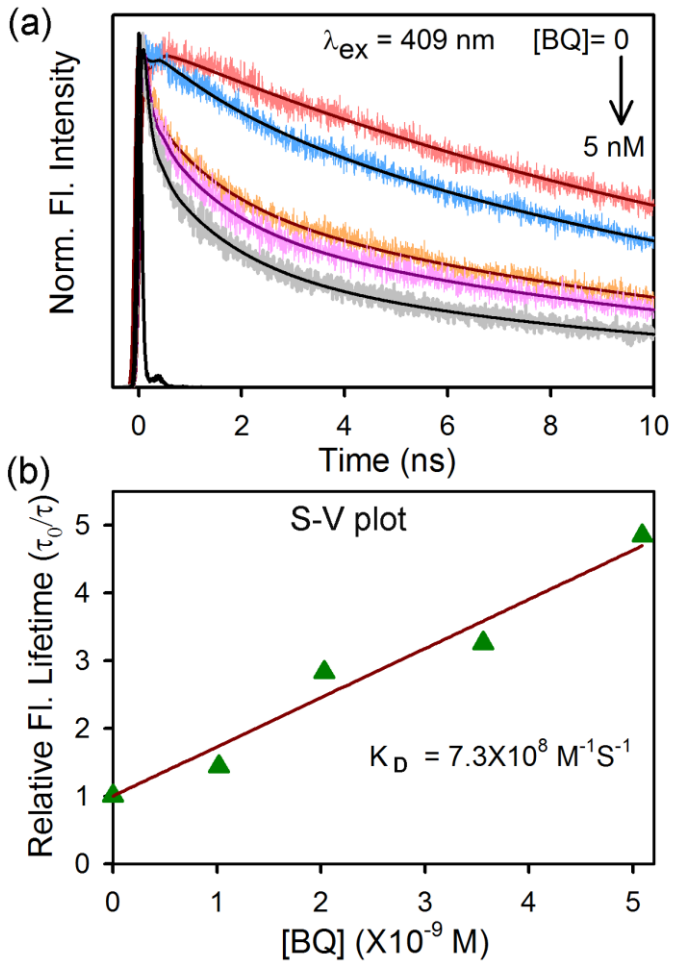

Figure 9.11. *(a) Fluorescence decay profiles of PP in DMSO with increasing concentrations of BQ (1.0, 2.0, 3.6, and 5.1 nM). (b) Plots of τ_0/τ vs BQ concentration, where τ_0 and τ represent excited-state lifetime of the fluorophore (PP) at 630 nm in the absence and presence of quencher (BQ), respectively. Excitation wavelength (λ_{ex} = 409 nm).*

reveals the dynamic quenching constant to be K_D = 7.3 ×10^8 M^{-1} S^{-1}. After highlighting the photoinduced charge migration pathway as one of the key aspects of a potential PS in the presence of organic molecules, it is necessary to understand the charge separation dynamics at the PP−ZnO interface to realize a superior ROS activity. Upon 409 nm photoexcitation, the strong fluorescence

Table 9.3. *Dynamics of picosecond-resolved luminescence transients of PP in the absence and presence of various BQ concentrations*[c]

Sample	τ_1 (ns)	τ_2 (ns)	τ_3 (ns)	τ_{avg} (ns)
PP (bare)			16.09 (100%)	16.09
PP−BQ (1.0 nM)	0.136 (19%)	1.50 (9%)	13.5 (72%)	10.46
PP−BQ (2.0 nM)	0.136 (43%)	1.50 (19%)	13.5 (38%)	5.47
PP−BQ (3.6 nM)	0.136 (49%)	1.50 (22%)	13.5 (29%)	4.75
PP−BQ (5.1 nM)	0.136 (54%)	1.50 (27%)	13.5 (19%)	3.19

[c]*The emission (monitored at 630 nm) was detected with 409 nm laser excitation. Numbers in the parenthesis indicate relative weightages.*

intensities of PP in the range of 620−720 nm were significantly suppressed when anchored to ZnO NPs as shown in Figure 9.12a. In addition, the fluorescence peak of PP in the PP−ZnO nanohybrids was found to be red-shifted by ~5 nm as compared to the fluorescence spectra of free PP. The fluorescence decays (Figure 9.12b) of PP, PP−ZnO (5 nm) and PP-ZnO (30 nm) were measured upon excitation with 409 nm laser, and monitored at wavelength of 630 nm. The spectroscopic and fitting parameters are shown in Table 9.4. The longer lifetime of PP quenches in the presence of both ZnO (5 nm) and ZnO (30 nm) NPs. The observed decrease in lifetime could be correlated to the electron transfer process from PP to ZnO NPs. The apparent rate constant, k_{nr}, is determined for the nonradiative processes by comparing the lifetimes of PP in the absence (τ_0) and the presence (τ) of ZnO NPs, using the following equation:

$$k_{nr} = 1/\langle\tau\rangle - 1/\langle\tau_0\rangle \qquad (9.1)$$

The apparent rate constant for the nonradiative process was estimated to be 1.75×10^9 s^{-1} for PP−ZnO (5 nm) and 1.70×10^8 s^{-1} for PP−ZnO (30 nm) adducts. As reported in previous studies [64], such k_{nr} values represent electron transport from LUMO of PP to the conduction band of ZnO NPs. These rules out the possibility of self-quenching due to the aggregation of PP molecules on ZnO surface [70-72].

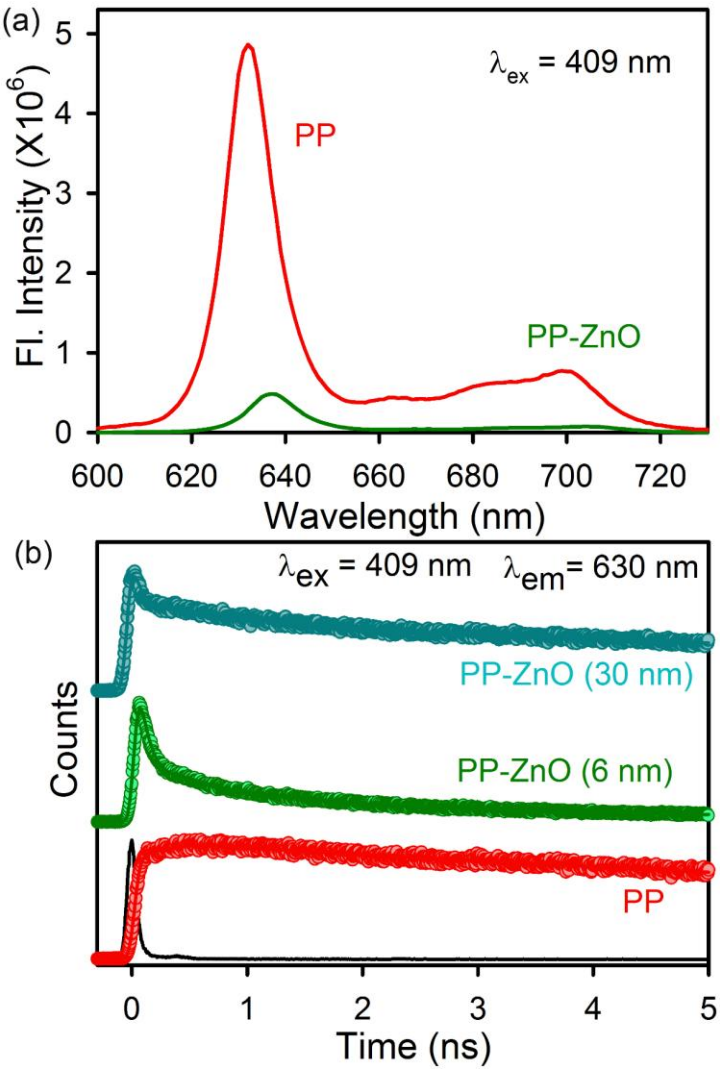

Figure 9.12. *(a) Room-temperature PL spectra (excitation at 409 nm) of free PP (red) and PP-ZnO (green). (b) Fluorescence decay profiles of PP (red), PP−ZnO (6 nm) (blue) and PP−ZnO (30 nm) (cyan) at 630 nm (excitation at 409 nm).*

Table 9.4. *Dynamics of picosecond-resolved luminescence transients of PP and PP-ZnO composites*[d]

Sample	τ_1 (ns)	τ_2 (ns)	τ_3 (ns)	τ_{avg} (ns)	$k_{nr}\times10^9$ (sec^{-1})
PP (bare)			16.09 (100%)	16.09	
PP-ZnO (5 nm) nanohybrid	0.06±0.03 (76.3%)	0.71±0.03 (13.4%)	4.00±0.08 (10.3%)	0.55±0.09	1.75
PP-ZnO (30 nm) nanohybrid	0.05±0.03 (58.8%)	0.93±0.04 (10.6%)	13.35±0.17 (30.6)	4.21±0.06	0.17

[d]*The emission (monitored at 630 nm) was detected with 409 nm laser excitation. k_{nr} represents nonradiative rate constant. Numbers in the parenthesis indicate relative weightages.*

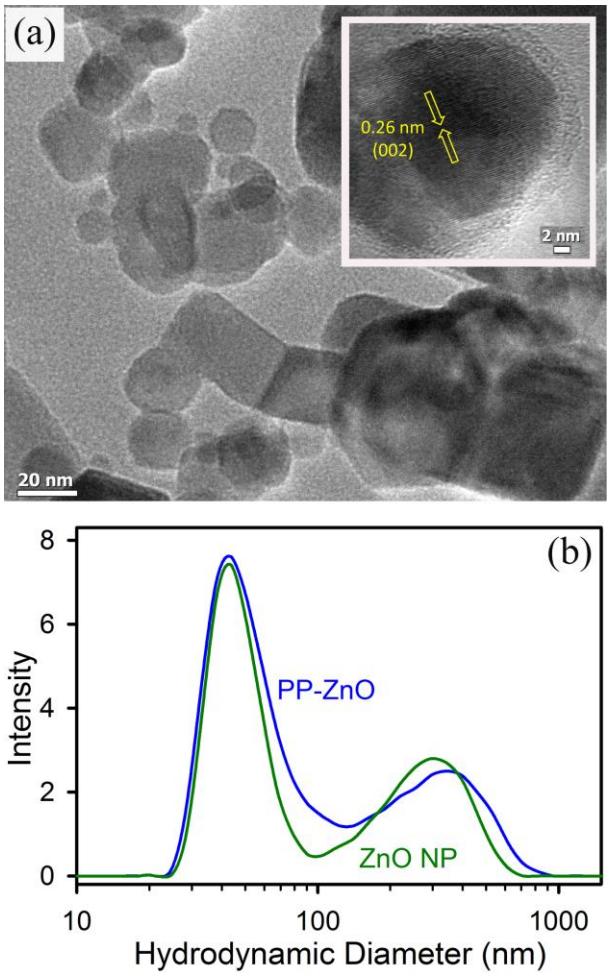

Figure 9.13. *(a) TEM images of PP-ZnO (~30 nm) Nanohybrids dispersed in water. Inset shows the HRTEM image of a PP-ZnO nanohybrid. (b) Dynamic light scattering spectra for PP-ZnO and ZnO NPs dispersed in water.*

A transmission electrom microscopy (TEM) image of PP-ZnO (~30 nm) nanohybrids dispersed in water confirms the presence of nearly spherical nanocrystals as shown in Figure 9.13a. The HR-TEM image of ZnO NP shows an interplanar distance of ~0.26 nm, corresponding to the spacing between two (002) planes as shown in Figure 9.13a, inset. The dynamic light scattering (DLS) spectra of PP-ZnO nanohybrid and ZnO NPs dispersed in water are shown in Figure 9.13b. ZnO NPs show a peak at 40 nm which is consistent with TEM results and a peak at 300 nm due to the aggregation in water. The DLS spectra remains almost similar when ZnO NPs are attached to the PP drug molecules. The observation

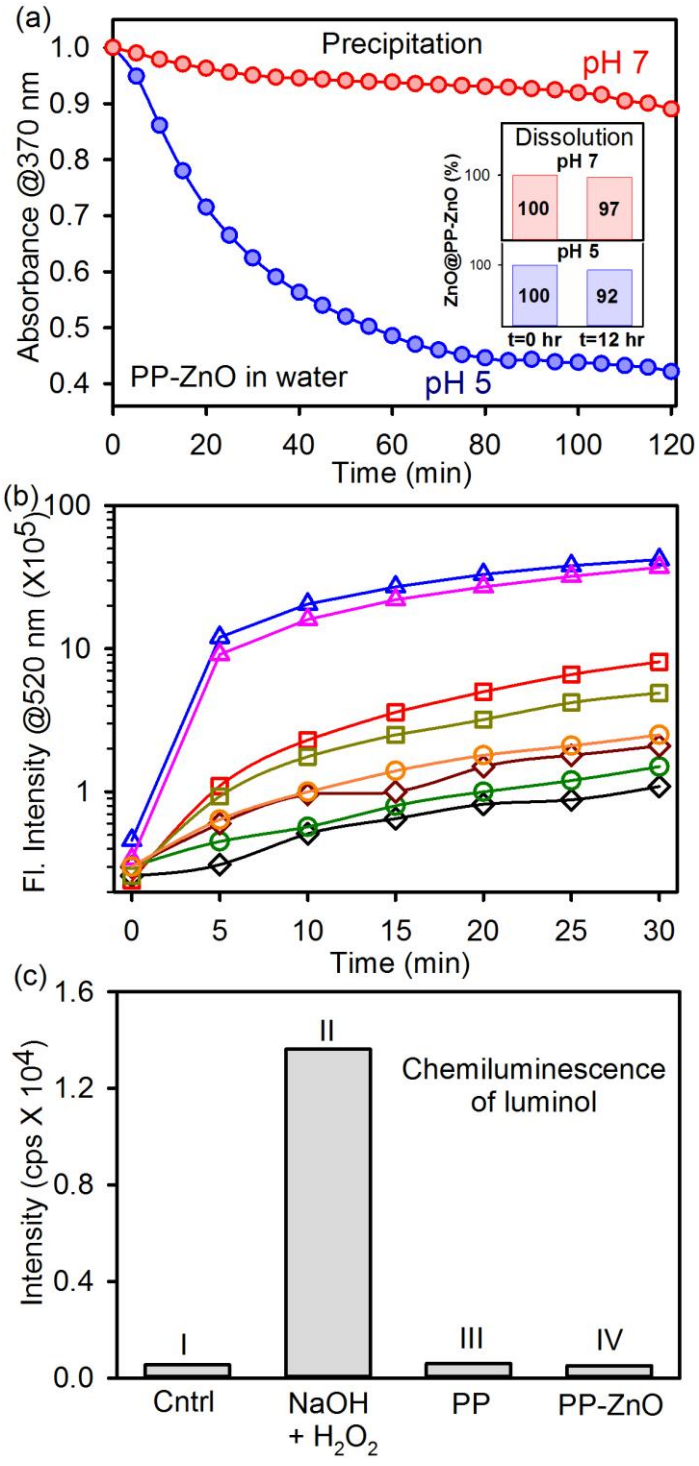

Figure 9.14. *(a) Stability of the nanohybrid from absorbance at 370 nm of PP-ZnO dispersed in water at pH 7 and pH 5. Inset shows the dissolution of PP-ZnO nanohybrids in water at pH 5 and pH 7 after 12 hours. (b) The DCFH oxidation with time in the presence of PP-ZnO (blue at pH 5 and pink at pH 7), PP (red at pH 5 and dark yellow at pH 7), ZnO (green at pH 5 and orange at pH 7) and DCFH only (black at pH 5 and dark red at pH 7) under green light irradiation. The excitation was at 488 nm. (c) Chemiluminescence of luminol after green light irradiation for 15 minutes in the presence of (I) control, (II) NaOH + H_2O_2, (III) PP and (IV) PP-ZnO.*

indicates the formation of stable dispersion of PP-ZnO nanohybrids in water. The time dependent stability of the PP-ZnO nanohybrid dispersion in water is monitored at different pH values (Figure 9.14a). The dispersion is less stable in acidic aqueous solution (pH=5) compared to that in neutral (pH=7) solution. As the cancer cells are generally acidic in nature, nanohybrids are expected to be deposited more in the cancer cells rather in the normal cells. The dissolution of the nanohybrids at different pH values is also monitored as shown in Figure 9.14a, inset. At pH 5, 8% PP-ZnO nanohybrids were dissolved, whereas, 3% dissolution occurs at pH 7 after 12 hours. The ROS generation was monitored directly by the dichlorofluorescin-dichlorofluorecein (DCFH-DCF) conversion in aqueous medium. The DCFH is a well-known marker for ROS detection [73]. ROS oxidize nonfluorescent DCFH to fluorescent DCF and the emission intensity of DCF was monitored with time as shown in Figure 9.14b. In the presence of PP-ZnO nanohybrids, maximum enhancement in fluorescence intensity was observed under green light irradiation. In a control experiment ZnO NPs show no ROS generation under green light illumination as the NPs lack photon absorption in the green region of optical spectrum. Thus the presence of ZnO NPs in the proximity of PP drugs not only acts as drug delivery vehicle as reported in the literature but also enhances the generation of ROS. The ROS generation by the nanohybrid in acidic aqueous solution (pH 5) compared with that in neutral pH=7 is monitored by DCFH oxidation and found to be comparable as shown in Figure 9.14b. It has to be noted that DCFH oxidation is not conclusive to confer the nature of ROS (singlet oxygen/superoxide formation). However, in the presence of superoxide, more specifically, luminol is oxidized to produce chemiluminescence [74]. As shown in Figure 9.14c, no chemiluminescence observed in the presence of PP and PP-ZnO after green light irradiation for 15 minutes. The above observations of DCFH oxidation and no oxidation of luminol in PP/PP-ZnO nanohybrids upon green light illumination indicate that the nature of ROS is essentially singlet oxygen rather superoxide anions. The conclusion of the

formation of singlet oxygen is consistent with the reported literature as Carraro et. al. have shown that photosensitized reactions in vitro and in vivo by porphyrin involves the production of $^1O_2$ but not O_2^- or $^\bullet OH$ radicals [75].

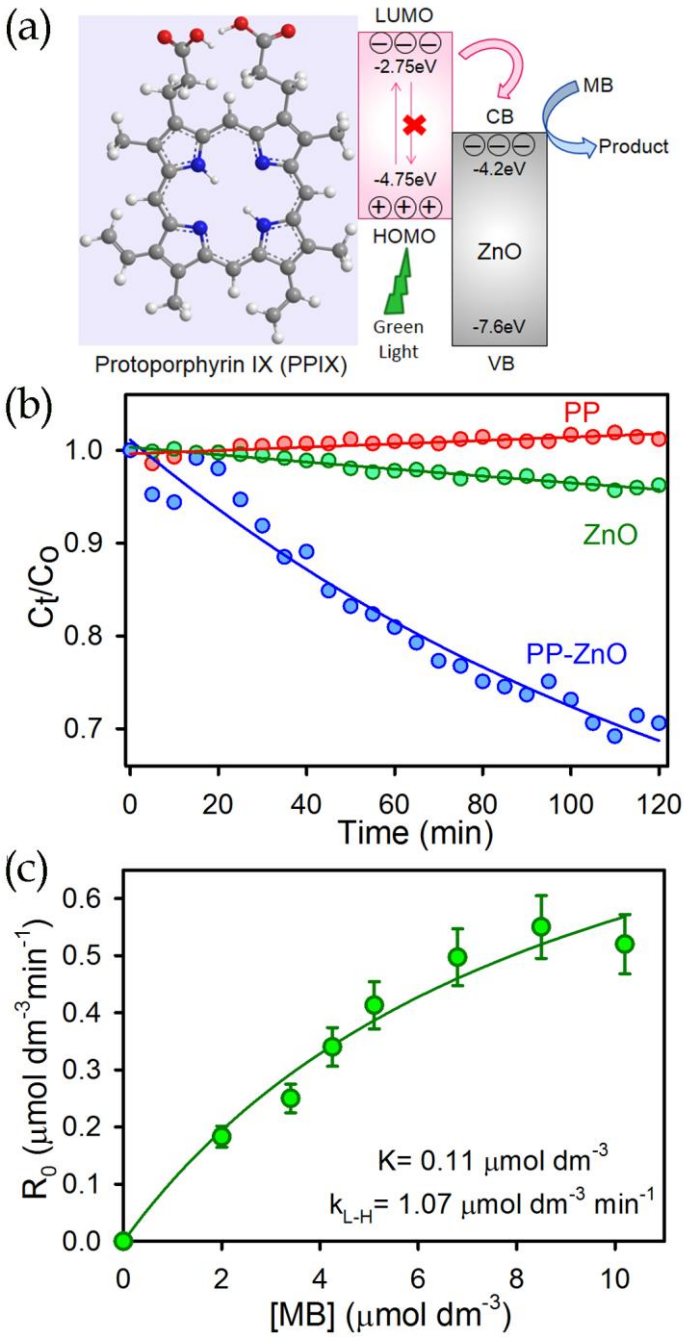

Figure 9.15. *(a) Schematic energy level diagram and charge separation path in PP−ZnO interface. (b) Photocatalytic degradation of MB in the presence of PP (red), ZnO (green) and PP-ZnO (blue) under green light irradiation. (c) Degradation rate (R_0) versus initial MB concentration (C_0) plots (with 10% error bar) in the presence of PP-ZnO under green light irradiation.*

A well known dye methylene blue (MB) is reported to be bleached to Leuco-methylene blue (LMB) in presence of ROS in several photocatalysis experiments [76-77]. However, under green light irradiation, in the presence of PP-ZnO nanohybrid 30% MB is reduced to LMB whereas no MB reduction occurs in the presence of PP only (Figure 9.15). The observation along with the conclusion made earlier clearly indicate that MB reduction in the present case is neither through singlet oxygen nor superoxide formation. The efficacy of direct electron transfer of PP to BQ (Figure 9.11) is concluded to be responsible for the MB reduction in the nanohybrid as shown in Figure 9.15a. It has to be noted that proximity of MB to PP without ZnO is hindered because of higher solubility of MB in aqueous solution. In the present PP sensitization approach, the photoexcited dye molecule transfers an electron into the conduction band (CB) of ZnO, thereby enhancing the charge separation at the dye−semiconductor interface. MB is reduced to LMB by taking the electron from ZnO CB. Concurrently water in the media acts as an electron donor to regenerate the sensitizer dye [63]. To confirm the surface catalysis mechanism, MB reduction is performed in the presence of PP-ZnO by varying the initial MB concentration. The MB degradation rate (R_0) versus initial MB concentration (C_0) curve as shown in Figure 9.15c is fitted using Langmuir–Hinshelwood equation. The values of K and k_{L-H} are given in Table 9.5 and are consistent with other surface catalyzed reaction [63].

Table 9.5. *Kinetic fitting parameters of Langmuir-Hinshelwood model*[e]

Sample	[MB] (μmol dm^{-3})	R_0 (μmol dm^{-3} min^{-1})	K (μmol dm^{-3})	k_{L-H} (μmol dm^{-3} min^{-1})
PP-ZnO	2.0000	0.1830	0.11	1.07
	3.4000	0.2500		
	4.2500	0.3400		
	5.1000	0.4130		
	6.8000	0.4970		
	8.5000	0.5500		
	10.2000	0.5200		

[e]*R_0 is the degradation rate, k_{L-H} is the Langmuir-Hinshelwood rate constant, and K is the Langmuir adsorption coefficient.*

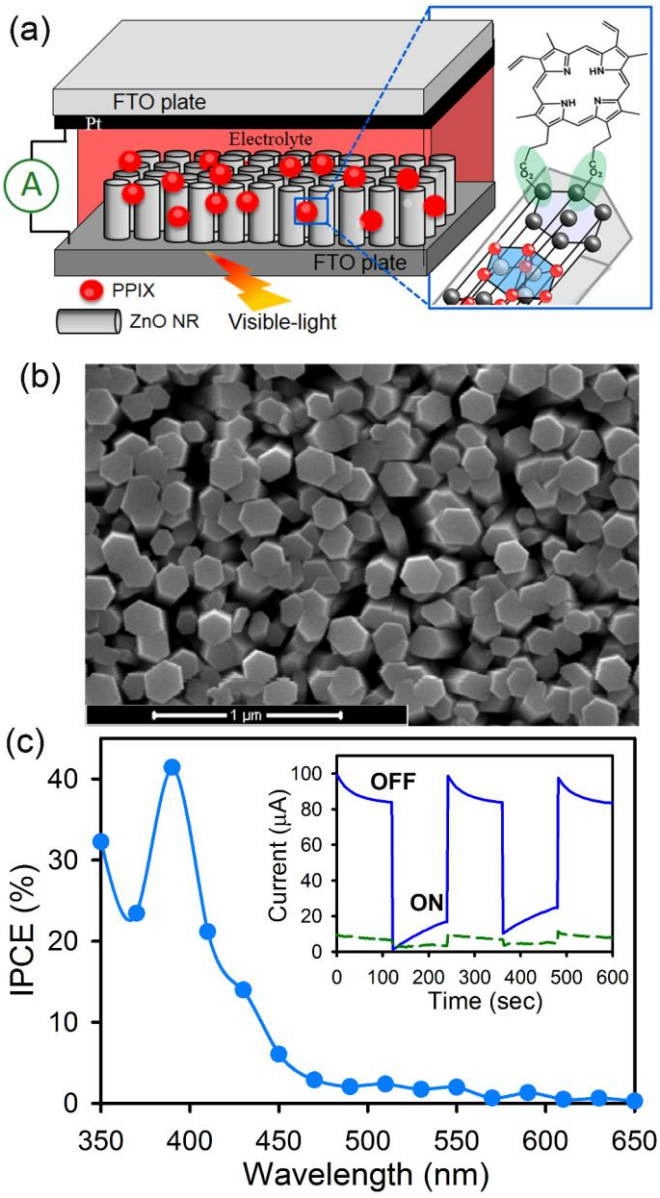

Figure 9.16. *(a) Schematic presentation of the fabricated dye sensitized solar cell geometry for photocurrent measurement. (b) SEM images of vertically aligned, hexagonal ZnO NRs decorated on a FTO plate. (c) Incident photon-to-current conversion efficiency (IPCE) spectra for PP-sensitized ZnO NRs.*

The evidence for electron transfer from PP dye to the host ZnO NP is apparent from an incident photon-to-current conversion efficiency (IPCE) measurement in a photocell as shown in Figure 9.16a. The SEM images of ZnO NRs used in the photocell are shown in Figure 9.16b. The light source (intensity 25 mW cm^{-2}) was turned on and off every 20 sec, and the obtained current values were continuously recorded using a multimeter. Inset of Figure 9.16c shows the

photocurrent response for the ZnO NR and PP-ZnO thin films, where an improved photocurrent was observed for the PP-modified ZnO thin film (~100 µA) under illuminated condition compared to the bare ZnO NR thin film (~10 µA). The incident photon-to-current conversion efficiency (IPCE) of the device as shown in Figure 9.16c is found to be closely identical as absorbance spectra of PP and as large as 40% at 395 nm. This shows that the PP sensitizers on the photo anode surface are indeed responsible for the photocurrent generation.

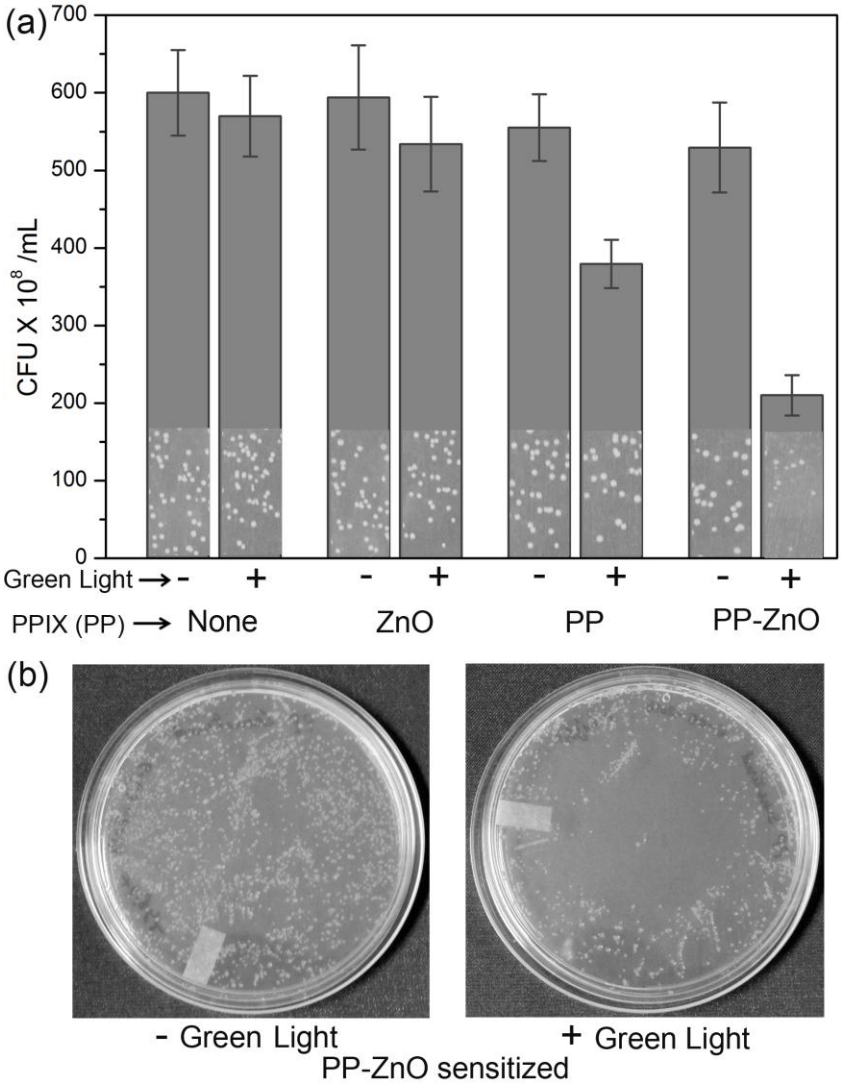

Figure 9.17. *(a) Antibacterial activity of PP-ZnO, PP and ZnO in the presence and absence of green light. (b) Images of E. Coli. in PP-ZnO sensitized plates before and after green light irradiation.*

After thorough characterization and investigation of photoinduced dynamics in PP-ZnO nanohybrid, we have employed the PP-ZnO nanohybrids as potential photodynamic agent for the inhibition of growth of Escherichia coli (*E. coli*). For photodynamic therapy experiments, we have used 30 nm ZnO NPs due to lower toxicity than that of 5 nm ZnO NPs [78]. Figure 9.17b shows the picture of *E. coli* cultures treated with PP-ZnO nanohybrids in the presence and absence of green light. The inhibition of bacterial growth after photodynamic treatment is clearly visible. The green light treated sample contains significantly less number of colonies. For comparison, the colonies were counted for control and treated with PP drugs, ZnO NPs and PP-ZnO nanohybrids in the presence and absence of green light as shown in Figure 9.17a. The images of the selected area for the corresponding samples are shown within the columns in the Figure 9.17a. In control and ZnO treated samples, the colony forming unit (CFU) are almost same in the presence and absence of green light. The observation indicates the absence of antibacterial activity of the ZnO NPs itself in our experimental concentration range. In case of PP treated samples, the bacteria growth is inhibited upto 34% after photodynamic treatment. The maximum inhibition of bacterial growth is obtained for PP-ZnO treated samples where 65% decrease in CFU is observed after photodynamic treatment. The results clearly indicate the enhanced ROS generation in the presence of PP-ZnO nanohybrids compared to that of PP only as the presence of ZnO NPs in the proximity of PP drugs facilitates the charge separation which is evident from our picosecond resolved fluorescence studies.

8.3. Conclusion: ZnO nanoparticles of about 5–6 nm diameters were synthesized and used as catalyst for studying the photocatalytic degradation of bilirubin. It has been demonstrated that through annealing process the surface defect states (mainly the oxygen vacancies) of the nanoparticles can be controlled, which plays an important role in the photocatalytic degradation of the BR molecules. From picosecond-resolved TCSPC studies, it was observed that the

energy related to the defect mediated photoluminescence from the ZnO nanoparticles that peaks at about 530 nm resonantly transfers to the surface adsorbed BR molecules via Förster Resonance Energy Transfer (FRET) process, leading to efficient photocatalytic degradation of the BR molecules. The energy transfer efficiency of the FRET process between the annealed ZnO nanoparticles and BR molecules was estimated and for the ZnO nanoparticles annealed at 250 °C, a maximum energy transfer efficiency of more than 93% was obtained, attributed to the highest concentration of the surface defect states present in these nanoparticles. Under continuous UV irradiation, the 250 °C annealed ZnO nanoparticles showed maximum photocatalytic activity, which was almost 3.5 times higher than that of the as-synthesized ZnO nanoparticles. In summary, from the present study, it is clear that for the efficient photocatalytic degradation of BR in blood, the role of the surface defect states in the ZnO nanoparticle catalysts is crucial, which can be modulated simply by a post-annealing treatment of the nanoparticles. Although DNA damage due to the exposure of the BR containing blood to the exposure to UV radiation can be a concern in case of the practical implementation of this type of FRET based phototherapeutic systems, we believe that such harmful effects can be circumvented in the presence of the ZnO nanoparticle layer due to their UV filtering action.

We have also investigated the crucial photoinduced dynamics in ZnO nanoparticles (NPs) upon complexation with the cancer drug protoporphyrin IX (PP). Association of ~7800 and ~5000 PP molecules per 5 nm and 30 nm ZnO NPs, respectively, is evidenced from our study. The PP-ZnO nanohybrid was characterized by Vibrational spectroscopy (FTIR), Raman scattering and UV-Vis absorption spectroscopy. To confirm the proximity of the drug and vehicle of delivery at the molecular level, we have employed picosecond-resolved Förster resonance energy transfer (FRET) from the defect mediated emission of ZnO NPs to PP and the distance between two is found to be 1.16 nm from P_2 states.

Picosecond-resolved fluorescence studies on PP−ZnO nanohybrid also reveal efficient electron migration from photoexcited PP to ZnO, eventually enhancing the ROS activity in the PP-ZnO nanostructures. The dichlorofluorescin (DCFH) oxidation and no oxidation of luminol in PP/PP-ZnO nanohybrids upon green light illumination indicate that the nature of ROS is essentially singlet oxygen rather superoxide anions. The photocurrent and incident photon-to-current conversion efficiency (IPCE) measurements confirm the enhanced charge separation in PP-ZnO nanohybrid under photoirradiation. The nanohybrid shows greater photodynamic activity for the inhibition of *E. coli* growth compared to that of free drug molecules. The exploration of key photoinduced dynamics in the porphyrin based nanohybrids will be helpful in designing future photodynamic agents.

References

[1] G.F. Paciotti, L. Myer, D. Weinreich, D. Goia, N. Pavel, R.E. McLaughlin, L. Tamarkin, Colloidal Gold: A Novel Nanoparticle Vector for Tumor Directed Drug Delivery, *Drug Deliv.* 11 (2004) 169-183.

[2] X. Wu, H. Liu, J. Liu, K.N. Haley, J.A. Treadway, J.P. Larson, N. Ge, F. Peale, M.P. Bruchez, Immunofluorescent Labeling of Cancer Marker Her2 and Other Cellular Targets with Semiconductor Quantum Dots, *Nat. Biotechnol.* 21 (2002) 41-46.

[3] L.R. Hirsch, R.J. Stafford, J.A. Bankson, S.R. Sershen, B. Rivera, R.E. Rrice, J.D. Hazle, N.J. Halas, J.L. West, Nanoshell-Mediated Near-Infrared Thermal Therapy of Tumors under Magnetic Resonance Guidance, *Proc. Natl. Acad. Sci. USA* 100 (2011) 13549-13554.

[4] J. Zhou, N.S. Xu, Z.L. Wang, Dissolving Behavior and Stability of ZnO Wires in Biofluids: A Study on Biodegradability and Biocompatibility of ZnO Nanostructures, *Adv. Mater.* 18 (2006) 2432–2435.

[5] S. Baruah, R.F. Rafique, J. Dutta, Visible Light Photocatalysis by Tailoring Crystal Defections in Zinc Oxide Nanostructures, *Nano* 3 (2008) 399-407.

[6] S. Baruah, S.S. Sinha, B. Ghosh, S.K. Pal, A.K. Raychaudhuri, J. Dutta, Photoreactivity of ZnO Nanoparticles in Visible Light: Effect of Surface States on Electron Transfer Reaction, *J. Appl. Phys.* 105 (2009) 0743081-0743086.

[7] D.M. Hofmann, D. Pfisterer, J. Sann, B.K. Meyer, R. Tena-Zaera, V. Munoz-Sanjose, T. Frank, G. Pensl, Properties of the Oxygen Vacancy in ZnO, *Appl. Phys. A* 88 (2007) 147-151.

[8] K. Vanheusden, C.H. Seager, W.L. Warren, D.R. Tallant, J.A. Voigt, Correlation between Photoluminescence and Oxygen Vacancies in ZnO Phosphors, *Appl. Phys. Lett.* 68 (1996) 403-405.

[9] A. Van Dijken, E.A. Meulenkamp, D. Vanmaekelbergh, A. Meijerink, The Kinetics of the Radiative and Nonradiative Processes in Nanocrystalline ZnO Particles upon Photoexcitation, *J. Phys. Chem. B* 104 (2000) 1715-1723.

[10] S. Sarkar, A. Makhal, S. Baruah, M.A. Mahmood, J. Dutta, S.K. Pal, Nanoparticle-Sensitized Photodegradation of Bilirubin and Potential Therapeutic Application, *J. Phys. Chem. C* 116 (2012) 9608-9615.

[11] Z.Q. Chen, S. Yamamoto, M. Maekawa, A. Kawasuso, X.L. Yuan, T. Sekiguchi, Postgrowth Annealing of Defects in ZnO Studied by Positron Annihilation, X-Ray Diffraction, Rutherford Backscattering, Cathodoluminescence, and Hall Measurements, *J. Appl. Phys.* 94 (2003) 4807-4812.

[12] J.P. Xu, S.B. Shi, L. Li, X.S. Zhang, Y.X. Wang, X.M. Chen, Effects of Annealing Temperature on Structural and Optical Properties of ZnO Thin Films, *Chin. Phys. Lett.* 27 (2010) 047803.

[13] B. Lin, Z. Fu, Y. Jia, G. Liao, Defect Photoluminescence of Undoping ZnO Films and Its Dependence on Annealing Conditions, *J. Electrochem. Soc.* 148 (2001) G110-G113.

[14] D. Sanyal, T.K. Roy, M. Chakrabarti, S. Dechoudhury, D. Bhowmick, A. Chakrabarti, Defect Studies in Annealed ZnO by Positron Annihilation Spectroscopy, *J. Phys. Condens. Matter* 20 (2008) 045217.

[15] Y. Zhang, W. Fa, F. Yang, Z. Zheng, P. Zhang, Effect of Annealing Temperature on the Structural and Optical Properties of ZnO Thin Films Prepared by Sol-Gel Method, *Ionics* 16 (2010) 815-820.

[16] H.B. Fan, S.Y. Yang, P.F. Zhang, H.Y. Wei, X.L. Liu, C.M. Jiao, Q.S. Zhu, Y.H. Chen, Z.G. Wang, Investigation of Oxygen Vacancy and Interstitial Oxygen Defects in ZnO Films by Photoluminescence and X-Ray Photoelectron Spectroscopy, *Chin. Phys. Lett.* 24 (2007) 2108-2111.

[17] W. Mtangi, F.D. Auret, M. Diale, W.E. Meyer, A. Chawanda, H. De Meyer, P.J. Janse Van Rensburg, J.M. Nel, Effects of High Temperature Annealing on Single Crystal ZnO and ZnO Devices, *J. Appl. Phys.* 111 (2012) 0845031-0845036.

[18] I.M. London, R. West, D. Shemin, D. Rittenberg, On the Origin of Bile Pigment in Normal Man, *J. Biol. Chem.* 184 (1950) 351-358.

[19] M.J. Maisels, A.F. McDonagh, Phototherapy for Neonatal Jaundice, *N. Engl. J. Med.* 358 (2008) 920-928.

[20] S.E. Robertson, B.P. Hull, O. Tomori, O. Bele, J.W. LeDuc, K. Esteves, Yellow Fever: A Decade of Reemergence, *JAMA* 276 (1996) 1157-1162.

[21] H.J. Vreman, R.J. Wong, D.K. Stevenson, Phototherapy: Current Methods and Future Directions, *Semin. Perinatol.* 28 (2004) 326-333.

[22] R. Stocker, A.N. Glazer, B.N. Ames, Antioxidant Activity of Albumin-Bound Bilirubin, *Proc. Natl. Acad. Sci. U. S. A.* 84 (1987) 5918-5922.

[23] Z. Yang, C. Zhang, Adsorption and Photocatalytic Degradation of Bilirubin on Hydroxyapatite Coatings with Nanostructural Surface, *J. Mol. Catal. A: Chem.* 302 (2009) 107-111.

[24] Z.P. Yang, J.L. Yan, C.J. Zhang, S.Q. Luo, Enhanced Removal of Bilirubin on Molecularly Imprinted Titania Film, *Colloids Surf., B* 87 (2011) 187-191.

[25] J. Park, P.M. Fong, J. Lu, K.S. Russell, C.J. Booth, W.M. Saltzman, T.M. Fahmy, Pegylated PLGA Nanoparticles for the Improved Delivery of Doxorubicin, *Nanomedicine* 5 (2009) 410-418.

[26] X. Wang, J. Li, Y. Wang, L. Koenig, A. Gjyrezi, P. Giannakakou, E.H. Shin, M. Tighiouart, Z. Chen, S. Nie, D.M. Shin, A Folate Receptor-Targeting Nanoparticle Minimizes Drug Resistance in a Human Cancer Model, *ACS Nano* 5 (2011) 6184-6194.

[27] L. Brannon-Peppas, J.O. Blanchette, Nanoparticle and Targeted Systems for Cancer Therapy, *Adv. Drug Deliv. Rev.* 56 (2004) 1649-1659.

[28] E.S. Kawasaki, A. Player, Nanotechnology, Nanomedicine, and the Development of New, Effective Therapies for Cancer, *Nanomedicine* 1 (2005) 101-109.

[29] L. Zhang, F.X. Gu, J.M. Chan, A.Z. Wang, R.S. Langer, O.C. Farokhzad, Nanoparticles in Medicine: Therapeutic Applications and Developments, *Clin. Pharmacol. Ther.* 83 (2008) 761-769.

[30] R.A. Petros, J.M. Desimone, Strategies in the Design of Nanoparticles for Therapeutic Applications, *Nat. Rev. Drug. Discov.* 9 (2010) 615-627.

[31] L. Gao, J. Fei, J. Zhao, H. Li, Y. Cui, J. Li, Hypocrellin-Loaded Gold Nanocages with High Two-Photon Efficiency for Photothermal/Photodynamic Cancer Therapy in Vitro, *ACS Nano* 6 (2012) 8030-8040.

[32] K. Wang, Q. He, X. Yan, Y. Cui, W. Qi, L. Duan, J. Li, Encapsulated Photosensitive Drugs by Biodegradable Microcapsules to Incapacitate Cancer Cells, *J. Mater. Chem.* 17 (2007) 4018-4021.

[33] T. Jamieson, R. Bakhshi, D. Petrova, R. Pocock, M. Imani, A.M. Seifalian, Biological Applications of Quantum Dots, *Biomaterials* 28 (2007) 4717-4732.

[34] J.L. Pelley, A.S. Daar, M.A. Saner, State of Academic Knowledge on Toxicity and Biological Fate of Quantum Dots, *Toxicol. Sci* 112 (2009) 276-296.

[35] N. Singh, B. Manshian, G.J. Jenkins, S.M. Griffiths, P.M. Williams, T.G. Maffeis, C.J. Wright, S.H. Doak, Nanogenotoxicology: The DNA Damaging Potential of Engineered Nanomaterials, *Biomaterials* 30 (2009) 3891-3914.

[36] H.-M. Xiong, ZnO Nanoparticles Applied to Bioimaging and Drug Delivery, *Adv. Mater.* 25 (2013) 5329-5335.

[37] K.C. Barick, S. Nigam, D. Bahadur, Nanoscale Assembly of Mesoporous ZnO: A Potential Drug Carrier, *J. Mater. Chem.* 20 (2010) 6446-6452.

[38] Q. Yuan, S. Hein, R.D.K. Misra, New Generation of Chitosan-Encapsulated ZnO Quantum Dots Loaded with Drug: Synthesis, Characterization and In Vitro Drug Delivery Response, *Acta Biomater.* 6 (2010) 2732-2739.

[39] M. Fakhar-e-Alam, S. Rahim, M. Atif, M.H. Aziz, M.I. Malick, S.S.Z. Zaidi, R. Suleman, A. Majid, ZnO Nanoparticles as Drug Delivery Agent for Photodynamic Therapy, *Laser Phys. Lett.* 11 (2014) 039501.

[40] G. Yang, L. Liu, Q. Yang, S. Wang, Tetraacenaphthoporphyrin: A л-Conjugated Porphyrin with Efficient Light-Activated Anticancer Activity, *Chem. Asian J.* 6 (2011) 1147-1150.

[41] T. Lopez, E. Ortiz, M. Alvarez, J. Navarrete, J.A. Odriozola, F. Martinez-Ortega, E.A. Paez-Mozo, P. Escobar, K.A. Espinoza, I.A. Rivero, Study of the Stabilization of Zinc Phthalocyanine in Sol-Gel TiO_2 for Photodynamic Therapy Applications, *Nanomedicine* 6 (2010) 777-785.

[42] M.-R. Ke, J.M. Eastel, K.L.K. Ngai, Y.-Y. Cheung, P.K.S. Chan, M. Hui, D.K.P. Ng, P.-C. Lo, Oligolysine-Conjugated Zinc(II) Phthalocyanines as Efficient Photosensitizers for Antimicrobial Photodynamic Therapy, *Chem. Asian J.* 9 (2014) 1868-1875.

[43] W.E. Grant, A. MacRobert, S.G. Bown, C. Hopper, P.M. Speight, Photodynamic Therapy of Oral Cancer: Photosensitisation with Systemic Aminolaevulinic Acid, *Lancet* 342 (1993) 147-148.

[44] K. Woodburn, D. Kessel, The Alteration of Plasma Lipoproteins by Cremophor El, *J. Photochem. Photobiol. B* 22 (1994) 197-201.

[45] D.C. Hone, P.I. Walker, R. Evans-Gowing, S. FitzGerald, A. Beeby, I. Chambrier, M.J. Cook, D.A. Russell, Generation of Cytotoxic Singlet Oxygen via Phthalocyanine-Stabilized Gold Nanoparticles: A Potential Delivery Vehicle for Photodynamic Therapy, *Langmuir* 18 (2002) 2985-2987.

[46] M.E. Wieder, D.C. Hone, M.J. Cook, M.M. Handsley, J. Gavrilovic, D.A. Russell, Intracellular Photodynamic Therapy with Photosensitizer-Nanoparticle Conjugates: Cancer Therapy Using a 'Trojan Horse', *Photochem. Photobiol. Sci.* 5 (2006) 727-734.

[47] R. Ideta, F. Tasaka, W.-D. Jang, N. Nishiyama, G.-D. Zhang, A. Harada, Y. Yanagi, Y. Tamaki, T. Aida, K. Kataoka, Nanotechnology-Based Photodynamic Therapy for Neovascular Disease Using a Supramolecular Nanocarrier Loaded with a Dendritic Photosensitizer, *Nano Lett.* 5 (2005) 2426-2431.

[48] B. Zhao, W. Duan, P.-C. Lo, L. Duan, C. Wu, D.K.P. Ng, Mono-Pegylated Zinc(II) Phthalocyanines: Preparation, Nanoparticle Formation, and in Vitro Photodynamic Activity, *Chem. Asian J.* 8 (2013) 55-59.

[49] Q. Zou, L. Zhang, X. Yan, A. Wang, G. Ma, J. Li, H. Möhwald, S. Mann, Multifunctional Porous Microspheres Based on Peptide–Porphyrin Hierarchical Co-Assembly, *Angew. Chem. Int. Ed.* 53 (2014) 2366-2370.

[50] W.-D. Jang, N. Nishiyama, G.-D. Zhang, A. Harada, D.-L. Jiang, S. Kawauchi, Y. Morimoto, M. Kikuchi, H. Koyama, T. Aida, K. Kataoka, Supramolecular Nanocarrier of Anionic Dendrimer Porphyrins with Cationic Block Copolymers Modified with Polyethylene Glycol to Enhance Intracellular Photodynamic Efficacy, *Angew. Chem. Int. Ed.* 44 (2005) 419-423.

[51] R.K. Chowdhary, N. Chansarkar, I. Sharif, N. Hioka, D. Dolphin, Formulation of Benzoporphyrin Derivatives in Pluronics, *Photochem. Photobiol.* 77 (2003) 299-303.

[52] Z.-Y. Zhang, Y.-D. Xu, Y.-Y. Ma, L.-L. Qiu, Y. Wang, J.-L. Kong, H.-M. Xiong, Biodegradable ZnO@Polymer Core–Shell Nanocarriers: pH-Triggered Release of Doxorubicin In Vitro, *Angew. Chem. Int. Ed.* 52 (2013) 4127-4131.

[53] T. Bora, K.K. Lakshman, S. Sarkar, A. Makhal, S. Sardar, S.K. Pal, J. Dutta, Modulation of Defect-Mediated Energy Transfer from ZnO Nanoparticles for the Photocatalytic Degradation of Bilirubin, *Beilstein J. Nanotechnol.* 4 (2013) 714-725.

[54] L. Irimpan, D. Ambika, V. Kumar, V.P.N. Nampoori, P. Radhakrishnan, Effect of Annealing on the Spectral and Nonlinear Optical Characteristics of Thin Films of Nano-ZnO, *J. Appl. Phys.* 104 (2008) 033118.

[55] P. Scardi, M. Leoni, R. Delhez, Line Broadening Analysis Using Integral Breadth Methods: A Critical Review, *J. Appl. Crystallogr.* 37 (2004) 381-390.

[56] J.D. Ye, S.L. Gu, F. Qin, S.M. Zhu, S.M. Liu, X. Zhou, W. Liu, L.Q. Hu, R. Zhang, Y. Shi, Y.D. Zheng, Correlation between Green Luminescence and Morphology Evolution of ZnO Films, *Appl. Phys. A* 81 (2005) 759-762.

[57] A. Van Dijken, E.A. Meulenkamp, D. Vanmaekelbergh, A. Meijerink, Identification of the Transition Responsible for the Visible Emission in ZnO Using Quantum Size Effects, *J. Lumin.* 90 (2000) 123-128.

[58] K. Vanheusden, W.L. Warren, C.H. Seager, D.R. Tallant, J.A. Voigt, B.E. Gnade, Mechanisms Behind Green Photoluminescence in ZnO Phosphor Powders, *J. Appl. Phys.* 79 (1996) 7983-7990.

[59] S. Wei, J. Lian, H. Wu, Annealing Effect on the Photoluminescence Properties of ZnO Nanorod Array Prepared by a PLD-Assistant Wet Chemical Method, *Mater. Charact.* 61 (2010) 1239-1244.

[60] M. Sleiman, D. Vildozo, C. Ferronato, J.M. Chovelon, Photocatalytic Degradation of Azo Dye Metanil Yellow: Optimization and Kinetic Modeling Using a Chemometric Approach, *Appl. Catal., B* 77 (2007) 1-11.

[61] S. Sardar, S. Chaudhuri, P. Kar, S. Sarkar, P. Lemmens, S.K. Pal, Direct Observation of Key Photoinduced Dynamics in a Potential Nano-Delivery Vehicle of Cancer Drugs, *Phys. Chem. Chem. Phys.* 17 (2015) 166-177.

[62] E.S. Jeong, H.J. Yu, S.W. Han, S.J. An, J. Yoo, Y.J. Kim, G.C. Yi, Local Structural Properties of ZnO Nanoparticles, Nanorods and Powder Studied by Extended X-Ray Absorption Fine Structure, *J. Korean Phys. Soc.* 53 (2008) 461-465.

[63] S. Sardar, S. Sarkar, M.T.Z. Myint, S. Al-Harthi, J. Dutta, S.K. Pal, Role of Central Metal Ions in Hematoporphyrin-Functionalized Titania in Solar Energy Conversion Dynamics, *Phys. Chem. Chem. Phys.* 15 (2013) 18562-18570.

[64] S. Sarkar, A. Makhal, T. Bora, K. Lakhsman, A. Singha, J. Dutta, S.K. Pal, Hematoporphyrin–ZnO Nanohybrids: Twin Applications in Efficient Visible-Light Photocatalysis and Dye-Sensitized Solar Cells, *ACS Appl. Mater. Interfaces* 4 (2012) 7027-7035.

[65] P. Kar, S. Sardar, E. Alarousu, J. Sun, Z.S. Seddigi, S.A. Ahmed, E.Y. Danish, O.F. Mohammed, S.K. Pal, Impact of Metal Ions in Porphyrin-Based Applied Materials for Visible-Light Photocatalysis: Key Information from Ultrafast Electronic Spectroscopy, *Chem. Eur. J.* 20 (2014) 10475-10483.

[66] G.B. Deacon, R.J. Phillips, Relationships between the Carbon-Oxygen Stretching Frequencies of Carboxylato Complexes and the Type of Carboxylate Coordination, *Coord. Chem. Rev.* 33 (1980) 227-250.

[67] J.R. Lakowicz, Principles of Fluorescence Spectroscopy, 2nd ed., Kluwer Academic/ Plenum, New York, 1999.

[68] R.M. Clegg, [18] Fluorescence Resonance Energy Transfer and Nucleic Acids, in: J.E.D. David M.J. Lilley (Ed.) Methods in Enzymology, Academic Press 1992, pp. 353-388.

[69] U. Rempel, B. von Maltzan, C. von Borczyskowski, Electron Transfer in Self-Organized Porphyrin-Quinone Compounds on a Picosecond Time Scale, *J. Lumin.* 53 (1992) 175-178.

[70] T. Hasobe, K. Saito, P.V. Kamat, V. Troiani, H. Qui, N. Solladie, K.S. Kim, J.K. Park, D. Kim, F. D'Souza, S. Fukuzumi, Organic Solar Cells. Supramolecular Composites of Porphyrins and Fullerenes Organized by Polypeptide Structures as Light Harvesters, *J. Mater. Chem.* 17 (2007) 4160-4170.

[71] H. Saarenpaa, E. Sariola-Leikas, A.P. Perros, J.M. Kontio, A. Efimov, H. Hayashi, H. Lipsanen, H. Imahori, H. Lemmetyinen, N.V. Tkachenko, Self-Assembled Porphyrins on Modified Zinc Oxide Nanorods: Development of Model Systems for Inorganic−Organic Semiconductor Interface Studies, *J. Phys. Chem. C* 116 (2012) 2336−2343.

[72] H.M. Cheng, W.F. Hsieh, Electron Transfer Properties of Organic Dye-Sensitized Solar Cells Based on Indoline Sensitizers with ZnO Nanoparticles, *Nanotechnology* 21 (2010) 485202.

[73] C.P. LeBel, H. Ischiropoulos, S.C. Bondy, Evaluation of the Probe 2',7'-Dichlorofluorescin as an Indicator of Reactive Oxygen Species Formation and Oxidative Stress, *Chem. Res. Toxicol.* 5 (1992) 227-231.

[74] M.M. Tarpey, I. Fridovich, Methods of Detection of Vascular Reactive Species: Nitric Oxide, Superoxide, Hydrogen Peroxide, and Peroxynitrite, *Circ. Res.* 89 (2001) 224-236.

[75] C. Carraro, M.A. Pathak, Studies on the Nature of Invitro and Invivo Photosensitization Reactions by Psoralens and Porphyrins, *J. Invest. Dermatol.* 90 (1988) 267-275.

[76] C. Yogi, K. Kojima, T. Takai, N. Wada, Photocatalytic Degradation of Methylene Blue by Au-Deposited TiO_2 Film under UV Irradiation, *J. Mater. Sci.* 44 (2009) 821-827.

[77] S. Lakshmi, R. Renganathan, S. Fujita, Study on TiO_2-Mediated Photocatalytic Degradation of Methylene Blue, *J. Photochem. Photobiol. A* 88 (1995) 163-167.

[78] S. Nair, A. Sasidharan, V.V. Divya Rani, D. Menon, S. Nair, K. Manzoor, S. Raina, Role of Size Scale of ZnO Nanoparticles and Microparticles on Toxicity toward Bacteria and Osteoblast Cancer Cells, *J. Mater. Sci. Mater. Med.* 20 (2009) 235-241.

List of Publications

(Peer-reviewed journals)

1. **S. Sardar**, S. Sarkar, M. T. Z. Myint, S. Al-Harthi, J. Dutta and S. K. Pal
"Role of central metal ions in hematoporphyrin-functionalized titania in solar energy conversion dynamics"
Phys. Chem. Chem. Phys. 15 (2013) 18562.

2. Z. S. Seddigi, S. A. Ahmed, **S. Sardar** and S. K. Pal
"Ultrafast Dynamics at the Zinc Phthalocyanine/Zinc Oxide Nanohybrid Interface for Efficient Solar Light Harvesting in the near Red Region"
Sol. Energ. Mat. Sol. Cells. 143 (2015) 63.

3. **S. Sardar**, P. Kar, S. Sarkar, P. Lemmens and S. K. Pal
"Interfacial Carrier Dynamics in PbS-ZnO Light Harvesting Assemblies and their Potential Implication in Photovoltaic/ Photocatalysis Application"
Sol. Energ. Mat. Sol. Cells. 134 (2015) 400.

4. **S. Sardar**, P. Kar, H. Remita, B. Liu, P. Lemmens, S. K. Pal and S. Ghosh
"Enhanced charge separation and FRET at heterojunctions between semiconductor nanoparticles and conducting polymer nanofibers for efficient solar light harvesting"
Sci. Rep. 5 (2015) 17313.

5. **S. Sardar**, S. Ghosh, H. Remita, P. Kar, B. Liu, C. Bhattacharya, P. Lemmens and S. K. Pal
"Enhanced Photovoltage in DSSC: Synergistic Combination of Silver Modified TiO_2 Photoanode and Low Cost Counter Electrode"
RSC Adv. 6 (2016) 33433.

6. Z. S. Seddigi[#], S. A. Ahmed[#], **S. Sardar[#]** and S. K. Pal[#](#contributed equally)
"Carbonate Doping in TiO_2 Microsphere: The Key Parameter Influencing Others for Efficient Dye Sensitized Solar Cell"
Sci. Rep. 6 (2016) 23209.

7. **S. Sardar**, S. Chaudhuri, P. Kar, S. Sarkar, P. Lemmens and S. K. Pal
"Direct Observation of Key Photoinduced Dynamics in a Potential Nano-delivery Vehicle of Cancer Drugs"
Phys. Chem. Chem. Phys. 17 (2015) 166.

8. T. Bora, K. K. Lakshman, S. Sarkar, A. Makhal, **S. Sardar**, S. K. Pal and J. Dutta
"Modulation of defect-mediated energy transfer from ZnO nanoparticles for the photocatalytic degradation of bilirubin"
Beilstein J. Nanotechnol. 4 (2013) 714.

9. **S. Sardar**, P. Kar and S. K. Pal
"The Impact of Central Metal Ions in Porphyrin Functionalized ZnO/TiO_2 for Enhanced Solar Energy Conversion"
J. Mat. NanoSci. 1 (2014) 12.

10. **S. Sardar** and S. K. Pal
"Ultrafast Photoinduced Carrier Dynamics at ZnO Nanohybrid Interfaces for Light Harvesting Applications"
Nanotechnol. Rev. 5 (2016) 113.

11.* **S. Sardar**[#], P. Kar[#], E. Alarousu, J. Sun, Z. S. Seddigi, S. A. Ahmed, E. Y. Danish, O. F. Mohammed and S. K. Pal ([#]co-first authors)
"The Impact of the Metal Ions in the Porphyrin-based Applied Materials for Visible Light Photocatalysis: Key Information from Ultrafast Electronic Spectroscopy"
Chem. Eur. J. 20 (2014) 10475.

12.* S. Chaudhuri, **S. Sardar**, D. Bagchi, S. Singha, P. Lemmens and S. K. Pal
"Sensitization of an Endogenous Photosensitizer: Electronic Spectroscopy of Riboflavin in the Proximity of Semiconductor, Insulator and Metal Nanoparticles"
J. Phys. Chem. A 119 (2015) 4162.

13.* S. Chaudhuri, **S. Sardar**, D. Bagchi, S. Dutta, S. Debnath, P. Saha, P. Lemmens and S. K. Pal
"Photoinduced Dynamics and Toxicity of a Cancer Drug in Proximity of Inorganic Nanoparticles under Visible Light"
ChemPhysChem 17 (2016) 270.

14.* P. Kar, **S. Sardar**, S. Ghosh, M. R. Parida, B. Liu, O. F. Mohammed, P. Lemmens and S. K. Pal
"Nano Surface Engineering of Mn_2O_3 for Potential Light-Harvesting Application"
J. Mat. Chem. C 3 (2015) 8200.

15.* D. Bagchi, S. Chaudhuri, **S. Sardar**, S. Choudhury, N. Polley, P. Lemmens and S. K. Pal
"Modulation of stability and functionality of a phyto-antioxidant by weakly interacting metal ions: curcumin in aqueous solution"
RSC Adv. 5 (2015) 102516.

16.* S. Ghosh, H. Remita, P. Kar, S. Choudhury, **S. Sardar**, P. Beaunier, P. S. Roy, S. K. Bhattacharya and S. K. Pal
"Facile synthesis of Pd nanostructures in hexagonal mesophases as a promising electrocatalyst for ethanol oxidation"
J. Mater. Chem. A 3 (2015) 9517.

17.* S. Ghosh, P. Kar, N. Bhandary, S. Basu, **S. Sardar**, T. Maiyalagan, D. Majumdar, S. K. Bhattacharya, A. Bhaumik, P. Lemmens and S. K. Pal
"Microwave-assisted synthesis of Mn_2O_3 porous Balls as Bifunctional Electrocatalyst for Oxygen Reduction and Evolution Reaction"
Catal. Sci. Tech. 6 (2016) 1417.

(Book Chapters)

1.* S. Sarkar, **S. Sardar**, A. Makhal, J. Dutta and S. K. Pal
"Engineering FRET-based solar cells: manipulation of energy and electron transfer processes in a light harvesting assembly"
Edited by X. Wang and Z. M. Wang, High-Efficiency Solar Cells, SPRINGER, USA 2013, Series Volume 190, Chapter 10, pp 267-318.

* Not included in the thesis.